الجمهورية الجزائرية الديمقراطية الشعبية
REPUBLIQUE ALGERIENNE DEMOCRATIQUE ET POPULAIRE
وزارة التعليم العالي و البحث العلمي
Ministère de l'Enseignement Supérieur et de la Recherche Scientifique
جامعة أبي بكر بلقايد– تلمسان
Université Aboubakr Belkaïd– Tlemcen
كلية التكنولوجيا
Faculté de TECHNOLOGIE

THESE

Présentée pour l'obtention du **grade** de **DOCTEUR EN SCIENCES**

En : Télécommunications

Spécialité : Télécommunications

Par : CHETIOUI Mohammed

Sujet

Design, Optimization and Diagnosis of Microwave Cascaded Filters and Patch Antennas using Coupling Matrix and DGS Techniques

Soutenue publiquement le 24 Novembre 2018, devant le jury composé de :

Mr Feham Mohammed	Professeur	Univ. Tlemcen	Président
Mr Benahmed Nasredine	Professeur	Univ. Tlemcen	Directeur de thèse
Mme Bouasria Fatima	MCA	Univ. Saida	Co-Directeur de thèse
Mr Lasri Boumedienne	Professeur	Univ. Saida	Examinateur 1
Mr Merad Lotfi	Professeur	ESSAT	Examinateur 2

Dedication

To My Parents, my wife and my children

Acknowledgements

I would like to express my deepest gratitude for my supervisor Prof Benahmed Nasredine for all the help, time and support he provided during my Phd degree. I would like to acknowledge the members of jury : Prof. Feham Mohammed, Dr. Bouasria Fatima , Prof. Lasri Boumedienne , Prof. Merad Lotfi for their guidance and for their time and extreme patience reading my thesis. I would like to express gratitude to my friends and colleagues Mr.Boudkhil Abdelhakim, Dr.Bouras Bouhafs and Dr.Bouhmidi Rachid for their valuable help as well as the moral support.

Abstract

Coupled resonator circuits are the basis for the design of two-port bandpass microwave filters. The design approach is based on synthesis of coupling matrix for multiple coupled resonators using Cauchy method and space mapping optimization. This behavior is achieved through the use of filters made up of resonant structures, which have resonators with electromagnetic coupling among them. Antennas present also an integral part of the microwave systems employed to transmit and receive electromagnetic waves for a multitude of purposes; they serve as a transducer that converts guided waves into free-space waves in the transmitting mode, or vice-versa in the receiving mode.

In this view, the present research work describes analytical problems of microwave cascaded filters and patch antennas and explains their physical behaviors with particular emphasis on major optimization challenges facing the device structure complexity. The different microwave devices are optimized using advanced computer aided tuning (CAT) techniques including coupling matrix, Defected Ground Structure (DGS) and Artificial Neural Networks (ANN) to vary the device geometry and maximize its performance with a high accuracy for the selective band of frequencies.

Key words: Coupled Resonator Filter, Space mapping, Cauchy method, Patch Antennas, Coupling Matrix, DGS, ANN Optimization.

Table of contents

Dedication II

Acknowledgement III

Abstract III

List of Figures III

List of Tables III

List of Abbreviations III

General Introduction 02

Chapter One: An Overview of Microwave Bandpass Filter Theory 05

1.1 Introduction 06

1.2 Filters Approximation 06

  1.2.1 Butterworth Function Approximation 06

  1.2.2 Chebyshev Function Approximation 08

  1.2.3 Elliptic Function Approximation 10

1.3 Elements Realization for Lowpass Prototype Filters 11

  1.3.1 Butterworth Lowpass Prototype Filters 12

  1.3.2 Chebyshev Lowpass Prototype Filters 12

  1.3.3 Elliptic Lowpass Prototype Filters 13

1.4 Lowpass Prototype to Bandpass Filter Transformation 14

  1.4.1 Lowpass Prototype Filter with ideal J and K inverters 15

1.5 Extraction Circuit Models for Chebyshev Bandpass Filters 16

1.6 Influences of losses on bandpass filters 18

1.7 Conclusion 19

Chapter Two: Defected ground structure (DGS) Technique 21

2.1 Introduction 22

2.2 Defected Ground Structure Element 22

2.3 Frequency Characteristics of DGS Unit 23

2.4 Analysis and Design of the DGS 24

- 2.4.1 DGS Frequency Features 24
- 2.4.2 Circuit Equivalent Modeling and Parameter Diagnostic 25
  - a. Circuit Modeling: Parallel LC 25
  - b. Circuit Modeling: Parallel RLC 29

2.5 Various DGS slots Topologies Modeling 33

- 2.5.1 Study of Double Triangular-Head DGS (DTH-DGS) 33
  - a. Effect of Slot Head Dimension (a=b) 33
  - b. Effect of Slot Width (g) 34
  - c. Effect of the slot length (d) 35
- 2.5.2 Study of Triangular-Head-DGS (TH-DGS) 36
  - a. Effect of Slot Head Dimension (a=b) 37
  - b. Effect of Slot Width (g) 38
  - c. Effect of the slot length (d) 39

2.6 Design of proposed Quasi-Elliptic Lowpass Filter with single attenuation pole 40

- 2.6.1 Conception of typical Hi-LO Lowpass Filter (LPF) 40
- 2.6.2 Propose of Quasi-Elliptic Lowpass Filter based semicircular- DGS 44

2.7 Conclusion 48

References **49**

Chapter Three: Microwave Filter Optimization: Polynomial and Coupling Matrix **50**

3.1 Introduction 51

3.2 Basic Equations for Polynomials Function for Filter Networks 51

- 3.2.1 Transmission and Reflection Polynomial Synthesis 53
- 3.2.2 Normalization of the transfer function and characteristic polynomials 55
- 3.2.3 Characteristic and properties of the design polynomials 57
- 3.2.4 Polynomial synthesis for Symmetric and Asymmetric Filtering Functions examples 60

3.3 Generalized Chebyshev Polynomials Approximation (Pseudo Elliptic) 62

  3.3.1 Polynomial Synthesis 63

  3.3.2 Recursive Cameron Algorithm 64

  3.3.3 Recursive Algorithm Implementation by Matlab 66

3.4 Coupling Matrix Synthesis of Microwave Filters 67

  3.4.1 Coupling Matrix Definition 67

  3.4.2 Impedance Matrix Calculation 68

  3.4.3 The Formulation General of the Coupling Matrix CM 72

3.5 Synthesis process of the (N +2) Transversal Coupling Matrix 73

  3.5.1 Basics for (N x N) Coupling Matrix Synthesis 73

  3.5.2 (N+2) Transversal Coupling Matrix Representation 74

    a. Calculation of Admittance Function [Y]-Parameters 74

    b. Circuit Approach: Transversal Microwave Filter Network 75

    c. Construction of Transversal Coupling Matrix (TCM) 76

    d. Reduction of Transversal Coupling Matrix to the Folded Canonical Form 77

3.6 Illustrative examples and discussions 78

  3.6.1 Illustrative Example I: Simulated fifth-Order Filter with Four TZs 78

  3.6.2 Illustrative Example II: Diagnosis of a Fourth-Order Filter with one TZ- 81

3.7 Computer–Aided Tuning and Diagnosis Techniques of Microwave Filters 84

  3.7.1 Bandpass Filter Modeling and Synthesis 84

  3.7.2 Generalized Formulation of Cauchy Method for Parameter Extraction (PE) 86

  3.7.3 General Formulation of Aggressive Space Mapping (ASM) Optimization Algorithm 88

3.8 Design and Optimization of Five Pole Coaxial Microwave Bandpass Filter 91

  3.8.1 Design Coaxial Filter Using the Coupling Matrix Model 91

  3.8.2 Physical Realization of Coupling Matrix 94

    a. Calculation of Resonance Frequency of Coaxial Resonator Cavity Configuration 94

    b. Calculation of wall Dimensions for Inter-resonator Coupling 94

    c. External Quality Factor (Q_{ext}) Calculation 95

  3.8.3 Hybrid Optimization Using the Cauchy and ASM techniques 96

    a. Dimensioning problem for coaxial microwave filter Design 96

    b. Proposed Solution Using the Combinations of Cauchy/ ASM Techniques 97

3.9 Conclusion 104

References 105

Chapter Four: Substrate Integrated Waveguide Antennas 108

4.1 Introduction 109

4.2 Principles and Classification of Antennas 112

4.3 Micro strip Antenna 114

4.4 Waves in Microstrip 115

  4.4.1 Surface Waves 116

  4.4.2 Leakey Waves 116

  4.4.3 Guided Waves 117

4.5 Basic Characteristics 117

4.6 Feeding Methods 119

  4.6.1 Microstrip Line 119

  4.6.2 Co-axial Probe 119

  4.6.3 Aperture Coupling 120

  4.6.4 Proximity Coupling 121

4.7 Methods of Analysis 121

  4.7.1 Transmission line model 122

    a. Effective Length, Resonant Frequency, and Effective Width 124

    b. Conductance Resonant, Input Resistance and Matching Techniques 125

  4.7.2 Cavity model 130

4.8 Substrate Integrated Waveguides 133

  4.8.1 SIW design rules 133

  4.8.2 Guided wave and Leaky wave Regions of Operation 137

  4.8.3 Circular Substrate Integrated Waveguide Cavity 138

4.9 Neural Network Algorithm 140

  4.9.1 Feed-forward (Input Signal) 144

  4.9.2 Back Propagation (Output Error) 145

4.10 Results and discussion 146

  4.10.1 Simulation Software 146

  4.10.2 Proposed antennas geometry and design procedures 147

4.10.3 Artificial neural network modeling of SIW antenna 148

a. Results and discussion of circular SIW antenna (microstrip-to-SIW transition) 149

a.1 Data generation 149

a.2 Network architecture and training 149

a.3 Optimization results 151

b. Results and discussion of SIW antenna (coax-to-SIW transition) 152

b.1 Design and data generation 152

b.2 Network architecture and training 154

b.3 Optimization Procedure 156

b.4 Simulated Return Losses 158

b.5 Input Impedance and Radiation Pattern 159

b.6 Equivalent Circuit Model 160

4.11 Conclusion 162

References 157

General Conclusion 170

List of publications 175

List of figures

Fig 1.1	Butterworth response for various filter order *n*	07
Fig 1.2	Pole distribution for Butterworth response	07
Fig 1.3	Chebyshev response for various filter order *n*	08
Fig 1.4	Pole distribution for Chebyshev response	09
Fig 1.5	Amplitude response of a Fourth-order elliptic function lowpass response	11
Fig 1.6	(a) The prototype of lowpass filters and (b) its dual	12
Fig 1.7	Elliptic lowpass prototype filter by using parallel resonators, even order (up), odd order (down)	14
Fig 1.8	Elliptic lowpass prototype filter by using series resonators odd order	14
Fig 1.9	Lowpass prototype filters modified to include immittance inverters (a)impedance inverter (b) admittance inverter	16
Fig 1.10	Operation of impedance and admittance inverters.	16
Fig 1.11	(a)Coupling matrix model for Chebyshev filters,(b)impedance inverter model for Chebyshev filters, and (c) admittance inverter model for Chebyshev filters .	17
Fig 1.12	Bandpass filter circuit including lossy resonators.	18
Fig 1.13	Dissipation effects on the insertion loss characteristic of the bandpass filter	19
Fig 2.1	Layouts of proposed DGS ,(a) semi-circular-DGS, (b) DTH-DGS, (c) TH-DGS	22
Fig 2.2	Three-dimensional view of the DGS	23
Fig 2.3	S_{11} and S_{12} of the DTH-DGS with EM simulation	23
Fig 2.4	E-field Circulation on the slot metallization (a) at 10 GHz, (b) at 3.1 GHz	24
Fig 2.5	Conventional design and analysis method of DGS	26
Fig 2.6	(a) DGS topology with the dimensions of g=0.4 mm and a=b=5mm ,(b) Equivalent circuit extracting (L=4.417nH and C=0.08017pF),(c) EM and circuit simulations result of proposed TH-DGS	27
Fig 2.7	(a) Equivalent circuit of the microstrip line with unit DGS. (b) Butterworth prototype of one pole lowpass filter [14]	28
Fig 2.8	The equivalent circuit of the DGS with parallel resistance	30
Fig 2.9	(a) DGS structure**,** (b) The equivalent circuit of the DGS**,** (c) S-parameters of the equivalent parallel RLC-circuit (R=3825 ohm) and the EM simulation responses	30
Fig 2.10	The current flow in an equivalent circuit model of a DGS: (a,b) Conventional model in lossless – (c,d) model with losses	32
Fig 2.10A	The E-Field distributions of the TH-DGS at (**a**) pass-band and **(b)** stop-band	32

Fig 2.11a 3-D view of the double triangular-head DGS 33
Fig 2.11b Wire frame view of the double triangular-head DGS 33
Fig 2.12 Simulated S-parameters of double triangular- head slot for different head lengths (**a**); with the gap (g=0.4) and (d=2) , (a=b) 33
Fig 2.13 EM simulation depending on different gap (g) dimensions 35
Fig 2.14 EM simulation depending on the different slot length (d) dimensions; the gap dimension is fixed as g=0.4 mm and a=b=5mm 36
Fig 2.15a 3-D view of the Triangular Head DGS 37
Fig 2.15b Wire frame view of the Triangular Head DGS 37
Fig 2.16 Simulated S-parameters of TH slot for different head lengths (a=b); with the gap dimension is fixed and d is fixed 37
Fig 2.17 EM simulation depending on different gap dimensions (g) 38
Fig 2.18 EM simulation depending on the different slot dimensions (d) 39
Fig 2.19 (a) Conventional LC ladder LPF ,(b) The S-Parameter Simulation 42
Fig 2.20 (a) layout of stepped impedance LPF and its dimensions (in mm) (b) S_{21} and S_{11} frequency response of Butterworth filter of 4th degree 44
Fig 2.21 (a) Lumped element circuit with zero transmission LPF, (b) the S-Parameter simulation 45
Fig 2.22 The improved semi-circular DGS LPF ,(a) 2D- LPF with semi-circular DGS (b) EM simulation , (c) 3D - LPF with semi-circular DGS 47
Fig 2.23 Comparison between simulated results of conventional stepped LPF and the proposed LPF with semi-circular –DGS 47
Fig 3.1 A general two-port doubly terminated lossless transmission network 52
Fig 3.2 Flow chart of microwave filter synthesis polynomial functions(reel coefficients) procedure 55
Fig 3.3 Insertion Loss (IL), S_{21} (dB) with Ripple value and Return Loss (RL) S_{11} (dB) 56
Fig 3.4 Characteristic Function $C(s)|_{s=j\omega}$ 56
Fig 3.5 Permissible zero locations of lowpass prototype characteristic polynomials,(a) zero locations of *F(s).* (b) zero locations of *P(s)* on the (jω) axis ,real axis, and as a complex quad 58
Fig 3.6 (a) asymmetric root locations of F(s) on the jω axis, (b) asymmetric root locations of P(s) in the upper band, (c) Root locations of P(s) as pairs symmetrically located , (d.) asymmetric root locations of P(s) in the upper and lower bands 59
Fig 3.7 The routing diagram and coupling values of the first example 60
Fig 3.8 Frequency response of the normalized filter 61
Fig 3.9 The routing diagram and coupling values of the fifth-order lowpass prototype circuit with one transmission zero 62

Fig 3.10	Fifth -order Bandpass prototype response (zero on the right)	62
Fig 3.11	Lowpass prototype transfer and reflection characteristics of four-degree asymmetric Chebyshev filters with two transmission zeros at s1=+j1.52 and s2=+1.95	67
Fig 3.12	The equivalent circuit representing a general two-port network	69
Fig 3.13	The equivalent circuit of n-coupled resonators	73
Fig 3.14	Equivalent two-port of a multicoupled microwave filter for the (N +2) Coupling Matrice	75
Fig 3.15	Canonical transversal array for reciprocal filters. (a) N-resonator transversal array including direct source–load coupling MSL (b) Equivalent circuit of the kth resonator in the transversal network	77
Fig 3.16	N +2 fully canonical coupling matrix M for the transversal array. The matrix is symmetric about the principal diagonal	77
Fig 3.17	The transversal topology	78
Fig 3.18	Folded N+2 canonical network coupling matrix: (a)folded coupling Matrix form “s” and “xa” couplings are in general zero for symmetric characteristics;(b) coupling and routing schematic	80
Fig 3.19	Five Degree Filter: (a)Transversal coupling matrix .(b)Coupling and routing schematic	80
Fig 3.20	Five degree filter: (a)Folded coupling matrix normalized.(b) Coupling-routing diagram	81
Fig 3.21	Transmission and return loss performance of fifth order filter	83
Fig 3.22	(a) Denormalized Coupling matrix of fourth order filter. (b) possible realization with coaxial cavities	84
Fig 3.23	Fourth degree canonical filter: analysis of S-parameters	85
Fig 3.24	Lossless coupled resonator Bandpass filter’s equivalent circuit	85
Fig 3.25	The $(N + 2)$ transversal matrix constructed by the parameters r_{22k}, r_{21k}, λ_k and M_{SL}	88
Fig 3.26	Representation of the fine and coarse models	91
Fig 3.27	Optimization Process Flow Chart of the ASM algorithm	93
Fig 3.28	(a) The topology of the Five-Degree filter, (b) Coupling scheme of the proposed coaxial coupled filter	93
Fig 3.29	The simulated ideal response of the microwave filter based on the coupling matrix model	94
Fig 3.30	(a) EM model of a coaxial resonator with air cavity and tuning screw. (b) Design curve for frequency Resonance Cavity	95
Fig 3.31	(a) Configuration for extracting coupling coefficient Mij (b) Design curve for Mij	95
Fig 3.32	(a) Configuration for extracting External Quality Factor. (b) Design curve for $Qext$	96

Fig 3.33 3D structure: A five-pole coaxial coupled resonator filter 94
Fig 3.34 The Initial Response :HFSS simulation results based on initial physical dimensions 94
Fig 3.35 The coarse model of the five pole microwave coaxial bandpass filter in ADS 102
Fig 3.36 Responses of the five resonators coaxial Bandpass filter in each iteration 102
Fig 3.37 Comparison of performance in the first, fourth and sixth iterations in the coaxial Bandpass filter 103
Fig 4.1 The antenna as a transition region between guided and propagating wave 112
Fig 4.2 Equivalent Circuit Diagram of the antenna as a guiding device 113
Fig 4.3 Classification of antenna on basis of physical structures 114
Fig 4.4 Rectangular Microstrip Patch Antenna 115
Fig 4.5 Hertz Dipole on a Microstrip Antenna 115
Fig 4.6 Surface Wave in Microstrip Patch 116
Fig 4.7 Leaky Waves on Microstrip Patch 116
Fig 4.8 Microstrip antenna and coordinate system. 117
Fig 4.9 Representative shapes of microstrip patch elements 118
Fig 4.10 Microstrip Line Feeding 119
Fig 4.11 Coaxial feeding method 120
Fig 4.12 Aperture-coupled feed 120
Fig 4.13 Proximity-coupled feed 121
Fig 4.14 Electric field lines and effective dielectric constant geometry. 123
Fig 4.15 Physical and effective lengths of rectangular microstrip patch. 123
Fig 4.16 Rectangular microstrip patch and its equivalent circuit transmission model 125
Fig 4.17 Slot conductance as a function of slot width. 127
Fig 4.18 Recessed microstrip-line feed and variation of normalized input resistance. 129
Fig 4.19 Charge distribution and current density creation on the microstrip patch 131
Fig 4.20 Configuration of an SIW 133
Fig 4.21 Tapered transition between a 50 Ω microstrip line and SIW. 136
Fig 4.22 Leakage loss curves from 10^{-6} to 10^{-2} Np/rad with respect to distance between the vias and their diameters normalized with the λ_c 138
Fig 4.23 Suitable region for SIW design parameters 138
Fig 4.24 Circular Waveguide Cavity 139
Fig 4.25 Example of Circular SIW Cavity 140
Fig 4.26 Generalized Neuron Model 141
Fig 4.27 Illustration of the directions of two basic signal flows in a multilayer perception: forward propagation of function signals and back propagation 142

of error signals.
Fig 4.28 Three-layer neural networks. 144
Fig 4.29 Proposed antenna geometry using (a) microstrip-to-SIW transition and (b) coax-to-SIW transition. 147
Fig 4.30 MLP-ANN architecture selected for the optimization of microstrip-to-SIW transition 150
Fig 4.31 Return loss graph in dual-band Ku/K bands of proposed circular SIW antenna 151
Fig 4.32 Return loss graph in dual-band Ku/K bands of circular SIW antenna based ANN modeling 152
Fig 4.33 MLP-ANN architecture selected for the optimization of coax-to-SIW transition 155
Fig 4.34 Adaptive CAT procedure for the optimization process 157
Fig 4.35 Return loss graph in dual-band X/K bands of the optimized dual band coaxial-fed SIW cavity resonator antenna based ANN modelling 158
Fig 4.36 Real Z_{in}, and imaginary Z_{in} plots of the cavity resonator 159
Fig 4.37 Radiation pattern graph of the optimized dual band coaxial-fed SIW cavity resonator antenna. 159
Fig 4.38 Equivalent circuit of the optimized dual band coaxial-fed SIW cavity resonator antenna 160

List of tables

Tab 2.1 DTH slot characteristics for different slot head lengths (a) 31

Tab 2.2 DTH-DGS slot characteristics for different slot width (g) 32

Tab 2.3 DTH slot characteristics for different slot lengths d 33

Tab 2.4 TH slot characteristics for different slot head lengths (a) 35

Tab 2.5 TH slot characteristics for different slot widths (g) 35

Tab 2.6 TH characteristics for different slot lengths (d) 36

Tab 2.7 Filter specifications 37

Tab 3.1 Singularities of Fourth -Degree Asymmetric Chebyshev Filter with two transmission Zeros 67

Tab 3.2 Filtering function :coefficients of numerator and denominator polynomials of $y_{12}(s)$ and $y_{22}(s)$ 79

Tab 3.3 Filtering function: residues, eigenvalues and eigenvectors 79

Tab 3.4 Physical sizes and parameters of the coaxial Bandpass filter in each iteration (mm) 99

Tab 3.5 Physical sizes and parameters of the coaxial Bandpass filter in each iteration (mm) 104

Tab 4.1 Proposed antenna and optimized parameters values according to the transition type 148

Tab 4.2 Geometrical parameters of the proposed dual band coaxial-fed SIW cavity resonator antenna 154

Tab 4.3 ANN parameters of the dual band coaxial-fed SIW cavity resonator antenna 156

Tab 4.4 Adaptive CAT variables for the optimization process 156

Tab 4.5 Geometrical parameters of the equivalent circuit of the optimized dual band coaxial-fed SIW cavity resonator antenna 161

Tab 4.6 Comparison of the optimized dual band coaxial-fed SIW cavity resonator antenna to antennas in 161

List of Abbreviations

RF	Radio Frequency
EM	Electromagnetic
LPF	Lowpass Filter
BPF	Bandpass Filter
FBW	Fractional Bandwidth
HFSS	High Frequency Structural Simulator
BW	BandWidth
DGS	Defected Ground Structure
DTH-DGS	Double Triangular-Head DGS
TH-DGS	Triangular-Head-DGS
ANN	Artificial Neural Network
MLP	Multi Layered Perceptron
BP	Back Propagation
LR	Learning Rate
MSE	Mean Square Error
LM	Levenberg-Marquardt
MLPFFBP	Multi Layered Perceptron Feed Forword Back Propagation

General Introduction

General Introduction

The fast development of microwave filters is important in the conception and design of modern mobile and satellite communication systems. The novel applications require increasingly compact and lightweight designs, without losing the selectivity and the ability to reject unwanted signals. There are several phases of filter design and usually require a lot of effort to achieve the suitable behavior. One of the most important phases is the desired synthesis of the transfer function [2 chap3]. We will calculate the coupling between resonators for obtaining a transfer function according to the needs of the application in this phase. The next step is its implementation with a specific technology.

Nowadays researchers give more importance and interest to the performance enhancement and low internal losses in Bandpass. The concept of lowpass microstrip filters (LPFs) with a reduced costs, low insertion loss (IL)[1 chap1], higher selectiveness, broad stopband and miniaturization of size are increasingly required in modern communication systems for eliminating the unwanted frequency rejection. The high impedance narrow microstrip lines that are unsuitable for fabrication and increases the length of LPF is subrogated by the DGS shapes. So The Defect ground structure (DGS) technique is achieved by etching slots in ground plane of the microwave filters. The method is applied for line microstrip. The slots are synthesized to realize an accurate the microstrip filters' performance, as increasing the sharpness of the cut-off slop, and to increase the stopband range frequency .In addition, by using this technique, the compact size of filter can also be achieved. The DGS technique disperses the shield current distribution in the ground plane. As a result, we maintain the control on the excitation and propagation of the electromagnetic waves through the substrate layer. This inconvenience will change the characteristics of a transmission line like it can increase the effective capacitance and inductance of a transmission line [8, 10 chap2].

In the present thesis, we intend to address the synthesis microwave filters through the coupling matrix technique, also studying different similarity transformations which are applied on the coupling matrix that will lead us to implement practical topology, either for bandpass or rejected band [1chap3]. The famous methods will be practical to design a high accuracy performance of microwave filters in many technologies. Finally, we will investigate some alternative topologies, as well as different practical examples [6,7chap3].The interesting design features of the microstrip antennas are mainly the complex resonant frequencies, the radiation pattern, and the input impedance. The main operational disadvantages of microstrip antennas are their low efficiency, low power, high quality factor (Q), low polarization purity, poor scanning performance, spurious radiation, and very narrow bandwidth, which typically represents only a fraction of a percentage or at most a few percent. In some applications, such as in government security systems, narrow bandwidths are desirable [3 chap4].

Objectives:

The main objective of my thesis is the investigation and application of the coupling matrix technique to the synthesis of different filter transfer functions for communications. After the first phase of study of the technique, it is required to implement a tool that is capable of calculating the necessary links between the elements of the filter, in order to synthesize various transfer functions of practical application. Finally we will propose a topology that we can synthesize in coaxial cavity microwave technology. Another main objective is to prove the use of a novel synthesis technique to transform the coupling matrix coefficients to physical parameters validated by a coaxial microwave filter examples. An important purposeis considered in this thesis is the development of accurate synthesis technique for microwave filters, based on coupling matrix approach corresponding equivalent circuit models.This work is also devoted to propose new optimization technique on microwave filters, which stand on the extraction of the coupling matrix from simulated S parameters by using the Cauchy method, then deduce the precise physical parameter by employing the space mapping technique. The next objective is to optimize SIW patch antenna using advanced computer aided tuning (CAT) technique and Artificial Neural Networks (ANN) in order to maximize its performance with a high accuracy for the selective band of frequencies. As a final goal of this thesis is also to miniaturize and reconfigure the microwave filters and antennas devices by using Defected Ground Structure (DGS) technique.

The thesis has been divided into 4 chapters. **The first chapter** includes the synthesis procedure for the characteristic polynomials to accomplish the ideal conventional prototype filters: Butterworth, Chebyshev, and elliptic function filters.

In Chapter 2 we addressed the different equivalent circuits of defected ground structures are investigated. A new shaped DGS has been studied to design Low Pass Filter DGS on the ground plane.

In the third chapter, we discussed and calculated the scattering parameter equations which were used in the polynomial illustration of the transfer and reflection characteristics of prototype filtering functions. We have also derived Cameron recursion method and used it to found the transfer and reflection polynomials for Chebyshev filtering characteristics of the microwave filter.We also study some of the different sequences of transformations that can be applied to the coupling matrix obtained, be it (N+2)x(N+2). We can thus cancel the desired coupling, and obtain the matrix in a more convenient way for the technology that we will use in the physical implementation. We will focus mainly on the configurations known as 'folded canonical form, In this chapter, we address the synthesis of filters with arbitrarily located attenuation poles, using non-resonant nodes [4,5 chap3]. We will propose the implementation of several examples. We will start from the type of filter , band pass / band rejected , the position of the zeroes transmission / reflection, the order of the filter and the desired return losses, and we will obtain the coupling matrix, the transfer functions, the Topology to be implemented and possible physical circuits.

In chapter four , the rectangular patch antennas will be designed by changing the feed position, size of the substrate, and shape of the patch to get our objective or target output. This elementary design is based on changing the dimension of length because here various losses are not considered. Microstrip antenna founded many applications in the real world due to its low-profile feature. Some of the applications are GPS, Bluetooth, Wi-Fi, missiles, and also in radio communication system etc. Many other applications are under research like multiband antenna, array antenna etc. This part presents the state of the art of SIW technology: recent advances in the field of antennas implemented in SIW technology will be described and discussed.

Chapter 1: An Overview of Microwave Bandpass Filter Theory

1.1. Introduction

Microwave filters are used to select or reject signals at different frequencies in a host of RF systems. Filters can be presented into several response functions, depending on the positions of the poles and zeros of the transfer function. In microwave filters where lumped elements are not realizable, they are applied by using distributed elements with coupling elements to obtain specified transfer characteristic functions. The performance of the microwave filters is generally controlled by the geometrical dimensions and the material parameters. The design process begins by assigning a rational function that closes the desired filter specifications [2,6] ,in which it consists of approximation of the transfer function ,synthesis of the filter circuit, scaling and conversion and physical implementation. The challenge of this procedure to transform the parameters of the equivalent circuit into physical dimensions. The operating frequency, return loss, bandwidth, etc…are needed to meet desired specification to determine accurate microwave filters topology [4].

In this chapter we will be concerned with the description of the synthesis process for the characteristic polynomials in order to achieve the ideal conventional prototype filters: Butterworth, Chebyshev, and elliptic function [2].

1.2. Filters Approximation

1.2.1. Butterworth Function Approximation

The frequency performance of the Butterworth microwave filter is maximally flat, (Not Ripple) in the passband and rolls off towards zero in the stopband. All poles are distributed on a unity circuit on the complex s-plane. The approximation is defined by [1, 7]:

$$|S_{21}(j\omega)|^2 = \frac{1}{1+\left(\frac{\omega}{\omega_c}\right)^{2n}} \tag{1.1}$$

Where n is the Degree of the prototype filter, which corresponds to the number of reactive elements, required in the lowpass prototype filter. It's all stopband zeros (transmission zeros) located at infinity. Which have an insertion loss $A_{\max} = 3.01\ dB$ at the cutoff frequency ω_c . This transition becomes more rapid when the order of the filter is higher. The calculated maximally flat prototype transmission characteristics corresponding to different circuit orders are illustrated in Figure 1.1

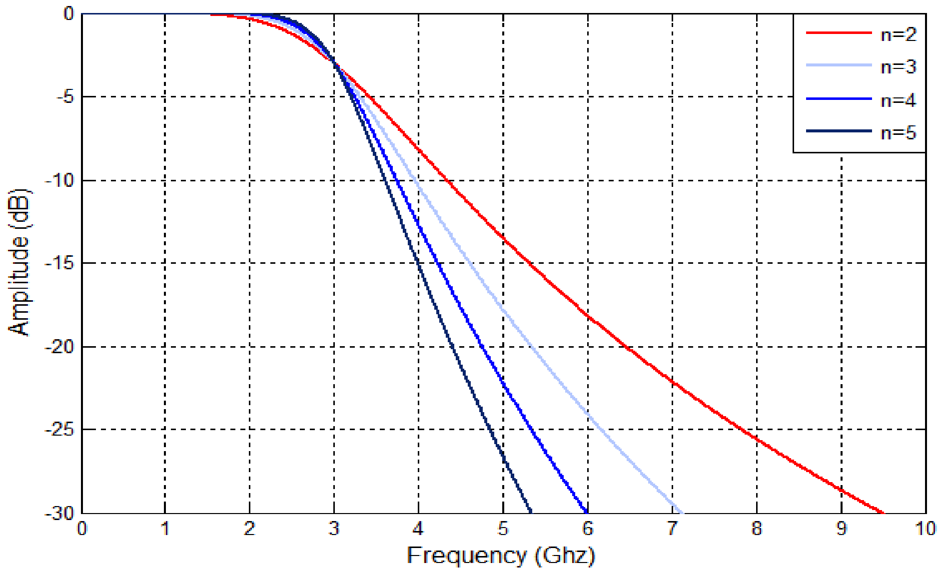

Figure 1.1: Butterworth response for various filter order n

A rational transmission and reflection coefficient function constructed from equation (1.1) are expressed by [9]:

$$S_{21}(s) = \frac{1}{\prod_{k=1}^{n}(s - s_k)} \quad \text{and} \quad S_{11}(s) = \frac{\pm s^n}{\prod_{k=1}^{n}(s - s_k)} \tag{1.2}$$

with

$$s_k = j\exp\left(\frac{2k-1}{2n}\right) \tag{1.3}$$

- All the transmission zeros of $s_{21}(s)$ are at infinity (all poles)
- The poles p_i lie on the unit circle in the left- half-plane at equal angular spacing, $|p_i| = 1$. The poles locations are illustrated in Figure 1.2.

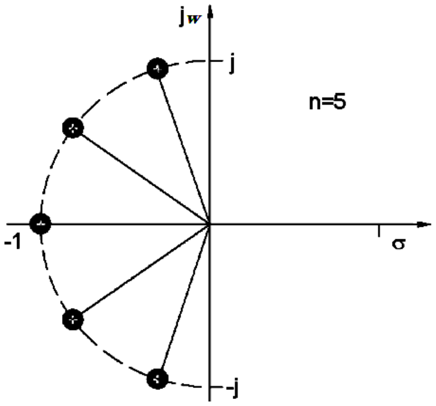

Figure 1.2: Pole distribution for Butterworth response

1.2.2. Chebyshev Function Approximation

Chebyshev frequency response offers sharper slope for lower filter order n, than that of the Butterworth response, but it shows the equi-ripple in the passband. The amplitude-square transfer function of the filter is given by [9]

$$|S_{21}(j\Omega)|^2 = \frac{1}{1+\varepsilon^2 C_n^2(\Omega)} \tag{1.4}$$

Where the ripple constant ε is related to a given passband ripple L_{Ar} in dB by

$$\varepsilon = \sqrt{10^{\frac{L_{Ar}}{10}} - 1} \tag{1.5}$$

Typical frequency response of the Chebyshev filter prototype is illustrated in Figure 1.3.

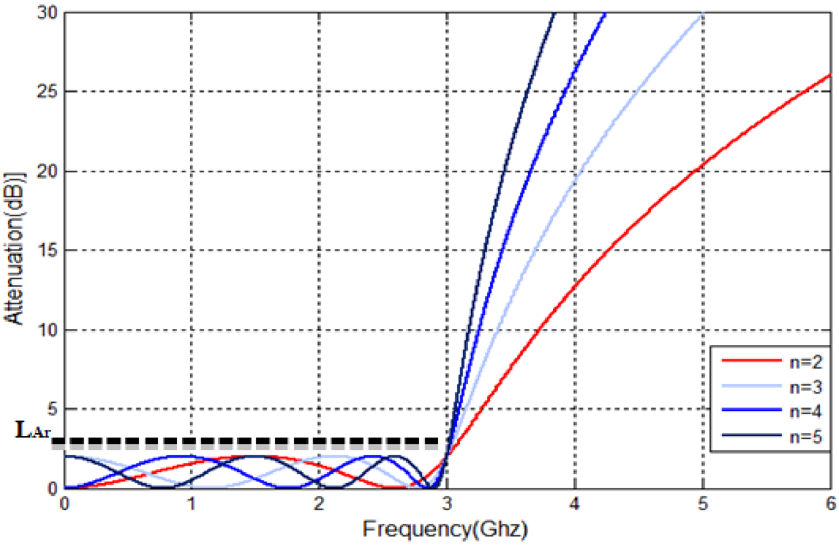

Figure 1.3: Chebyshev response for various filter order *n*

$C_n(\omega)$ is a Chebyshev function of the first kind of order n, which is defined as

$$C_n(\omega) = \begin{cases} \cos(ncos^{-1}\omega)\,, |\omega| \le 1 \\ \cosh(ncosh^{-1}\omega)\,, |\omega| \ge 1 \end{cases} \tag{1.6}$$

The same as in the case of Butterworth, all transmission zeros are located at infinity. We can derive a general formula of the rational transfer function from (1.4) for the Chebyshev filter that is [9]

$$S_{21}(p) = \prod_{i=1}^{n} \left\{ \frac{\left[\eta^2 + \sin^2(i\pi/n)\right]^{1/2}}{p + j\cos\left[\sin^{-1}(j\eta) + \theta_i\right]} \right\} \tag{1.7}$$

where

$$\theta_i = \frac{(2i-1)\pi}{2n} \qquad \text{and} \qquad \eta = \sinh\left(\frac{1}{n}\sinh^{-1}\frac{1}{\varepsilon}\right) \tag{1.8}$$

Now $\left|S_{21}(j\omega)\right|^2 = 1 - \left|S_{11}(j\omega)\right|^2$ then

$$S_{11}(p) = \prod_{i=1}^{n}\left\{\frac{p^2 + j\cos^2(\theta_i)}{p + j\cos\left[\sin^{-1}(j\eta) + \theta_i\right]}\right\} \tag{1.9}$$

The microwave filter can then be synthesized as a lowpass ladder network by formulating:

$$Z_{in}(p) = \frac{1 + S_{11}(p)}{1 - S_{11}(p)} \tag{1.10}$$

The poles p_i lie on the elliptic circle in the left- half-plane at equal angular spacing, $|p_i| \neq 1$. The poles locations are illustrated in Figure 1.4.

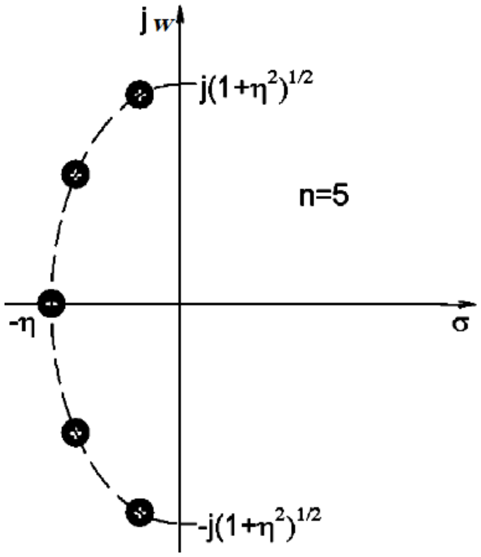

Figure 1.4: Pole distribution for Chebyshev response [1]

Similar to the maximally flat case, all the transmission zeros of $S_{21}(p)$ are located at infinity. Therefore, the Butterworth and Chebyshev filters dealt with so far are sometimes referred to as all-pole filters. However, the pole locations for the Chebyshev case are different and lie on an ellipse in the left half-plane. The pole distribution is shown, for n = 5, in Figure (1.4).

1.2.3. Elliptic Function Approximation

The elliptic function approximation is equi-ripple in both the passband and the stopband. It thus has the optimum response in terms of selectivity from passband to stopband. Elliptic filters are also characterized by equi-ripple responses in the stop and pass bands. They are also known as Cauer filters, but are normally called elliptical filters because of the use of elliptical integrals in the synthesis. The amplitude-squared transfer function is given in (1.11). [2]

$$\left|S_{21}(j\omega)\right|^2 = \frac{1}{1+\varepsilon^2 . C_n^2(\omega)} \tag{1.11}$$

Where $C_n(\omega)$ is a rational function of ω, and is derived from complete elliptical integral of the first kind and Jacobian elliptic functions, ε is the ripple factor. The major feature of the transfer function $S_{21}(\omega)$ is to have equal ripples in the passband and stopband regions, with sharp transition in between them. The skirt created is very steep. Approximation Elliptic function offers greater selectivity than Chebyshev, for this reason it is sometimes considered the ultimate approximation to the ideal filter response there are no other filter of the same order which can give a faster transition for a given ripple [9].

The Elliptic response that exhibits the equal-ripple in both the passband (poles) and stopband (zeros) is depicted in Figure (1.5)

$$C_n(\omega) = \begin{cases} M.\dfrac{\prod\limits_{i=1}^{n/2}(\omega_i^2-\omega^2)}{\prod\limits_{i=1}^{n/2}(\omega_s^2/\omega_i^2-\omega^2)} & \text{for n even} \\[2ex] N.\dfrac{\prod\limits_{i=1}^{(n-1)/2}(\omega_i^2-\omega^2)}{\prod\limits_{i=1}^{(n-1)/2}(\omega_s^2/\omega_i^2-\omega^2)} & \text{for n} \geq 3 \text{ (odd)} \end{cases} \tag{1.12}$$

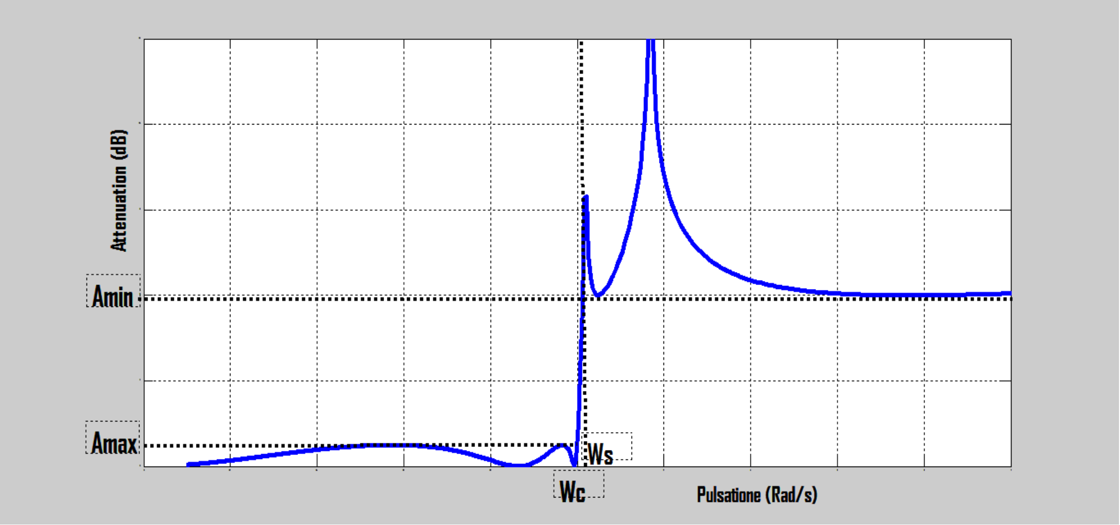

Figure 1.5: Amplitude response of a Fourth-order elliptic function lowpass response

The parameter ω_s is the frequency at which the equal-ripple stopband starts, which is greater than one and where ω_i ($0<\omega_i<1$) and $\omega_s>1$ clarify some critical frequencies, M and N are constants to be defined [1]. Function $C_n(\omega)$ will oscillate between ±1 for $|\omega|\le1$ and $|C_n(\omega=\pm1)|=1$

1.3. Elements Realization for Lowpass Prototype Filters

The lumped-element circuit of an n-order lowpass prototype filter is shown in Figure 1.6. The circuit shown in Figure 1.6(b) is the dual form of that shown in figure 1.6(a). Both forms give identical responses. In Figure 1.6, g_1 to g_n are the values of the inductances or capacitances of the reactive elements g_0 and g_{n+1} are the values of terminal immittances (usually pure resistances or conductance) of the source and load respectively. The g -values for different types of lowpass filters are given in the following sections. **[7]**

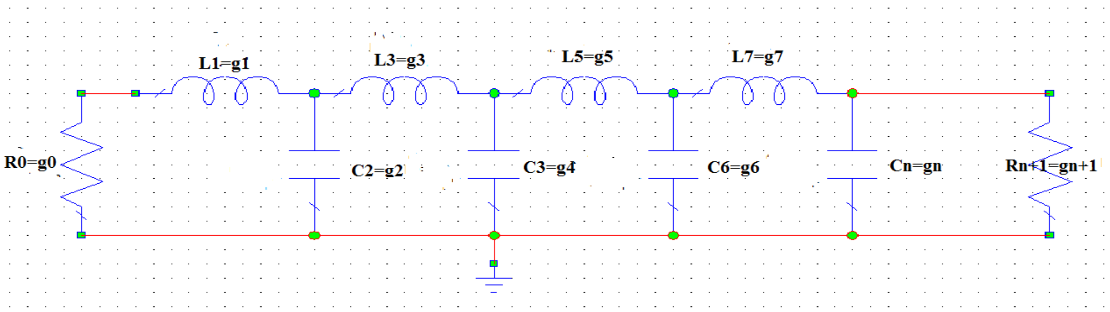

(a)

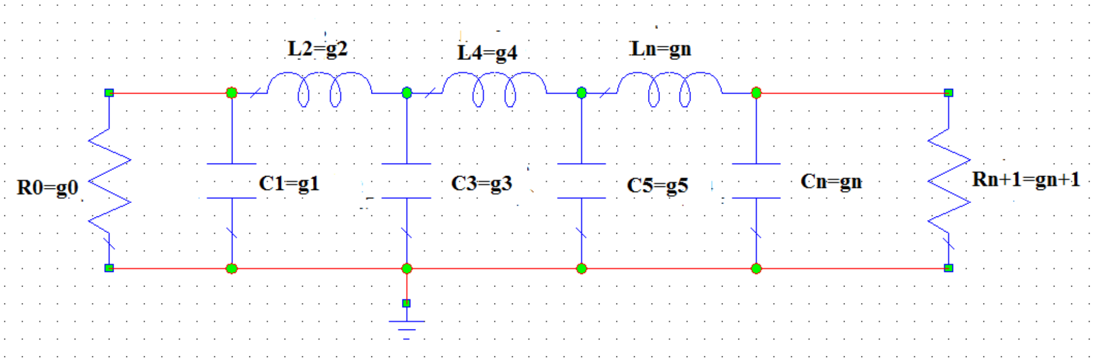

(b)

Figure 1.6: (a) The prototype of lowpass filters and (b) its dual

1.3.1. Butterworth Lowpass Prototype Filters

For the Butterworth filters with response of the form shown in Figure2.4, the element values, normalized to make $g_0 = 1$ and $\omega_c = 1$, can be calculated by **[7].**

$$g_0 = g_{n+1} = 1.0 \tag{1.13}$$

$$g_i = 2\sin\left(\frac{(2i-1)\ \pi}{2n}\right) \quad for \quad \mathrm{i=1\ to\ n}$$

From these two equations, we can notice that Butterworth filter is always symmetrical network, which means that $g_1 = g_{n+1}$, $g_2 = g_n$ and so on.

Whenever the order of the filter increases, steepness of the cut-off slope becomes higher and the rejection at the stopband is better. Thus, increasing the order of the filter or the user reactive elements would lead to better filter, to determine the degree of a Butterworth lowpass prototype, a specification that is usually the minimum $L_{As} = A_{\min}$ dB at $\Omega=\Omega_s$ for $\Omega_s > 1$ can be written as [3]

$$n \ge 0.5\frac{Log\left[\left(10^{0.1A_{\min}}-1\right)/\left(10^{0.1A_{\max}}-1\right)\right]}{Log\left(\omega_s/\omega_c\right)} \tag{1.14}$$

Where $L_{Ar} = A_{\max}$ is the passband ripple and $L_{As} = A_{\min}$ is the stopband attenuation in dB at ω_s

1.3.2. Chebyshev Lowpass Prototype Filters

Similarly, Chebyshev response can be easily realized by reactive elements by applying the following equations [5, 8].

$$\begin{aligned}
&g_0 = 1.0\\
&g_1 = \frac{2}{\gamma}\sin\left(\frac{\pi}{2n}\right)\\
&g_i = \frac{1}{g_{i-1}}\,\frac{4\sin\left[\frac{(2i-1)\pi}{2n}\right].\sin\left[\frac{(2i-3)\pi}{2n}\right]}{\gamma^2+\sin^2\left[\frac{(2i-1)\pi}{n}\right]} \qquad for\quad i=2 \quad \text{to} \quad n\\
&g_{n+1} = \begin{cases}1.0 & \text{for} \quad \text{n} \quad \text{odd}\\ \coth^2\left(\frac{\beta}{4}\right) & \text{n} \quad \text{even}\end{cases} \qquad \beta = \ln\left(\coth\left(\frac{\mathrm{A}_{\max}}{17.37}\right)\right)\\
&\gamma = \sinh\left(\frac{\beta}{2n}\right)
\end{aligned} \tag{1.15}$$

The order of the filter can be simply calculated by applying the following equation:

$$n \geq \frac{\cosh\left(\sqrt{\frac{10^{0.1A_{\min}}-1}{10^{0.1A_{\max}}-1}}\right)}{\cosh\left(\frac{\omega_s}{\omega_c}\right)} \tag{1.16}$$

Where $A_{\min}$, $A_{\max}$ are the minimum stopband rejection and the various ripple at the passband in dB, respectively.

1.3.3. Elliptic Lowpass Prototype Filters

Elliptic filters has equal-ripple at the passband and stopband, which means that this filter has similar response at the passband that Chebyshev has, therefore it is called Chebyshev-Cauer filter. Elliptic lowpass prototype filter is realized by implementing either parallel resonator instead of series inductor as it is shown in Figure (1.7), or by implementing series resonator instead of shunt capacitance as shown in Figure (1.8).

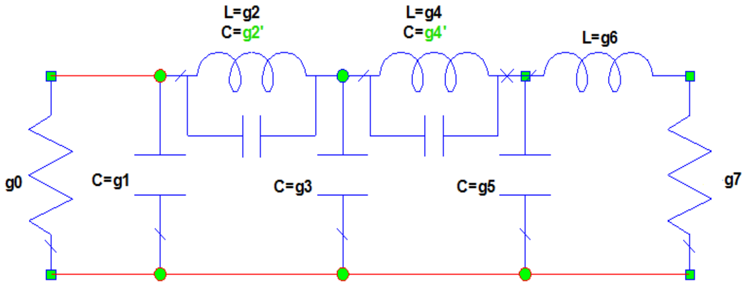

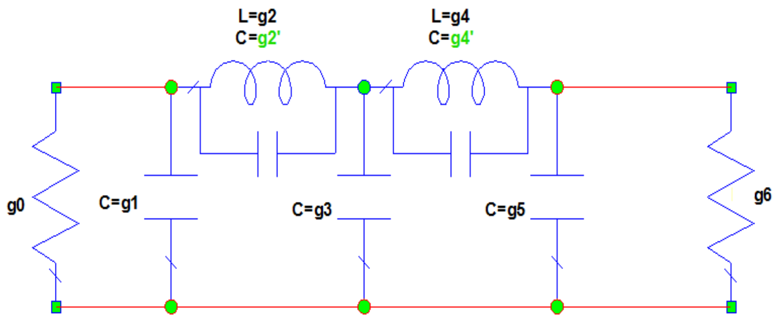

Figure 1.7: Elliptic lowpass prototype filter by using parallel resonators, even order (up), odd order (down)

Unfortunately, there is no simple equation to realize the values of the elliptic lowpass filter elements as in the case of Chebyshev and Butterworth, but still there are some tables of the normalized filter element values [4, 2].

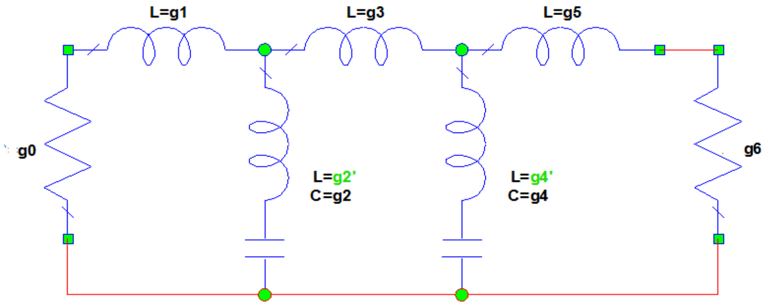

Figure 1.8: Elliptic lowpass prototype filter by using series resonators odd order

Unfortunately, there is no simple equation to realize the values of the elliptic lowpass filter elements as in the case of Chebyshev and Butterworth, but still there are some tables of the normalized filter element values [8].

1.4. Lowpass Prototype to Bandpass Filter Transformation

The lowpass filter (LPF) can be transformed to Bandpass filter (BPF) through the required frequency transformation can be described as [1.7]:

$$\cdots\frac{\Omega}{\Omega_c}=\frac{1}{FBW}\left(\frac{\omega}{\omega_0}-\frac{\omega_0}{\omega}\right) \qquad FBW=\frac{\omega_2-\omega_1}{\omega_0} \tag{1.17}$$

$$\omega_0=\sqrt{\omega_1\omega_2}$$

The Ω and ω are angular frequencies of the LPF and BPF respectively, the lowpass prototype filter has a cutoff frequency $\Omega_C = 1$ and $\omega_0 = 2\pi.f_0$ (f_0 denotes the center frequency of the passband and FBW is defined as the fractional bandwidth .If we apply this frequency transformation to a reactive element ***g*** of the lowpass prototype. Then, we have:

the impedance scaling factor $\gamma_0$is defined as [1]:

$$\gamma_0 = \begin{cases} Z_0 / g_0 & \text{for } g_0 \text{ being the resistance} \\ g_0 Z_0 & \text{for } g_0 \text{ being the conductance} \end{cases}$$

Applying this frequency transformation to a reactive element ***g*** (parallel capacitor **C** or series inductor **L**) of the lowpass prototype, we have:

$$j\,\Omega\,g = j\left[\frac{\Omega_c}{FBW}\left(\frac{\omega}{\omega_0}-\frac{\omega_0}{\omega}\right)\right]g = \begin{cases} j\omega\left(\dfrac{\Omega_c C}{\omega_0 FBW}\right)+\dfrac{1}{j\omega\left(\dfrac{FBW}{\Omega_c\omega_0 C}\right)} & \text{if } g=C \\ j\omega\left(\dfrac{\Omega_c L}{\omega_0 FBW}\right)+\dfrac{1}{j\omega\left(\dfrac{FBW}{\Omega_c\omega_0 L}\right)} & \text{if } g=L \end{cases} \qquad (1.18)$$

which implies that an inductive/capacitive element g in the lowpass prototype will transform to a series/parallel LC resonant circuit in the bandpass filter, where, the impedance scaling has been taken into account as well **[**1]. Then, we obtain:

For **g** represent the inductance

$$L_s = \left(\frac{\Omega_c}{\omega_0 FBW}\right)\gamma_0 g \qquad C_s = \left(\frac{FBW}{\omega_0\Omega_c}\right)\frac{1}{\gamma_0 g}$$

For **g** represent the capacitance

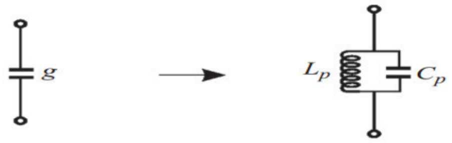

$$L_p = \left(\frac{FBW}{\Omega_c.\omega_0}\right)\frac{\gamma_0}{g} \qquad C_p = \left(\frac{\Omega_c}{FBW\omega_0}\right)\frac{g}{\gamma_0}$$

1.4.1 Lowpass Prototype Filter with ideal J and K inverters

The lowpass prototype filter design includes capacitive and inductive elements organized alternately in series and parallel arrangement in a ladder network as depicted in Figure 1.9. In the physical realization of microwave filters, with impedance or admittance inverters, it is feasible to convert the ladder lumped circuit into new circuit with only one type of component. The equivalent circuit is formed of either series inductors (see Figure1.9a) or shunt capacitors (see Figure1.9b).

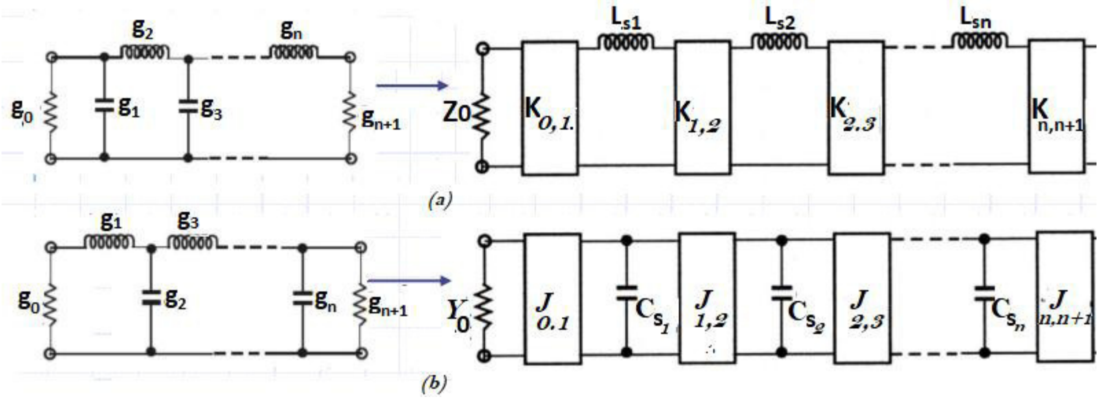

Figure 1.9: Lowpass prototype filters modified to include immittance inverters.(a)impedance inverter (b) admittance inverter

Figure1.10 describes an impedance and admittance inverter. It is equivalent to an ideal quarter-wave transformer with characteristic impedance $\sqrt{K}$ connected to impedance Z_L. The quarter-wave line transforms the impedance given by the relationship

$$Z_{in} = \frac{K^2}{Z_L} \quad \text{and} \quad Y_{in} = \frac{J^2}{Y_L} \tag{1.19}$$

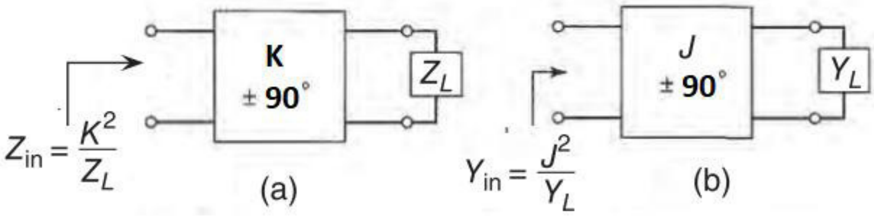

Figure 1.10: Operation of impedance and admittance inverters.

Where **K** is real and defined as the characteristic impedance of the **K**-inverter, ***J*** is real and defined as the characteristic admittance of the J-inverter.

1.5. Extraction Circuit Models for Chebyshev Bandpass Filters

Figure 1.11 gives the bandpass filters transformed from the low-pass ones in Figure 1.9 In this section Chebyshev filters is used to examine the extraction of equivalent circuit model and using EM simulator to synthesize the physical parameters of the microwave filter. This extraction is not concerned only with Chebyshev filters but it can also suit other filter functions. We have three equivalent circuit models for Chebyshev filters [2] such as the K-impedance inverter model, the J-admittance inverter model and the coupling matrix model which are illustrated in Figure 1.11. The coupling elements $M_{n,n+1}$, the impedance inverters

$K_{n,n+1}$ and admittance inverters $J_{n,n+1}$ are dependent to the elements gj (j=0,…,N+1) of the lumped-element lowpass prototype as shown [2]:

- *Coupling Matrix Model:*

$$M_{j,j+1} = \frac{1}{\sqrt{g_j g_{j+1}}}, \quad j = 1, 2, \ldots, N-1$$
$$R_1 = \frac{1}{g_0 g_1}, \qquad R_N = \frac{1}{g_N g_{N+1}} \tag{1.20}$$

- *K-Impedance Inverter Model*

$$\frac{K_{j,j+1}}{Z_0} = \frac{\pi\Delta}{2\sqrt{g_j g_{j+1}}}, \quad j = 1, 2, \ldots, N-1$$
$$\frac{K_{01}}{Z_0} = \sqrt{\frac{\pi\Delta}{2 g_0 g_1}}, \quad \frac{K_{N,N+1}}{Z_0} = \sqrt{\frac{\pi\Delta}{2\ g_N g_{N+1}}} \tag{1.21}$$

- J-Admittance Inverter Model

$$\frac{J_{j,j+1}}{Y_0} = \frac{\pi\Delta}{2\sqrt{g_j g_{j+1}}}, \quad j = 1, 2, \ldots, N-1$$
$$\frac{J_{01}}{Y_0} = \sqrt{\frac{\pi\Delta}{2 g_0 g_1}}, \quad \frac{J_{N,N+1}}{Y_0} = \sqrt{\frac{\pi\Delta}{2 g_N g_{N+1}}} \tag{1.22}$$

The Figure1.11 clarifies the circuit equivalent of coupling matrix model and two bandpass filters using immittances inverters. In the case of Figure 1.11b, only series resonators are associated, whereas the filter in Figure 1.11c be composed of only shunt-parallel resonators.

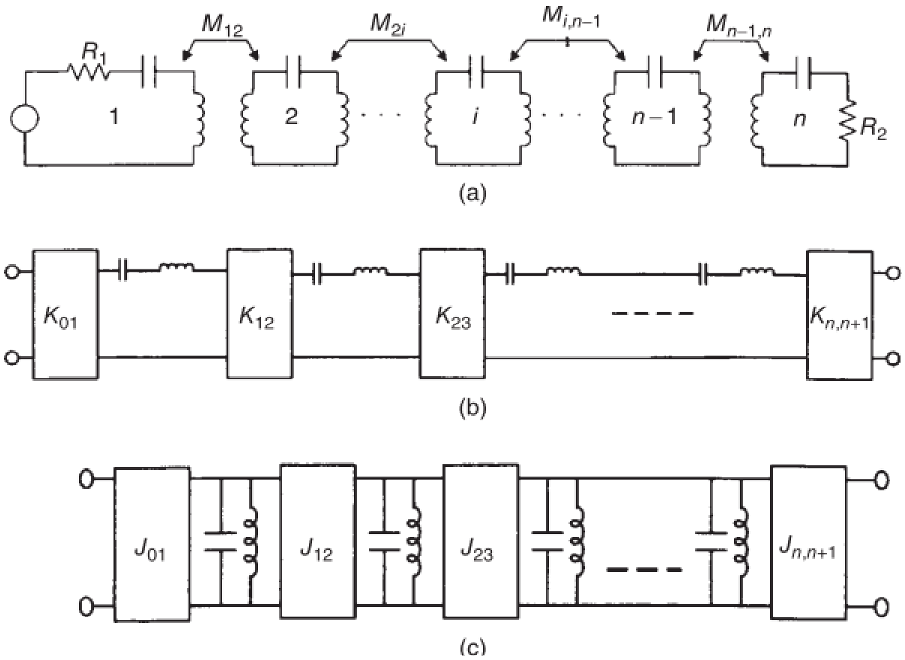

Figure 1.11: (a)Coupling matrix model for Chebyshev filters,(b)impedance inverter model for Chebyshev filters, and (c) admittance inverter model for Chebyshev filters [2]

1.6 Influences of losses on bandpass filters

In general, the losses in the equivalent circuits RLC of resonator (see Figure 1.12a) are conventionally represented by a resistance R, which will produce degradation in performance. The effects of this resistance R can be related directly to the unloaded quality factor (Q_u) of individual components used in the filter design. The unloaded quality factor (Q_u) is defined as the ratio of the energy stored and power lost in the reactive element per unit time. The description is given as:

$$Q_u = \omega\left(\frac{\text{Energy stored}}{\text{Average power loss}}\right) \tag{1.23}$$

$$Q_u = 2\pi\left(\frac{\text{Energy stored}}{\text{Energy dissipated per cycle}}\right)$$

The lumped RLC elements represent the five synchronously resonators and the quarter-wavelength transmission lines, which have electrical length $\theta = \pi/2$ at the center frequency $f_0 = 302.85$ MHz , are used to represent the couplings (K-impedance inverter Model) using equation (1.21). We can find the circuit parameters in Figure 1.12 which in related to the bandpass filter design parameters by using the equations (1.20), (1.21),(1.22) and (1.23).

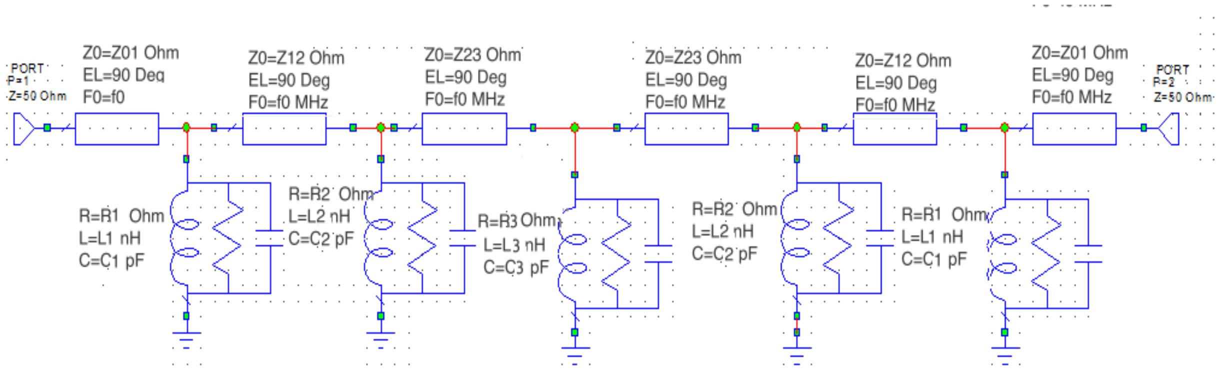

Figure 1.12: Bandpass filter circuit including lossy resonators.

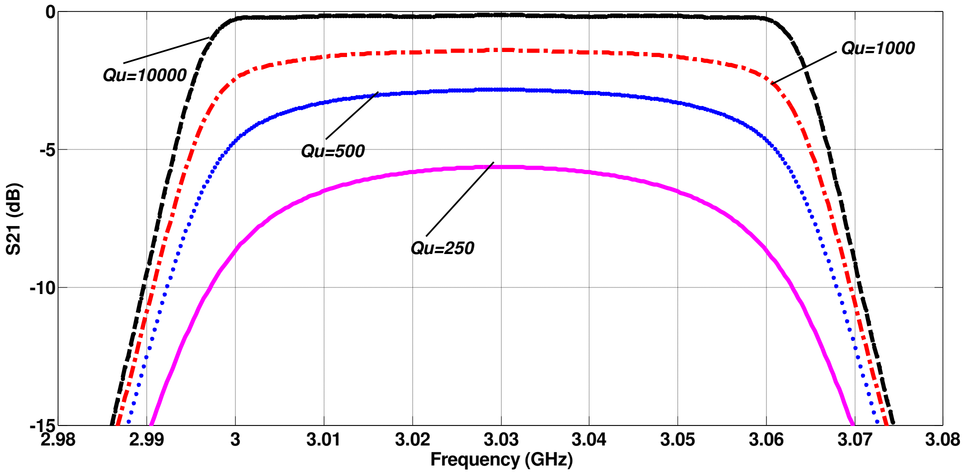

(b)

Figure 1.13: Dissipation effects on the insertion loss characteristic of the bandpass filter.

The resultant filter circuit, including the dissipative elements for the resonators, is illustrated in Figure 1.12; the insertion loss response is plotted in Figure 1.13 for different values of the unloaded quality factor (Q_u). These Q_u values are supposed to be evaluated at the resonant frequency, which, in this case, is the center frequency of the filter. We see that as the Q_u is reduced the passband insertion loss increases and the selectivity becomes worse as the Q_u is decreased.

1.7 Conclusion

In this Chapter, we describe the conventional filters, namely, the Butterworth, Chebyshev, and elliptic function filters. This chapter describes the synthesis process for the characteristic polynomials to realize the ideal classical prototype filters: Butterworth, Chebyshev, and elliptic function filters. The effect of uniform dissipation in filter elements is included by shifting the pole/zero pattern of the transfer function by the dissipation factor for the practical filter. The dissipation factor is derived in terms of the quality factor (unloaded Q_u) of the proposed structure and the bandwidth requirements of the practical filter. A brief review of the scaling of frequency and impedance of the prototype networks to realize practical filter networks is also included.

[1] J.S. Hong and M.J. Lancaster, Micrsotrip filters for RF/microwave applications, Wiley, New York, NY, 2001.

[2] Richard J Cameron, Chandra M Kudsia, and Raafat R Mansour. Microwave filters for communication systems. Wiley-Interscience, 2007.

[3] G. Matthaei, L. Young, and E.M.T. Jones, Microwave Filters, Impedance-Matching Networks, and Coupling Structures, Artech House, 1980.

[4] Talal F. Skaik, ‘’ Synthesis of Coupled Resonator Circuits with Multiple Outputs using Coupling Matrix Optimization ‘’, The University of Birmingham ,2011.

[5] D. G. Swanson, “Narrow-band microwave filter design,” IEEE Microwave Magazine, pp. 105-114. Oct. 2007.

[6] Pozar D. "*Microwave Engineering*", Third Edition. John Wiley and Sons, USA, 2005, pp. 278- 279, 370-430.

[7] Ian Hunter. Theory and design of microwave filters. Number 48. Iet, 2001.

[8] David M Pozar. Microwave engineering. John Wiley & Sons, 2009.

Chapter 2: Defected Ground Structure (DGS) Technique

2.1. Introduction

Defected ground structures are presented in [1, 9], it is called in the literature as DGS. This method is achieved by etching slots in ground plane of the microwave filters. The technique is applied for microwave transmission line. The slots are synthesized to realize an accurate the microwave filters' performance, as increasing the sharpness of the cut-off slop, and to increase the stopband range frequency .In addition, by using this technique, the compact size of filter can also be achieved. The DGS technique disperses the shield current distribution in the ground plane. As a result, we maintain the control on the excitation and propagation of the electromagnetic waves through the substrate layer. This inconvenience will change the characteristics of a transmission line like it can increase the effective capacitance and inductance of a transmission line [8,10].To study the characteristics of the DGS, we can use an equivalent circuit which represented the DGS structure. A defect etched in the ground plane of the microstrip can increase the impact of the effective capacitance and inductance. This clarifies the DGS resonance property which permit its application in different microwave circuits , such as filters ,antennas and amplifiers etc [2,6].Figure 2.1 depicts the backside of the substrate of three different slots forms.

2.2. Defected Ground Structure Element

Figure (2.1) represents the DGS structures in which will be studied. It is shown that various form of etched pattern shapes including semi-circular head and arrowhead shape slots. Each DGS structure has special characteristics performance [7].

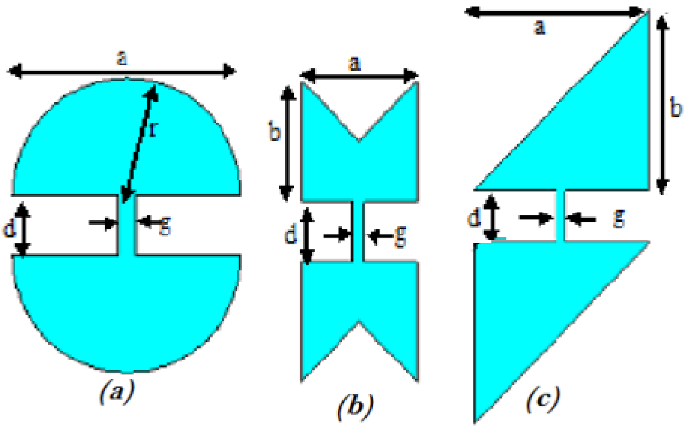

Figure 2.1: Layouts of proposed DGS , (a) Semi-circular-DGS, (b) DTH-DGS, (c) TH-DGS

In this section, two kinds of DGSs will be examined for achieving lowpass filter (LPF), they are called Double-Triangle-Head Defected ground structure (DTH-DGS),and Triangular-Head- Defected ground structure (TH-DGS), as depicted in Figure 2.1.

2.3. Frequency Characteristics of DGS Unit

We achieve a DGS element by etching a defect process from the ground plane of a microstrip line. It can obtain a simple or sophisticated geometry defect form. Defect ground structures perturb the shielded current distribution in the ground plane [6,4]. This inconvenience changes characteristics of microstrip line such as its capacitance and inductance to obtain slow-wave effect and stopband in some frequency ranges [9]. A DGS element acts as an equivalent parallel RLC or LC resonant circuit connected in series with transmission lines at both of their ends [4].

Generally, the DGS can give both slow wave propagation in the passband and better attenuation properties in the stopband [3]. In this thesis, we dealt with two DGS unit shapes and compare their characteristics. Moreover, the elements are used in lowpass filter synthesis and the obtained performances are analyzed.

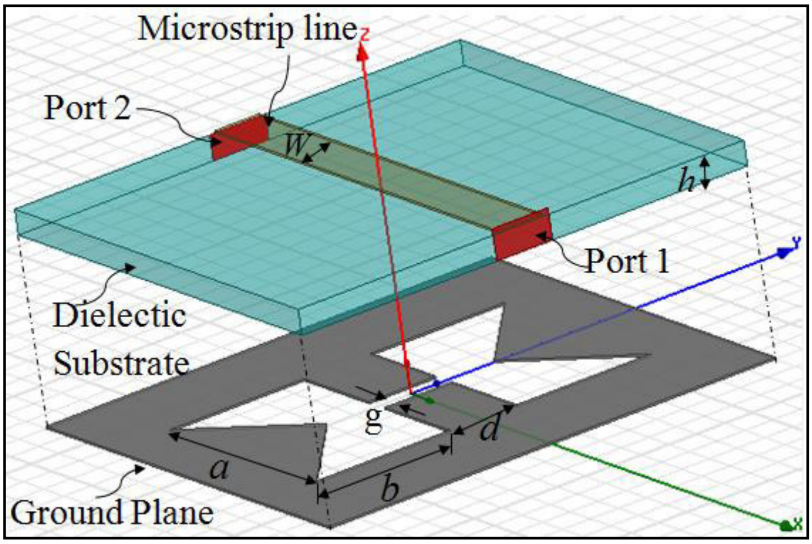

Figure 2.2: Three-dimensional view of the DGS

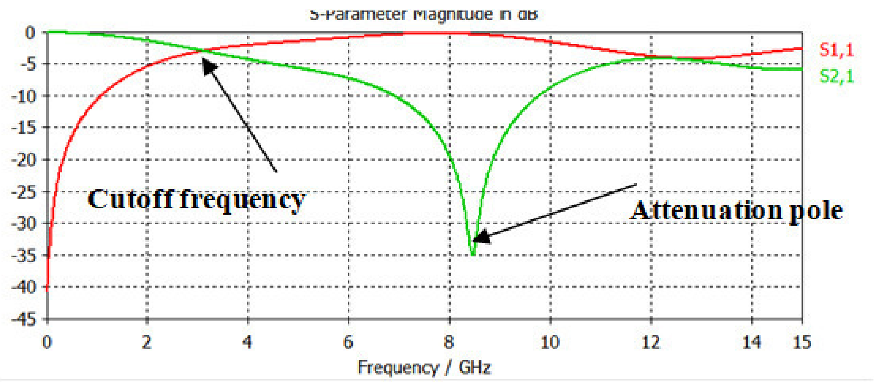

Figure 2.3: S_{11} and S_{12} of the DTH-DGS with EM simulation

DGSs contain narrow and broad etched areas in the metallic ground plane as presented in Figure 2.2, which increases the effective capacitance and inductance of a transmission line, respectively. To synthesis a circuit with a DGS element, the equivalent circuit parameters for the DGS section should be determined.

A straightforward examination is accomplished on the DTH-DGS slot with dimensions a=b=5 mm, and g=0.4 mm etched under 50 Ω line to illustrate how this structure behave over broad frequency band. The transfer and reflection of this structure are presented in Figure 2.3.The E-field distribution at the slot metallization is depicted in Figure 2.4

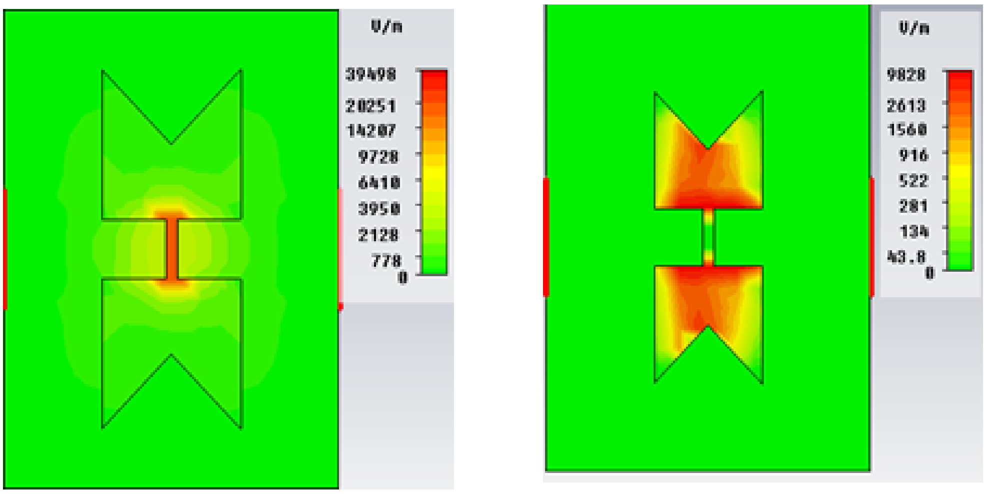

(a) (b)

Figure 2.4: E-field circulation on the slot metallization (a) at 10 GHz, (b) at 3.1 GHz

2.4. Analysis and Design of the DGS

2.4.1. DGS Frequency Features

The EM simulation is the essential resourcefulness to design and analyze DGS. Figure 2.2 presents the etched element form of the Double Triangle-Head DGS (DTH DGS) section, which is situated on the bottom metallic ground plane of a microstrip line. To examine the frequency features of this DGS unit. The figure 2.3 presents the DGS unit section which can give cut-off frequency and attenuation pole in some frequencies.

EM simulation of the single DGS is illustrated in figure 2.3:

- ✓ A 3dB cutoff frequency of 3.1GHz
- ✓ An anti-resonant frequency (Zero Transmission TZ) of 8.57 GHz.
- ✓ Just one anti-resonant pole is observed at 8.57 GHz, namely that the inductance and capacitance due to the DGS dimensions are unique over the frequencies.
- ✓ Concerning the performance bands from 1.0 GHz to 8.5GHz, the DGS presents the same S-parameter characteristics as a Butterworth type Lowpass filter (order one N=1) designed to have the same cutoff frequency of 3.1 GHz.

The results of simulation illustrate that one-pole lowpass filter characteristics. The use of the DGS unit operating at less than its pole frequency increases the effective inductance of a microstrip line. The cutoff frequency is fundamentally related on the etched slot head zone in the ground plane. In addition, the attenuation pole position is thanks to the width slot etch. In fact, it is noted that a zero transmission can be extracted by making a combination of the inductance and capacitance components. Therefore, the DGS unit is entirely demonstrated by the etched slot width, length and head area in case of slots with certain head shape.

2.4.2. Circuit Equivalent Modeling and Parameter Diagnostic

a. Circuit Modeling: Parallel LC

To use the proposed DGS unit to a convenient circuit design example, it is needful to elicit the equivalent circuit parameters. To get the equivalent circuit parameters of DGS element at the reference plane, the S-parameters versus frequency shall be evaluated by electromagnetic EM simulation to clarify the cutoff frequency and attenuation pole characteristics of the DGS unit. The coming flow chart in Figure 2.5 presents the DGSs classical design and analysis techniques. The EM simulator is used to determine the S-parameters versus frequency behavior of the DGS

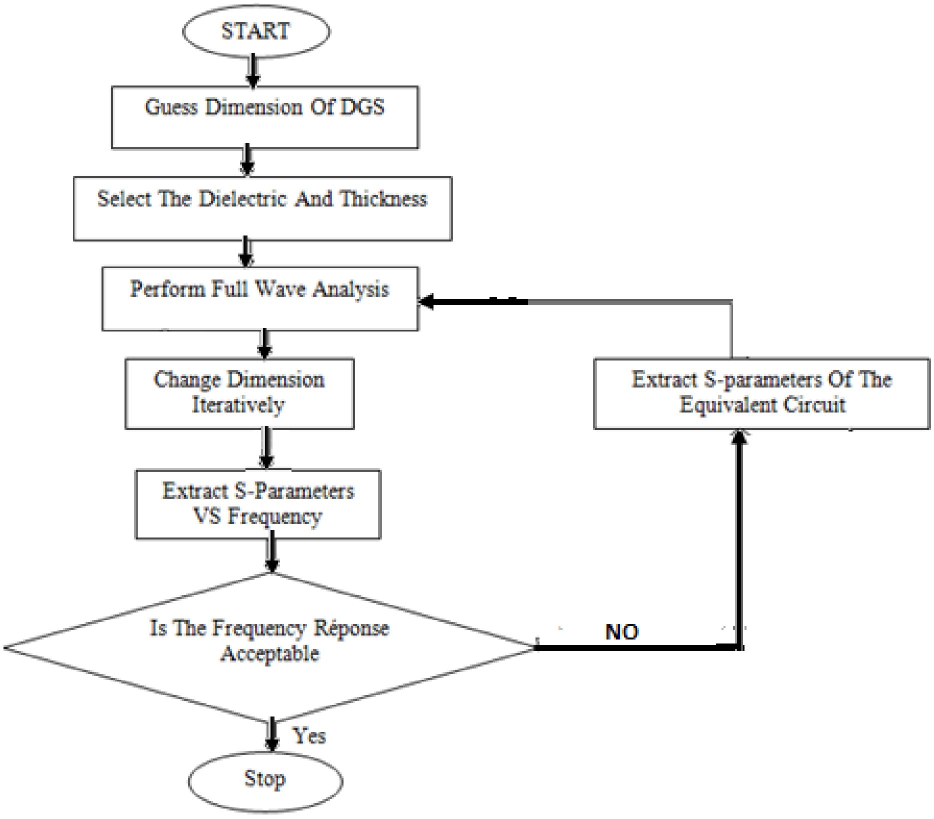

Figure 2.5: DGS Classical design and analysis technique

As referred previously, this part deals with DGS on the ground plane as a parallel LC element due to its band-stop frequency performance characteristic. EM simulation of a DGS structure is desired because the 3dB cutoff and anti-resonant frequency of the DGS are the main information to extract the equivalent inductance (L) and capacitance (C). As the frequency information is obtained, the equivalent inductance and capacitance of the DGS will be evaluated by the coefficient transmission equation of the lowpass filter and a network theory. The microstrip structure is composed of a 50 ohm transmission line and a DGS beneath the microstrip line is presented in figure 2.6.

The parallel LC component (see Figure 2.6) depicts the equivalent circuit of the DGS as represented from its performance. Figure 2.6 represents the DGS element dimensions a, b and g which have been selected to be 5.5 and 0.4 mm respectively. The substrate material RO4003C with 0.813 mm thick and a dielectric constant ε_r of 3.38 was used for the design. Figure 2.6 depicts the simulation performance, in which we obtain a zero transmission at 8.51 GHz. For the explanation of simultaneously of the cutoff and attenuation pole characteristic of the DGS unit, the equivalent circuit must illustrate the low-pass and reject-band filter performances at the gather. The equivalent circuit LC behaves as an inductor when the frequency is less than the cutoff frequency. The simulation results determine the circuit parameters for the equivalent circuit. The Defected Ground Structure unit simulation result may be similar to the one pole Butterworth lowpass prototype, whichever has 3-dB cutoff frequency around 3.1 GHz.

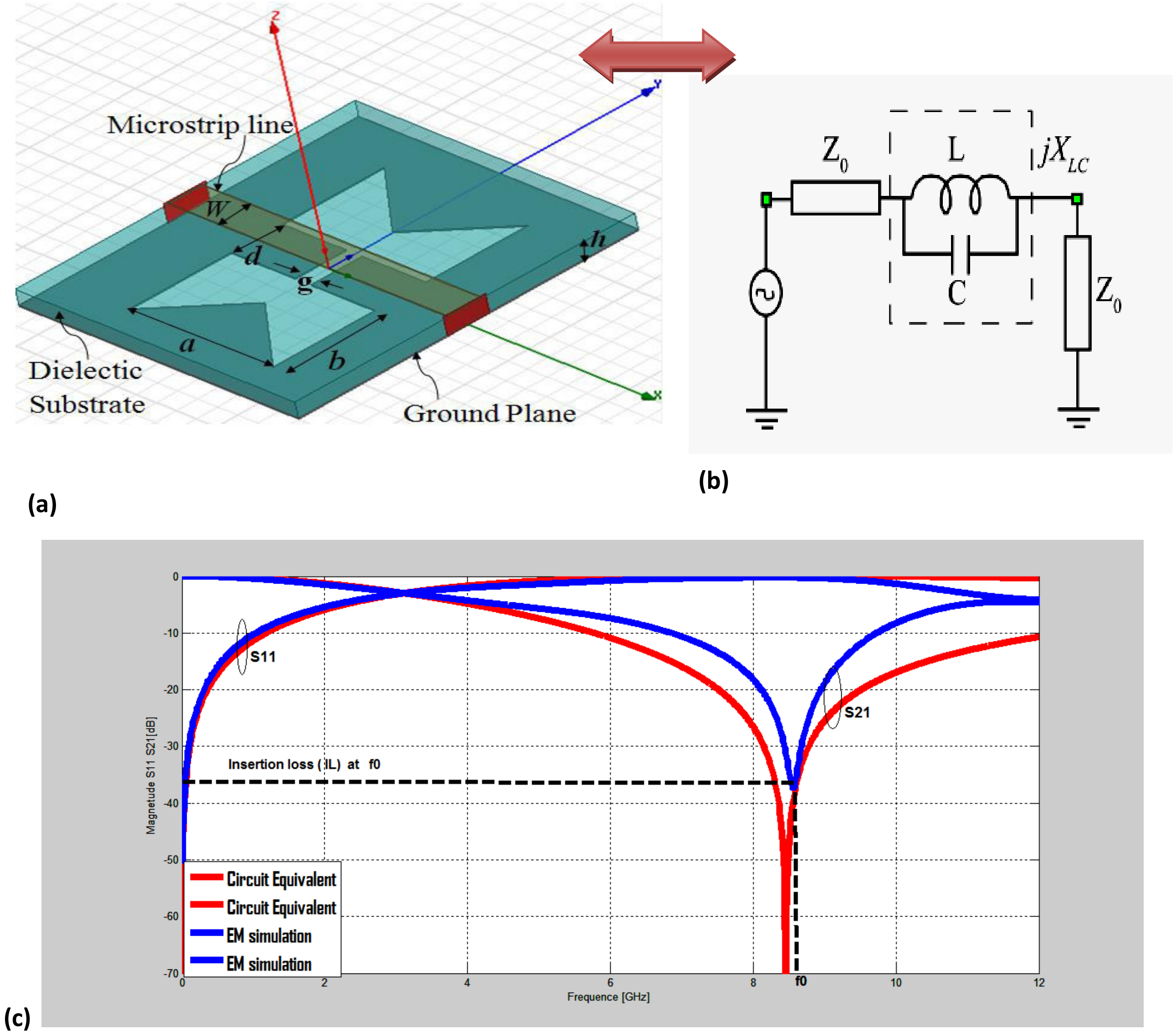

(a)

(b)

(c)

Figure 2.6: (a) DGS topology with the dimensions of g=0.4 mm and a=b=5mm ,(b) Equivalent circuit diagnosing (L=4.417nH and C=0.08017pF), (c) Amplitude response: circuit model EM simulations of proposed TH-DGS

Figure 2.6c depicts the circuit model and EM simulations of the proposed LPF. It shows that a 3-dB cutoff frequency ($f_{C,3dB}$) and the resonant frequency (f_0) of the DGS. According to the response of simulation, we can deduce that the equivalent circuit has the characteristics of Butterworth function, because the frequency response of the Butterworth-function filters is known with its 3-dB cutoff frequency in passband and it’s not good sharp transition response as shown in Figure 2.6c.The equivalent circuit of the DGS and one-pole Butterworth prototype of the LPF are presented in Figure (2.7) [10].

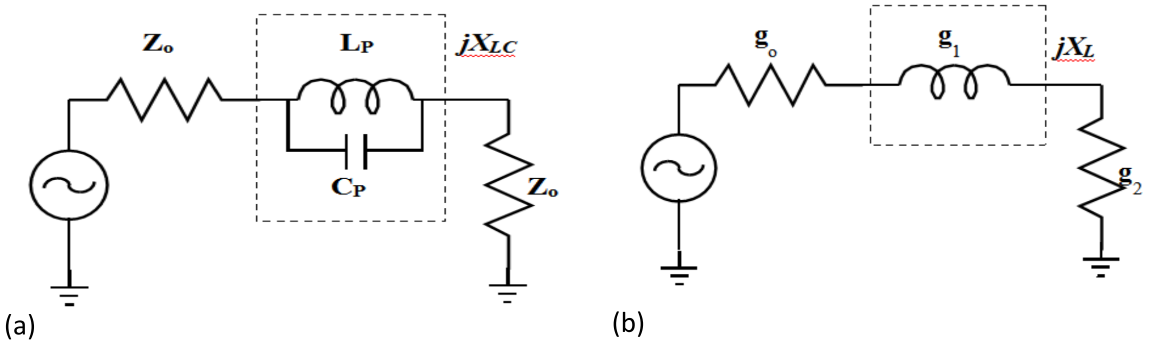

Figure 2.7: (a) Equivalent circuit of the microstrip line with unit DGS. (b) Butterworth prototype of one pole lowpass filter [14]

The equivalent circuit LC parameters are evaluated by Eq. (2.1)–(2.6) because the two equivalent reactance values of Figure 2.7 (a) and (b) may be equal around $\omega_{C,3dB}$,it can be expressed as follows [4]:

$$jX_{LC} = \frac{j\omega L_p \times \frac{1}{j\omega C_P}}{j\omega L_p + \frac{1}{j\omega C_P}} = \frac{j\omega L_P}{1-\omega^2 L_P C_P} \tag{2.1}$$

$$\omega_o^2 = \frac{1}{L_P C_P} \tag{2.2}$$

$$X_{LC} = \frac{1}{\omega_o C\left(\frac{\omega_o}{\omega} - \frac{\omega}{\omega_o}\right)} \tag{2.3}$$

$$X_L = \omega' Z_0 g_1 \tag{2.4}$$

$$X_{LC}\big|_{\omega=\omega_C} = X_L\big|_{\omega'=1} \tag{2.5}$$

$$X_L = \omega' Z_0 g_1 \tag{2.6}$$

In this design input/output terminal impedance, the normalized cutoff frequency and the value of one-pole Butterworth LPF prototype are chosen as Z_0=50 Ω, ω'=1 and g_1=2 respectively. The DGS is depicts to be equivalent circuit to a standard parallel LC circuit as presented in Figure 2.7a, the parallel equivalent capacitance C_p and inductance L_p are extracted as follows [5,8]:

$$C = \frac{w_c}{Z_0 g_1}\frac{1}{\left(w_0^2 - w_c^2\right)} = \frac{2\pi f_c}{Z_0 g_1}\frac{1}{4\pi^2\left(f_0^2 - f_c^2\right)} = \frac{5f_c}{10 Z_0 g_1 \pi\left(f_0^2 - f_c^2\right)} \qquad g_1 = 2$$

$$\Rightarrow C = \frac{5f_c}{\pi\left(f_0^2 - f_c^2\right)} pF \quad \Rightarrow L = \frac{1}{w_0^2 C} = \frac{\left(f_0^2 - f_c^2\right)}{4\pi^2 f_0^2 5 f_c} = \frac{\left(f_0^2 - f_c^2\right)}{20\pi f_0^2 f_c}$$

$$\Rightarrow L = \frac{1}{C\left(4\pi^2 f_0^2\right)} = \frac{0.25}{C(\pi f_0)^2} = \frac{250}{C(\pi f_0)^2} nH$$

After all, the circuit elements parallel capacitance C_p and inductance L_p are evaluated using the following expressions [8]:

$$C_p = \frac{5f_c}{\pi\left(f_o^2 - f_c^2\right)} \quad pF \tag{2.7}$$

$$L_p = \frac{250}{C_p\left(\pi f_o\right)^2} \quad nH \tag{2.8}$$

The f_0 (GHz) and f_c (GHz) are respectively the frequency resonant and 3-dB cutoff frequencies of the DGS pattern. For each frequency below the pole frequency i.e. the resonance frequency (f_0) of the equivalent circuit element LC as through an inductor and its equivalent inductance parameter is get from the following:

$$L_{eq} = \frac{L_p}{[1 - (\frac{f}{f_0})^2]} \quad \text{nH} \tag{2.9}$$

b. Circuit Modeling: Parallel RLC

In the prior part, we examined the equivalent circuit parameter of the DGS which depends only on the lumped elements, L and C diagnosed from EM simulations. In this part, radiation losses are taken in consideration by adding the parallel resistance R in the equivalent circuit [6,8], as illustrated in Figure (2.8).

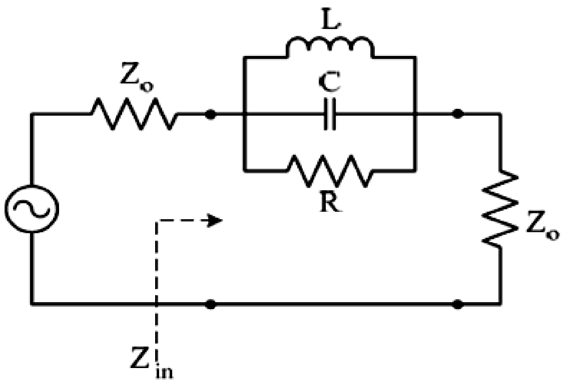

Figure 2.8: The equivalent circuit of the DGS with parallel resistance

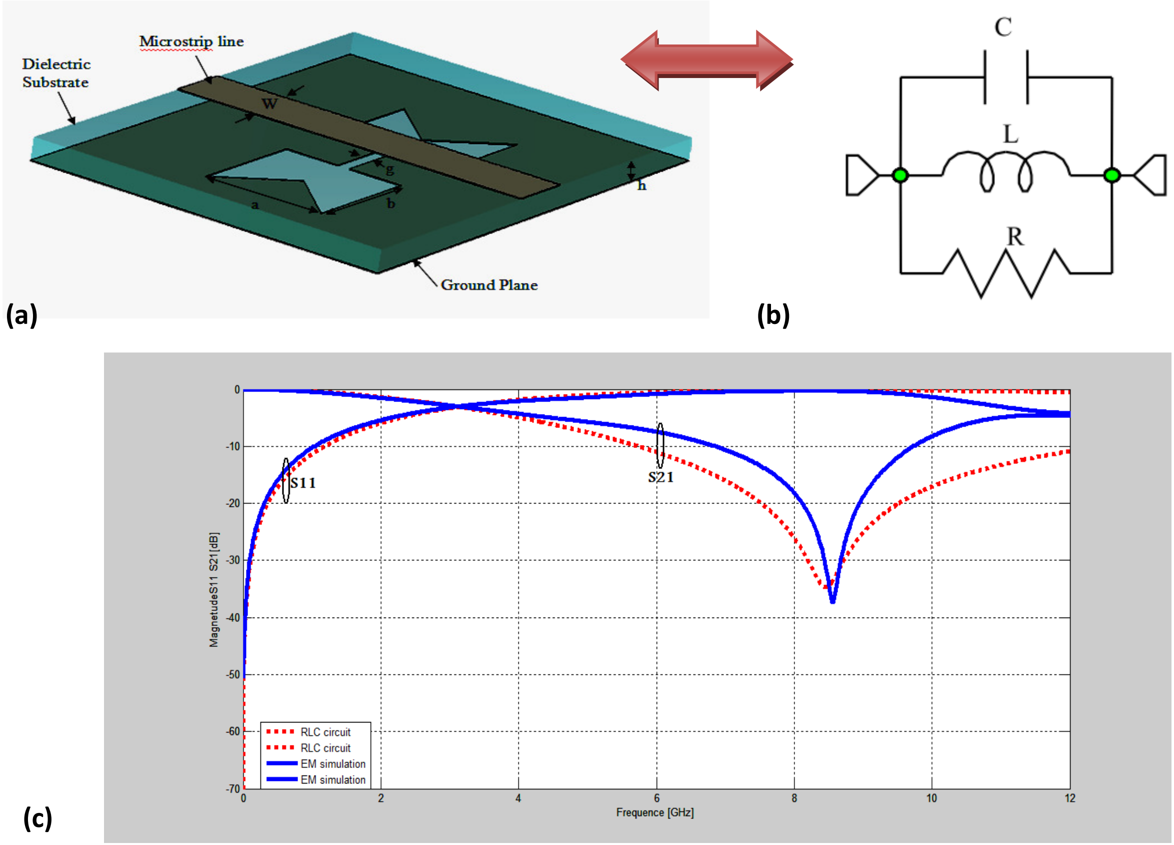

Figure 2.9: (a) DGS topology, (b) The equivalent circuit of the DGS, (c) S-parameters of the equivalent parallel RLC-circuit (R=3825 ohm) and the EM simulation responses

As mentioned above, the pole frequency ($\omega_0 = 2\pi f_0$) and the 3 dB cut-off frequency ($\omega_{C,3dB} = 2\pi f_C$) of the resonating DGS slot are noted from its S21 curve of S-parameter response got with help of EM simulator. The inductance and capacitance for the variable area of slot head are obtained from the following expressions [9]:

$$C = \frac{1}{2Z_0}\left[\frac{w_c}{\left(w_0^2 - w_c^2\right)}\right] \quad (2.10)$$

$$L = \frac{1}{w_0^2 C} \quad (2.11)$$

- ✓ For the introduction of the radiation loss, we add the resistance (R) is to a LC parallel circuit which is the equivalent circuit model of the DGS unit in lossless situation.
- ✓ The equivalent circuit parameter of the DGS unit is presented in Figure (2.8).
- ✓ The DGS pattern impedance is extracted using the following expressions:

$$Z_{in} = \frac{1}{Y_{in}} = \frac{1}{\frac{1}{R} + j(\omega C - \frac{1}{\omega L})} \quad (2.12)$$

- ✓ For the resonance frequency, the imaginary part of the precedent equation is zero. So we obtain :

$$Z_{in} = R \quad \text{at } \omega = \omega_0 \quad (2.13)$$

The resistance R depicting the radiation loss may be evaluated by EM simulation from S-parameters responses.

$$R = \frac{2Z_0}{\sqrt{\frac{1}{\left|S_{11}(\omega_0)\right|^2} - \left(2Z_0\left(\omega_0 C - \frac{1}{\omega_0 L}\right)\right)^2 - 1}} \quad (2.14)$$

$$R = 2Z_0[(\left|S_{21}(\omega_0)\right|)^{-1} - 1] \quad (2.15)$$

In the low frequency band (pass-band), the current of the equivalent circuit model passes in which an inductance is dominant [5](see Figure 2.10a).The input impedance in Figure (2.10b) is almost infinity at resonance frequency, so the transmitted power is reflected reverse to the input circuit. The inductance of the circuit in Figure (2.10c) is as well dominant, so the current passes through the inductance in low frequency band. Since the reactance is infinity in Figure (2.10d), the resistance is prevailing. Therefore, the current passes through the resistor.

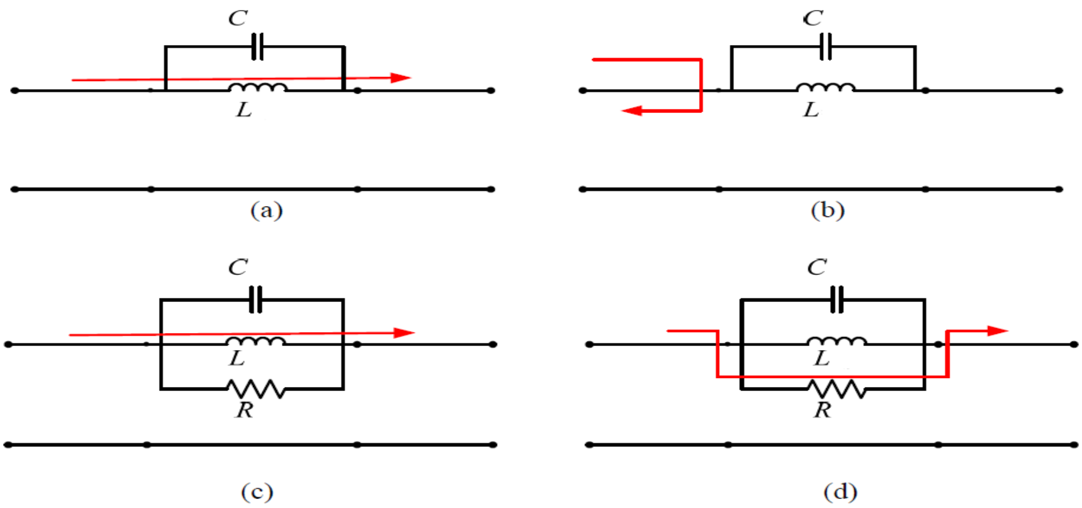

Figure 2.10: The current flow in an equivalent circuit model of a DGS: (a,b) Classical Model in Lossless – (c,d) Model with Losses

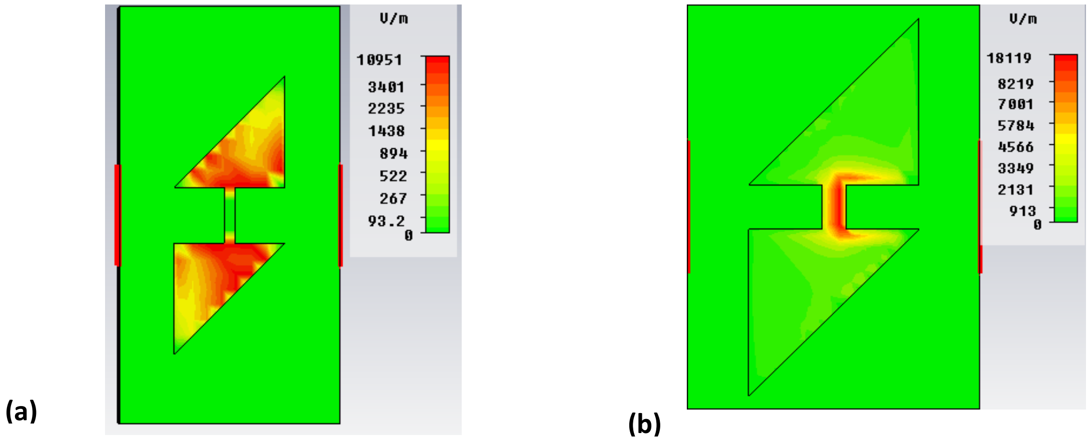

Figure 2.10A: The E-Field distributions of the TH-DGS at **(a)** pass-band and **(b)** reject-band

The currents passes through the TH slotted area, and which produces the currents long trip distance. Consequently, the corresponding quantity of inductance in lower frequency range (passband)is created by the current long distance travel (see Figure 2.10A (a)).In the same figure ,the current does not pass in a gap area because the input impedance value of the capacitance of the parallel LC circuit is very large in the passband region. In the reject band region, the capacitance becomes dominant. Figure2.10A (b), presents the current distributions of the slotted ground plan in high frequency region (stop-band). Since the input impedance of the inductance of the parallel LC circuit becomes very large, while the frequency augmented, the currents only pass through the gap.

2.5. Various DGS slots Topologies Modeling

2.5.1. Study of Double-Triangular-Head DGS (DTH-DGS)

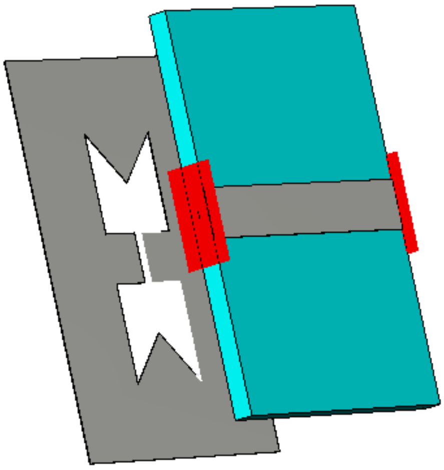

Figure 2.11a: Three-dimensional view of the Cell **d**ouble triangular-head DGS

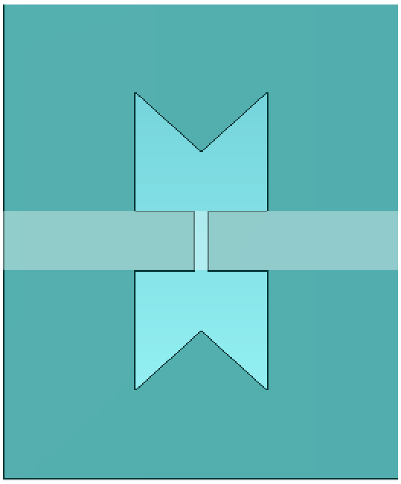

Figure 2.11b: Wire frame view of the double triangular-head DGS

a. Effect of Slot Head Dimension (a=b)

The microstrip line width was select to be the characteristic impedance of the 50 Ω for EM simulations. Different DGS element circuits are simulated with various parameters. For examining the effect of the double triangular slot head dimension, the etched slot width and the length remained constant to 0.4 mm and 2 mm respectively for all the situations and the etched double triangular head was changed. The substrate material used for the all simulations is RO4003 material with a dielectric permittivity of 3.38 and a thickness of 0.813 mm. The EM simulations performances are presented in Figure (2.12).The evaluated the parameters of capacitances and inductances are depicted in the Table 2.1.

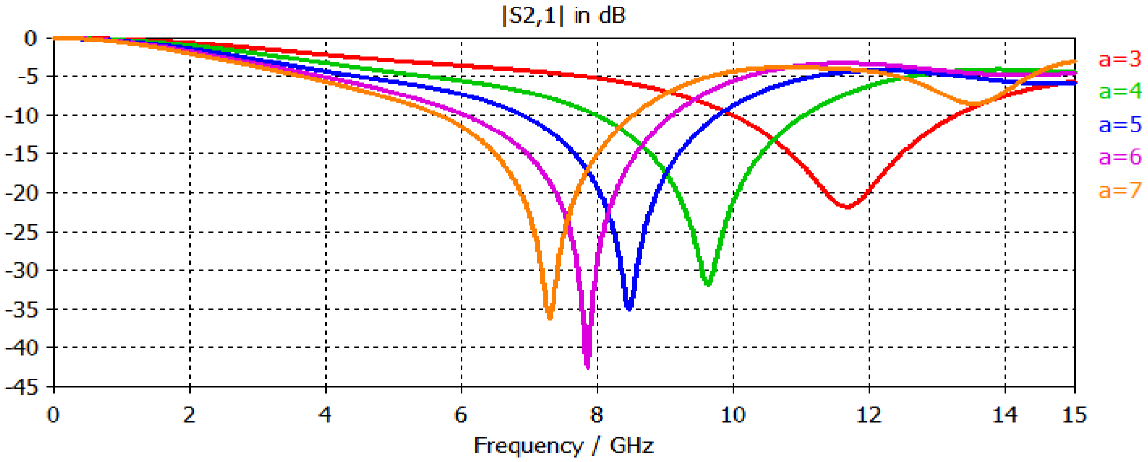

Figure 2.12: Simulated S-parameters of double triangular- head slot for different head lengths (**a**); with the gap (g=0.4) and (d=2) , (a=b)

It is obviously noticed that using the etched DTH-DGS slot head area augments the series inductance (L) to the microstrip line, so there won't be much change in the capacitance (C). This effective series inductance creates the cut-off features at some frequency (see Figure 2.12). Once the etched area of the double triangular slot head is raised, the effective series inductance augments and this rising series inductance increases the lower cut-off frequency, as observed in Table (2.1). We have attenuation poles in simulation results on the etched double triangular slot head area. Which can be illustrated by parallel LC circuit as cited in the previous part.

Table 2 .1: DTH slot characteristics for different slot head lengths (a)

a=b	f_c(GHz)	f_0(GHz)	L(nH)	C(pF)
3 mm	5.1109	11.641	2.5137	0.07435
4 mm	3.7757	9.6259	3.5667	0.07664
5 mm	3.1144	8.4572	4.4172	0.08017
6 mm	2.7808	7.845	4.4279	0.1674
7 mm	2.566	7.3352	5.4434	0.0864

b. Effect of Slot Width (g)

We will study the effect of the etched slot width (g) which will be used. The DTH head dimension a and slot length, d remain constant to 5 mm and 2 mm respectively for all the situation and the etched slot width g was changed. The simulation results are presented in Figure (2.13).According to the constant DTH head dimensions; we intend that the effective series inductances are also constant for all situations. In the other hand there is no change in the cutoff frequency despite the changing of the slot width. Namely, the effective series inductance of a microstrip line is not affected by the slot width. The tuning of the effective capacitance affects only the attenuation pole position. Ones the etched slot width augments, the effective capacitance diminishes. As result, the attenuation pole position shift to higher frequency. Table (2.2) presents the evaluated parameters capacitances and inductances.

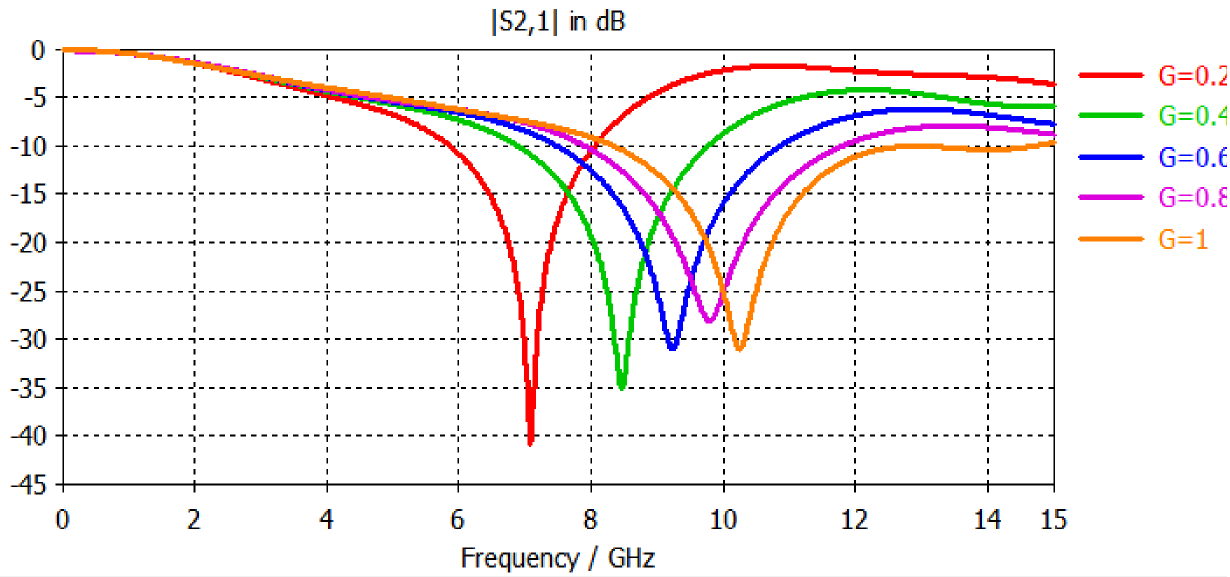

Figure 2.13: EM simulation depending on different gap (g) dimensions

Table 2.2: DTH-DGS slot characteristics for different slot width (g)

g	f_c(GHz)	f_0(GHz)	L(nH)	C(pF)
0.2 mm	2.9841	7.1017	4.3917	0.1143
0.4 mm	3.1004	8.5701	4.4615	0.0773
0.6 mm	3.1684	9.3552	4.4470	0.0650
0.8 mm	3.2005	9.8931	4.4523	0.0581
1 mm	3.1454	10.198	4.5785	0.0532

c. Effect of the Slot length (d)

We extend our study to the influence of the slot length, (d). The slot width, (g) remain constant to 0.4 mm for all the situation and the slot etched length, d was changed. The substrate material used for the all simulations is RO4003 material with a dielectric permittivity of 3.38 and a thickness of 0.813 mm. The simulation performances are depicted in Figure (2.14). Table (2.3) presents the evaluated parameters capacitances and inductances. From Table (2.3), by raising the etched slot length (d), the capacitance will be rise.

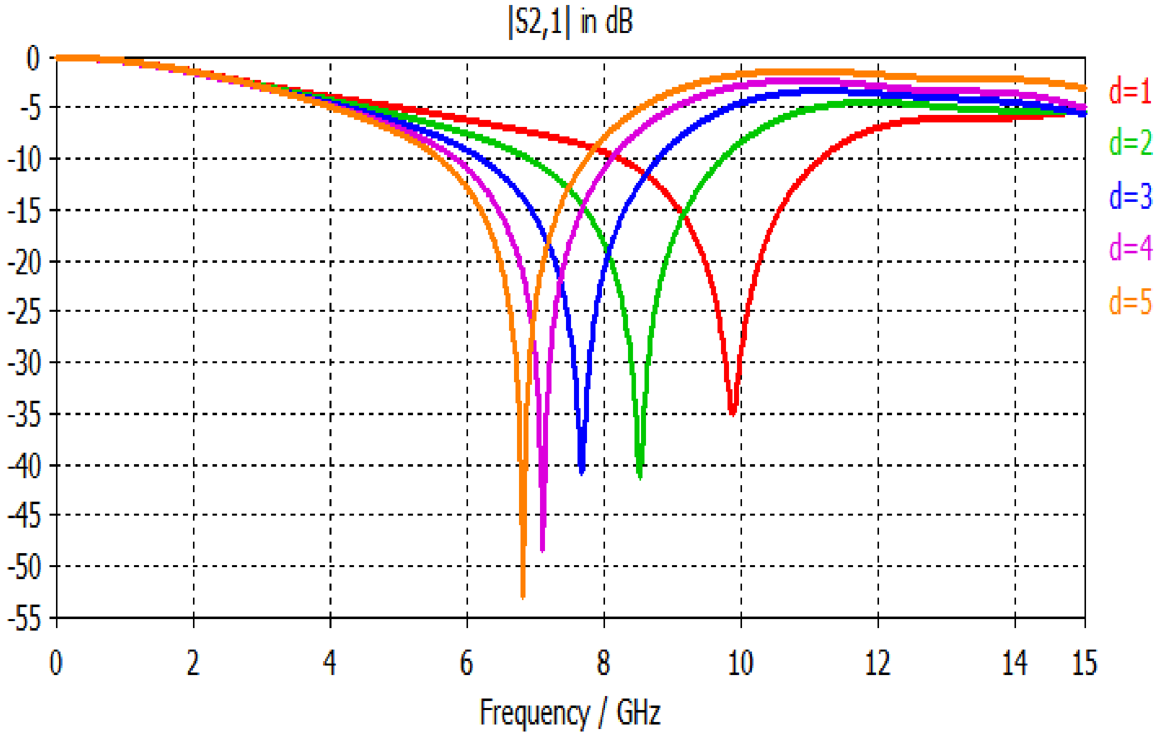

Figure 2.14: EM simulation depending on the different slot length (d) dimensions; the gap dimension is fixed as g=0.4 mm and a=b=5mm

Table 2.3: DTH slot characteristics for different slot lengths d

d	f_c(GHz)	f_0(GHz)	L(nH)	C(pF)
1 mm	3.2231	9.8868	4.4131	0.05871
2 mm	3.1287	8.5151	4.4001	0.0793
3 mm	3.0389	7.6713	4.4154	0.0974
4 mm	3.0153	7.1105	4.3290	0.1157
5 mm	3.0578	6.8137	4.1566	0.1312

2.5.2. Study of Triangular-Head-DGS (TH-DGS)

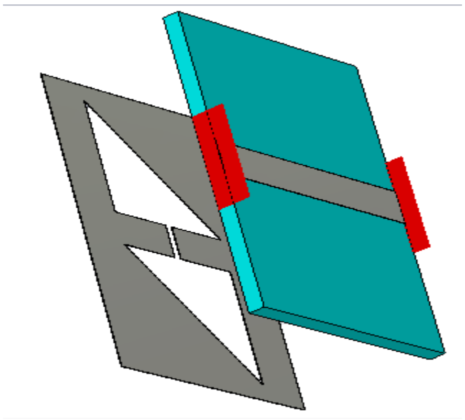

Figure 2.15a: 3-D view of the Triangular Head DGS

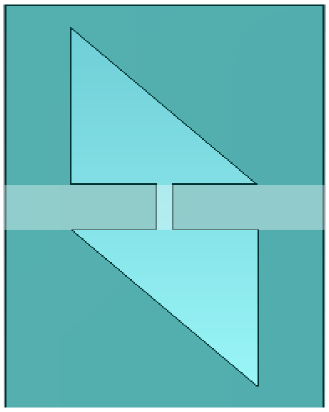

Figure 2.15b: Wire frame view of the Triangular Head DGS

a. Effect of Slot Head Dimension (a=b)

The microstrip line width was select to be the characteristic impedance of the 50 Ω for EM simulations. Different DGS element circuits are simulated with various parameters. In order to investigate the effect of the dimension (a=b), the etched slot width (g) and the length (d) remain constant to 0.4 mm and 2 mm. The simulation performances are presented in Figure (2.16).The evaluated capacitances and inductances are depicted in Table (2.4). From Figure (2.16), we obviously notes that using the dimension (a) augments the series inductance to the microstrip line. This effective series inductance offers the cutoff characteristic at some frequency. Consequently the etched area of the TH-DGS is raised, the effective series inductance increases, and rising the series inductance gives a lower cutoff frequency, as seen in Table (2.4).

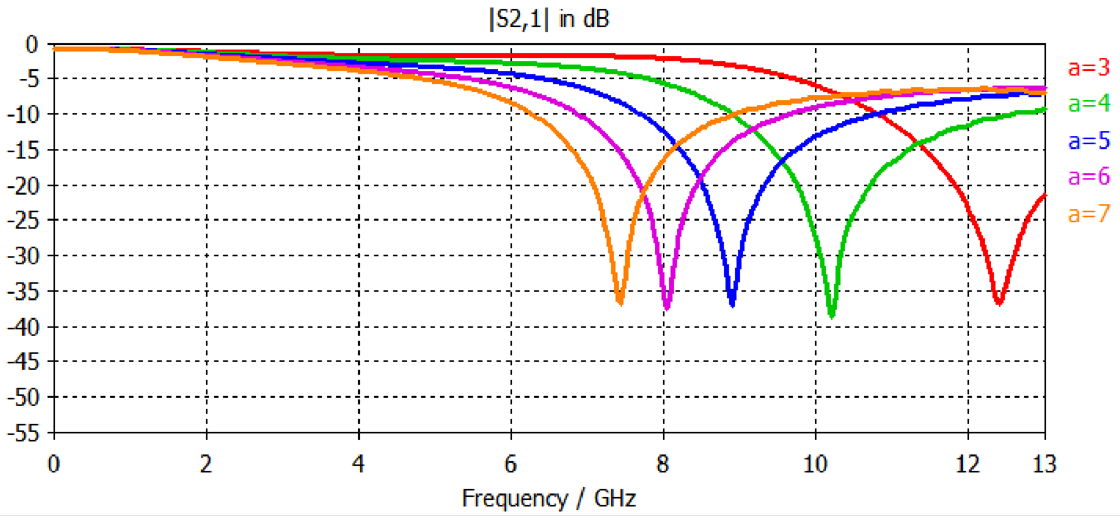

Figure 2.16: Simulated S-parameters of TH slot for different head lengths (a=b); with the gap dimension is fixed and d is fixed

Table 2.4: TH slot characteristics for different slot head lengths (a)

a=b	f_c(GHz)	f_0(GHz)	L(nH)	C(pF)
3 mm	8.5842	12.442	0.9715	0.1684
4 mm	6.4239	10.155	1.486	0.1652
5 mm	5.0063	8.9262	2.179	0.146
6 mm	4.3144	8.0363	2.6257	0.149
7 mm	3.8419	7.3847	3.02	0.1537

b. Effect of Slot Width (g)

An inquiry on the effect of the etched slot width will be used. The dimension a and slot length, d remain constant to 7 mm and 2 mm respectively for all the situations and the etched slot width s was changed. The simulation performances are illustrated in Figure (2.17). According to the constant triangular head dimensions, we intend that the effective series inductances are also constant for all situations. In the other hand the influence of the head dimension, there is no change in the cutoff frequency despite the variation of the slot width (g). Namely, the slot width does not impact the effective series inductance of a microstrip line. The tuning of the effective capacitance only affects the attenuation pole position. As result, the etched slot width increases, the effective capacitance diminishes so that the attenuation pole position shifts to higher frequency. The evaluated parameters capacitances and inductances are presented in Table (2.5).

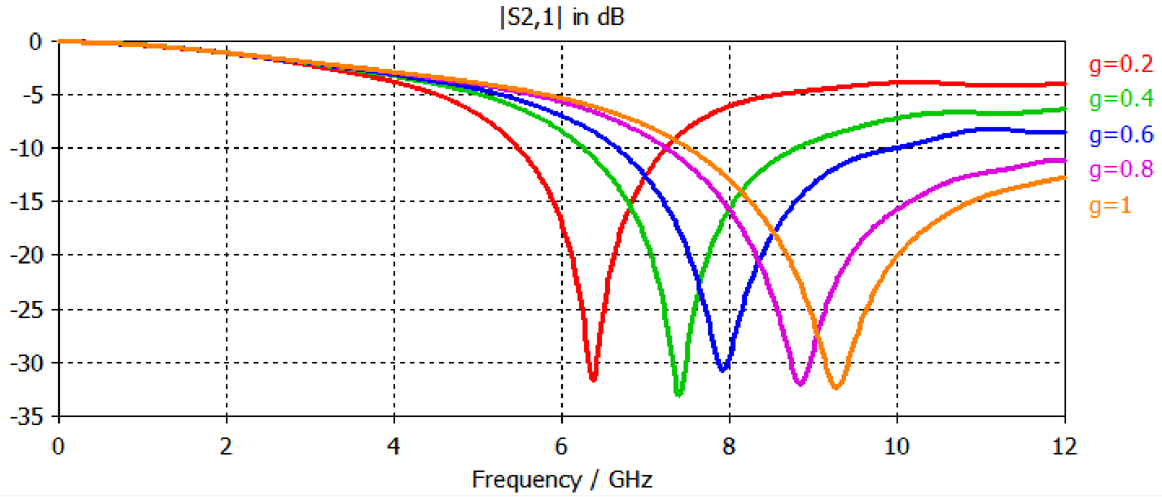

Figure 2.17: EM simulation depending on different gap dimensions (g)

Table 2.5: TH slot characteristics for different slot widths (g)

g	f_c(GHz)	f_0(GHz)	L(nH)	C(pF)
0.2 mm	3.5027	6.3748	3.172	0.1965
0.4 mm	3.7734	7.3853	3.1167	0.149
0.6 mm	3.8736	7.9283	3.128	0.1288
0.8 mm	4.0201	8.8438	3.14	0.1031
1 mm	4.0491	9.2254	3.1734	0.0937

c. Effect of the Slot length (d)

We stretch our study to the effect of the slot length (d). The TH dimension (a) and the slot width (g) remains constant to 5 mm and 0.4 mm respectively for all the situations and the slot etched length (d) was changed. The simulation performances are presented in Figure (2.18). The evaluated parameters capacitances and inductances are depicted in Table (2.6).

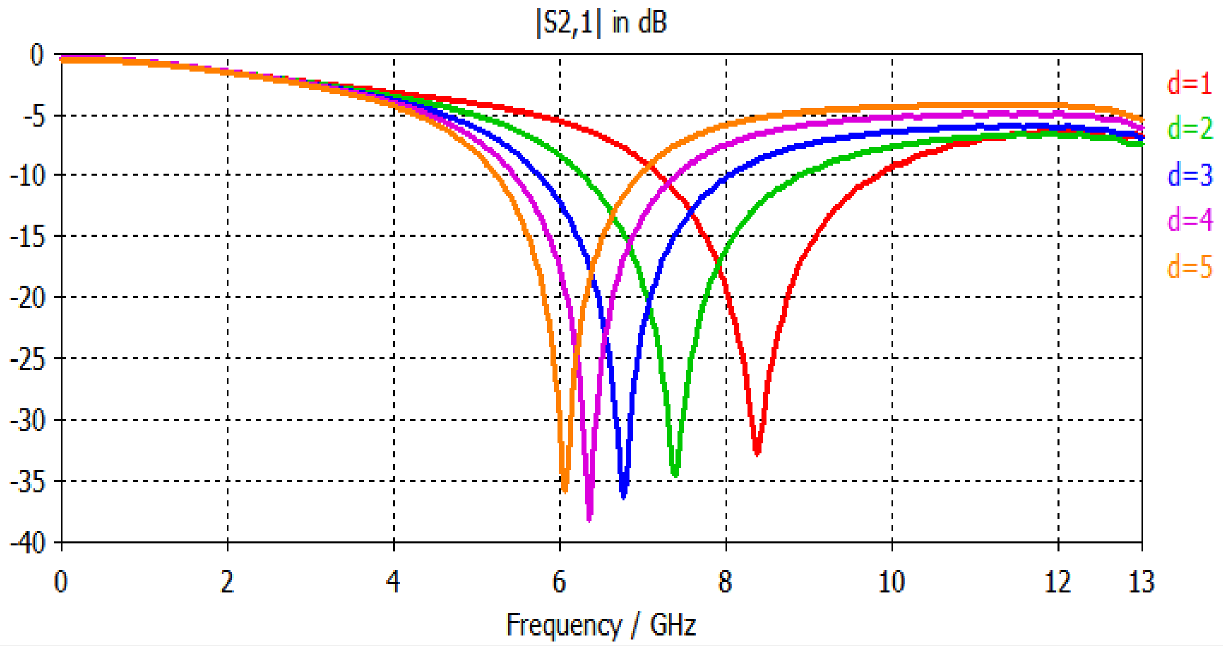

Figure 2.18: EM simulation depending on the different slot dimensions (d)

Table 2.6: TH characteristics for different slot lengths (d)

D	f_c(GHz)	f_0(GHz)	L(nH)	C(pF)
1 mm	4.1152	8.3357	2.925	0.1246
2 mm	3.8122	7.3834	3.06	0.1517
3 mm	3.6271	6.7672	3.1273	0.177
4 mm	3.5784	6.3697	3.044	0.205
5 mm	3.5265	6.0842	2.9967	0.2283

2.6. Design of proposed Quasi-Elliptic Lowpass Filter with single Attenuation pole

This section proposes for microwave communication areas a new design of Quasi-Elliptic High-Low Microstrip Lowpass Filter (QE-HL-MLPF) based on a Semicircular Defected Ground Structure (SC-DGS). The filter design employs a new technique of cascading high (Hi) and low (Lo) impedance elements in simulating the ladder LC lumped-circuit prototype. MATLAB and full wave electromagnetic simulator are used to model the proposed design and extract the scattering parameters. A semicircular-shaped resonator is implemented into the 4th order Butterworth filter structure which uses a Quasi-Elliptic function.

2.6.1. Conception of typical Hi-LO Lowpass Filter (LPF)

LPF is implemented by series connected high-low (Hi-Lo) stepped-impedance microstrip line sections and lowpass filter specifications is illustrated in Table (2.7):

Table 2.7: Filter specifications

Parameters	LPF
Cutoff frequency f_c [GHz]	1.5
Source/Load impedance Zo [Ω]	50
Return Loss	20dB
Filter Type	Butterworth
Constant dielectric	4.2
h (mm)	1.5
Z_{0L} [Ω]	110
Z_{0C} [Ω+]	15

The impedance of source $Z_0 = 50\Omega$; the highest practical line impedance is Z_{0L}, the lowest is Z_{0C} and the minimum stop band insertion loss is more than 25dB at 3GHz.

First step: Four –poles low-pass prototype with Butterworth (n=4) response is chosen, by using the equations described in chapter 01, whose element values are:

$$g_o = g_5 = 1$$

$$g_1 = g_4 = 0.765$$

$$g_2 ==g_4 =1.1848$$

Second step: the two numbers of series inductances and two numbers of shunt capacitances of the prototype are scaled to Z_0 and $f_c(\omega_c = 2\pi f_c)$, can be determined as given in [1]:

$$L_1 = \frac{\Omega_C Z_0}{\omega_c} g_1 = 4.061\,nH$$

$$C_2 = \frac{\Omega_C}{Z_0\,\omega_c} g2 = 3.921\,pF$$

$$L_3 = \frac{\Omega_C Z_0}{\omega_c} g_3 = 9.81\,nH$$

$$C_4 = \frac{\Omega_C}{Z_0\,\omega_c} g4 = 1.624\,pF$$

The lumped equivalent circuit configuration of stepped LPF is shown in Figure 2.19a and the simulated response of the conventional stepped-impedance low-pass filter is shown in Figure 2.19b.

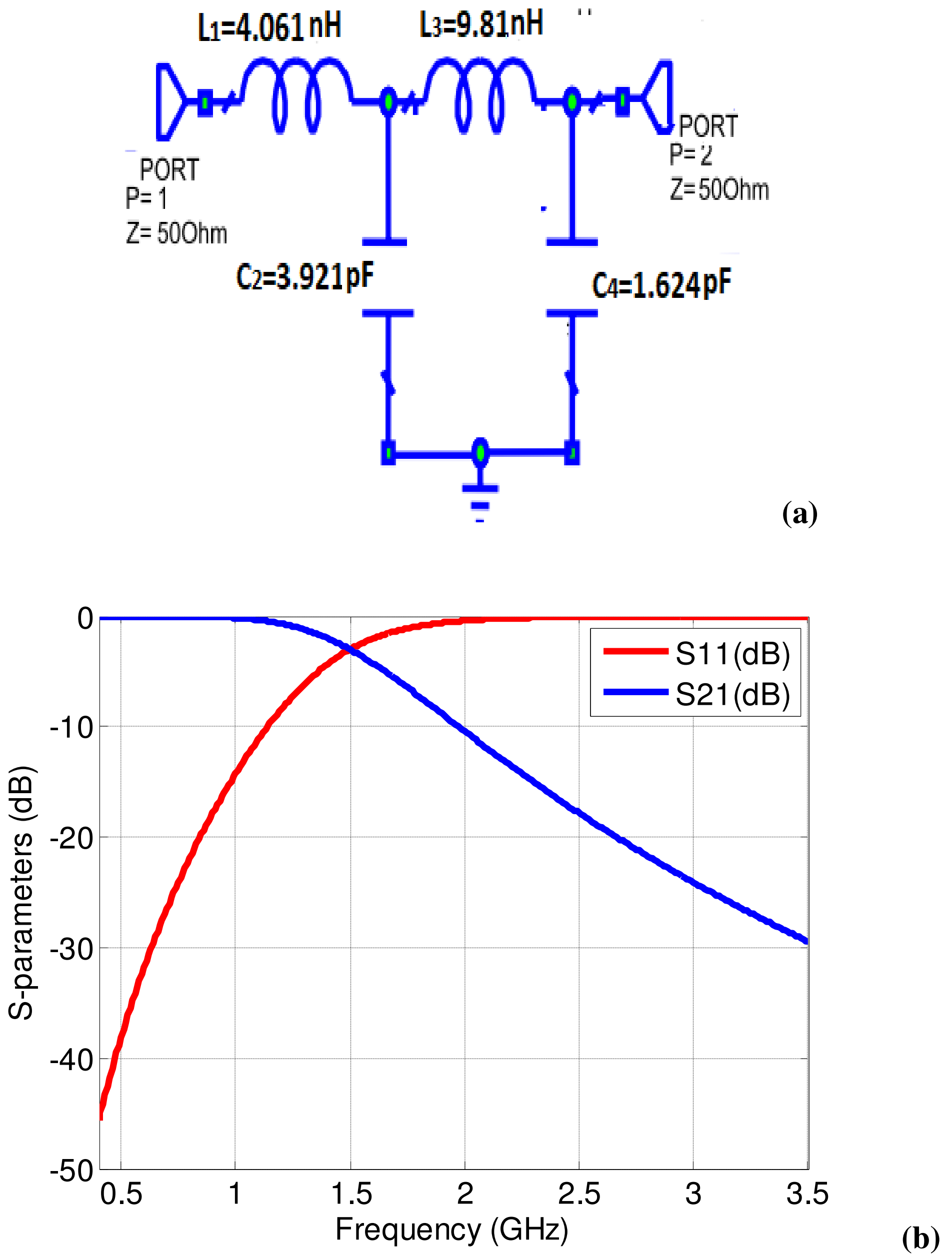

Figure 2.19: (a) Conventional LC ladder LPF ,(b) The S-Parameter Simulation

Third step: The filter is to be implemented on a substrate with a relative dielectric constant ε_r of 4.2 and a substrate height (h) of 1.5 mm. Then, the relevant design parameters of microstrip lines are listed in Table 2.8, which are determined using the formulas in [1].

Table 2.8: Design parameters of High- Low LPF

Characteristic impedance (Ω)	$Z_{0L}=110$	$Z_0=50$	$Z_{0C}=15$
Guided-wavelengths (mm)	$\lambda_{gL}=0.6$	$\lambda_{g0}=0.6$	$\lambda_{gC}=0.6$
Microstrip line width (mm)	$W_L=0.6$	$W_0=3$	$W_C=0.6$
Effective Dielectric Constant	$\varepsilon_{eL}=2.9$	$\varepsilon_{e0}=3.21$	$\varepsilon_{eC}=3.68$

In this design, stepped impedance lowpass filter, which use a cascaded structure of alternating high- and low-impedance transmission lines, is used to realize microstrip structure. Inductors behave high impedance lines and capacitors are modeled low impedance ones. Because of stepped impedance design is valid only short transmission line $l<\lambda/8$. Physical length (in mm) proposed of the high and low impedance lines (inductance and capacitance respectively) is calculated by solving a set of following equations:

$$\begin{aligned}
\omega_c L_1 &= Z_{0L}\ \sin\left(\frac{2\pi l_{L1}}{\lambda_{gL}}\right)+Z_{0C}\ tan\left(\frac{\pi l_{C2}}{\lambda_{gC}}\right)\\
\omega_c C_2 &= \frac{1}{Z_{0C}}\ sin\left(\frac{2\pi l_{C2}}{\lambda_{gC}}\right)+\frac{1}{Z_{0L}}\ \tan\left(\frac{\pi l_{L1}}{\lambda_{gL}}\right)+\frac{1}{Z_{0L}}\ \tan\left(\frac{\pi l_{L3}}{\lambda_{gL}}\right)\\
\omega_c L_3 &= Z_{0L}\sin\left(\frac{2\pi l_{L3}}{\lambda_{gL}}\right)+Z_{0C}\ \tan\left(\frac{\pi l_{C2}}{\lambda_{gC}}\right)+Z_{0C}\ \tan\left(\frac{\pi l_{C4}}{\lambda_{gC}}\right)\\
\omega_c C_4 &= \frac{1}{Z_{0C}}\sin\left(\frac{2\pi l_{C4}}{\lambda_{gC}}\right)+\frac{1}{Z_{0L}}\ \tan\left(\frac{\pi l_{L3}}{\lambda_{gL}}\right)
\end{aligned}\tag{2.16}$$

The overall results came from set of equations (2.17) by using Newton-Raphson are listed in Table 2.9.

Table 2.9: Physical Dimension of Parameters elements.

Dimensions	l_{L1}	l_{C2}	l_{L3}	l_{C4}	l_{50}
Physical [mm]	6.5	9.2	15.65	2.7	2

The dimensions of the filter and its simulated responses are shown in Figure(2.20a) and Figure (2.20b), respectively.

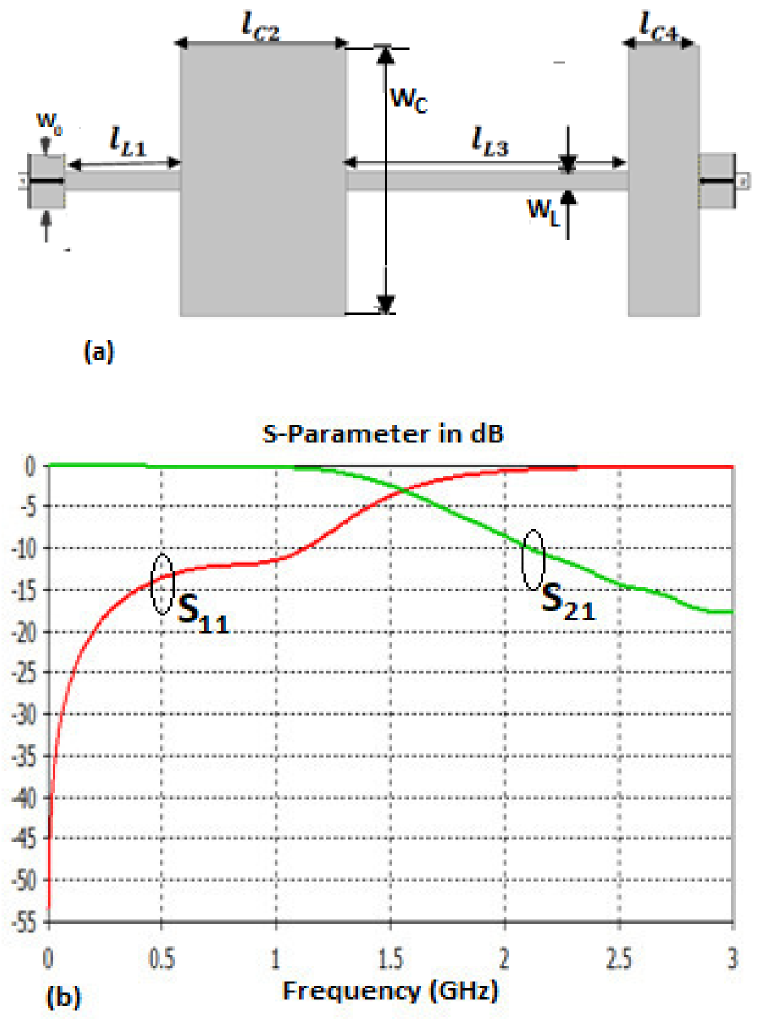

Figure 2.20 : (a) layout of stepped impedance LPF and its dimensions (in mm)
(b) S_{21} and S_{11} frequency response of Butterworth filter of 4th degree

Figure 2.20b shows simulated S-parameters of proposed High-Low LPF unit .The 3dB cutoff frequency of the LPF is 1.53GHz and the bandwidth of stop-band of 1.94 GHz. The maximum attenuation value of insertion loss is equal to 19dB at 2.95GHz frequency

2.6.2. Proposed of Quasi-Elliptic Lowpass Filter based semicircular-DGS

The preview type of microstrip lowpass filter represent the lowpass prototype filter having their frequencies of infinite attenuation at f =∞. In order to obtain an even sharper rate of cutoff for a given number of reactive elements, it is desirable to use filter structures giving infinite attenuation at finite frequencies. A prototype of this type may have an elliptic-function response.

Last step is to etch ground plane and investigate of different frequency characteristics of the design. In the design procedure, some kind of different geometry like square dumbbell, fractal dumbbell and semicircular DGSs are applied to ground plane. Figure 2.21a shows a Quasi-elliptic-function lowpass filter that has one parallel-resonant branche connected in a series that open out transmission at their resonant frequency, and this gives one finite-frequency attenuation pole. Figure 2.21b shows the simulated results of proposed equivalent circuit LPF with zero transmission.

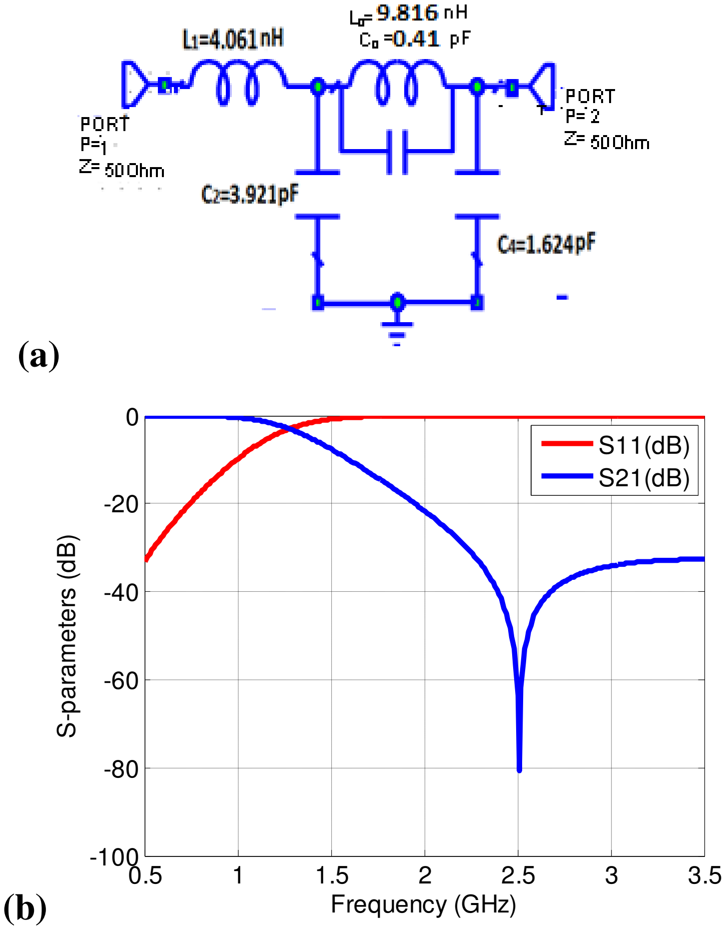

Figure 2.21: (a) The equivalent circuit of the Cross-DGS element. (b) the S-Parameter simulation

As a final step of the filter designing, a new-shaped defected ground structure is applied to the Quasi-Elliptic High-Low Microstrip Lowpass Filter (QE-HL-MLPF) ground plane by implementing two semicircular slots in order to replace the resonant-series microstrip line already used for providing a sharp cut-off frequency response that significantly increases the filter length. Figure (2.22c) shows the proposed SC-DGS-HL-MLPF layout containing one parallel-resonant branches connected in series to open out transmission at the resonant frequency and gives one finite frequency attenuation pole as shown Figure (2.22b) .Semicircular slots provide the same insertion loss at the cut-off frequency, and improve the filter stopband performance reaching a sharp roll-off at 2.5 GHz, and less than -40dB of rejection around the location of the finite zero frequency

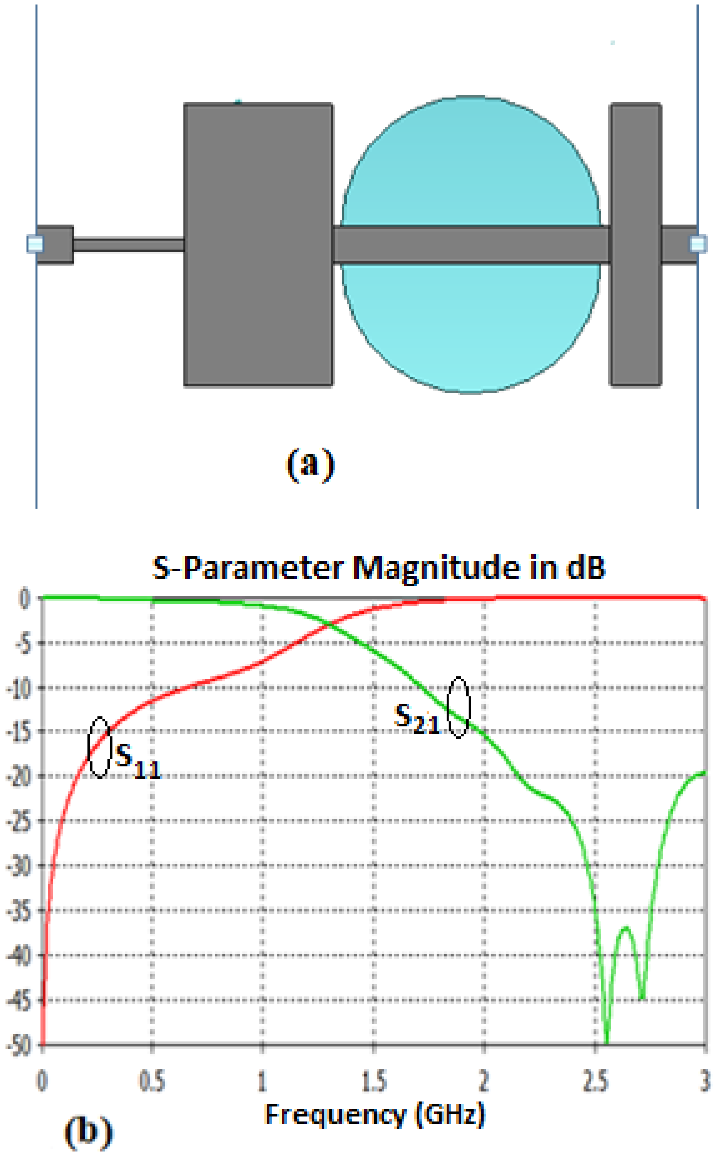

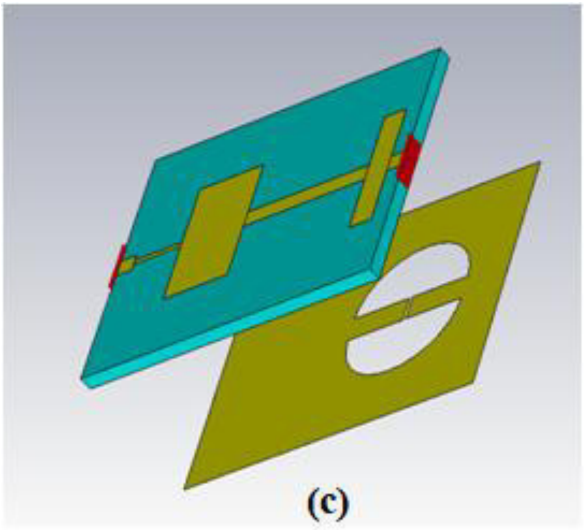

Figure 2.22: The improved semi-circular DGS LPF ,(a) 2D- LPF with semi-circular DGS (b) EM simulation , (c) 3D - LPF with semi-circular DGS

- The proposed structure of the semi-circular- DGS-LPF is shown in Figure(2.22a)
- The EM simulation results of the proposed DGS-LPF are shown in Figure (2.22b).

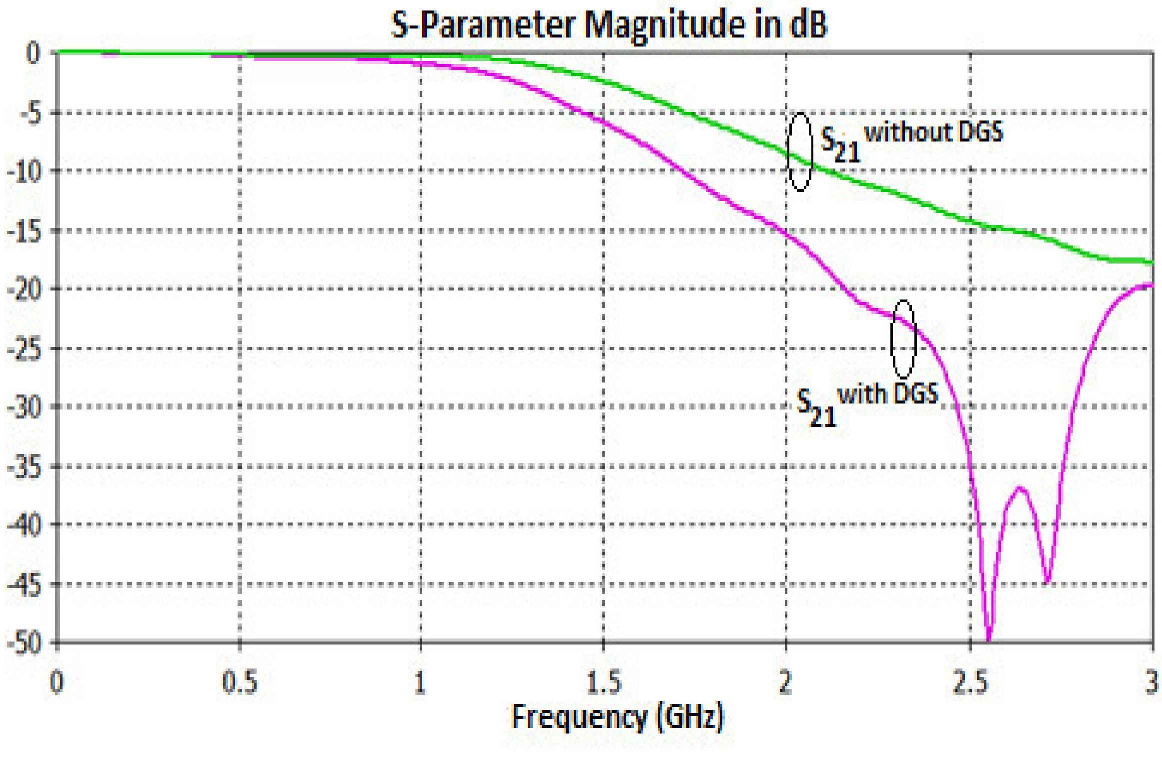

Figure 2.23: Comparison between simulated results of conventional stepped LPF and the proposed LPF with semi-circular –DGS

- **Comparison between simulated results of conventional stepped LPF and proposed semi-circular-DGS LPF**
  - Figure (2.23) compares the EM simulation performance of the stepped LPF with semicircular-DGS with conventional stepped LPF
  - The semi-circular-DGS which could minimize the size of the LPF and improve the stopband performance
  - From figure (2.23), reasonably good agreement between conventional stepped LPF and proposed semi-circular-DGS LPF for insertion loss can be seen below 1.19 GHz

2.7. Conclusion

In this chapter, the different equivalent circuits of defected ground structures are investigated. A new shaped DGS has been studied to design Low Pass Filter DGS on the ground plane. The studied DGS shows sharp rejection with high frequency selectivity along with low in band loss. The Low Pass Filter designed with this DGS shows a size reduction as compared to the conventional DGS as proposed. In this chapter also , a new quasi-elliptic low-pass filter using the semi circular-DGS was presented. The proposed prototype quasi-elliptic lowpass filter was simulated by CST MWS .By carefully choosing the attenuation pole; a shaper cut-off frequency response can be achieved. A 4-pole quasi-elliptic low-pass filter has been designed as an example. The proposed filter design is easy to fabricate and shows compatibility with the different microwave technologies. Moreover, these features DGS with the compactness and simplicity of the structure make the proposed filter a strong candidate for applications in various integrated microwave circuits and it is expected that the proposed structure can be applied to improve the stopband performances of other microwave circuits as well as other types of filters.

[1] Jia-Sheng Hong and M. J. Lancaster. Microstrip Filters for RF/Microwave Applications. New York: John Wiley & Sons, Inc., 2001.

[2] D.M.Pozar, Microwave Engeneering, John Wiley and Sons, 1998.

[3] D. Ahn, J. S. Seok, C. S. Kim, J.Kim, Y. Qian, and I. Itoh, "A design of lowpass filter using the novel microstrip defected ground structure," IEEE Trans.Microwave Theory Tech., vol. 49, no. 1, pp. 86–93, Jan. 2001.

[4] H. J. Chen, T. H. Huang, C. S. Chang, L. S. Chen, N. F. Wang, Y. H. Wang, and M. P. Houng, "A novel cross-shap DGS appied to design ultra-wide stopband low-pass filters," IEEE Microwave Wireless Compon. Lett., vol. 16, no. 5, pp.252–254, May 2006.

[5] A. B. Rahman, A. K. Verma, A. Boutejdar, and A. S. Omar, "Control of bandstop response of hi-lo microstrip low-pass filter using slot in ground plane," IEEE Trans. Microwave Theory Tech., vol. 52, no. 3, pp. 1008–1013, Mar. 2004.

[6] S. W. Ting, K. W. Tam, and R. P. Martins, "Compact microstrip quasi-elliptic bandpass filter using open-loop dumbbell shaped defected ground structure," in 2006 IEEE MTT-S Int.Microw. Symp. Digest, 2006, pp. 527–530.

[7] J. S. Lim, C. S. Kim, D. Ahn, Y. C. Jeong and S. Nam "Design of low-pass filters using defected ground structure," IEEE Trans. Microwave Theory Tech., Vol. 53, No.8, pp. 2539–2545, Jan. 2005.

[8] Ahmed. Boutejdar, G. Nadim, S. Amari and A.S. Omar, "Control of bandstop response of cascaded microstrip lowpass-bandstop filters using arrowhead slots in backside metallic ground plane," IEEE AP-S Symp (Washington DC), 2005.

[9] A. Rahman, A. K. Verma, A. Boutejdar and A. S.Omar, "Control of bandstop response of Hi-Lo microstrip lowpass filter using slot in ground plane," IEEE Trans Microwave Theory Tech., vol. 52, pp. 1008-1013, 2004.

[10] Chen, X., Wang, L., Weng, L., Shi, X. : Compact low pass filter using novel elliptic shape DGS. In: Microw. and Optical Technology Lett, vol. 51, no. 4, pp. 1088-1091, (2009).

Chapter 3: Microwave Filter Optimization: Polynomial and Coupling Matrix

3.1. Introduction

In this chapter, we discuss the scattering parameter equations which are going to be used in the polynomial illustration of the transfer and reflection characteristics of prototype filtering functions. After that, the recursion method is derived and used to create the transfer and reflection polynomials for Chebyshev filtering characteristics of the microwave filters.

In the following chapter, the method was founded to deduce the transfer and reflection polynomials of lowpass prototype filter functions. Then the synthesis process transforms the polynomials into a prototype electrical circuit in which there will be a realizable microwave filter.

The following section in this chapter dealt with the calculation coupling matrix of microwave filter circuits. It is Useful to design the circuit in matrix operations form. It can be put in application like similarity transformation, partitioning and inversion. Those operations can facilitate the, reconfiguration of the structure, the synthesis and the response simulation of complex circuits. In addition, the coupling matrix contains the discrete elements of the practical microwave filter. As an outcome, for each element in the coupling matrix may be assigned uniquely with an element in the accomplished microwave filter equipment. The equivalent circuit which is represented by the coupling matrix is outlined. Next, the synthesis (N+2) coupling matrix from the transfer and reflection polynomials is presented.

The derivation of a function able of respecting the specifications is considered in the first step in filter design. In the next step, a link between the approximation theory and circuit realization is founded through the design polynomials.

Numerical examples are presented in this chapter to illustrate the approach application to the design of coaxial microwave filter . This part provides also various simulation results for the design of microwave filter**.**

3.2. Basic Equations for Polynomials Function for Filter Networks

Most microwave filters can be represented by a two-port lossless, lumped element, reciprocal network as shown in Figure 3.1.This is a general representation of a dual termination filter network capable of maximum power transfer. This means that any signal incident at the source port of the network is either transmitted to the load port$S_{21}(s)$ or reflected back at the source port $S_{11}(s)$.

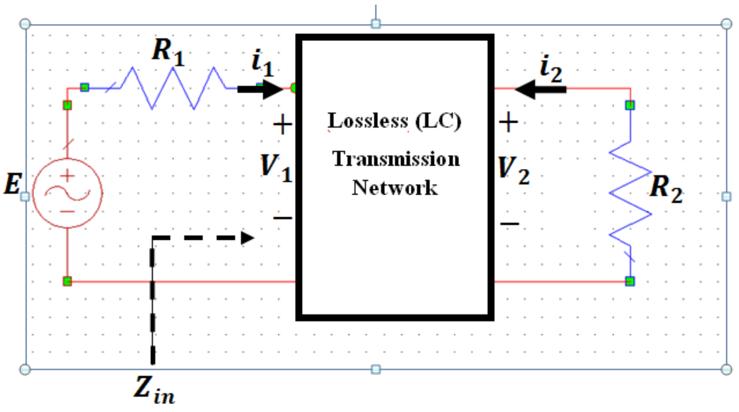

Figure 3.1: A general two-port doubly terminated lossless transmission network

The maximum power that can be taken from the source is P_{Max}=$E^2/4R_1$, the power delivered to the load$R_2$is $|V_2|^2/R_2$. For the quotient of the maximum available power and the power delivered to the load [2] :

$$\frac{P_{max}}{P_2} = \frac{1}{4}\sqrt{\frac{R_2}{R_1}}\left|\frac{E}{V_2}\right|^2 \tag{3.1}$$

$$\text{for } R_2 = R_1 \ : \quad \frac{P_{max}}{P_2} = \frac{1}{4}\left|\frac{E}{V_2}\right|^2$$

In the case of passive lossless networks,P_2 should be only equal to or less than P_{max}.For these filtering networks, it is more practical to define a characteristic function C (s) with the complex frequency variable s by [2]:

$$\frac{P_{max}}{P_2} = 1 + |C(s)|^2_{s=j\omega} \quad \text{with} \quad |C(s)|^2 = \begin{cases} \ll 1 & in\ bandpass \\ \gg 1 & in\ stopband \end{cases} \tag{3.2}$$

C(s) is a rational function in s domain with real coefficients, taking in consideration the lumped, linear, and time-invariant circuits. The ratio P_{max}/P_2 is determined by the transmission function H(s), where the relationship between the characteristic and the transmission function H(s) is shown in equation (3.3)[2].

$$|H(s)|^2_{s=j\omega} = 1 + |C(s)|^2_{s=j\omega} \tag{3.3}$$

H(s) is also called transducer function and can be written in the alternative form [2]:

$$H(s)H(-s) = 1 + C(s)C(-s) \tag{3.4}$$

The former equation indicates that H(s) and C(s) have the same denominator polynomial; thus if H(s) is written as:

$$\mathrm{H(s)} = \frac{\mathrm{E(s)}}{\mathrm{P(s)}} \tag{3.5}$$

C(s) can be written as:

$$\mathrm{C(s)} = \frac{\mathrm{F(s)}}{\mathrm{P(s)}} \tag{3.6}$$

Making use of (3.4), (3.5), and (3.6), we can relate the polynomials by:

$$\mathrm{E(s)E(-s)} = \mathrm{P(s)P(-s)} + \mathrm{F(s)F(-s)} \tag{3.7}$$

The attenuation of the network is given by:

$$\begin{aligned} A(j\omega) &= 10log|H(j\omega)|^2 \\ &= 10\mathrm{log}(1 + |C(j\omega)|^2) \end{aligned} \tag{3.8}$$

Thus, when either $H(j\omega)$ or $C(j\omega)$ is infinite, the attenuation is infinite. However, onlywhen $C(j\omega)$is zero is there an attenuation zero. The characteristic function is thus the more useful, because it eliminates the unity constant and focuses attention on the attenuation zeros (reflection zeros) and attenuation poles (transmission zeros).

3.2.1. Transmission and Reflection Polynomial Synthesis

It should be noted that in terms of scattering parameters, the reflection and insertion losses can be alternatively represented as rational function

$$|S_{11}(j\omega)|^2 = \frac{\text{reflected power}}{\text{avialable power}}$$

$$|S_{21}(j\omega)|^2 = \frac{\text{transmitted power}}{\text{avialable power}} \tag{3.9}$$

For the lossless filter circuit in Figure 3.1 and also in addition, the unitarity condition must be apply

$$\frac{\text{Reflected power}}{\text{Avialable power}} + \frac{\text{transmitted power}}{\text{avialable power}} = 1 \quad \text{or} \quad \frac{\mathrm{P_r}}{\mathrm{P_{max}}} + \frac{\mathrm{P_2}}{\mathrm{P_{max}}} = 1 \tag{3.10}$$

$$|S_{11}(j\omega)|^2 + |S_{21}(j\omega)|^2 = 1 \tag{3.11}$$

In terms of decibels, the transmission (often termed the insertion loss IL) and reflection loss (often termed the return loss RL) are defined as [2]

$$IL = 10\log\frac{1}{|S_{21}(j\omega)|^2} = -10\log|S_{21}(j\omega)|^2 \qquad dB \tag{3.12}$$

$$RL = 10\log\frac{1}{|S_{11}(j\omega)|^2} = -10\log|S_{11}(j\omega)|^2 \qquad dB$$

An equivalent definition of the reflection coefficient in the transmission line theory is given by :

$$\mathrm{S_{11}(s)} = \frac{\mathrm{Z_{in}(s) - R_1}}{\mathrm{Z_{in}(s) + R_1}} = \frac{\mathrm{z_{in}(s) - 1}}{\mathrm{z_{in}(s) + 1}} \ \text{ with } \ \mathrm{z_{in}(s)} = \frac{\mathrm{Z_{in}(s)}}{\mathrm{R_1}} \tag{3.13}$$

The quantity $\mathrm{Z_{in}(s)}$ represents the input impedance of the circuit to the right of R_1.Since this is an LTI network (linear time invariant), so, $\mathrm{z_{in}(s)}$ can be expressed as a quotient of two polynomials in the complex frequency variable s as follows [18]:

$$\mathrm{z_{in}(s)} = \frac{N(s)}{D(s)} \tag{3.14}$$

In order to represent a physical system, the input impedance $\mathrm{z_{in}(s)}$ must be positive real function, i.e. $\mathrm{Re\{z_{in}(s)\}} \geq 0 \iff \mathrm{Re\{s\}} \geq 0$, $\mathrm{z_{in}(s)} \in \mathbb{R} \iff \mathrm{s} \in \mathbb{R}$ [18].

The input reflection coefficient $\mathrm{S_{11}(s)}$ of the circuit also becomes:

$$\mathrm{S_{11}(s)} = \frac{\mathrm{z_{in}(s) - 1}}{\mathrm{z_{in}(s) + 1}} = \frac{N(s) - D(s)}{N(s) + D(s)} = \frac{F(s)}{E(s)} \tag{3.15}$$

The reflection coefficient $\mathrm{S_{11}(s)}$of a filter of order N can be represented by the filter characteristic polynomials, F(s) and E(s). Figure 3.2 shows a flow chart of microwave filter synthesis polynomial process for lowpass prototype filter networks with **symmetric characteristics**.

The transfer and reflection parameters ($\mathrm{S_{21}}(j\omega)$ and $\mathrm{S_{21}}(j\omega)$) **,** along the imaginary axis ($s = j\omega$), can be expressed as the ratio of two polynomials

$$\mathrm{S_{21}}(j\omega) = \frac{P(s)}{E(s)} \quad \Rightarrow \quad |\mathrm{S_{21}}(j\omega)|^2 = \frac{P(s)P^*(s)}{E(s)E^*(s)}$$

$$\mathrm{S_{11}}(j\omega) = \frac{F(s)}{E(s)} \quad \Rightarrow \quad |\mathrm{S_{11}}(j\omega)|^2 = \frac{F(s)F(-s)}{E(s)E(-s)} \tag{3.15a}$$

Where $s = j\omega$, $F^*(s) = F(-s)$ and $E^*(s) = E(-s)$, and the characteristic function is then expressed as the ratio of the polynomials in the form

$$C(s) = \frac{F(s)}{P(s)} \tag{3.16}$$

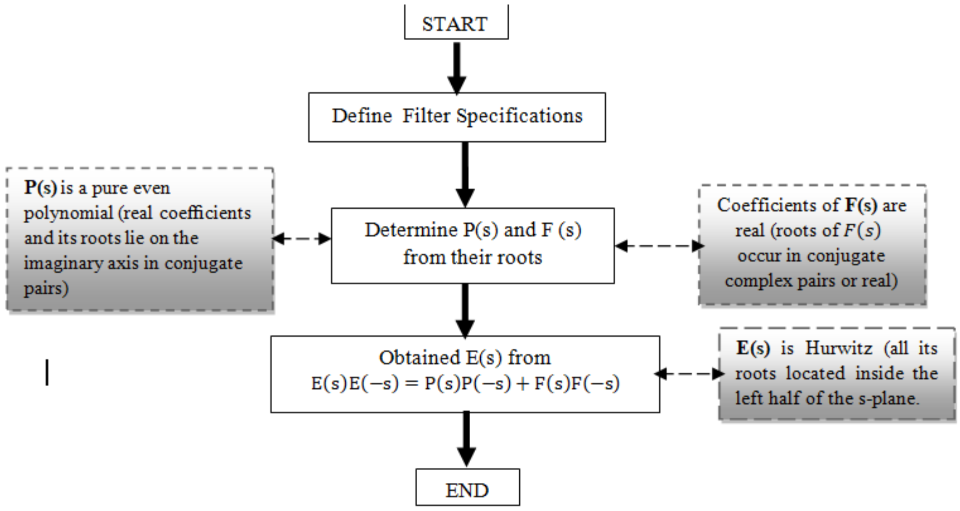

Figure 3.2: Flow chart of microwave filter synthesis polynomial functions(reel coefficients) procedure

3.2.2. Normalization of the transfer function and characteristic polynomials

The transfer function of lossless network filter is defined in terms of the characteristic funcion C(s) in (3.3) and (3.9) as [2]

$$|S_{21}(s)|^2_{s=jw} = \frac{1}{1+|C(s)|^2_{s=jw}} \tag{3.17}$$

A real constant ε can be added, with lossless generality, and reformulate the relation as

$$|S_{21}(s)|^2_{s=jw} = \frac{1}{1+\varepsilon^2|C(s)|^2_{s=jw}} \tag{3.18}$$

Where, ε is the ripple constant . It is used to normalize the maximum amplitude the transfer function of the network filter in the passband.

The expression for ε which is given bellow is achieved when the frequency ω_1 is the bandwidth corresponding to the maximum ripple in the passband.

$$\varepsilon = \sqrt{\frac{|S_{21}(j\omega_1)|^{-2} - 1}{|C(j\omega_1)|^2}} \tag{3.19}$$

The insertion loss and return loss at ripple in the passband are expressed as :

$$IL = 10Log[1+\varepsilon^2|C(s)|^2_{s=jw}] \tag{3.20}$$

$$RL = 10Log[\frac{\varepsilon^2|C(s)|^2_{s=jw}}{1+\varepsilon^2|C(s)|^2_{s=jw}}]$$

From equation (3.20) it may readily be seen that there are two S-parameters shown in figure (3.3).

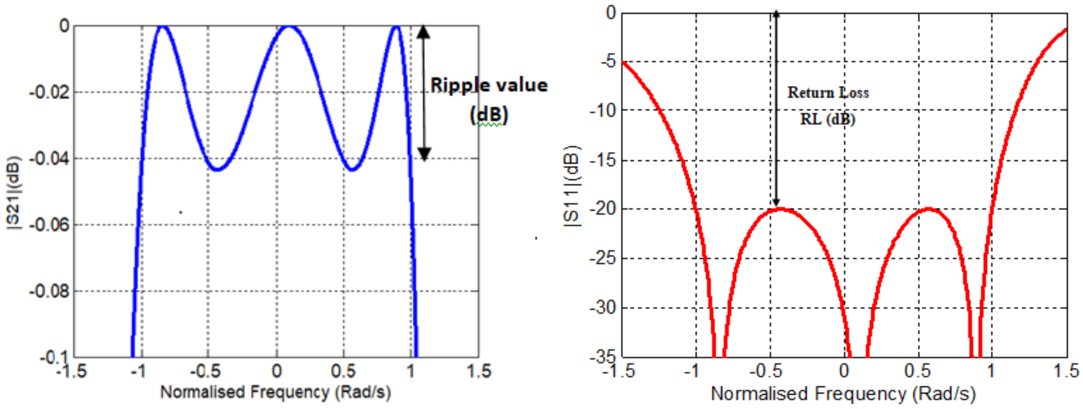

Figure 3.3: Insertion Loss (IL), S21 (dB) with Ripple value and Return Loss (RL) S11 (dB)

For normalized lowpass filter network prototype, ω_1 is presented to as the cutoff frequency and is normally chosen to be unity (at $\omega_1 = \mp 1$).The ε is related to the insertion loss (IL) ripple and hence the passband return loss (RL),then ,the ripple constant ε can also be expressed as

$$\varepsilon = \sqrt{\frac{10^{IL/10} - 1}{|C(j\omega_1)|^2_{\omega_1=\mp 1}}} = \sqrt{\frac{[10^{-RL/10} - 1]^{-1}}{|C(j\omega_1)|^2_{\omega_1=\mp 1}}} \tag{3.21}$$

$C(s)|_{s=j\omega}$ is a characteritic function which must then obtain the maximum value of 1 at the maximum number of points in the region $|\omega| \le 1$ $(\omega_1 = \mp 1)$. $C(s)|_{s=j\omega}$ is thus of the form shown in Figure (3.4) .

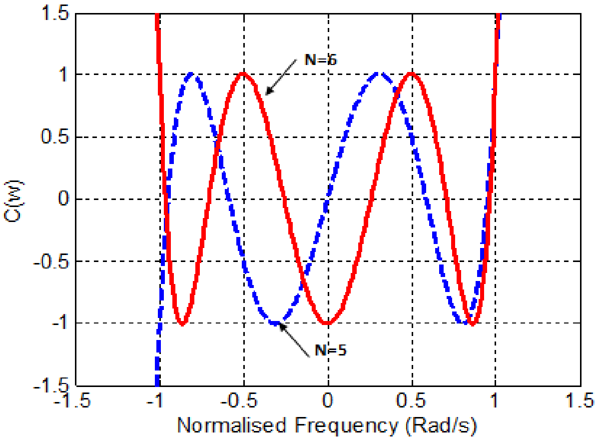

Figure 3.4: Characteristic Function $C(s)|_{s=j\omega}$

Since the polynomial C(s) represents the ratio of polynomials F(s) and P(s), it is more appropriate to represent C(s) in the form.

$$C(s) = \frac{F(s)}{P(s)/\varepsilon} \tag{3.22}$$

The polynomials F(s) and P(s) are normalized in the filter synthesis procedure, so that their highest coefficients are unity. The ripple factor ε is used to normalize F(s) and P(s).From (3.18), the transmitted and reflected coefficients can be rewritten by

$$\begin{gathered} |S_{21}(s)|^2 = \frac{1}{1+\varepsilon^2|C(s)|^2} = \frac{1}{\varepsilon^2}\frac{|P(s)|^2}{|E(s)|^2} \\ S_{21}(s) = \frac{P(s)/\varepsilon}{E(s)} \quad and \quad S_{11}(s) = \frac{F(s)}{E(s)} \end{gathered} \tag{3.23}$$

Polynomials F(s) and P(s) are formed by the zeros of reflection and transmission, respectively, and are assumed known with their highest coefficients as unity. Finally the polynomial E(s) is determined as:

$$E(s)E(-s) = \frac{1}{\varepsilon^2}P(s)P(-s) + F(s)F(-s) \tag{3.24}$$

3.2.3. Characteristic and properties of the design polynomials

Filter design requirements needs a low loss in the passband and a high loss in the stopband**.** Such a design requirement could be best realized by assigning all the roots of $F(s)$ to the $(j\omega)$ axis in the passband region, and all roots of $P(s)$ to the $(j\omega)$ is in the stopband region. For some cases, the roots of P(s) have a non-jω-axis position. This help as to obtain an enhancement phase and group delay response in the passband at the expense of a loss in the stopband. To guarantee that the characteristic polynomials ($C(s) = F(s)/P(s)$) fit to be positive real functions ($Z_{in}(s)$ in function of $F(s)$ and $E(s)$) the pole/zero positions of lossless lowpass prototype networks normalized to a unity cutoff frequency are limited as follows :

1. All the roots of $F(s)$ must be located symmetrically on the imaginary (jω) axis in the passband space.(see figure 3.5.a.)

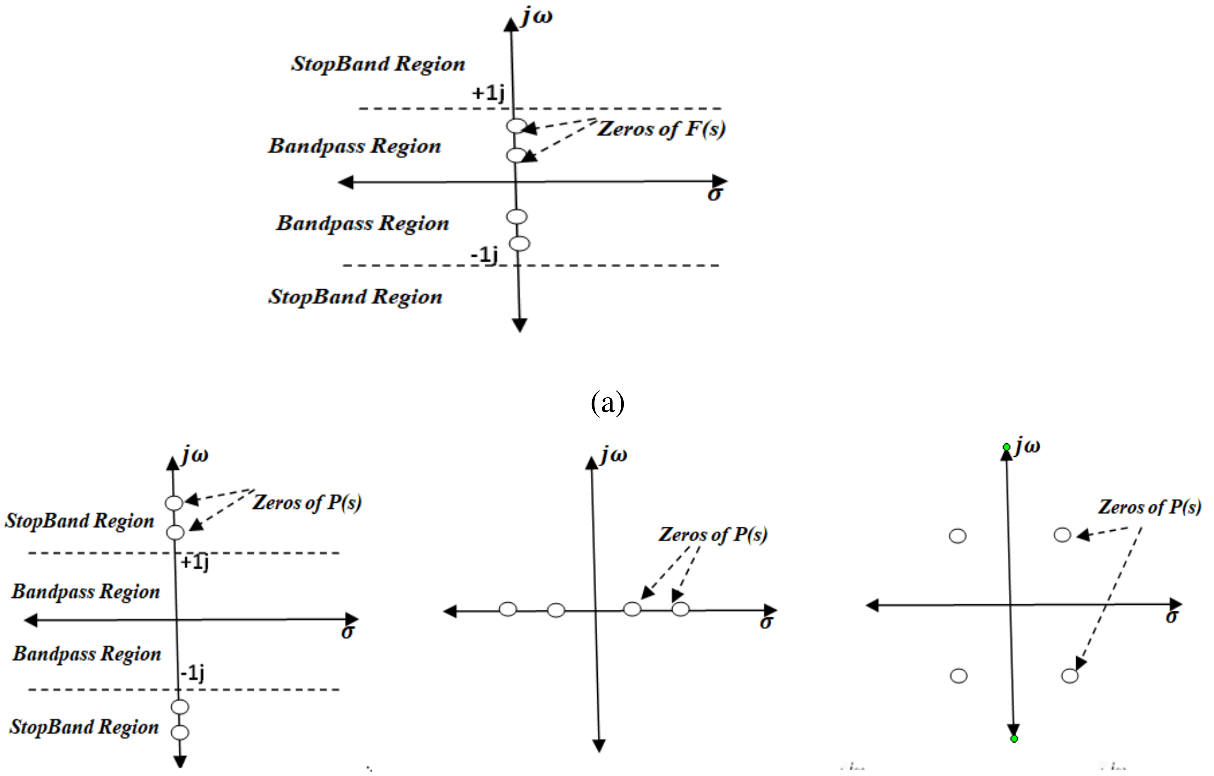

(a)

(b)

Figure 3.5: Permissible zero locations of lowpass prototype characteristic polynomials,(a) zero locations of *F(s)*. (b) zero locations of *P(s)* on the (jω) axis, real axis, and as a complex quad

2. All the roots of *P(s)* must be located symmetrically on the imaginary (jω) axis or real axis, or be distributed symmetrically along the real and imaginary axes, constructing a conjugate complex quad in the **s** plane.(see figure 3.5.b.)

Under the previous assumptions, the characteristic function C(s) may be written as:

$$C(s) = \varepsilon \frac{F(s)}{P(s)} = \begin{cases} \varepsilon \dfrac{s(s^2+\alpha_1^2)(s^2+\alpha_2^2)\ldots}{(s^2 \pm \beta_1^2)(s^2 \pm \beta_2^2)\ldots(s^4 \pm \gamma_1 s^2 + \mu_1)\ldots} & \text{for odd order network} \\ \varepsilon \dfrac{(s^2+\alpha_1^2)(s^2+\alpha_2^2)\ldots}{(s^2 \pm \beta_1^2)(s^2 \pm \beta_2^2)\ldots(s^4 \pm \gamma_1 s^2 + \mu_1)\ldots} & \text{for even order network} \\ |\alpha_1|, |\alpha_2|, \ldots < 1 \ \ and \ \ |\beta_1|, |\beta_2|, \ldots > 1 & \\ \alpha, \beta = \text{zeros and poles of the function} & \end{cases} \tag{3.25}$$

These relationships clearly show that all the F(s) and P(s) are real coefficients polynomials and are either pure even or pure odd, reflecting the nature of positive real functions to realize Lowpass prototype networks.

In the case an asymmetric response, the design polynomials can produce complex coefficients and the realization of asymmetric lowpass prototype filters, the characteristic polynomials have the following properties:

1. The roots of F(s) must lie on the imaginary axis, but they need not be distributed symmetrically around zero frequency (see figure 3.6.a.).
2. The roots of P(s) lie on the imaginary axis but no pairs are needed (see figure 3.6.b) and the roots of P(s) can appear as pairs of roots located symmetrically with respect to the imaginary axis (see figure 3.6.c), but when they are placed in the imaginary axis asymmetric root locations in the upper and lower bands (see figure 3.6.d.).
3. E(s) remains as a strict Hurwitz polynomial. All its roots lie in the left half-plane of s

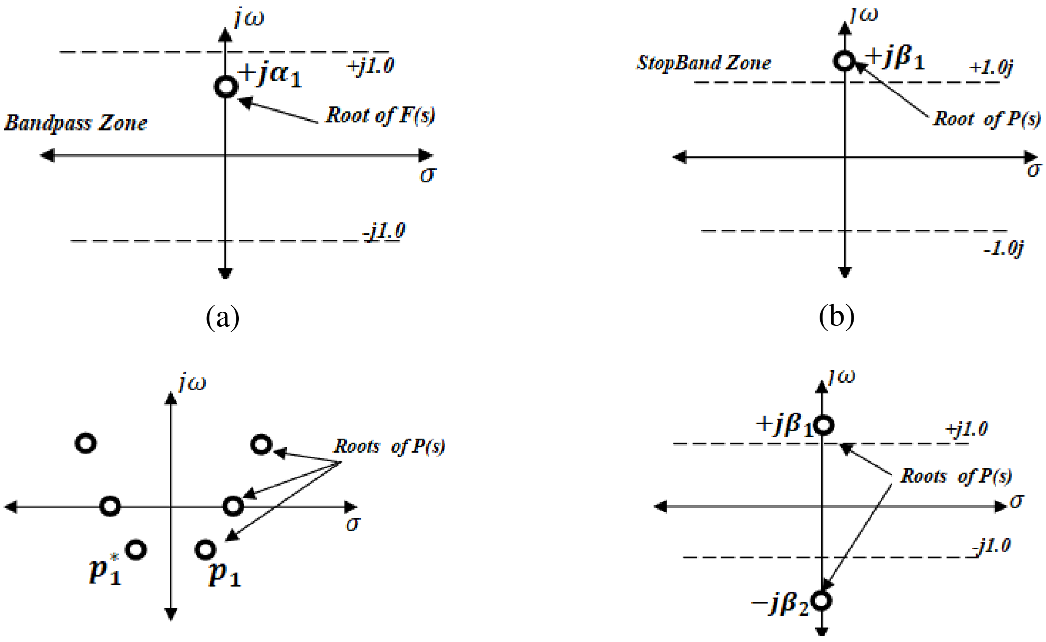

(a) (b)

(c) (d)

Figure 3.6: (a) asymmetric root locations of F(s) on the j*ω* axis, (b) asymmetric root locations of P(s) in the upper band, (c) Root locations of P(s) as pairs symmetrically located , (d.) asymmetric root locations of P(s) in the upper and lower bands

Under the previous assumptions, the characteristic polynomial C(s) may be written as:

$$C(s) = \varepsilon\frac{F(s)}{P(s)} = \left[\begin{array}{c} \varepsilon\dfrac{\mathrm{s^n + ja_{n-1}s^{n-1} + a_{n-2}s^{n-2} + ja_{n-3}s^{n-3} + \cdots + a_0}}{\mathrm{s^m + jb_{m-1}s^{m-1} + b_{m-2}s^{m-2} + jb_{n-3}s^{n-3} + \cdots + b_0}} \\ \\ |\mathrm{a_1}|, |\mathrm{a_2}|, \ldots < 1 \;\; and \;\; |\mathrm{b_1}|, |\mathrm{b_2}|, \ldots > 1 \\ \mathrm{a, b = coefficient\ of\ the\ polynomial} \end{array}\right. \tag{3.26}$$

Where n is the order of the filter and m is the number of zero transmission of P(s).

3.2.4. Polynomial synthesis for Symmetric and Asymmetric Filtering Functions examples

To verify the method outlined in the previous section, two examples are provided.

Example 1:

The first example consists of a fifth-order symmetric filter with a Chebyshev passband with the following specifications:

- Central frequency: f0=3029.85 MHz
- Bandwidth: BW=60 MHz
- Return loss: RL =20 dB
- Order filter N=5,
- nfz =0 (nfz is the degree of $P(s)$ corresponds to the number of finite zeros TZ (transmission zeros))

The coupling scheme is shown in Figure 3.7 as a two-port filter, whose response is reported in Figure 3.8. The lowpass transmission function of the fifth-order Chebyshev function is then given by

$$S_{21}(s) = \varepsilon \frac{P(s)}{E(s)} = \frac{0.6219}{s^5 + 2.055s^4 + 3.36s^3 + 3.2s^2 + 2.02s + 0.62} \quad \text{where } \varepsilon = 1.6$$

and the lowpass reflection function is given by

$$S_{11}(s) = \frac{F(s)}{E(s)} = \frac{s^5 + 1.25s^3 + 0.3125s}{s^5 + 2.055s^4 + 3.36s^3 + 3.2s^2 + 2.02s + 0.62}$$

- E(s) is an Nth-degree polynomial with real coefficients.
- P(s) is an even polynomial of degree (nfz =0) with real coefficients (all-pole function).
- F(s) is an Nth-degree (N=5) polynomial with real coefficients.

The polynomials E(s), F(s) and P(s) are all monic polynomials, i.e., the coefficients of their highest degrees are unity.

The polynomial response is shown in Figure 3.7 (note: this is the response at the normalized low-pass frequency range). The response in Bandpass real frequency (f) is obtained by the following transformation: $f = \frac{\text{BW}+\sqrt{(\text{BW})^2+4(f_0)^2}}{2}$

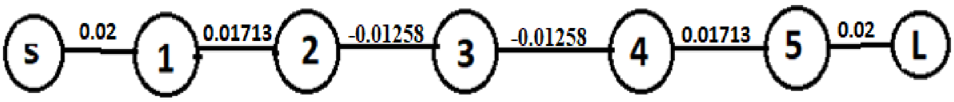

Figure 3.7: The routing diagram and coupling values of the first example

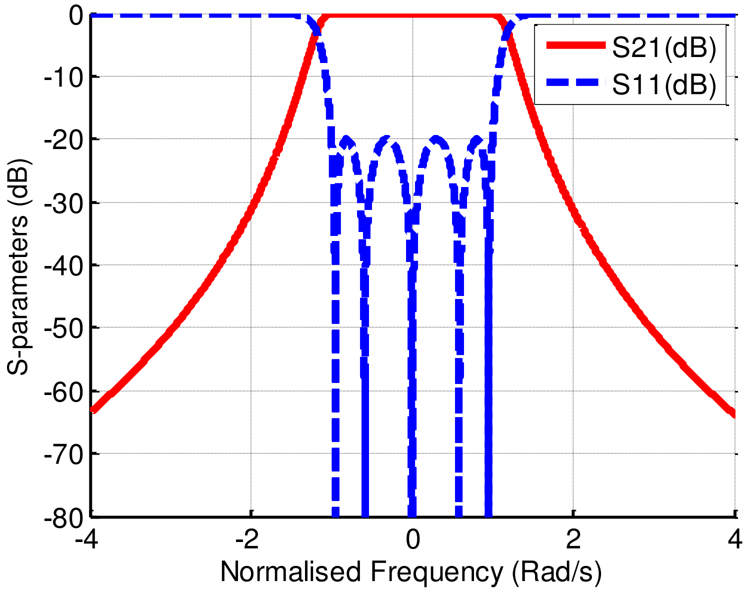

Figure 3.8: Frequency response of the normalized filter

Example 2:

The second example consists of a fifth order filter with a transmission zero on the right side of the passband. The only difference from the first example is the location of the zero. This filter has the following specifications:

- Central frequency: f0=3029.85 MHz
- Bandwidth: BW=60 MHz
- Return loss: RL =20 dB
- Order filter- N=5,
- nfz =1 (Transmission zero frequency: 3136.7 MHz correspond Normalized frequency wz=3.5)

The lowpass transmission function of the fifth -order chebyshev function is then given by:

$$S_{21}(s) = \varepsilon \frac{P(s)}{E(s)}$$

$$= \frac{5.51js + 19.88}{s^5 + (2.05 - 0.14i)s^4 + (3.35 - 0.33i)s^3 + (3.2 - 0.5i)s^2 + (2 - 0.43i)s + (0.6 - 0.19i)}$$

$$\text{where } \varepsilon = 5.51$$

and the lowpass reflection function is given by

$$S_{11}(s) = \frac{F(s)}{E(s)}$$

$$= \frac{s^5 - 0.145js^4 + 1.2s^3 - 0.1458js^2 + 0.308s - 0.0182j}{s^5 + (2.05 - 0.14i)s^4 + (3.35 - 0.33i)s^3 + (3.2 - 0.5i)s^2 + (2 - 0.43i)s + (0.6 - 0.19i)}$$

Where F(s) ,E(s) and P(s) are finite degree polynomials with complex coefficients and their degrees corresponding to the order and number of transmission zeros of a filter. The structure of filter is shown in Figure 3.9.The frequency response of the synthesis polynomial is shown in figure 3.10.

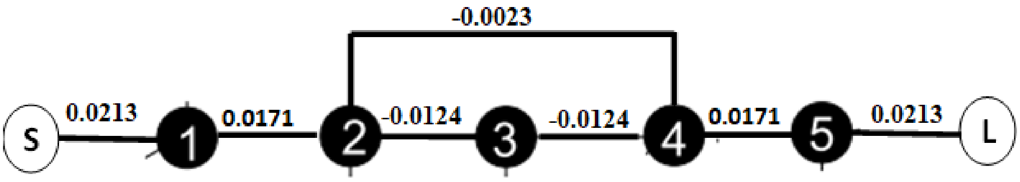

Figure 3.9: The routing diagram and coupling values of the fifth-order lowpass prototype circuit with one transmission zero

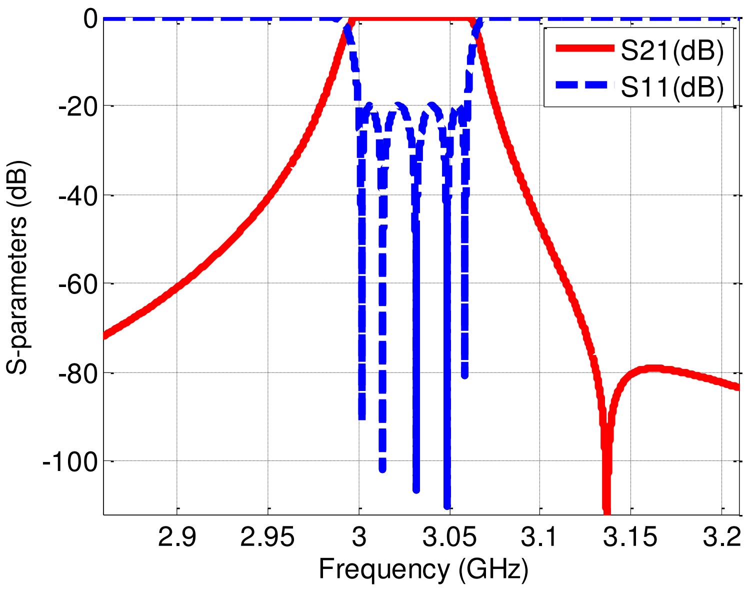

Figure 3.10: Fifth -order Bandpass prototype response (zero on the right)

3.3. Generalized Chebyshev Polynomials Approximation (Pseudo Elliptic)

The methods introduced in this chapter include the design of the transfer functions and the synthesis of the prototype filters networks with characteristics belonging to the generalized Chebyshev polynomial filters.

3.3.1. Polynomial Synthesis

For any Microwave lossless filter composed of a series of N inter-coupled resonators, the reflection and transfer functions may be expressed by a quotient of two polynomials of degree N (order of filter): [2]

$$\text{Reflection Function} \quad S_{11}(\omega) = \frac{F(\omega)}{E(\omega)} \tag{3.27}$$

$$\text{Transfer Function} \quad S_{21}(\omega) = \frac{P(\omega)/\varepsilon}{E(\omega)}$$

Where ω is the real frequency variable, related to the complex frequency variable by $s = j\omega$. The polynomial $P(\omega) = \prod_{n=1}^{n_{fz}}(\omega - \omega_n)$, numerator of $S_{21}(\omega)$, which contains the transmission zeros (TZs) is of degree n_{fz} , where n_{fz} is the number of finite position transmission zeros that have been prescribed (for a realizable filter, $n_{fz} \leq N$). In addition, for a Chebyshev filtering function , ε is a constant that normalizes the value of $S_{21}(\omega)$ to the equiripple level at $\omega = \mp 1$ as follows:

$$\varepsilon = \left(10^{0.1RL} - 1\right)^{-0.5} \left|\frac{P(s)}{F(s)}\right|_{s=\mp j} = \left(10^{0.1RL} - 1\right)^{-0.5} \left|\frac{P(\omega)}{F(\omega)}\right|_{\omega=\mp 1} \tag{3.28}$$

Where RL represents the level return loss level in decibels and it assumed that all polynomials $P(\omega)$, $F(\omega)$and $E(\omega)$ have been normalized such that their highest-degree coefficients are equal to one.

We can develop the expression of the transfer function (3.27) , by using the conservation of energy formula for a lossless network $|S_{21}(\omega)|^2 + |S_{11}(\omega)|^2 = 1$, we obtain the generalized Chebychev filtering function formula [2]:

$$|S_{21}(\omega)|^2 = \frac{1}{1+\varepsilon^2 C_N^2(\omega)} = \frac{1}{(1+j\varepsilon C_N(\omega))(1-j\varepsilon C_N(\omega))} \tag{3.29}$$

In the previous development, we have defined a new function $C_N(\omega)$, which it is known as characteristic function, and Nth-order general Chebyshev filtering function is written as [5]:

$$C_N(\omega) = \frac{F(\omega)}{P(\omega)} = \cosh\left[\sum_{n=1}^{N} \cosh^{-1}\left(\frac{\omega - 1/\omega_n}{1 - \omega/\omega_n}\right)\right] \tag{3.30}$$

Where $s = j\omega$ is the complex angular frequency variable in the complex s-plane or the lowpass domain and $s_n = j\omega_n$, is the position of the nth transmission zero in the complex s-plane. It can be shown that the characteristic function, which define a typical Chebyshev function [6]

$$\begin{aligned} &|\omega| < 1 && -1 < C_N(\omega) < 1, \\ &|\omega| = 1 && C_N(\omega) = 1, \\ &|\omega| > 1 && C_N(\omega) < -1, \quad \text{and} \quad C_N(\omega) > 1, \end{aligned} \tag{3.31}$$

After certain polynomial synthesis procedures of rearrangement described in [2], we may now have its final expression as follows:

$$C_N(\omega) = 0.5.\left[\frac{\prod_{n=1}^{N}[c_n + d_n] + \prod_{n=1}^{N}[c_n - d_n]}{\prod_1^N\left(1 - \frac{\omega}{\omega_n}\right)}\right] \tag{3.32}$$

The frequency variable is ω and ω_n is the position of the n^{th} prescribed transmission zero. where, we define now $c_n = \omega - \frac{1}{\omega_n}$, $d_n = \omega'\sqrt{(1 - 1/\omega_n^2)}$ and $\omega' = \sqrt{(\omega^2 - 1)}$

It may be seen that the denominator of $C_N(\omega)$ is the numerator polynomial of $S_{21}(\omega)$, generated from the prescribed transmission zeros ω_n(the denominator of $C_N(\omega)$ has the same zeros as P(ω)).

3.3.2. Recursive Cameron Algorithm

The numerator of $C_N(\omega)$ is the numerator of $S_{11}(\omega)$,$F(\omega)$ which can be detemined by the recursive algorithm is presented as following:

$$\text{Num}[C_N(\omega)] = F(\omega) = 0.5\left[G_N(\omega) + G_N'(\omega)\right]$$

Where
$$G_N(\omega) = \prod_{n=1}^{N}\left[\left(\omega - \frac{1}{\omega_n}\right) + \omega'.\sqrt{1 - \frac{1}{\omega_n^2}}\right] \tag{3.33}$$

$$G_N'(\omega) = \prod_{n=1}^{N}\left[\left(\omega - \frac{1}{\omega_n}\right) - \omega'.\sqrt{1 - \frac{1}{\omega_n^2}}\right]$$

The technique for calculating the coefficients of $F(\omega)$ consists of a recursive algorithm in which the solution for the N^{th} degree is constructed using the results obtained for $(N - 1)th$ degree. Firstly, considering the polynomial $G_N(\omega)$, it can be written as the sum of two polynomials $U_N(\omega)$ and $V_N(\omega)$, where the $U_N(\omega)$ polynomial contains the coefficients of the terms in the variable ω only, while each coefficient of the auxiliary polynomial $V_N(\omega)$ is multiplied by the transformed variable $\omega' = \sqrt{\omega^2 - 1}$

$$G_N(\omega) = U_N(\omega) + V_N(\omega) \tag{3.34}$$

where $$U_N(\omega) = u_0 + u_1\omega + u_2\omega^2 + \cdots u_N\omega^N$$
$$V_N(\omega) = \omega'(v_0 + v_1\omega + v_2\omega^2 + \cdots v_N\omega^N$$

The recursion cycle begins with N = 1, the first zero transmission ω_1.

$$\begin{aligned} \mathrm{G}_1(\omega) &= [c_1 + d_1] \\ &= \left(\omega - \frac{1}{\omega_1}\right) + \omega'.\sqrt{1 - \frac{1}{\omega_1^2}} \\ &= U_1(\omega) + V_1(\omega) \end{aligned} \tag{3.35}$$

Next, as a first step of the process, $\mathrm{G}_1(\omega)$ must be multiplied by the terms corresponding to the second zero transmission ω_2 ,given by:

$$\begin{aligned} &\mathrm{G}_2(\omega) \\ &= \mathrm{G}_1(\omega)[c_2 + d_2] \\ &= [U_1(\omega) + V_1(\omega)].\left[\left(\omega - \frac{1}{\omega_2}\right) + \omega'.\sqrt{1 - \frac{1}{\omega_2^2}}\right] \\ &= [U_2(\omega) + V_2(\omega)] \end{aligned} \tag{3.36}$$

Where

$$\mathrm{U}_2(\omega) = \mathrm{U}_1(\omega).\left(\omega - \frac{1}{\omega_2}\right) + \mathrm{V}_1(\omega).\omega'\sqrt{1 - \frac{1}{\omega_2^2}}$$

$$\mathrm{V}_2(\omega) = \mathrm{V}_1(\omega)\left(\omega - \frac{1}{\omega_2}\right) + \mathrm{U}_1(\omega).\omega'\sqrt{1 - \frac{1}{\omega_2^2}}$$

Then, the cycle is repeated until all N of transmission zeros (including those at $\omega_n = \infty$) are introduced, i.e, (N — 1) cycles. Similarly, the same recursive process is repeated for $G_N'(\omega) = U_N'(\omega) + V_N'(\omega)$, so , we have $\begin{cases} U_N'(\omega) = \mathrm{U_N}(\omega) \\ V_N'(\omega) = -\mathrm{V_N}(\omega) \end{cases}$

Therefore,

$$\begin{aligned} &F(\omega) \\ &= 0.5.\left[G_N(\omega) + G_N'(\omega)\right] \\ &= \mathrm{U_N}(\omega) \end{aligned} \tag{3.37}$$

Now, the reflection zeros of $S_{11}(\omega)$ can be found by solving the roots of $\mathrm{U_N}(\omega)$, and then the polynomial $\mathrm{E}(\omega)$ found from the conservation of energy principle [2]. To conclude, it can be observed that as a generalized method, deriving the all-pole pure Chebyshev response from it is a must. In fact, if all the transmission zeros ω_n toward infinity, $C_N(\omega)$ degenerates to the well-known all-pole function:

$$C_N(\omega)|\omega_{n\to\infty} = \cosh[N\cosh^{-1}(\omega)] \tag{3.38}$$

3.3.3. Recursive Algorithm Implementation by Matlab

This Recursive algorithm can be programmed easily by Matlab. One selected example with detailed results is presented below here.

- **Illustration Example:**

The polynomials of a microwave Asymmetric Chebyshev filter with fourth-order filtering response with finite transmission zeros located at +1.52j and +j1.95j are synthesized here. It has a return loss of 20 dB. The polynomial $F(\omega)$ is found by applying the recursive technique presented previosly The recursive process starts by substitution of $\omega_1 = 1.52$, into equation (3.34) ,which results to :

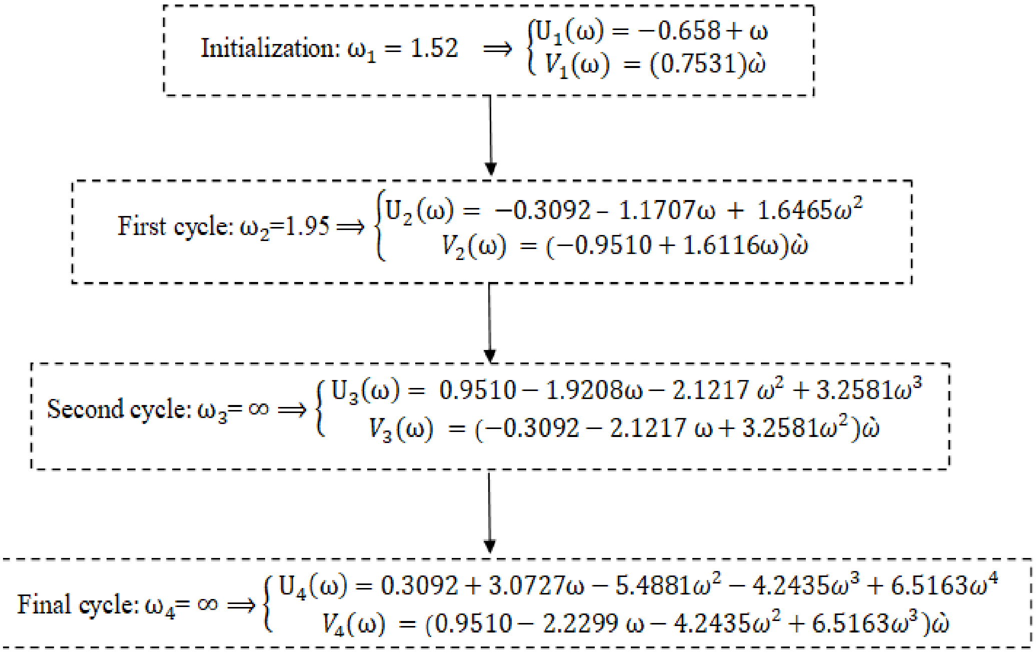

Initialization: $\omega_1 = 1.52 \Rightarrow \begin{cases} U_1(\omega) = -0.658 + \omega \\ V_1(\omega) = (0.7531)\dot{\omega} \end{cases}$

First cycle: ω_2=1.95 $\Rightarrow \begin{cases} U_2(\omega) = -0.3092 - 1.1707\omega + 1.6465\omega^2 \\ V_2(\omega) = (-0.9510 + 1.6116\omega)\dot{\omega} \end{cases}$

Second cycle: $\omega_3 = \infty \Rightarrow \begin{cases} U_3(\omega) = 0.9510 - 1.9208\omega - 2.1217\,\omega^2 + 3.2581\omega^3 \\ V_3(\omega) = (-0.3092 - 2.1217\,\omega + 3.2581\omega^2)\dot{\omega} \end{cases}$

Final cycle: $\omega_4 = \infty \Rightarrow \begin{cases} U_4(\omega) = 0.3092 + 3.0727\omega - 5.4881\omega^2 - 4.2435\omega^3 + 6.5163\omega^4 \\ V_4(\omega) = (0.9510 - 2.2299\,\omega - 4.2435\omega^2 + 6.5163\omega^3)\dot{\omega} \end{cases}$

- At last iteration, normalizing the polynomial $U_4(\omega)$ gives the polynomial $F(\omega)$(numerator of $S_{11}(\omega)$) and finding its roots yields the N reflection zeroes, where N is the order of the filtering function
- The roots of $V_4(\omega)$ are the (N-1) frequency locations in-band reflection maxima.
- The polynomial $P(\omega)$ is constructed from its transmission zeros.
- The constants **ε** is calculated from equation (3.28).
- Finally, the polynomial $E(\omega)$ can be determinate from the equation (3.24).

Table 3.1 shows the transmission zeros, the reflection zeros, the reflection maxima locations and the poles of the filtering microwave filter and plots of the transfer and reflection characteristic are shown in Figure 3.11.

Table 3.1 Singularities of Fourth -Degree Asymmetric Chebyshev Filter with two transmission Zeros

	Transmission Zeros	Reflection Zeros (Roots of $U_4(\omega)= F(\omega)$)	Transmission/Reflection Poles (Roots of $E(\omega)$)	In-Band Reflection Maxima (Roots of $V_4(\omega)$)
1	+j1.52	-j0.8693	-0.6079-j1.3108	-j0.5262
2	+j1.95	-j0.08788	0.9699+j0.00269	+j0.3256
3	$j\infty$	+j0.6437	-0.4815+j0.8628	+j0.8693
4	$j\infty$	+j0.9646	-0.1195+j1.0964	

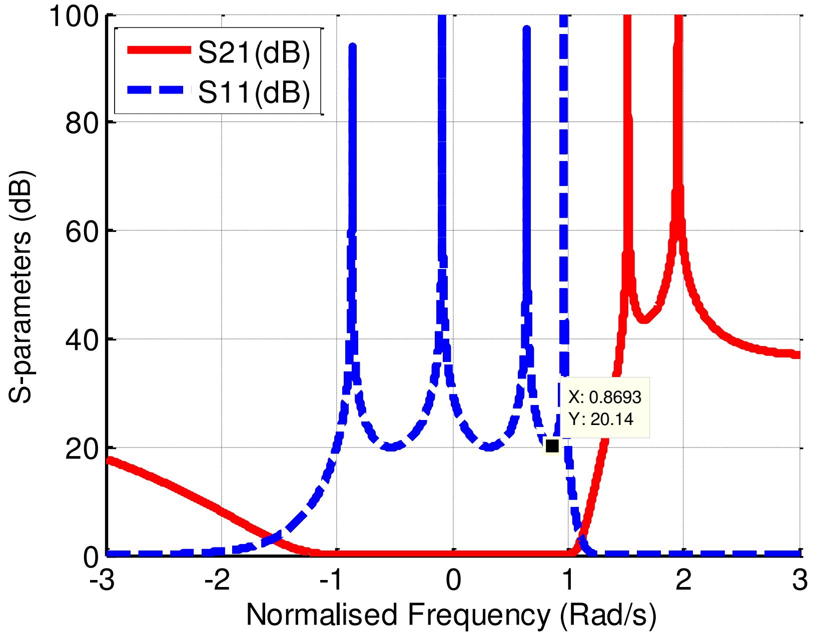

Figure 3.11: Lowpass prototype transfer and reflection characteristics of four-degree asymmetric Chebyshev filters with two transmission zeros at s1=+j1.52 and s2=+1.95

3.4. Coupling Matrix Synthesis of Microwave Filters

3.4.1. Coupling Matrix Definition

In this section, we will examine the coupling matrix representation of microwave filter circuits. When the polynomials synthesis is found, the next step is to establish a link between the approximation theory and circuit realization. The coupling matrix filter synthesis technique provides an alternative to the diagnostic of electrical elements one by one. The coupling matrix is simply a representation of the microwave filter, which may be used for the initial design, then the tuning, modeling and analysis of microwave filter performance. Modeling the circuit in matrix form is particularly useful because the coupling matrix is able to include some of the real-world properties of the elements of the filter. Each coupling element in the matrix can be identified uniquely with a physical element in the finished microwave filter. Finally this part presents the coupling matrix formulation of coupled-resonator filters. One of the benefits is that matrix operations such as a similarity or an inversion transformation can be applied to the coupling matrix directly resorting to network transformations. These operations simplify both the analysis and the synthesis of the microwave filter [2].

3.4.2. Impedance Matrix Calculation

As described before, one key step in the filter synthesis is to convert the rational polynomials to a coupling matrix. Most microwave filters can be represented by a two-ports filter as shown in Figure 3.11A, where V_1, $V_2$and I_1,$I_2$are the voltage and current variables at the ports 1 and 2, R_1, R_2 are the terminal impedances, $e_s$is the voltage source. To measure the signals' intensity at microwave frequencies, the wave variables a_1, $b_1$and a_2, $b_2$are introduced, with 'a' indicating the incident waves and 'b' the reflected waves. [1]

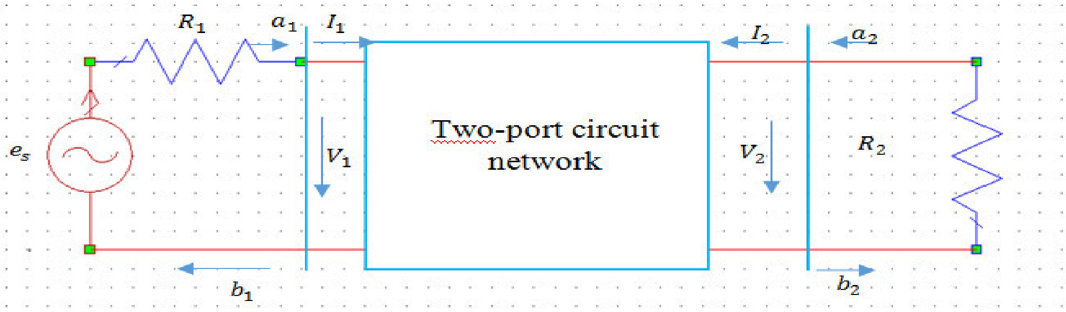

Figure 3.11A: The equivalent circuit representing a general two-port network

The relationships between the wave variables and the voltage and current variables are defined as:

$$\begin{cases} a_n = \dfrac{1}{2}\left(\dfrac{V_n}{\sqrt{R_n}}\right) + \sqrt{R_n I_n} \\ b_n = \dfrac{1}{2}\left(\dfrac{V_n}{\sqrt{R_n}}\right) - \sqrt{R_n I_n} \end{cases} \qquad n = 1 \text{ and } 2 \qquad (3.39)$$

The above definitions guarantee that the power at port n (n=1 and 2) is:

$$P_n = \frac{1}{2} Re(V_n . I_n^*) = \frac{1}{2}(a_n a_n^* - b_n b_n^*) \tag{3.40}$$

As illustrated in Figure 3.12, coupling matrix will be obtained by synthesizing the elements values. Next, we consider the equivalent circuit of n-coupled resonators, where L, C, R denote the inductance, capacitance and resistance, M_{ij} represents the mutual inductance between resonators i and j.

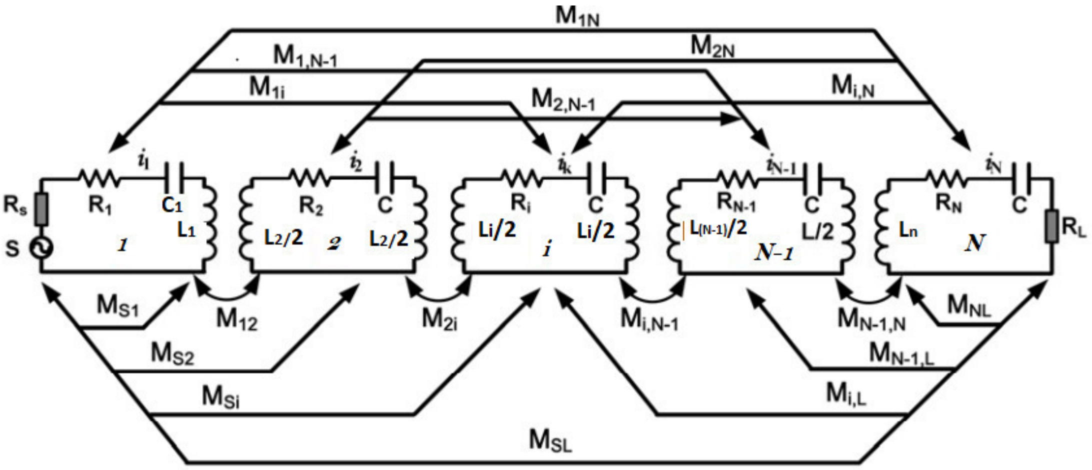

Figure 3.12: The equivalent circuit of n-coupled resonators

Applying circuit analysis of Kirchhoff's current law to this prototype,, we can write down the loop equations for this equivalent circuit: **[1]**

$$\begin{cases} \left(R_1 + j\omega L_1 + \frac{1}{j\omega C_1}\right) i_1 - j\omega M_{12} i_2 \ldots - j\omega M_{1n} i_n = e_s \\ -j\omega M_{21} i_1 + \left(j\omega L_2 + \frac{1}{j\omega C_2}\right) i_2 \ldots - j\omega M_{2n} i_n = 0 \\ \vdots \\ -j\omega M_{n1} i_1 - j\omega M_{n2} i_2 \ldots + \left(R_n + j\omega L_n + \frac{1}{j\omega C_n}\right) i_n = 0 \end{cases} \tag{3.41}$$

In which $L_{ij} = L_{ji}$ represents the mutual inductance between resonators i and j and the all loop currents are supposed to have the same direction, as shown in Figure 3.12. The equations listed in equation (3.41) can be represented in matrix form:

$$\begin{bmatrix} R_1 + j\omega L_1 + \frac{1}{j\omega C_1} & -j\omega M_{12} & \cdots & -j\omega M_{1n} \\ -j\omega M_{21} & -j\omega L_2 + \frac{1}{j\omega C_2} & \cdots & -j\omega M_{2n} \\ \cdots & \cdots & & \cdots \\ -j\omega M_{n1} & -j\omega M_{n2} & \cdots & R_n + j\omega L_n + \frac{1}{j\omega C_n} \end{bmatrix} \begin{bmatrix} i_1 \\ i_2 \\ \cdots \\ i_n \end{bmatrix} = \tag{3.42}$$

We define the impedance matrix of the circuit in Figure 3.12, defined as

$$[Z].[i] = [e] \tag{3.43}$$

Where $[i]$ and $[e]$ are vectors corresponding to the currents and voltages, respectively, of each resonator ,and the [Z] is the impedance matrix (nxn) [.To normalise the $[\bar{Z}]$ matrix of a synchronously tuned circuit, the capacitance and inductance of each resonator are assumed to be the same. The center frequency of filter $\omega_0 = 1/\sqrt{LC}$, then $[\bar{Z}]$ is given as :

$$[Z] = \omega_0 L.FBW[\bar{Z}]$$

$$[\bar{Z}] = \begin{bmatrix} \frac{R_1}{\omega_0 L.FBW} + p & -j\frac{\omega}{\omega_0}\frac{L_{12}}{L}\cdot\frac{1}{FBW} & \cdots & -j\frac{\omega}{\omega_0}\frac{L_{1n}}{L}\cdot\frac{1}{FBW} \\ -j\frac{\omega}{\omega_0}\frac{L_{21}}{L}\cdot\frac{1}{FBW} & p & \cdots & -j\frac{\omega}{\omega_0}\frac{L_{2n}}{L}\cdot\frac{1}{FBW} \\ \vdots & \vdots & \vdots & \vdots \\ -j\frac{\omega}{\omega_0}\frac{L_{n1}}{L}\cdot\frac{1}{FBW} & -j\frac{\omega}{\omega_0}\frac{L_{n2}}{L}\cdot\frac{1}{FBW} & \cdots & \frac{R_n}{\omega_0 L.FBW} + p \end{bmatrix} \tag{3.44}$$

Where $FBW = \Delta\omega/\omega_0$ is the fractional bandwidth and with $p = j\frac{1}{FBW}\left(\frac{\omega}{\omega_0} - \frac{\omega_0}{\omega}\right)$ as the complex lowpass frequency variable.

$$\frac{R_i}{\omega_0 L} = \frac{1}{Q_{ei}} \quad for \quad i = 1, n \tag{3.45}$$

$Q_{e1}$and Q_{en} are the external quality factors of the input and output resonators, respectively. The coupling coefficients are defined as:

$$M_{ij} = \frac{L_{ij}}{L} \tag{3.46}$$

Where m_{ij} is defined as the normalized coupling coefficient, $m_{ij} = \frac{M_{ij}}{FBW}$.

Since the filter works in a narrow-band then $\omega/\omega_0 \cong 1$, we obtain by simplification equation (3.44) for Bandpass filter (BPF) prototype as follow:

$$[\bar{Z}] = \begin{bmatrix} \frac{1}{q_{e1}} + p & -jm_{12} & \cdots & -jm_{1n} \\ -jm_{21} & p & \cdots & -jm_{2n} \\ \vdots & \vdots & \vdots & \vdots \\ -jm_{n1} & -jm_{n2} & \cdots & \frac{1}{q_{en}} + p \end{bmatrix} \tag{3.47}$$

Where q_{e1} and q_{en} are the scaled external quality factors and defined as:

$$q_{ei} = Q_{ei}.FBW \quad \text{for } i=1,n \tag{3.48}$$

As given in [1], the *S*-parameters can be calculated using the scaled external quality factors q_{ei}(i=1 and n) and normalized matrix $[\bar{Z}]$ as:

$$S_{21} = 2\frac{1}{\sqrt{q_{e1}q_{en}}}[\bar{Z}]_{n1}^{-1}$$
$$S_{11} = 1 - \frac{2}{q_{e1}}[\bar{Z}]_{11}^{-1} \tag{3.49}$$

In the case of asynchronously tuned coupled-resonator circuit, the resonant frequency of Resonator i is given by $\omega_{0i} = 1/\sqrt{L_iC_i}$, the coupling coefficient between Resonator i and j of the asynchronously tuned filter is defined as

$$M_{ij} = \frac{L_{ij}}{\sqrt{L_iL_j}} \quad \text{for} \quad i \neq j \tag{3.50}$$

And the normalized matrix $[\bar{Z}]$ becomes

$$[\bar{Z}] = \begin{bmatrix} \frac{1}{q_{e1}} + p - jm_{11} & -jm_{12} & \cdots & -jm_{1n} \\ -jm_{21} & p - jm_{22} & \cdots & -jm_{2n} \\ \vdots & \vdots & \vdots & \vdots \\ -jm_{n1} & -jm_{n2} & \cdots & \frac{1}{q_{en}} + p - jm_{nm} \end{bmatrix} \tag{3.51}$$

The resonator frequency shifting with respect to the central frequency ω_0 is included in the model as frequency invariant susceptance m_{ii} , so $m_{i,i}$ is the self coupling of resonator *i*. The filter is an asynchronously tuned one if some of $m_{i,i}$are non-zero entries

3.4.3. The Formulation General of the Coupling Matrix CM

The determination of the general coupling matrix of a microwave coupled filter has been depicted in [1] and the derivations show that the normalised admittance matrix $[Y]$ has a form identical to that of the normalized impedance matrix $[Z]$ [1, 2] that is much important because it means that we can have a unified formulation for a multiple coupled resonator filter, regardless of whether the couplings are electrical or magnetic or mixed coupling. Accordingly equation (3.49), so we can generalize coupling matrix [A] between the resonators no matter what the coupling nature is, by

$$\begin{aligned} S_{21} &= \frac{2}{\sqrt{q_{e1}q_{en}}}[A]_{n1}^{-1} \\ S_{11} &= \pm(1 - \frac{2}{q_{e1}}[A]_{11}^{-1}) \end{aligned} \tag{3.52}$$

Where $[A]$ is n × n matrix and formed as

$$[A] = [q] + p[U] - j[m]$$

The (n+2) coupling matrix also includes the external couplings from source and load to each resonator. It is very easy to transform one form of coupling matrix to another [2].

The general matrix $[A]$ formed of coupling coefficients $m_{p,q}$ and external quality factors q_{ei} is re-written in [3] as:

$$[A] = [q] + p[U] - j[m] = \begin{bmatrix} \frac{1}{q_{e1}} & 0 \cdots & 0 \\ 0 & 0 & 0 \\ \vdots & \ddots & \vdots \\ 0 & \cdots & \frac{1}{q_{en}} \end{bmatrix} + p\begin{bmatrix} 1 & 0 \ldots & 0 \\ 0 & 1 \ldots & 0 \\ \vdots & \vdots \cdots & \vdots \\ 0 & 0 \ldots & 1 \end{bmatrix} - j\begin{bmatrix} m_{1,1} & m_{1,2} \ldots & m_{1,n} \\ m_{2,1} & m_{2,2} & m_{2,n} \\ \vdots & \vdots \cdots & \vdots \\ m_{n,1} & m_{n,2} \cdots & m_{n,n} \end{bmatrix} \tag{3.53}$$

$$where \qquad p = j\frac{1}{FBW}\left(\frac{\omega}{\omega_0} - \frac{\omega_0}{\omega}\right)$$

Where $[q]$ is (N × N) matrix with all entries zeros, except $q_{11} = 1/q_{e1}$ and $q_{nn} = 1/q_{en}$ and $[m]$ is (N × N) general coupling matrix. Note that, [U] represents an (N × N) unitary matrix and p is the complex lowpass frequency variable, $\omega_0$is the centre frequency of the filter, FBW is the fractional bandwidth of the filter. q_{ei} (i=1 and n) is the scaled external quality factors of the resonator i. $m_{i,j}$is the normalised coupling coefficients between the resonator i and j.

3.5. Synthesis process of the (N +2) Transversal Coupling Matrix

3.5.1. Basics for (N x N) Coupling Matrix Synthesis

The next step in the synthesis process, the values of the coupling elements of a canonical coupling matrix are determined from the transfer and reflection polynomials. Three basic forms of the canonical coupling matrix are generally used as follow [2] : the folded form, the arrow form and the transversal form.

Figure 3.13 presents a microwave resonator lossless filter structure , which is injected by a voltage source with internal impedance R1=Rs and terminated with a load impedance RN=RL .

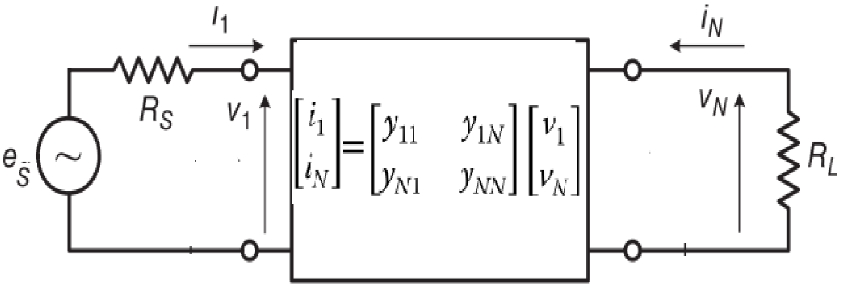

Figure 3.13: Equivalent two-port of a multi-coupled microwave filter for the (N +2) Coupling Matrix

Consider, the input impedance of this filter in terms of its [Z]-parameters and [Y]-parameters is [11]:

$$Z_{in}(s) = \frac{V_1(s)}{I_1(s)} = \frac{z_{11}.[1/y_{22} + R_N]}{z_{22} + R_N} = \frac{z_{11}.[1/y_{22} + 1]}{z_{22} + 1} \quad if \;\; R_N = 1\Omega \tag{3.54}$$

Consequently, if $R_N = 1\Omega$, the input impedance of the equivalent microwave filter is written in terms of the design $S_{11}(s)$,and then polynomials $E(s)$ and $F(s)$as:

$$Z_{in}(s) = \frac{1 - S_{11}(s)}{1 + S_{11}(s)} = \frac{1 - \frac{F(s)}{E(s)}}{1 + \frac{F(s)}{E(s)}} = \frac{E(s) \pm F(s)}{E(s) \mp F(s)} = \frac{m_1 + n_1}{m_2 + n_2} \tag{3.55}$$

If complex-even and complex-odd polynomials of the numerator are expressed by m_1,n_1 respectively, then those of denominator are expressed by m_2, n_2 .The input impedance Z_{in} can thus be expressed as

$$Z_{in}(s) = \begin{cases} \dfrac{m_1+n_1}{m_2+n_2} = \dfrac{n_1\left[{}^{m_1}\!/_{n_1}+1\right]}{m_2+n_2} & \text{If the order of E(s) and F\{s) is even} \\ \dfrac{m_1+n_1}{m_2+n_2} = \dfrac{m_1\left[{}^{n_1}\!/_{m_1}+1\right]}{m_2+n_2} & \text{If the order of E(s) and F\{s) is odd} \end{cases} \tag{3.56}$$

Suppose the source and the load terminations are both 1Ω [21] and when comparing directly equations (3.54) and (3.56), it may be observed that, the [Y]-parameters of the circuit (see figure 3.13) are represented by: [11, 18]

$$\begin{cases} y_{22}(s) = {}^{m_1}\!/_{n_1} \quad and \quad y_{21}(s) = {}^{P(s)}\!/_{\epsilon n_1} & \text{for } \quad \text{odd} - \text{degree filters} \\ y_{22}(s) = {}^{n_1}\!/_{m_1} \quad \text{and} \quad y_{21}(s) = {}^{P(s)}\!/_{\epsilon m_1} & \text{for } \quad \text{even} - \text{degree filters} \end{cases} \tag{3.57}$$

Knowing that the polynomials m_1 and n_1 may be expressed as:

$$\begin{cases} m_1 + n_1 = E(s) + F(s) \\ m_1 = \mathrm{Re}(e_0+f_0) + \mathrm{Im}\,(e_1+f_1)\mathrm{s} + \mathrm{Re}\,(e_2+f_2)\mathrm{s}^2 + \cdots \\ n_1 = \mathrm{Im}(e_0+f_0) + \mathrm{Re}\,(e_1+f_1)\mathrm{s} + \mathrm{Im}\,(e_2+f_2)\mathrm{s}^2 + \cdots \end{cases} \tag{3.58}$$

In which e_i and f_i, are respectively the complex coefficients of $E(s)$ and $F(s)$ (i = 0, 1, 2, 3 …N). $E(s)$ and $F(s)$ represent the numerator and denominator polynomials of the reflection function $S_{11}(s)$

3.5.2. (N+2) Transversal Coupling Matrix Representation

a. Calculation of Admittance Function [Y]-Parameters

In order to synthesize microwave filter easily, we may choose the transversal form in particular, and the other two can be extracted from it easy by applying a formal series of analytically calculated similarity transforms.

Since the denominator and numerator polynomials for $y_{21}(s)$ and $y_{22}(s)$ are known, the equations (3.57) will be written in matrix form yields the following equation for the admittance matrix Y-parameters for the overall microwave filter:

$$\begin{aligned} [Y] &= \begin{bmatrix} y_{11}(s) & y_{12}(s) \\ y_{21}(s) & y_{22}(s) \end{bmatrix} = \frac{1}{y_d(s)} \begin{bmatrix} y_{11n}(s) & y_{12n}(s) \\ y_{21n}(s) & y_{22n}(s) \end{bmatrix} \\ &= j\begin{bmatrix} 0 & K_\infty \\ K_\infty & 0 \end{bmatrix} + \sum_{k=1}^{N} \frac{1}{(s-j\lambda_k)} \begin{bmatrix} r_{11k} & r_{12k} \\ r_{21k} & r_{22k} \end{bmatrix} \end{aligned} \tag{3.59}$$

- The residues r_{21k} and r_{22k} (k=1, 2, …, N) of the denominator and numerator polynomials for $y_{21}(s)$ and $y_{22}(s)$ can be calculated from partial fraction expansions method .

- $y_d(s)$ is the common denominator polynomial ,while $y_{11n}(s)$, $y_{21n}(s)$, and $y_{22n}(s)$ refer to the respective numerator polynomials of Y-parameters $y_{11}(s)$, $y_{21}(s)$,and $y_{22}(s)$.
- The poles $j\lambda_k$ are the roots of the denominator polynomial $y_d(s)$ (λ_k are sometimes known as the eigenvalues of the filtering function).
- The real constant $K_\infty = 0$, except for the fully canonical case case where the number of finite-position transmission zeros n_{fz} in the filtering function is equal to the filter degree N.

b. Circuit Approach: Transversal Microwave Filter Network

The general form of a transversal network is shown in Figure 3.14(a). The transversal coupling matrix comprises a series of N individual resonator, low pass sections, connected in parallel between the source and load terminations. The direct source-load coupling inverter M_{SL} is included to allow fully canonical transfer functions to be realized.

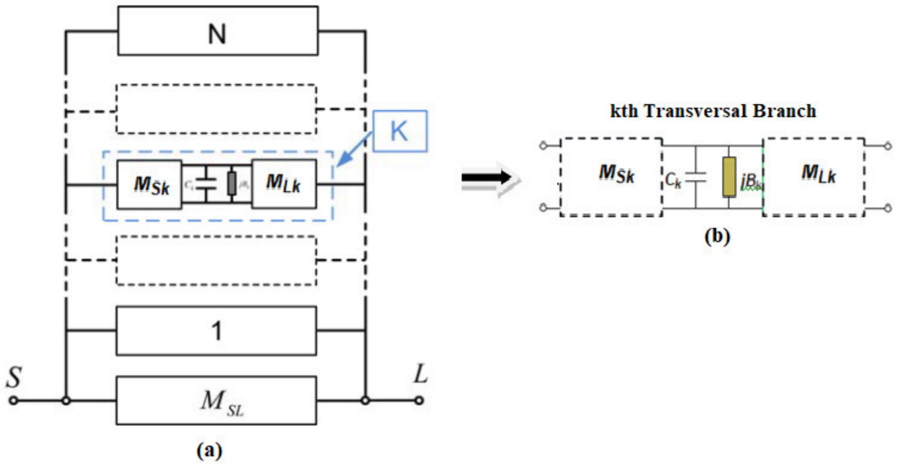

(a)

(b)

Figure 3.14: Canonical transversal array for reciprocal filters. (a) N-resonator transversal array including direct source–load coupling MSL (b) Equivalent circuit of the kth resonator in the transversal network

The admittance matrix $[Y]$ for the overall microwave resonator filter circuit can be synthesized from the fully canonical transversal network. Each of the N lowpass sections comprises one parallel-connected capacitor C_k and one frequency-invariant susceptance B_k connected through admittance inverters of characteristic admittances M_{Sk} and M_{Lk} to the source and load terminations, respectively. The circuit of the kth lowpass section is shown in Figure 3.14(b).

c. Construction of Transversal Coupling Matrix (TCM)

- We cascade the elements of Figure 3.14 (b), so it can be derived that the [ABCD] matrix for the kth resonator in the transversal filter as:

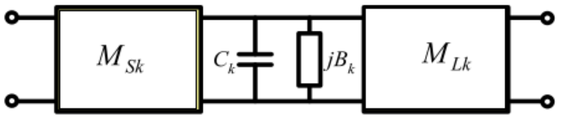

$$[ABCD]_k = -\begin{bmatrix} \dfrac{M_{Lk}}{M_{Sk}} & \dfrac{(sC_k + jB_k)}{M_{Sk}M_{Lk}} \\ 0 & \dfrac{M_{Sk}}{M_{Lk}} \end{bmatrix}$$

- Which may then be directly converted into [Y]-parameters matrix ,then the [Y]-parameters of the individual section presented in Figure 3.14(b) may be expressed in the following form :

$$[y_k] = \begin{bmatrix} y_{11k}(s) & y_{12k}(s) \\ y_{21k}(s) & y_{22k}(s) \end{bmatrix} = \frac{1}{sC_S + jB_k} \begin{bmatrix} M_{Sk}^2 & M_{Sk}M_{Lk} \\ M_{Sk}M_{Lk} & M_{Lk}^2 \end{bmatrix} \tag{3.60}$$

- From the circuit of figure 3.14(a), to determine the admittance parameters of the overall transversal network, a summation over all individual sections plus source–load connection is performed. Such a procedure leads to

$$[Y] = \begin{bmatrix} y_{11}(s) & y_{12}(s) \\ y_{21}(s) & y_{22}(s) \end{bmatrix} = j \begin{bmatrix} 0 & M_{SL} \\ M_{SL} & 0 \end{bmatrix} + \sum_{k=1}^{N} \frac{1}{sC_S + jB_k} \begin{bmatrix} M_{Sk}^2 & M_{Sk}M_{Lk} \\ M_{Sk}M_{Lk} & M_{Lk}^2 \end{bmatrix} \tag{3.61}$$

- The final step in the synthesis of the transversal coupling matrix is to compare the coefficients of the admittance parameters obtained from the scattering parameters with those obtained from the circuit approach , so the residues r_{21k} , $r_{22k}$and the eigenvalues λ_k expressed in the equation (3.59) are equated to those in circuit elements form in the equation (3.61). This leads to the following relationships between the residues and the transversal coupling matrix elements:

$$\begin{gathered} M_{SL} = K_0 \\ C_k = 1 \text{ and } B_k = M_{kk} = -\lambda_k \\ M_{Lk}^2 = r_{22k} \ and \ M_{kk}M_{kk} = r_{21k} \\ M_{Lk} = \sqrt{r_{22k}} \qquad\qquad \text{k=1,2,…,N} \\ M_{Sk} = r_{21k}/\sqrt{r_{22k}} \end{gathered} \tag{3.62}$$

Finally, the reciprocal (N +2) transversal coupling matrix **M** representing the network in Figure 3.15 a may now be constructed.

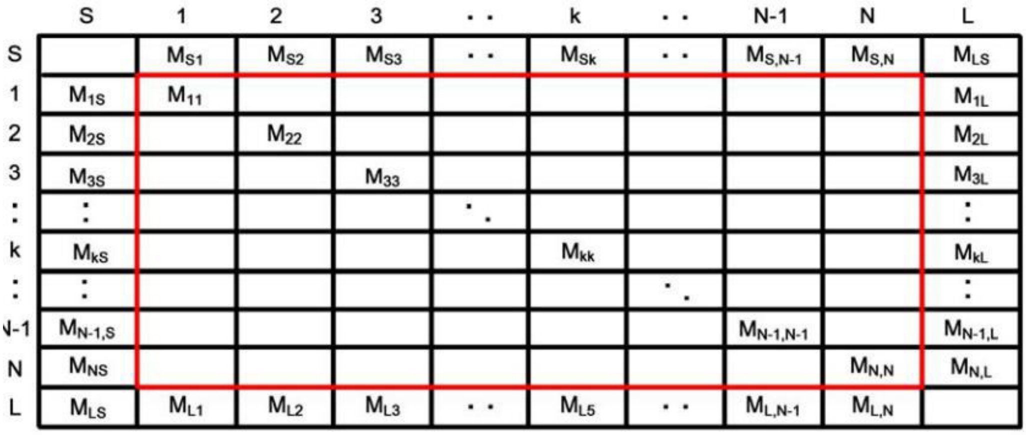

	S	1	2	3	· ·	k	· ·	N-1	N	L
S		M_{S1}	M_{S2}	M_{S3}	· ·	M_{Sk}	· ·	$M_{S,N-1}$	$M_{S,N}$	M_{LS}
1	M_{1S}	M_{11}								M_{1L}
2	M_{2S}		M_{22}							M_{2L}
3	M_{3S}			M_{33}						M_{3L}
:	:				⋱					:
k	M_{kS}					M_{kk}				M_{kL}
:	:						⋱			:
N-1	$M_{N-1,S}$							$M_{N-1,N-1}$		$M_{N-1,L}$
N	M_{NS}								$M_{N,N}$	$M_{N,L}$
L	M_{LS}	M_{L1}	M_{L2}	M_{L3}	· ·	M_{L5}	· ·	$M_{L,N-1}$	$M_{L,N}$	

Figure 3.15: N +2 fully canonical coupling matrix M for the transversal array. The matrix is symmetric about the principal diagonal

The corresponding coupling routing diagram of the transversal coupling matrix topology is shown in Figure 3.16

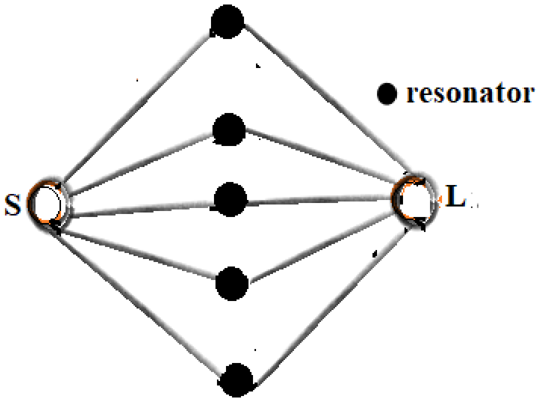

Figure 3.16: The transversal topology

d. Reduction of Transversal Coupling Matrix to the Folded Canonical Form

It is remarkable that the previous calculation of transversal matrix is impractical to be realized. Therefore, It becomes necessary to transform the transversal matrix with a sequence of similarity reconfigurations (sometimes called rotations) until a more suitable topology is achieved [21]. According to Cameron [21],to reduce the transversal matrix to a folded form, repeated similarity transformations are then used to eliminate the unwanted or unrealizable coupling elements alternately right to left along rows and top to bottom down columns .Until the remaining suitable coupling matrix that can be realized to obtain a folded structure (see

Figure (3.17) ,For more details the specific algorithm for coupling matrix reduction(Similarity Transformations) is presented in [21].

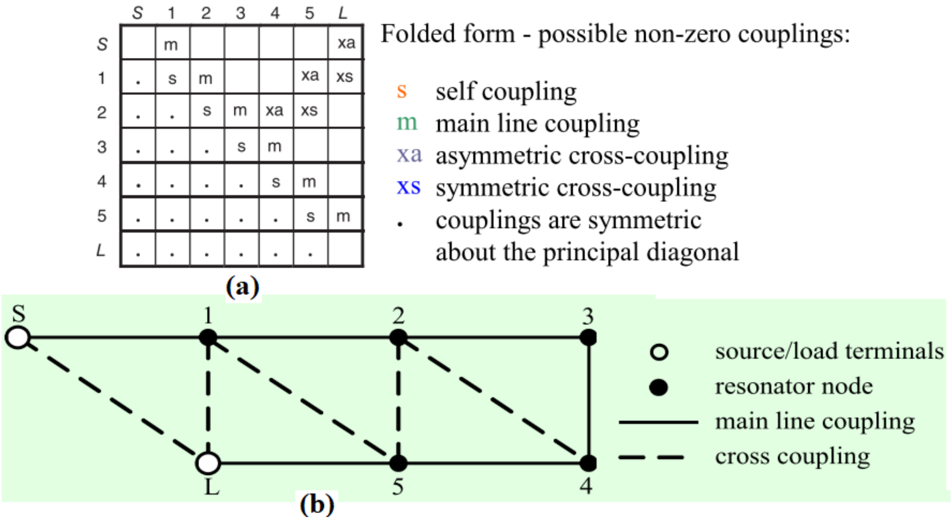

	S	1	2	3	4	5	L
S		m					xa
1	.	s	m			xa	xs
2	.	.	s	m	xa	xs	
3	.	.	.	s	m		
4	.	.	.	.	s	m	
5	.	.	.	.	.	s	m
L	.	.	.	.	.	.	

Folded form - possible non-zero couplings:

s self coupling
m main line coupling
xa asymmetric cross-coupling
xs symmetric cross-coupling
. couplings are symmetric about the principal diagonal

Figure 3.17: Folded N +2 canonical network coupling matrix: (a)folded coupling Matrix form “s” and “xa” couplings are in general zero for symmetric characteristics;(b) coupling and routing schematic

3.6. Illustrative examples and discussions

3.6.1. Illustrative Example I: Simulated fifth-Order Filter with Four TZs

A fifth order microwave filer is synthesized according to the procedure introduced in this chapter. The design parameters include frequency center at 3029.85MHz ,bandwidth of 60MHz, with maximum in-band return loss of 20dB four prescribed transmission zeros (TZs) at -j3 , -j1.7 ,+j2 and +j 4.5.

1) As a first step, the application Cameron technique produces the coefficients for the numerator and denominator polynomials of $S_{21}(s)$ and $S_{11}(s)$.

2) Then, the calculation of the numerator and denominator polynomials of $y_{21}(s)$ and $y_{22}(s)$is obtained by using (3.57). The coefficients of $y_d(s)$, $y_{22n}(s)$ and $y_{21n}(s)$, normalized to the highest degree coefficient of are presented in Table 3.2

3) After that, the partial fraction expansions is used to determine the residues of $y_{21}(s)$ and $y_{22}(s)$. Finally ,by using the equations (6.62) the residues ,the eigenvalues λ_k and the eigenvectors $T_{1k} = \sqrt{r_{22k}}$ and $T_{Nk} = r_{21k}/\sqrt{r_{22k}}$ are summarized in Table 3.3

Table 3.2: Filtering function :coefficients of numerator and denominator polynomials of $y_{12}(s)$ and $y_{22}(s)$

s^i $i=$	Coefficients of denominator polynomial of $y_{22}(s)$ and $y_{21}(s)$ ($y_d(s)$)	Coefficients of numerator polynomial of $y_{22}(s)$ ($y_{22n}(s)$)	Coefficients of numerator polynomial of $y_{21}(s)$ ($y_{21n}(s)$)
0	0.0974i	0.3738	0.3842
1	1.2448	0.1719i	- 0.0766i
2	0.2554i	1.6189	0.1377
3	2.3229	0.1252i	- 0.0151i
4	0.1163i	1.0123	0.0084
5	1.0000		

Table 3.3: Filtering function: residues, eigenvalues values and eigenvectors

	Eigenvalues	Residues		Eigenvectors	
k	λ_k	r_{22k}	r_{21k}	$T_{Nk}=\sqrt{r_{22k}}$	$T_{1k}=r_{21k}/\sqrt{r_{22k}}$
1	1.2295	0.1101	0.1101	0.3318	0.3318
2	-1.2019	0.0965	0.0965	0.3106	0.3106
3	-0.9536	0.2356	-0.2356	0.4854	-0.4854
4	0.8875	0.2664	-0.2664	0.5161	-0.5161
5	-0.0779	0.3038	0.3038	0.5512	0.5512

4) And, after evaluating the values of the eigenvectors λ_k and the eigenvectors T_{1k} and T_{Nk}, the (N +2) transversal coupling matrix (Figure 3.15) could be put as given in Figure 3.18.

	S	1	2	3	4	5	L
S	0	0.3318	0.3106	-0.4854	-0.5161	0.5512	0
1	0.3318	-1.2295	0	0	0	0	0.3318
2	0.3106	0	1.2019	0	0	0	0.3106
3	-0.4854	0	0	0.9536	0	0	0.4854
4	-0.5161	0	0	0	-0.8875	0	0.5161
5	0.5512	0	0	0	0	0.0779	0.5512
L	0	0.3318	0.3106	0.4854	0.5161	0.5512	0

(a)

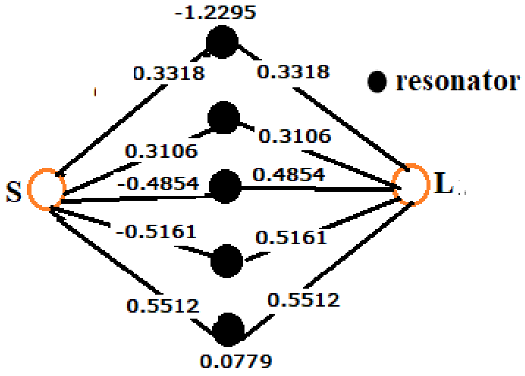

(b)

Figure 3.18: Five Degree Filter: (a)Transversal coupling matrix .(b)Coupling and routing schematic

5) Finally, the series of similarity transformation process which is described in paper [21] is applied on the transversal coupling matrix in order to transformed it to the folded coupling matrix. Consequently, the folded configuration coupling matrix normalized is presented in Figure 3.19(a). Then, its equivalent coupling and routing schematic is illustrated in Figure 3.19(b). The S-parameters of the described microwave filter is depicted in 3.20

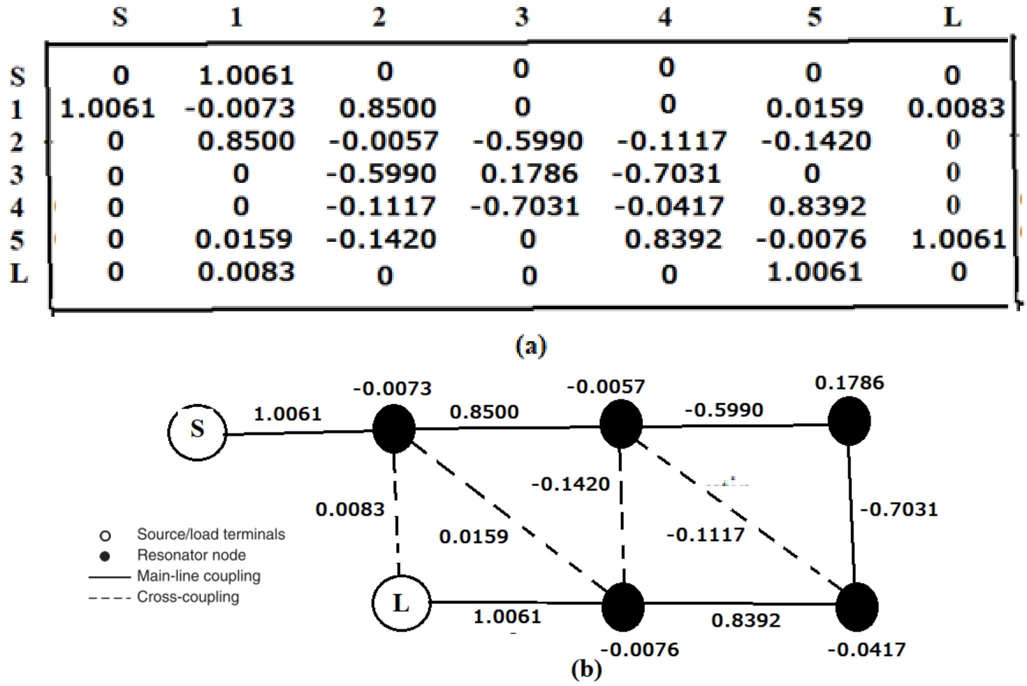

	S	1	2	3	4	5	L
S	0	1.0061	0	0	0	0	0
1	1.0061	-0.0073	0.8500	0	0	0.0159	0.0083
2	0	0.8500	-0.0057	-0.5990	-0.1117	-0.1420	0
3	0	0	-0.5990	0.1786	-0.7031	0	0
4	0	0	-0.1117	-0.7031	-0.0417	0.8392	0
5	0	0.0159	-0.1420	0	0.8392	-0.0076	1.0061
L	0	0.0083	0	0	0	1.0061	0

(a)

(b)

Figure 3.19: Five degree filter: (a)Folded coupling matrix normalized.(b) Coupling-routing diagram

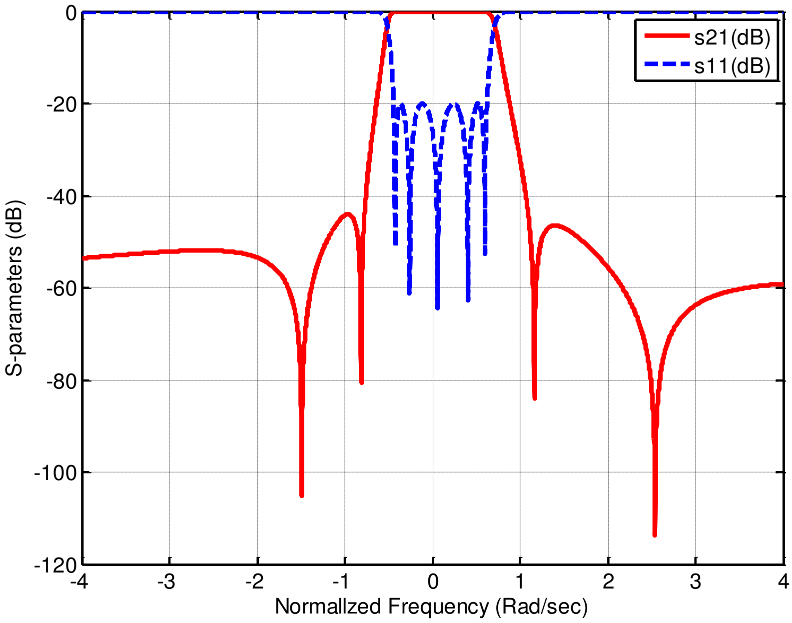

Figure 3.20: Transmission and return loss performance of fifth order filter

3.6.2. Illustrative Example II: Diagnosis of a Fourth-Order Filter with one TZ-

Let us illustrate the previous step with a second example a cross-coupled fourth-order Chebyshev filter .The center frequency and fractional bandwidth of the filter are $f_0 = 3029.85$ MHz and $BW = 60$MHz respectively, with a maximum in-band return loss of 25 dB. Let us add one prescribed TZ at frequency 2950.0MHz.

- The characteristic polynomials F, P, and E are solved in one step as

F=[1 ,j0.1922 , 0.9908 , j0.1441 , 0.1204]

E=[1 , 2.1398 + 0.1922i , 3.2802 + 0.4807i , 2.7826 + 0.7328i ,1.1832 + 0.5270i]

P=[1 , 2.6977i].

- Then the same process as outlined in precedent part can be applied to find the residues and eigenvalues, so the desired parameters are obtained as follows:

$$\lambda_k = [1.3579 \ \ -1.2818 \ -0.7606 \ \ 0.4923]$$
$$r_{22k} = [0.2003, 0.1387 \ , 0.3347 \ ,0.3963 \ ]$$
$$r_{21k} = [-0.2003 \ ,0.1387 \ ,-0.3347, 0.3963].$$

k=1,2,3,4.

- Once r_{22k} , r_{21k} and λ_k are evaluated , the (N+2) generated transversal coupling matrix can be constructed as :

$$M_{\text{transversal}} = \begin{array}{c} \\ \mathbf{S} \\ \mathbf{R_1} \\ \mathbf{R_2} \\ \mathbf{R_3} \\ \mathbf{R_4} \\ \mathbf{L} \end{array} \begin{array}{c} \begin{array}{cccccc} \mathbf{S} & \mathbf{R_1} & \mathbf{R_2} & \mathbf{R_3} & \mathbf{R_4} & \mathbf{L} \end{array} \\ \left[\begin{array}{cccccc} 0 & -0.4475 & 0.3724 & -0.5785 & 0.6295 & 0 \\ -0.4475 & -1.3579 & 0 & 0 & 0 & 0.4475 \\ 0.3724 & 0 & 1.2818 & 0 & 0 & 0.3724 \\ -0.5785 & 0 & 0 & -0.7606 & 0 & 0.5785 \\ 0.6295 & 0 & 0 & 0 & -0.4923 & 0.6295 \\ 0 & 0.4475 & 0.3724 & 0.5785 & 0.6295 & 0 \end{array}\right] \end{array}$$

It clearly that, there are no couplings among any of the resonators, whereas all of them are coupled to the load and to the source simultaneously.

- As the result, the transversal matrix can be transformed by applying the similarity transformations to the folded form corresponding to the physical layout. The general Normalized coupling matrix **m** and the Normalized scaled quality factors ($\boldsymbol{q_{ei}}$) of the filter are synthesized, and found to be

$$\mathbf{m} = \begin{array}{c} \\ \mathbf{S} \\ \mathbf{1} \\ \mathbf{2} \\ \mathbf{3} \\ \mathbf{4} \\ \mathbf{L} \end{array} \begin{array}{c} \begin{array}{cccccc} \mathbf{S} & \mathbf{1} & \mathbf{2} & \mathbf{3} & \mathbf{4} & \mathbf{L} \end{array} \\ \left[\begin{array}{cccccc} 0 & -1.0344 & 0 & 0 & 0 & 0 \\ -1.0344 & -0.0325 & -0.9098 & 0 & 0 & 0 \\ 0 & -0.9098 & -0.0586 & 0.6677 & -0.2456 & 0 \\ 0 & 0 & 0.6677 & 0.3157 & 0.8761 & 0 \\ 0 & 0 & -0.2456 & 0.8761 & -0.0325 & 1.0344 \\ 0 & 0 & 0 & 0 & 1.0344 & 0 \end{array}\right] \end{array}$$

Note that, in the folded topology, there are couplings only among consecutive resonators and one cross-coupling corresponding to the transmission zero (Tz) are present .The $m_{s1} = 1.0344$ and $m_{4L} = 1.0344$ represent the input and output coupling from the source and the first resonator and from the load and the fourth resonator respectively, those can be also defined in the normalized external quality factors, $q_{e1} = {}^{1}/{m_{s1}}^{2}$ and $q_{e1} = {}^{1}/{m_{4L}}^{2}$ respectively. The later can be converted to denormalized external quality factors by [1]

$$Q_{e,S1} = \frac{1}{m_{S1}^2 . FBW} \qquad (3.63)$$
$$Q_{e,4L} = \frac{1}{m_{4L}^2 . FBW}$$

The normalized coupling matrix must be de-normalized for using in the physical dimensioning of the filter. The de-normalized coupling coefficients ($M_{i,j}$) are computed by:

$$M_{i,j} = \text{FBW}. m_{i,j} \ , \qquad i \neq j \quad i,j = 1,2 \dots . N \qquad (3.64)$$
$$f_{0i} = 0.5. f_0 . \left[\sqrt{4 + {M_{i,i}}^2} - f_0 M_{i,i} \right] \qquad i = 1,2 \dots . N$$

where, FBW is the fractional bandwidth of Bandpass filter , $M_{i,j}$represent the coupling coefficient between two resonators i and j , f_{0i} is the resonant frequency of the resonator (**i**),

- Now, the de-normalized coupling matrix coefficients (M) and external quality factors are extracted in Figure(3.21a) .Figure 3.21(b) shows a possible coaxial-resonator realization

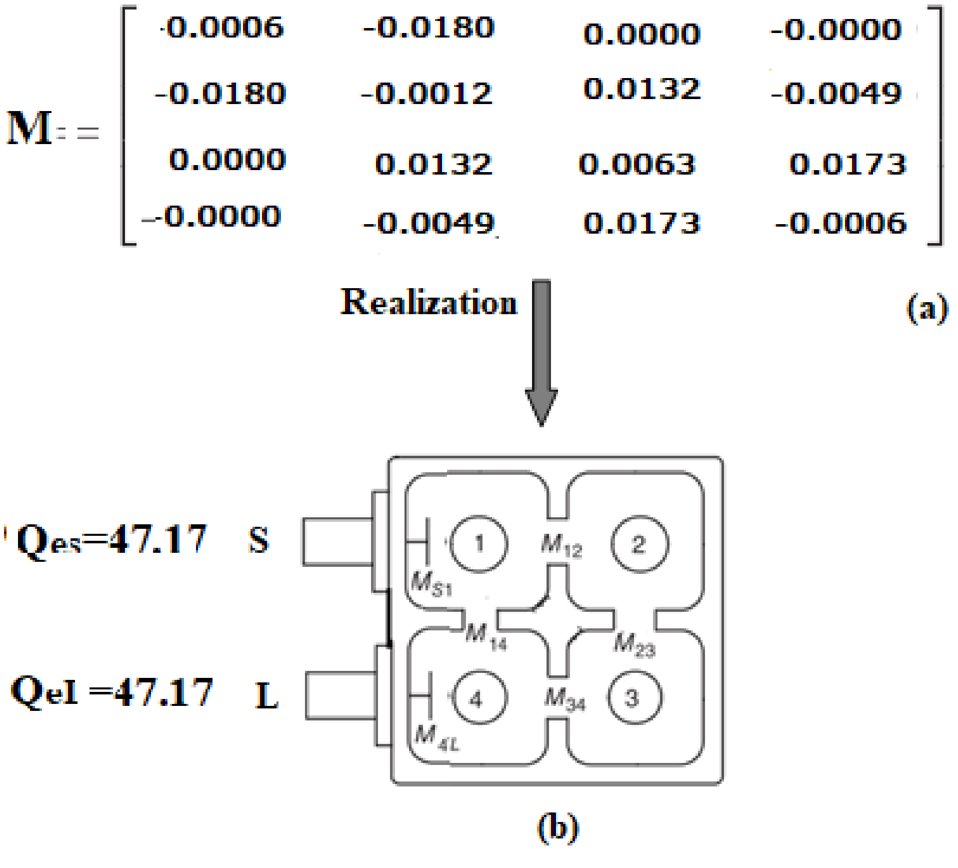

$$\mathbf{M} = \begin{bmatrix} 0.0006 & -0.0180 & 0.0000 & -0.0000 \\ -0.0180 & -0.0012 & 0.0132 & -0.0049 \\ 0.0000 & 0.0132 & 0.0063 & 0.0173 \\ -0.0000 & -0.0049 & 0.0173 & -0.0006 \end{bmatrix}$$

Figure 3.21: (a) Denormalized Coupling matrix of fourth order filter. (b) possible realization with coaxial cavities

The analysis of folded Denormalized coupling matrix (M) is shown in Figure (3.22).

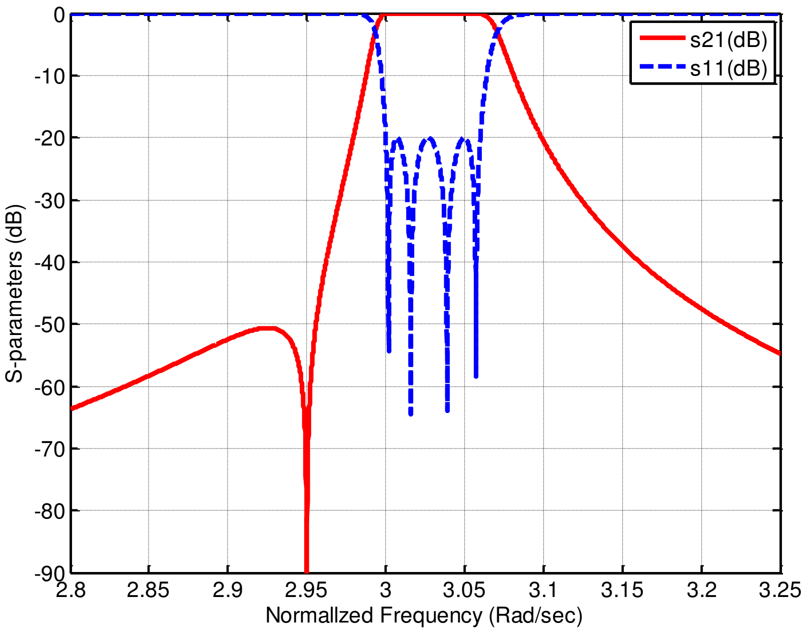

Figure 3.22: Fourth degree canonical filter: analysis of S-parameters

3.7. Computer-Aided Tuning and Diagnosis Techniques of Microwave Filters

3.7.1. Bandpass Filter Modeling and Synthesis

Rejection and return loss functions of any microwave filter lossless composed of a multiple of *N* coupled resonators can be expressed using polynomial characteristics P(s), F(S) and E(s) as described in [21-22].

$$\begin{cases} S_{21}(s) = \dfrac{P(s)}{\varepsilon \; E(s)} \\ S_{11}(s) = \dfrac{F(s)}{E(s)} \end{cases} \tag{3.65}$$

Where ε is a constant used to normalize the highest degree coefficients of the polynomials to one, and $s = j\omega$ is the related complex frequency variable with ω is the frequency variable of the low-pass prototype. The polynomial characteristics are related to each other due to the conservation of energy defined as:

$$|E(s)|^2 = |F(s)|^2 + \frac{|F(s)|^2}{\varepsilon^2} \tag{3.66}$$

The polynomial *P(s)* containing the prescribed transmission zeros of the transfer function is of degree $\leq N - 1$. The polynomial *E(s)* is a strict **Hurwitz** polynomial of degree *N*, whose zeros must lie in the left half of the complex *s*-plane. Figure 3.23 depicts the equivalent circuit of a sequentially coupled resonator Bandpass filter [2].

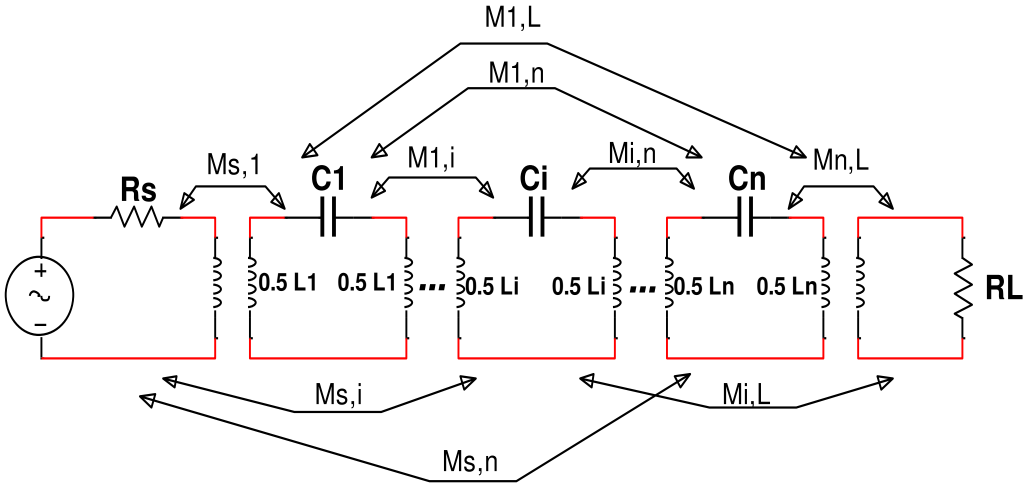

Figure 3.23: Lossless coupled resonator Bandpass filter's equivalent circuit

The circuit consists of *N* synchronously tuned resonators. All the resonators are represented by a *LC* circuit loop. The parameters r_{21k}, r_{22k} , and λ_k for (k = 1, 2, …, N) used to construct the $(N + 2)$ transversal matrix, can be extracted from the polynomials *F*, *P* and *E* by the method presented previously in this chapter . The $(N+2)$ transversal coupling matrix named $[M_t]$ is then determined as shown in Figure.3.24 (whose entries are normalized coupling coefficients $m_{ij} = M_{ij}/FBW$).

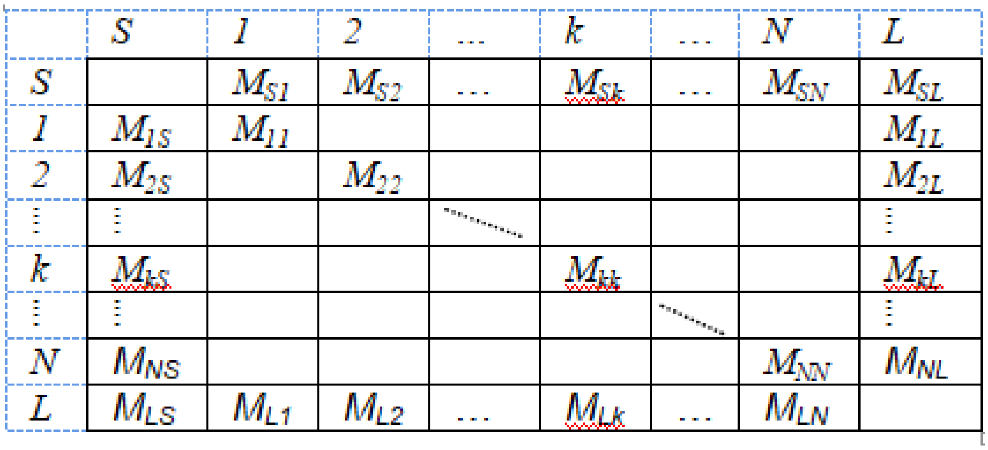

	S	*1*	*2*	…	*k*	…	*N*	*L*
S		M_{S1}	M_{S2}	…	M_{Sk}	…	M_{SN}	M_{SL}
1	M_{1S}	M_{11}						M_{1L}
2	M_{2S}		M_{22}					M_{2L}
⋮	⋮			⋱				⋮
k	M_{kS}				M_{kk}			M_{kL}
⋮	⋮					⋱		⋮
N	M_{NS}						M_{NN}	M_{NL}
L	M_{LS}	M_{L1}	M_{L2}	…	M_{Lk}	…	M_{LN}	

(***S*: Source, *L*: Load, M_{SL}: Source-Load coupling, $M_{Lk} = M_{kL}$, $M_{Sk} = M_{kS}$,** $M_{kk} = -\lambda_k$, $M_{Lk} = \sqrt{r_{22k}}$, $M_{Sk} = r_{21k}/M_{Lk}$)

Figure 3.24: The $(N + 2)$ transversal matrix constructed by the parameters r_{22k}, r_{21k}, λ_k **and** M_{SL}

Knowing that ,the source-load coupling (M_{SL}) in Figure 3.24 is equal to zero, except for the case of $nz = N$ (nz is the number of finite transmission zeros). Once the normalized coupling matrix [M] is calculated, the scattering parameters from the transversal model can be obtained via the following equations [23-24]:

$$S_{21} = -2j\ [A]^{-1}_{(N+2,1)}\ ,\ S_{11} = 1 + 2j\ [A]^{-1}_{(1,1)} \tag{3.67}$$

Where $$[A] = [M] + \Omega[U] - j\ [q]$$

In which [U] is similar to the (N + 2)×(N + 2) unit matrix, except that U(1,1) = U(N + 2, N + 2) = 0. [q] is the (N + 2)×(N + 2) whose only nonzero entries are q(1,1) = q(N + 2, N + 2) = 1, and *Ω* is the normalized frequency variable of lowpass prototype, which can be written in terms of FBW and the filter center frequency (ω_0) as:

$$s = j\Omega = j\frac{1}{\mathrm{FBW}}\left(\frac{\omega}{\omega_0} - \frac{\omega_0}{\omega}\right) \tag{3.68}$$

3.7.2. Generalized Formulation of Cauchy Method for Parameter Extraction (PE)

The Cauchy method is the curve fitting technique for extracting an approximate rational polynomial to a specified response from measurements electromagnetic (EM) simulations of passive devices. The *S*-parameters are extracted from (EM) simulation at some sampled frequency points from which characteristic polynomials are determined by solving a determined or over determined linear system of equations [25]. A general microwave filter lossless network presented by its scattering parameters S_{11} and S_{21}, three characteristic polynomials F,P and E. All this parameters define a rational polynomials model in the normalized low-pass domain s [11].From the data samples of the filter responses, the formulation of the Cauchy method can be used to evaluate the coefficients of polynomials *F*, *P* and *E* [26]. Therefore, the approximated rational polynomials of $S_{11}(s)$ and $S_{21}(s)$ are expressed in the following form:

$$\begin{cases} S_{11}(s) = F(s)/E(s) = \left(\sum_{k=0}^{N} f_k s^k\right) \Big/ \left(\sum_{k=0}^{N} e_k s^k\right) \\ S_{21}(s) = P(s)/E(s) = \left(\sum_{k=0}^{nz} p_k s^k\right) \Big/ \left(\sum_{k=0}^{N} e_k s^k\right) \end{cases} \tag{3.69}$$

Where *N* is the order of the filter, and *nz* is the number of transmission zeros. Knowing that **s** is the normalized lowpass frequency which is calculated by Bandpass-to-Lowpass frequency transformation (3.68). If $S_{11}(s)$ and $S_{21}(s)$ are calculated by EM simulation at a reduced number of frequency samples s_i (i= 1,…, Ns) , Ns is the number of frequency points, then given a set of Ns sample frequency points, equations in (3.69) can be rewritten as:

$$\begin{cases} \sum_{k=0}^{N} f_k s_i^k - S_{11}(s_i)\sum_{k=0}^{N} e_k s_i^k = 0\ , \ \ i = 1,...Ns \\ \sum_{k=0}^{nz} p_k s_i^k - S_{21}(s_i)\sum_{k=0}^{N} e_k s_i^k = 0\ \ , i = 1,...Ns \end{cases} \tag{3.70}$$

Where $S_{11}(s_i)$ and $S_{21}(s_i)$ are the simulated *S*-parameters at frequency points s_i. Using the matrix notation, formulation (3.70) is rewritten as a linear system of equations in the following form:

$$\begin{bmatrix} V_N & 0_{Ns\times(nz+1)} & -S_{11}V_N \\ 0_{Ns\times(N+1)} & V_{nz} & -S_{21}V_N \end{bmatrix} \begin{bmatrix} f \\ p \\ e \end{bmatrix} = H \begin{bmatrix} f \\ p \\ e \end{bmatrix} = [0] \tag{3.71}$$

Where *f*, *p* and *e* are the vectors containing the polynomial coefficients $f = [f_0,\dots,f_N]^T$, $p = [p_0,\dots,p_{nz}]^T$, $e = [e_0,\dots,e_N]^T$, $S_{11} = \mathrm{diag}\{S_{11}(s_i)\}_{i=1,\dots,Ns}$, $S_{21} = \mathrm{diag}\{S_{21}(s_i)\}_{i=1,\dots,Ns}$, and $V_r \in C^{Ns\times(r+1)}$ is an increasing-power order Vandermonde matrix which can be defined as:

$$V_r = \begin{bmatrix} 1 & s_1 & s_1^2 & \dots & s_1^r \\ 1 & s_2 & s_2^2 & \dots & s_2^r \\ & . & & & \\ & . & & & \\ 1 & s_n & s_n^2 & \dots & s_n^r \end{bmatrix} \tag{3.72}$$

The complex coefficients f, *p* and *e* (and then F(s), P(s), and E(s)) may be evaluated in one step by rooting the over determined system in (3.71) using the Cauchy method. The root of equation (3.71) can found by computing singular value decomposition (SVD) [26] to the matrix [H]. In order to guarantee that the system matrix (3.71) has a solution, the sampled frequency points Ns should be greater than or equal to (N + nz +1). Applying the total least square method (TLS) [27, 28], the system (3.71) can be solved, obtaining the coefficients *f*, *p* and *e*; the polynomials F(s) , P(s) and E(s) are then available through (3.70). After applying (SVD) to the system matrix [H] in (3.71) gives the required complex coefficients for f, p and e, it can be written as:

$$H \begin{bmatrix} f \\ p \\ e \end{bmatrix} = U\Sigma V \begin{bmatrix} f \\ p \\ e \end{bmatrix} = 0 \tag{3.73}$$

Where U and V are unitary matrices, ∑ is a diagonal matrix containing the singular values. The solution to (3.71) is proportional to the last column of matrix [V]:

$$\begin{bmatrix} f \\ p \\ e \end{bmatrix} = [V]_{N+nz+2} \tag{3.74}$$

That is the elements in the last column of [V] give us the solution.

3.7.3. General Formulation of Aggressive Space Mapping (ASM) Optimization Algorithm

Space mapping (SM) is a technique widely used for the design and optimization of microwave filter components [29-30]. The SM algorithm assumes the existence of two simulation tools of different accuracy and efficiency, one is more precise but more complex and CPU intensive model, namely the fine model; two is simple and computationally efficient, although not accurate model, namely the coarse model. The theory of Space Mapping is to use a coarse model to find optimization results, and then use a fine model to test the results. During this process, if the error after the testing in the fine model was over a certain tolerance, the error returns to the coarse model for another re-optimization is performed to gain a new result. The new result would be resend to fine model for testing. Space Mapping repeats these steps until the error is lower than a user define. The Aggressive Space Mapping technique has been considered in [30]. The ASM algorithm is an improvement of the original SM previously mentioned because Quasi-Newton iteration is introduced using the classical Broyden formula [31]. Here, the coarse model is the equivalent circuit shown in Figure 3.23 and the fine model is the physical model.

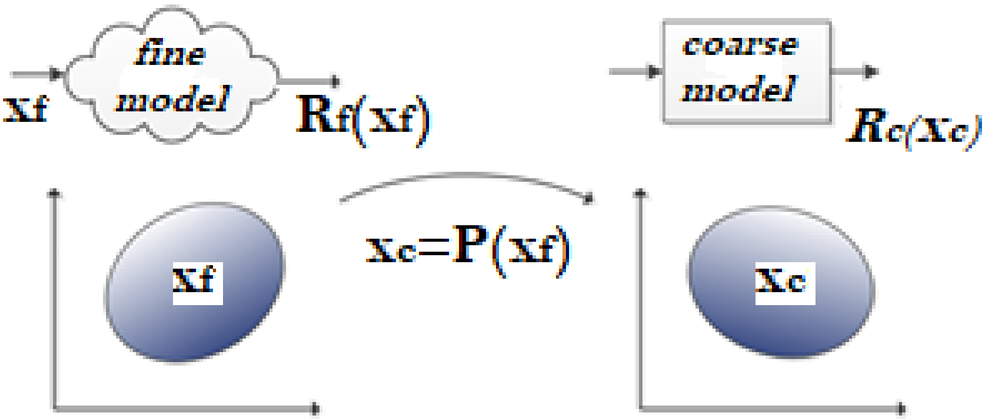

Figure 3.25: Representation of the fine and coarse models

Figure 3.25 presents a fine and coarse model, where $\boldsymbol{x_f}$ is a vector of parameters in fine model, which represents the dimensions of the filter, and $\boldsymbol{x_c}$ is a vector of parameters in coarse model, which consists of quality factor, frequency and coefficient coupling value. $\boldsymbol{x_c}^*$ is the coarse model solution that gives the target response. The responses of the fine model as $R_f(x_f)$ and that of the coarse model as $R_c(x_c)$ are denoted as depicted in Figure 3.25. The key idea is to find the transformation *P* that relates the parameters of the fine model **($\boldsymbol{x_f}$)** with the parameters of the coarse model **($\boldsymbol{x_c}$):**

$$x_c = P\left(x_f\right) \tag{3.75}$$

Mapping the fine model parameter space to the coarse model parameter space is such that:

$$\left\| R_f\left(x_f\right) - R_c\left(x_c\right) \right\| \leq \varepsilon \tag{3.76}$$

If the mapping P is established, then the inverse transformation is used to find the fine model solution, which is the image of the coarse model solution, $\mathbf{x_c^*}$**,** giving the target response, $R_c(x_c^*)$.

$$x_f = P^{-1}\left(x_c^*\right) \tag{3.77}$$

The goal is to find a root of the following system of non linear equations $f(x_f) = 0$, where:

$$f\left(x_f\right) = P\left(x_f\right) - x_c^* \tag{3.78}$$

Where $\mathbf{x_f^{(i)}}$ is the $\mathbf{j^{th}}$ approximation to the solution of (3.78) in the validation space, and $\mathbf{f^{(j)}}$ the error function corresponding to $\mathbf{f(x_f^{(i)})}$**.** The next iterate $\mathbf{x_f^{(j+1)}}$ is found by applying a Quasi-Newton step $\mathbf{h^{(j)}}$**:**

$$x_f^{(j+1)} = x_f^{(j)} + h^{(j)} \tag{3.79}$$

Where $\mathbf{h^{(j)}}$ is the increasing value of the tuning vectors and it is the solution of:

$$B^{(j)} h^{(j)} = -f^{(j)} \tag{3.80}$$

Being $\mathbf{B^{(j)}}$ the mapping matrix, which is an approximation of the Jacobian matrix of the vector *f* with respect to $\mathbf{x_f}$ at the $\mathbf{j^{th}}$ iteration. At each iteration, this mapping matrix is updated according to the Broyden formula:

$$B^{(j+1)} = B^{(j)} + \frac{f^{(j+1)} h^{(j)T}}{h^{(j)T} h^{(j)}} \tag{3.81}$$

In (3.81), $\mathbf{f}^{(j+1)}$ is obtained by evaluating (3.78), and the super-index ***T*** stands for transpose. The variables in the fine and coarse model spaces are as: $x_{f1},\ldots, x_{f2}, x_{f6}$ and $x_{c1},\ldots, x_{c2}, x_{c6}$, respectively, where ($m$=$6$) in this case, is the dimension of the vectors in both spaces. From the initial geometry, the circuit parameters are extracted. The next step is the determination of the first approach to the Broyden matrix. To this end, each geometrical parameter is slightly perturbed from the value obtained in the first layout, and the circuit parameters are extracted corresponding to each geometry variation. The first Broyden matrix $B^{(1)}$ is initiated as follows:

$$B^{(1)} = \begin{bmatrix} \frac{\partial x_{c1}}{\partial x_{f1}} & \frac{\partial x_{c1}}{\partial x_{f2}} & \cdots & \frac{\partial x_{c1}}{\partial x_{f6}} \\ \frac{\partial x_{c2}}{\partial x_{f1}} & \frac{\partial x_{c2}}{\partial x_{f2}} & \cdots & \frac{\partial x_{c2}}{\partial x_{f6}} \\ . & & & \\ . & & & \\ . & & & \\ \frac{\partial x_{c6}}{\partial x_{f1}} & \frac{\partial x_{c6}}{\partial x_{f2}} & \cdots & \frac{\partial x_{c6}}{\partial x_{f6}} \end{bmatrix} \tag{3.82}$$

Where the derivatives are obtained from the variation of the coarse model parameters, ∂x_{ci}, that results after introducing a small perturbation of the parameters in the fine model, ∂x_{fi}. Once the Broyden matrix is known, the geometry of the following iteration can be derived from (3.78), and the process is iterated as explained earlier until convergence is obtained. The implementation of the ASM algorithm is described by means of the flow chart depicted in Figure 3.26.

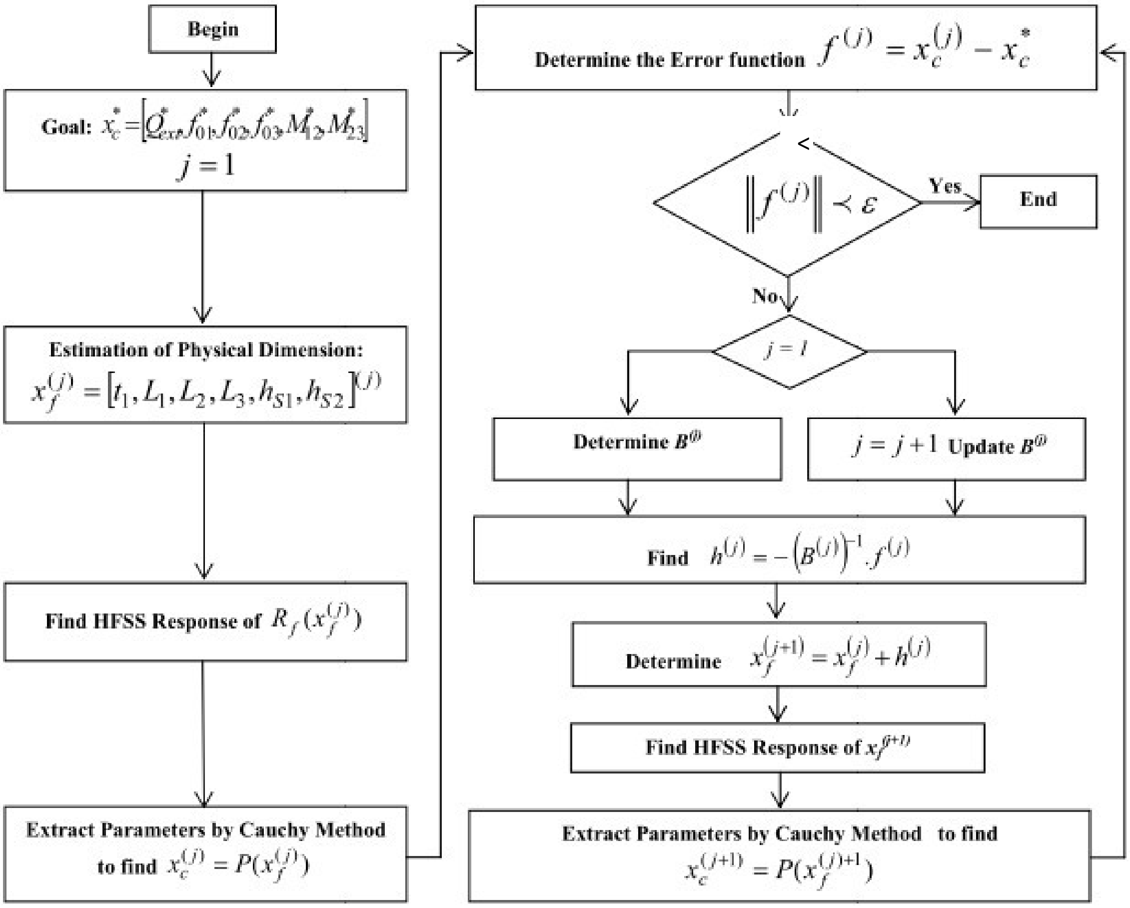

Figure 3.26: .Optimization Process Flow Chart of the ASM algorithm

3.8. Design and Optimization of Five Pole Coaxial Microwave Bandpass Filter

To validate the precedent method for using the coupling matrix filter circuit equivalent and EM software to synthesize the physical dimensions of the filter, we consider the design is specified in terms of the Chebyshev Bandpass response. The aim is to translate the elements coupling matrix into physical dimensions.

3.8.1. Design Coaxial Filter Using the Coupling Matrix Model

The microwave coaxial Bandpass filter is assumed to have the following specifications:

- Filter Order N=5
- Center frequency $f_0 = 3029.85\text{ MHz}$
- Bandwidth BW=60 MHz (fractional Bandwidth $\mathrm{FBW} = \frac{\mathrm{BW}}{\mathrm{f_0}} = 1.98\%$)
- Return loss RL=20dB (a equivalent to passband ripple of 0.0436 dB)

Figure 3.27 shows the five-pole Coaxial microwave resonator filter topology .The normalized ($N+2$) degree coupling matrix (m) elements and the normalized external quality factors of the filter as obtained from synthesis applying the theory of Cameron in [2] are given as follows:

$$m=\begin{bmatrix} 0 & 1.0137 & 0 & 0 & 0 & 0 & 0 \\ 1.0137 & 0 & 0.8653 & 0 & 0 & 0 & 0 \\ 0 & 0.8653 & 0 & 0.6357 & 0 & 0 & 0 \\ 0 & 0 & 0.6357 & 0 & 0.6357 & 0 & 0 \\ 0 & 0 & 0 & 0.6357 & 0 & 0.8653 & 0 \\ 0 & 0 & 0 & 0 & 0.8653 & 0 & 1.0137 \\ 0 & 0 & 0 & 0 & 0 & 1.0137 & 0 \end{bmatrix}$$

$$q_{ext,S}=q_{ext,L}=0.973153$$

The normalized coupling matrix must be denormalized for using in the physical dimensioning of the microwave filter. Using equations (3.63) and (3.64), the denormalized coupling matrix [M] and external quality factors ($Q_{ext,S}$,$Q_{ext,L}$) of the filter are given as follows:

$$M=\begin{bmatrix} 0 & 0.0171 & 0 & 0 & 0 \\ 0.0171 & 0 & 0.0126 & 0 & 0 \\ 0 & 0.0126 & 0 & 0.0126 & 0 \\ 0 & 0 & 0.0126 & 0 & 0.0171 \\ 0 & 0 & 0 & 0.0171 & 0 \end{bmatrix}$$

$$Q_{ext,S}=Q_{ext,L}=49.1446$$

Figure 3.28 illustrates the simulated ideal response using the coupling matrix elements of the five-Degree microwave coaxial coupled filter.

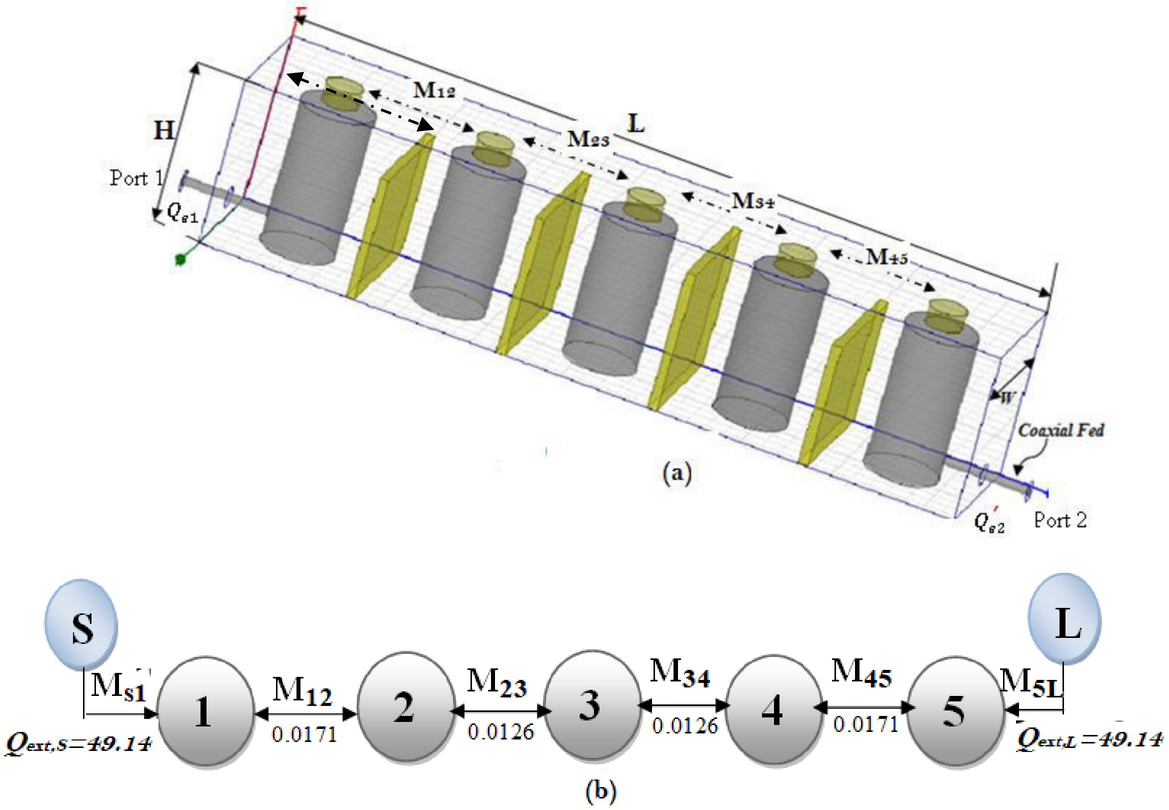

Figure 3.27: (a) The topology of the Five-Degree filter, (b) Coupling scheme of the proposed coaxial coupled filter

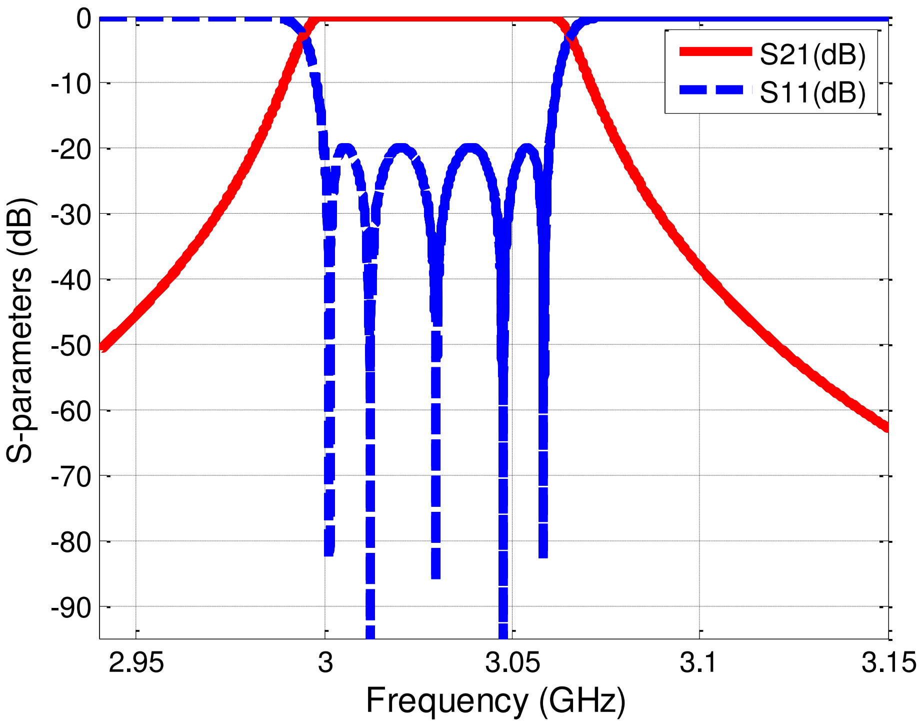

Figure 3.28: The simulated ideal response of the microwave filter based on the coupling matrix model

3.8.2. Physical Realization of Coupling Matrix

Having determined the de-normalized coupling matrix [*M*], the next step is to find the physical dimensions for a coaxial microwave coupled resonator topology. Full-wave electromagnetic (EM) simulations are performed to extract the cavity frequency resonance, the coupling coefficients and external quality factors using HFSS eigenmode. This enables us to implement the required coupling matrix [*M*] physically..

a. Calculation of Resonance Frequency of Coaxial Resonator Cavity Configuration

Full-wave EM simulation is carried out to determine the desired cavity resonant frequency using eigenmode HFSS. Figure 3.29(a) shows the topology of cavity resonator where we determine the resonance frequency by tuning the screw (**Li**).A design curve for cavity frequency resonance (**f**) against (**Li**) can be obtained, as shown in Figure 3.29(b)

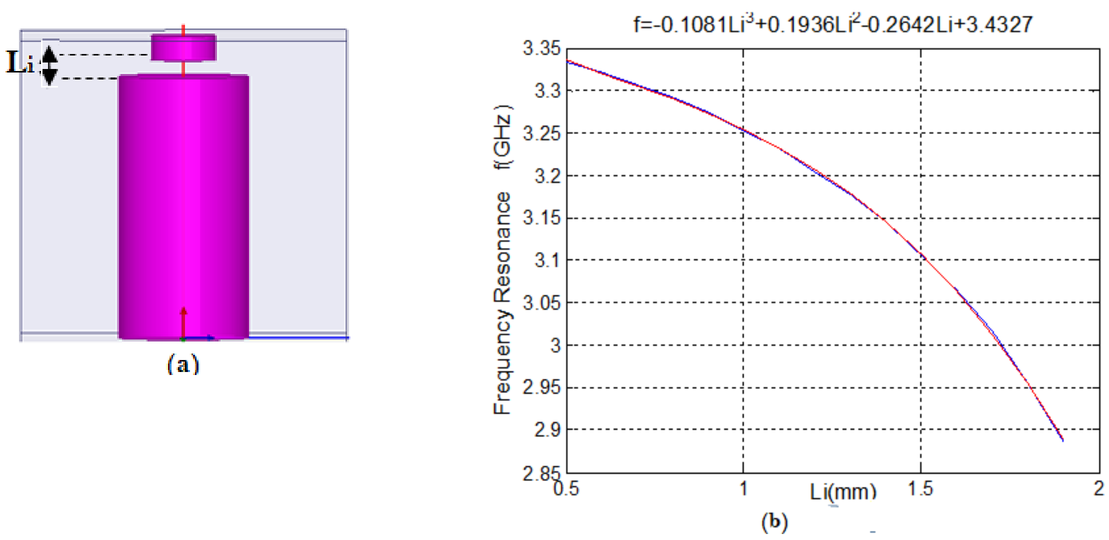

(a)

(b)

Figure 3.29: (a) EM model of a coaxial resonator with air cavity and tuning screw. (b) Design curve for frequency Resonance Cavity

b. Calculation of wall Dimensions for Inter-resonator Coupling

The use of electric and magnetic wall symmetry to evaluate inter-resonator coupling is hard to be implemented. It requires the use of an eigenmode solver HFSS. It employs the calculation of the resonant frequency peaks of even and odd modes (f_m and f_e),which diagnostics the coupling coefficient $M_{i,j}$. It is defined as follow:

$$M_{i,j} = \frac{f_e^2 - f_m^2}{f_e^2 + f_m^2} \tag{3.83}$$

In Figure 3.30, the coupling between resonators (i) and (j) of the coaxial microwave filter topology may be determined from eigenmode solver HFSS using the configuration in

Figure 3.30a. Both resonators have the same size and resonant frequency. The space **hs** controls the coefficient coupling (**Mij**) between the two resonators.

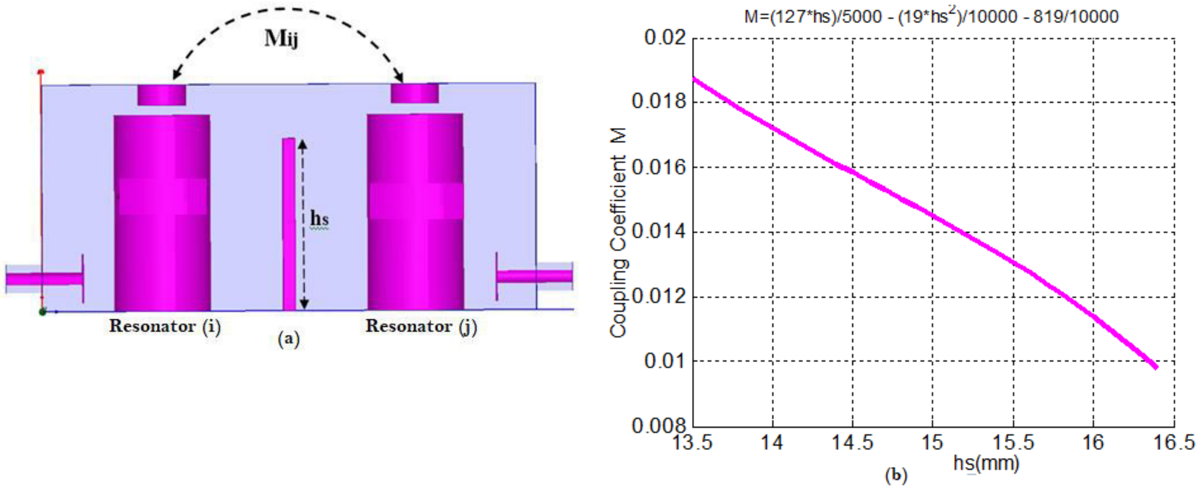

Figure 3.30: (a) Configuration for extracting coupling coefficient Mij (b) Design curve for Mij

c. External Quality Factor (Q_{ext}) Calculation

The input /output coupling of a single resonator are found by simulating $|S_{21}|$ result with one port weakly coupled. Figure 3.31(a) depicts a configuration to determine the external quality factor of the I/O resonator. A synthesis curve for Q_{ext} against **t** could be achieved, as shown in Figure 3.31(b).After that, the external quality factor Q_{ext} can be extracted from the simulated $|S_{21}|$ response using the following formula [2]:

$$Q_{ext} = \frac{\omega_0}{\Delta\omega_{\pm 3dB}} \tag{3.84}$$

Where, ω_0 is the resonant frequency of the loaded resonator and $\Delta\omega_{\pm 3dB}$ is the 3 dB bandwidth.

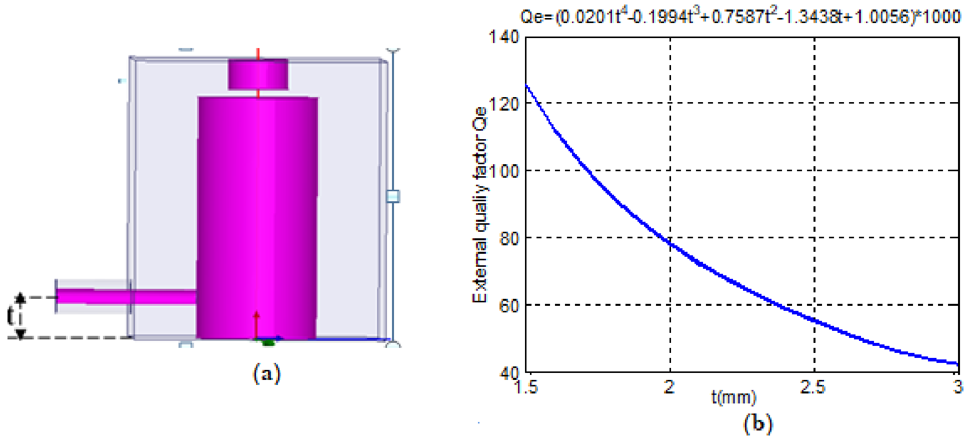

Figure 3.31: (a) Configuration for extracting External Quality Factor. (b) Design curve for *Qext*

3.8.3. Hybrid Optimization Using the Cauchy and ASM techniques

a. Dimensioning problem for coaxial microwave filter Design

The initial dimensions which have been extracted from eigenmode solver in the previous section are depicted in Figure 3.32.

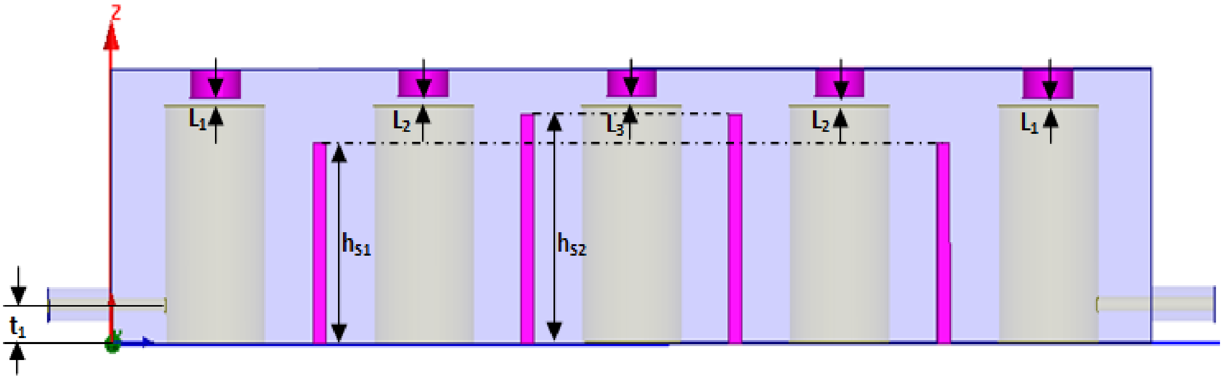

Figure 3.32: 3D structure: A five-pole coaxial coupled resonator filter

Figure 3.33 illustrates the HFSS simulated results of the filter based on EM-based synthesis methods are useful in obtaining an initial design which were calculated previously.

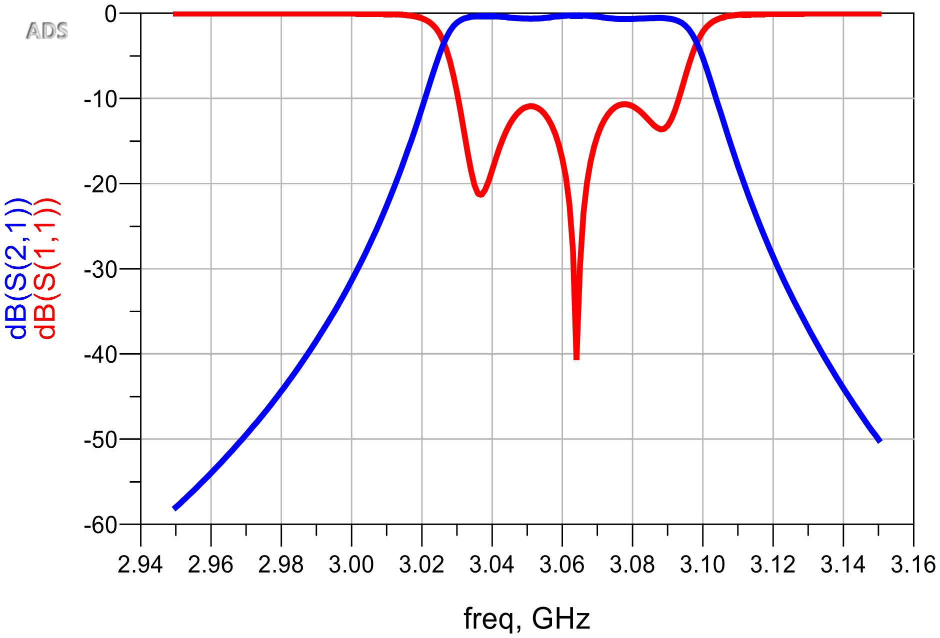

Figure 3.33: The Initial Response :HFSS simulation results based on initial physical dimensions

However, the result obtained in Figure 3.33 from EM-based synthesis technique is not satisfied the design specifications. To obtain more accurate performance, an hybrid Cauchy and ASM techniques can be applied which will be described in the next section or can be Optimized by manual tuning.

b. Proposed Solution Using the Combinations of Cauchy/ ASM Techniques

Figure 3.32 illustrates the fine filter model using HFSS software. All the cavities are constructed in the same size with varying length tuning screw. The corresponding relation between screw length and resonant frequency can be established through HFSS Eigen-mode solver. In the ASM optimization, the coarse model is implemented using ADS simulator as shown in Figure 3.34. The LC resonant circuit represents the coaxial cavity, and the phase-shifter relates with the coupling coefficient. The parameters of coarse model are:

$$x_c = \left[Q_{ext}, f_{01}, f_{02}, f_{03}, M_{12}, M_{23}\right] \tag{3.85}$$

Where Q_{ext} is the extern quality factor of input port and output ports, f_{0i} is the resonant frequency of each resonator, M_{ij} is the coupling coefficient between two adjacent resonators. The fine model is simulated with full-wave method, and implemented using HFSS as shown in Figure 3.32.

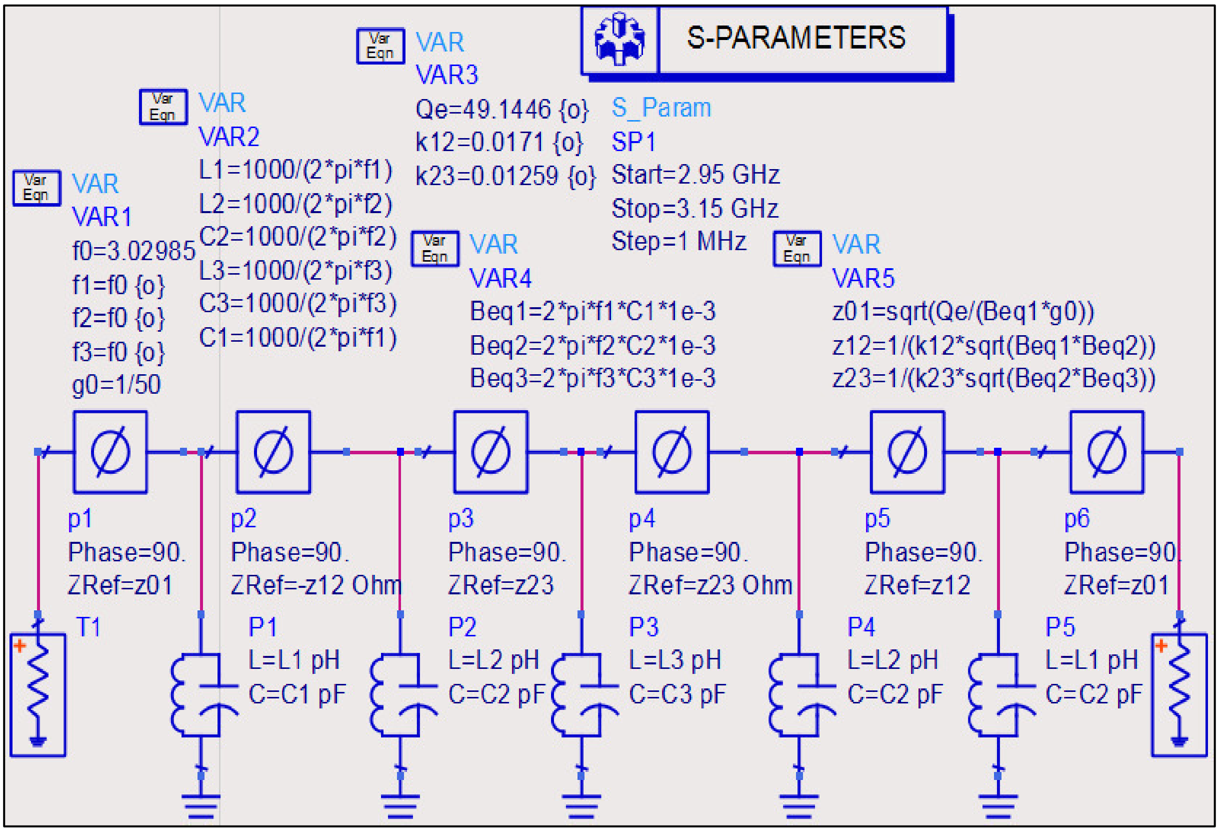

VAR
VAR1
f0=3.02985
f1=f0 {o}
f2=f0 {o}
f3=f0 {o}
g0=1/50

VAR
VAR2
L1=1000/(2*pi*f1)
L2=1000/(2*pi*f2)
C2=1000/(2*pi*f2)
L3=1000/(2*pi*f3)
C3=1000/(2*pi*f3)
C1=1000/(2*pi*f1)

VAR
VAR3
Qe=49.1446 {o}
k12=0.0171 {o}
k23=0.01259 {o}

S-PARAMETERS
S_Param
SP1
Start=2.95 GHz
Stop=3.15 GHz
Step=1 MHz

VAR
VAR4
Beq1=2*pi*f1*C1*1e-3
Beq2=2*pi*f2*C2*1e-3
Beq3=2*pi*f3*C3*1e-3

VAR
VAR5
z01=sqrt(Qe/(Beq1*g0))
z12=1/(k12*sqrt(Beq1*Beq2))
z23=1/(k23*sqrt(Beq2*Beq3))

Figure 3.34: The coarse model of the five pole microwave coaxial bandpass filter in ADS

The optimized parameters of fine model are:

$$x_f = \left[t_1, L_1, L_2, L_3, h_{S1}, h_{S2}\right] \tag{3.86}$$

The optimal response (coupling matrix model) result in the coarse model is presented in Figure 3.28. Responses of the coarse model meet in fact the design specifications. The optimization procedure is displayed as the following steps:

<u>Step 1</u> - Firstly, optimize parameters of the filter coarse model in ADS and obtain the optimal solution of coarse model:

$$x_c^* = \left[Q_{ext}, f_{01}, f_{02}, f_{03}, M_{12}, M_{23}\right] \tag{3.87}$$

$$\begin{aligned} x_c^* = [&49.1446,\ 3029.85,\ 3029.85 \\ &3029.85,\ 0.0171,\ 0.0126] \end{aligned}$$

<u>Step 2-</u> Measure the filter twice with different tuning positions $\boldsymbol{x_{f1}}$ and $\boldsymbol{x_{f2}}$ to obtain the *S*-parameters, then obtain two groups equivalent circuit parameters $\boldsymbol{x_{c1}}$ and $\boldsymbol{x_{c2}}$**.** The initial position of tuning screws and walls are:

$$\begin{aligned} x_f &= \left[t_1, L_1, L_2, L_3, h_{S1}, h_{S2}\right]\ (mm) \\ &= \left[1.39,\ 1.68\ ,\ \ 1.59\ ,\ 1.62, 13.4277, 15.4964\right] \end{aligned} \tag{3.88}$$

Then using Cauchy method to extract the equivalent circuit parameters as follows:

$$\begin{aligned} x_{c1} &= \left[Q_{ext}, f_{01}, f_{02}, f_{03}, M_{12}, M_{23}\right] \\ &= [55.2605\ ,\ 3.01891,\ 3.02145, \\ &\quad 3.01844,\ 0.0208776\ ,0.0148232] \end{aligned} \tag{3.89}$$

The second initial position x_{c2} of the fine model is obtained from perturbation of x_{c1}.

$$x_{f2} = x_{f1} \times \left(1 + 0.05 * per\right),$$

$$per = sign(x_{c1} - x_c^*) = \begin{cases} +1 \ \ if \ \left(x_{c1} - x_c^*\right) \ > 0 \\ -1 \ \ if \ \left(x_{c1} - x_c^*\right) \ < 0 \end{cases} \tag{3.90}$$

$$\begin{aligned} x_{f1} &= \left[t_1, L_1, L_2, L_3, h_{S1}, h_{S2}\right]\ mm \\ &= [1.4595,\ 1.5960,\ \ 1.5105, \\ &\quad 1.5390,\ 14.0991,\ 16.2712] \end{aligned}$$

Then obtaining the equivalent circuit parameters by Cauchy technique:

$$x_{c2} = \left[Q_{ext}, f_{01}, f_{02}, f_{03}, M_{12}, M_{23}\right] \\ = \left[50.3975,\ 3.06475,\ 3.06201,\ 3.06206,\ 0.0185937,\ 0.0121253\right] \tag{3.91}$$

Step 3 – Calculate the initial *Broyden* matrix B_0 through the equation:

$$B^{(1)} = B_0 = \left(\frac{x_{c2} - x_{c1}}{x_{f2} - x_{f1}} \right) \\ = diag\left[-69.9712 \quad -0.5457 \quad -0.5102 \quad -0.5385 \quad -0.0034 \quad -0.0035\right] \tag{3.92}$$

Step 4 - Start to iterate and evaluate the difference.

$$f^{(1)} = x_c^{(0)} - x_c^* = \left[1.2575,\ 0.0349,\ 0.03216,\ 0.03221,\ 0.0014537,\ -0.0004647\right]^T \tag{3.93}$$

Here $x_c^{(0)} = x_{c2}$ stops if $\left\|f^{(1)}\right\| < \varepsilon$. Where ε is the convergence precision. After, calculate the increased value of the tuning screws:

$$h^{(1)} = \left(B^{(1)}\right)^{-1}\left(-f^{(1)}\right) \tag{3.94}$$

Step 5 – the second, third, fourth and fifth iteration are similar as the first iteration. In order to reproduce the tuning methodology, there result of the all iterations is shown in the following Table 3.4.

Table 3.4: Physical sizes and parameters of the coaxial Bandpass filter in each iteration (mm)

Iter.	Physical sizes(mm)						Parameters of coarse model					
N°	t_1	L_1	L_2	L_3	h_{s1}	h_{s2}	Q_{ext}	f_{01} (MHz)	f_{02} (MHz)	f_{03} (MHz)	M_{12}	M_{23}
1	1.4595	1.5960	1.5105	1.5390	14.099	16.27	50.397	3064.7	3062	3062.6	0.0185	0.0121
2	1.4775	1.6600	1.5735	1.5988	14.526	16.137	50.397	3064.8	3062	3062.1	0.0186	0.0121
3	1.5205	1.6754	1.5918	1.6113	14.609	16.139	51.681	3037.0	3037.7	3035.5	0.0174	0.0126
4	1.5387	1.6752	1.5913	1.6103	14.578	16.138	51.350	3030.3	3030.2	3029.5	0.0170	0.0126
5	1.5601	1.6762	1.5915	1.6102	14.543	16.116	51.471	3031.0	3030.5	3030.1	0.0170	0.0125
6	1.5832	1.6771	1.5915	1.6103	14.526	16.100	40.4Z	3030.2	3029.9	3030.0	0.0171	0.0126

The corresponding responses of the six iterations are shown in Figure 3.35. The performance of the first, fourth and sixth iterations are compared in Figure 3.36. After six iterations, the measured optimized filter response agrees with the required specifications that validates the efficiency of proposed tuning technique. Figure 3.37 compares the simulated response of the proposed five pole coaxial Bandpass filter after the sixth iteration to the ideal coupling matrix response.

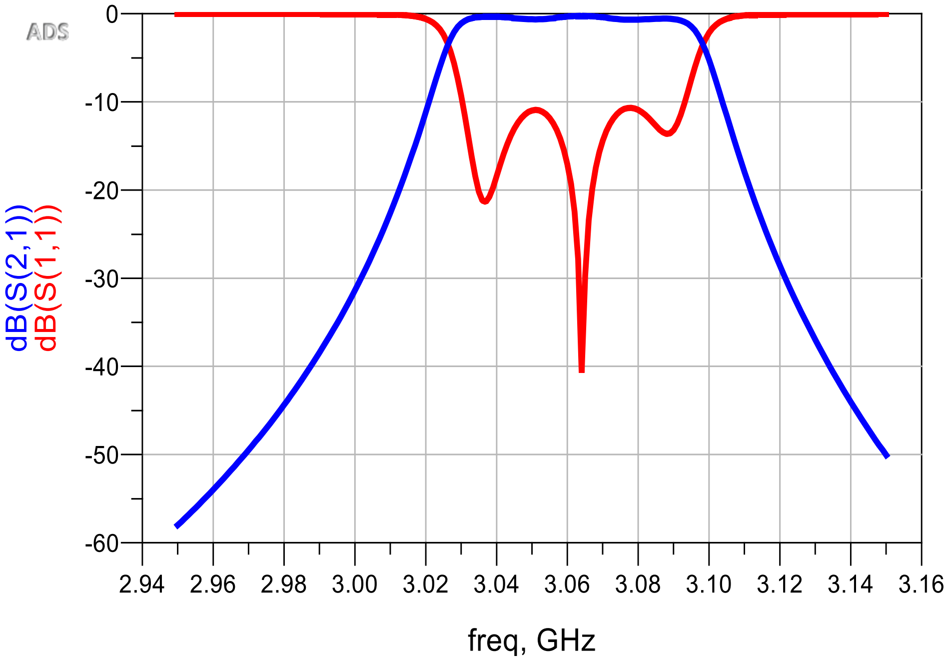

Iteration01

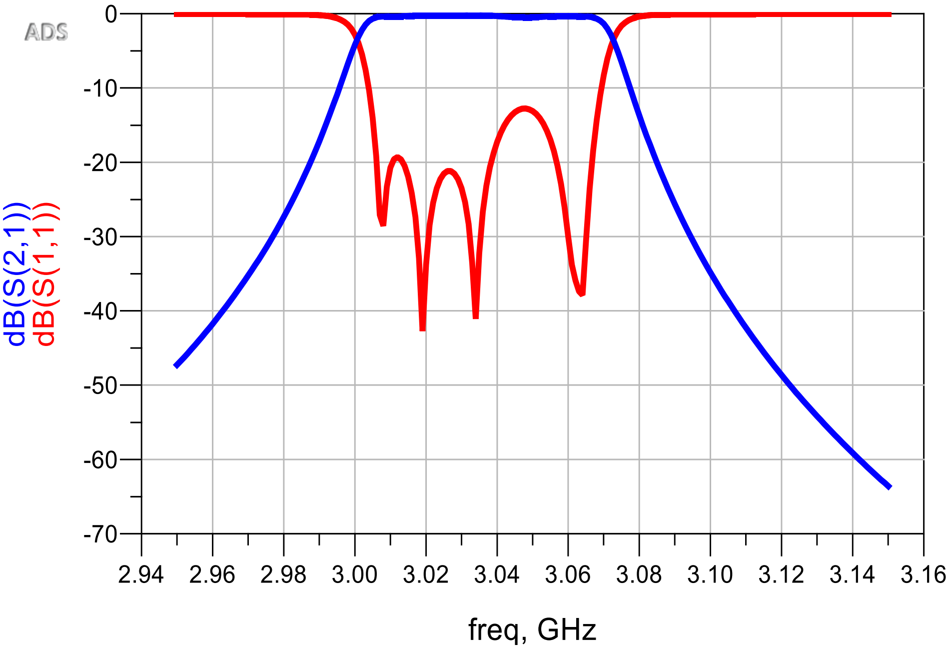

Iteration02

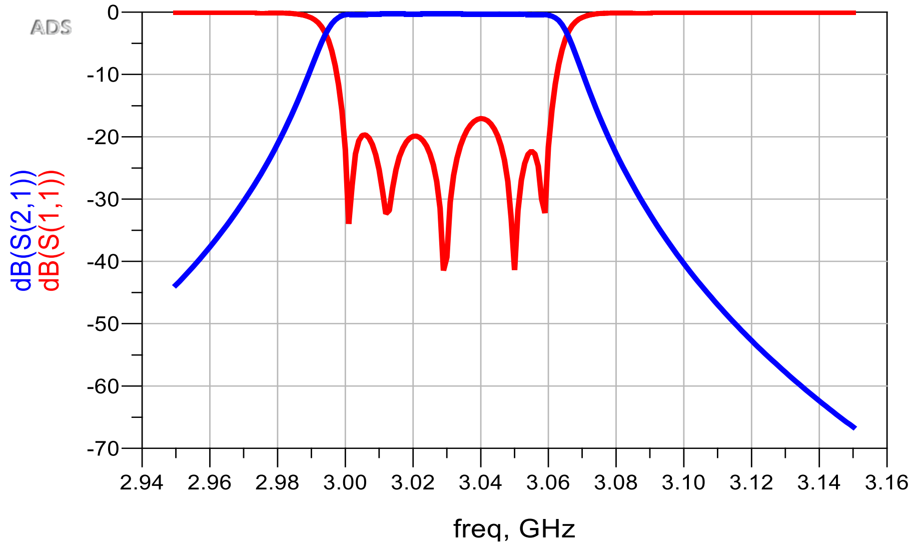

Iteration03

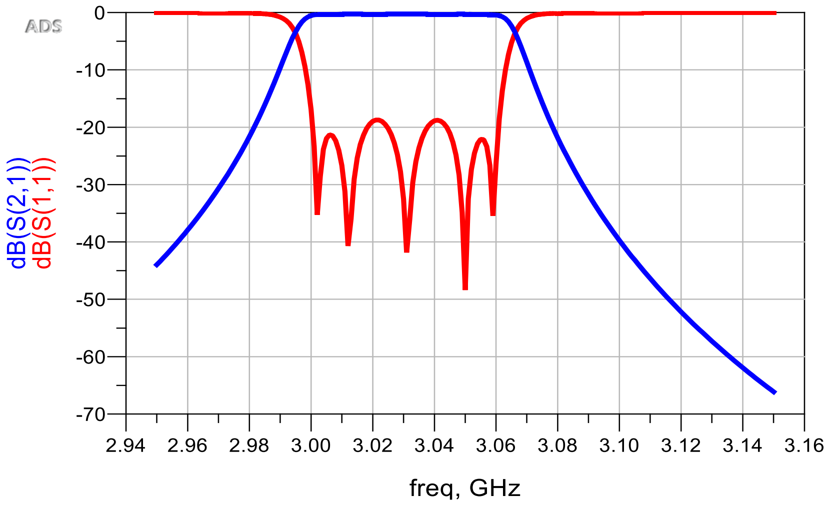

Iteration04

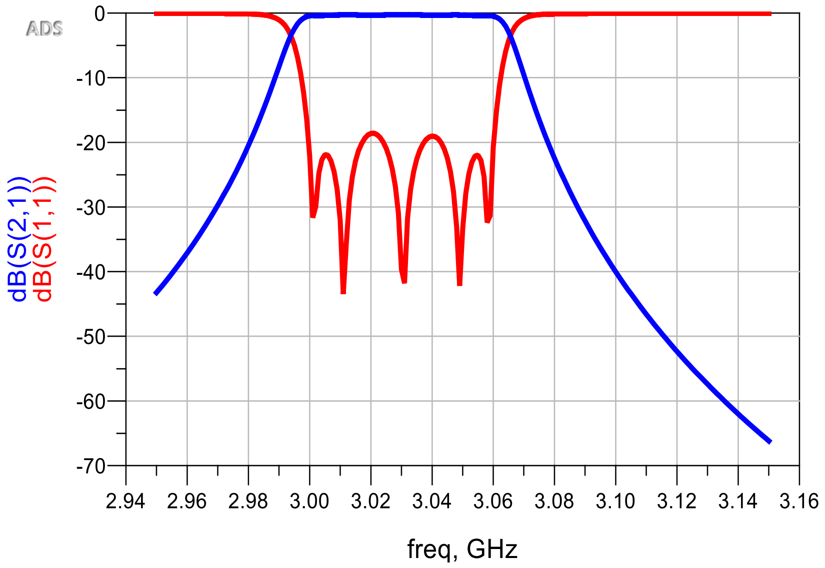

Iteration05

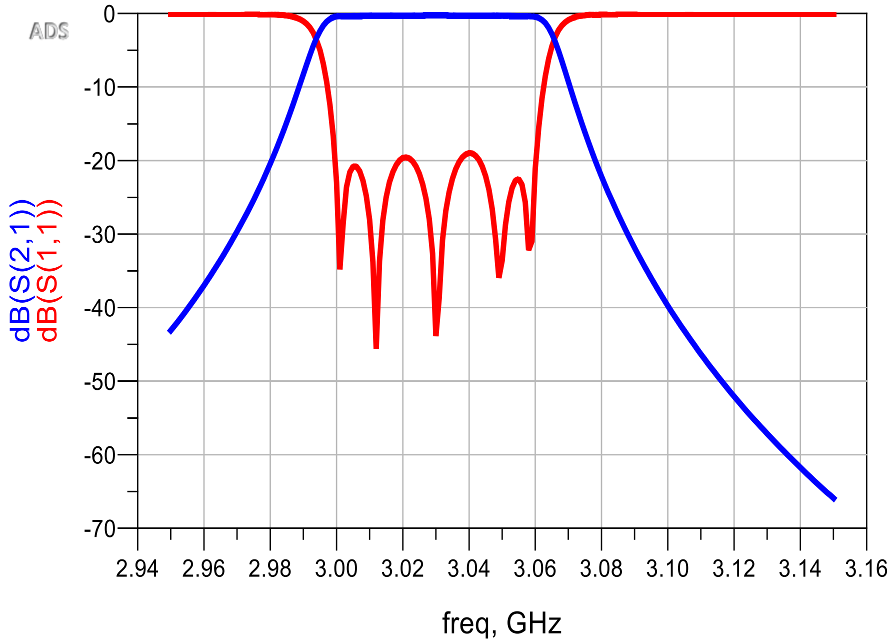

Iteration06

Figure 3.35: Responses of the five resonators coaxial Bandpass filter in each iteration

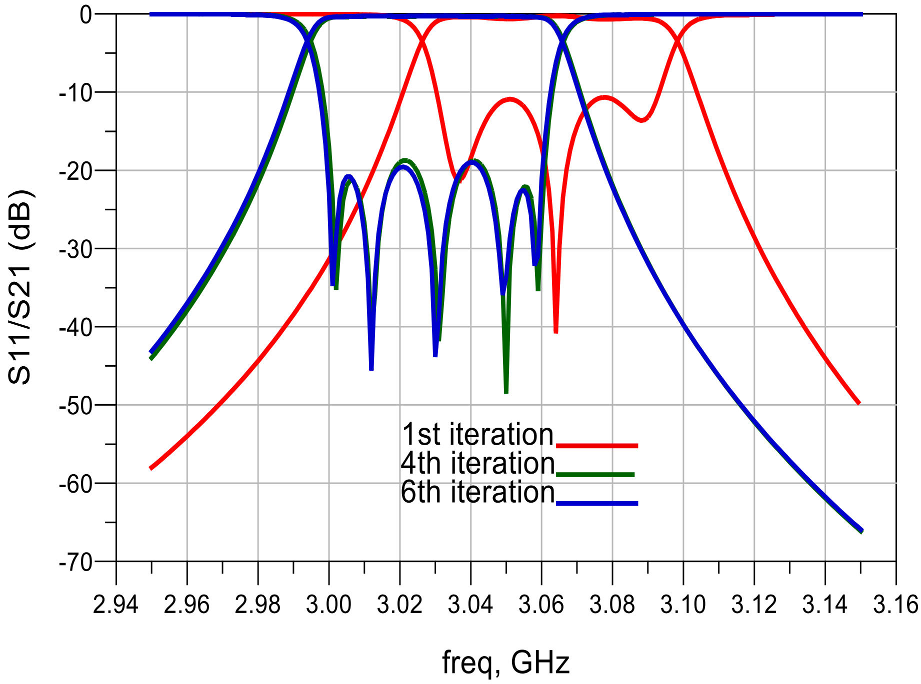

Figure 3.36: Comparison of performance in the first, fourth and sixth iterations in the coaxial Bandpass filter

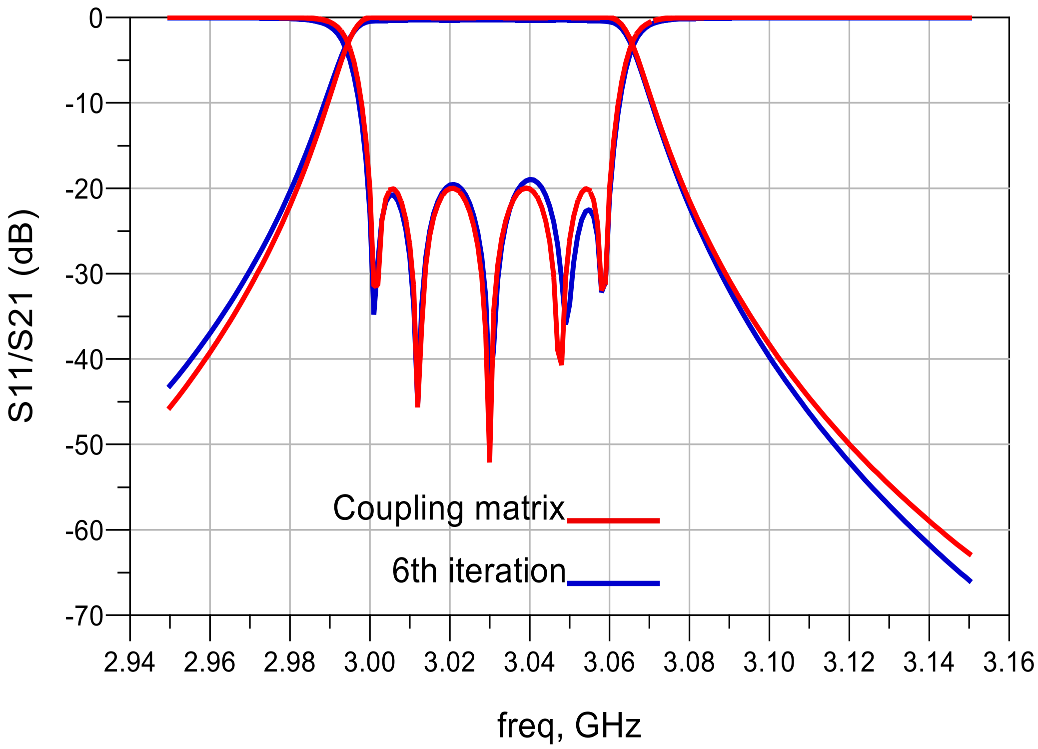

Figure 3.37: Comparison performance of sixth iteration and the ideal coupling matrix of coaxial bandpass filter.

Excellent agreement of simulated and ideal coupling matrix responses can be clearly observed. The optimized filter layout with optimal physical dimensions significantly exhibits an ideal frequency response and satisfies the design specifications. Finally, the proposed method used for optimizing the microwave coaxial Bandpass filter, is compared to the methods previously presented in [26, 32] as clarified in Table 3.5. The proposed optimization method introduces high efficiency, essentially, in terms of consuming time and simplicity to develop a new filter design.

Table 3.5: Performance Comparisons of the proposed optimization to previous methods

Opt. Method	Sample of points	Consummation time for each iteration	Evaluation
Proposed	90	About 5 s	Fast, simple and more efficient
[26]	150	About 20 s	Slow, complex and efficient
[32]	150	About 60 s	Slow and complex

3.9. Conclusion

This chapter starts with the general Chebyshev polynomial, which can be used in producing filter functions to obtain in the passband equi-ripple amplitude peaks for a random location of the zeros transmission of the transfer function. To guarantee realizable microwave filters, the zeros transmission have to be positioned symmetrically about the imaginary axis. The previous restrictions achieve the unitary condition. The recursion method is outlined in this chapter. It includes examples for more illustration for Cameron technique. Practical coaxial microwave filter can be synthesized after a transformation of polynomials into a prototype electrical circuit. The design process results in the impractical coupling matrix. As a next step, we have transformed the coupling matrix into a folded form which can be achieved. It can be realized by the application of similarity transformations. Knowing that this transformations keep the eigenvalues and eigenvectors of the coupling matrix, thus guaranteed that the required microwave filter response stays unchanged.

This is achieved by applying similarity transformations to the coupling matrix. Such transformations preserve the eigenvalues and eigenvectors of the matrix, thus ensuring that the desired filter response remains unaltered. In this chapter we examine the practical aspects of making physical microwave Bandpass filters based on coupling matrix synthesis. By using EM simulator HFSS, the design physical parameters and the coupling matrix representation introduce a link between them. A new technique to extract or diagnosis a coupling matrix of coaxial microwave filter, based on Cauchy and ASM techniques is introduced in this chapter. To determine the parameters of the equivalent circuit model, from the simulated S-parameters, we apply the Cauchy method. In addition, to predict the tuning values of screws directions, it is suitable to use the ASM method. The coaxial microwave filter needs only six iterations to obtain the required specifications. Consequently, the Cauchy and ASM methods are validated.

[1] J.S. Hong and M.J. Lancaster, Micrsotrip filters for RF/microwave applications,

Wiley, New York, NY, 2001.

[2] Richard J Cameron, Chandra M Kudsia, and Raafat R Mansour. Microwave filters for communication systems. Wiley-Interscience, 2007.

[3] W. Xia, X. Shang, and M. J. Lancaster., "Responses comparisons for coupled-resonator based diplexers," in Passive RF and Microwave Components, 3rd Annual Seminar on, 2012, pp. 67-75.

[4] G. Matthaei, L. Young, and E.M.T. Jones, Microwave Filters, Impedance-Matching Networks, and Coupling Structures, Artech House, 1980.

[5] Ana Morán López, ‘’ Filter design in coaxial cavities’’ June 2015 University of Madrid.

[6] W. Xia, X. Shang, and M. J. Lancaster., "Responses comparisons for coupled-resonator based diplexers," in Passive RF and Microwave Components, 3rd Annual Seminar on, 2012, pp. 67- 75.

[7] Talal F. Skaik, ‘’ Synthesis of Coupled Resonator Circuits with Multiple Outputs using Coupling Matrix Optimization ‘’, The University of Birmingham, 2011.

[8] D. G. Swanson, “Narrow-band microwave filter design,” IEEE Microwave Magazine, pp. 105-114. Oct. 2007.

[9] Atia W.A., Zaki K.A., and Atia A.E.’Synthesis of general topology multiple coupled resonator filters by optimization‘, IEEE MTT-S Int. Microw. Symp, Baltimore, USA, 1998, pp. 821-824

[10] Pozar D. "*Microwave Engineering*", Third Edition. John Wiley and Sons, USA, 2005, pp. 278- 279, 370-430.

[11] R. Cameron, General coupling matrix synthesis methods for Chebyshev filtering functions, IEEE Trans Microwave Theory Tech 47 (1999), 433–442.

[12] Xiaobang Shang, Wenlin Xia, and Michael J Lancaster. ‘’The design of waveguide filters based on cross-coupled resonators. Microwave and Optical Technology Letters, 56(1):3–8,2014.

[13] E. Nugoolcharoenlap, X. Shang, and M. J. Lancaster, "Design of Waveguide Aperture Antenna-Filters using Coupling Matrix Theory," submitted to MTT.

[14] A. E. Williams, “A Four-Cavity Elliptic Waveguide Filter,” IEEE Trans. Microw. Theory & Techn., Vol. 18, pp. 1109-1113, Dec. 1970.

[15] J. D. Rhodes, R.J. Cameron, “General extracted pole synthesis technique with applications to low-loss TE011 mode filters,” IEEE Trans. Microw. Theory & Techn., Vol. 28, pp. 1018-1028, Sep. 1980.

[16] G. Macchiarella, “An efficient technique for the synthesis of an equiripple low-pass prototype filter with asymmetric frequency response and arbitrary transfer function zeros,” in 24th European Microwave Conf., Bologna, Italy, Sept. 1995, pp. 722–724.

[17] S. Amari, Synthesis of cross-coupled resonator filters using an analytical gradient-based optimization technique, IEEE Trans Microwave Theory Tech 48 (2000) 1559–1564.

[18] Ian Hunter. Theory and design of microwave filters. Number 48. Iet, 2001.

[19] David M Pozar. Microwave engineering. John Wiley & Sons, 2009.

[20] Xiaobang Shang, Wenlin Xia, and Michael J Lancaster. The design of waveguide filters based on cross-coupled resonators. Microwave and Optical Technology Letters, 56(1):3–8, 2014.

[21] Cameron, R.J. (2003) Advanced coupling matrix synthesis techniques for microwave filters.IEEE Transactions on Microwave Theory and Techniques, 51, 1–10.

[22] J. W. Bandler, et al., “Electromagnetic optimization exploiting aggressive space mapping,” *IEEE Trans. on Microw. Theory and Tech.,* Vol. 43, 2874–2882, Dec. 1995.

[23] S. Amari, U. Rosenberg, and J. Bornemann, “Adaptive synthesis and design of resonator filters with source/load-multi resonator coupling,” *IEEE Trans. on Microwave Theory and Tech*, vol. 50, no. 8, pp. 1969–1978, Aug. 2002.

[24] V. Miraftab and M. Yu, “Generalized lossy microwave filter coupling matrix synthesis and design using mixed technologies,” *IEEE Trans. on Microwave Theory Tech.*, Vol. 56, No. 12, 3016–3027, August. 2008.

[25] G. Macchiarella and D. Traina, “A formulation of the Cauchy method suitable for the synthesis of lossless circuit models of microwave filters from lossy measurement,” IEEE Microwave Wire. Compon. Lett., Vol. 16,No.5, 243–245, May 2006.

[26] A. G. Lamperez, T. K. Sarkar, and M. S. Palma, “Generation of accurate rational models of lossy systems using the Cauchy method,” IEEE Microwave Wire. Compon. Lett., Vol. 14, No. 10,490–492, Oct. 2004.

[27] W. Bandler, D.M. Hailu, K. Madsen, and F. Pedersen, “A space mapping interpolating surrogate algorithm for highly optimized EM-based design of microwave devices,” IEEE Trans. on Microwave Theory Tech., 2593-2600,Sept. 2004.

[28] JS. Koziel, J.W. Bandler, and K. Madsen, “A space mapping framework for engineering optimization-Theory and implementation,” IEEE Trans. on Microwave Theory Tech., 3721-3730, Sept. 2006.

[29] M. Bakr, J.W. Bandler, K. Madsen, J.E. Sanchez, and J. Sndergaard, “Space mapping optimization of microwave circuits exploiting surrogate models, IEEE Trans Microwave Theory Tech, 2297-2306, Feb. 2000.

[30] A. G. Lampérez, S. L. Romano, M. S. Palma, and T. K. Sarkar, “Efficient electromagnetic optimization of microwave filters and multiplexers using rational models,” IEEE Trans. on Microwave Theory and Tech., Vol. 52, No. 2, pp.508-520, Feb. 2004.

[31] C. G. Broyden, “A Class of Methods for Solving Non linear Simultaneous Equations,” Mathematics of Computation, vol. 19, no. 92, pp. 577-593, Oct.1965.

[32] D. Wolansky and R. Tkadlec, “Coaxial filters optimization using tuning space mapping in CST,” Radio Eng., pp. 289-294, Sept. 2011.

Chapter 4: Substrate Integrated Waveguide Antennas

4.1. Introduction

In aeronautical, space, satellite and high-performance missile applications, where size, weight, cost, performance, ease of installation and aerodynamic profile are constraints, low profile antennas are widely required. Currently, there are many other government and commercial applications, such as mobile radio and wireless communications that have similar specifications. To meet these requirements, microstrip antennas [4] can be used.

Designed in the year 1953 [4], microstrip patch antenna has "matured considerably over the past 33 years with the beginning of serious work in 1972" Major advances in microstrip patch antennas are included; in bandwidth enhancement, the fight against surface wave effects, the development of compact antennas, active antennas and the development of analytical tools.

Microstrip antennas offer many interesting features and it is therefore very difficult to effectively model their resonance and radiation characteristics (Pozar & Schaubert, 1995). In particular, microstrip antennas composed of perfectly electric conductive plates (PEC) mounted on spherical surfaces has fundamental advantages over the planar ones. These antennas are contoured, conform to planar and non-planar surfaces, simple and inexpensive to manufacture using modern printed circuit board technology, mechanically robust when mounted on rigid surfaces, compatible with MMIC designs. They are very versatile in terms of resonant frequency, polarization, pattern and impedance [3].

The interesting design features of the microstrip antennas are mainly the complex resonant frequencies, the radiation pattern, and the input impedance. An extensive literature review of the analysis of non-planar radiating microstrip structures, as well as research on the aforementioned design features, is included in the classic book (Wong, 1999). The main operational disadvantages of microstrip antennas are their low efficiency, low power, high quality factor (Q), low polarization purity, poor scanning performance, spurious radiation, and very narrow bandwidth, which typically represents only a fraction of a percentage or at most a few percent. In some applications, such as in government security systems, narrow bandwidths are desirable [3].

As long as these antennas correspond to planar and non-planar surfaces, these surfaces have significant disadvantages, so hybrid designs that merge technologies to eliminate drawbacks have become highly preferable in many applications. In addition to this advantage of hybrid structures, they still have some disadvantages related to the transition between the planar and non-planar parts, especially in the high frequencies.

A major challenge, however, is related to its integration with active devices and other conventional planar transmission lines, such as microstrip or coplanar waveguide (CPW), etc. Substrate Integrated Circuits (SICs) techniques including substrate integrated waveguide (SIW), which can be integrated in planar dielectric substrate with low insertion loss, high Q and low radiation loss, present a family of new guided wave structures. This scheme provides a bridge between planar and non-planar structures. Until now, microwave components and sub-systems based on SIW technology have been extensively studied and developed.

In this chapter, the main features of the substrate-integrated waveguide (SIW) technology are discussed. In addition, some of its main applications, which have already been reported for SIW devices, are also introduced. However, some aspects discussed in this chapter have been discussed only briefly and can be supplemented with other work on SIW, such as [23] and [24]. Although SIW devices have better loss characteristics than their counterparts in planar technologies, the use of dielectric materials, which inherently losses, reduces the SIW quality factor compared to RWG [19] - [24]. Nevertheless, it is still better than that obtained in conventional planar technologies such as microstrip and coplanar. Therefore, it allows the design of components with a high quality factor, while using a low cost manufacturing technique. In addition, the flexibility of using different substrates allows SIW devices to be integrated with other existing planar components.

But this technology has disadvantages as:

- ✓ Losses Leakage losses are significant and depend on the separation of the vias placed on the higher planes.
- ✓ Due to the use of dielectric in the waveguide structure, dielectric losses will occur with respect to the air used in the normal rectangular waveguide. Moreover, it depends on the frequency and, therefore, the applications of the millimeter wave (millimeter wave) must be carefully studied.
- ✓ Due to its waveguide structure, SIW has a lower cutoff frequency.

For these we tried to improve these disadvantages that are why we chose in this chapter the artificial intelligence technique is used to optimize the parameters used in the design of antennas. The network architecture is most often used with the Backpropagation algorithm and the multilayer feed forward network. Matlab programming can be used to form more general networks. To overcome the practical limitations of the perceptron and BP(Back propagation) algorithm, we turn to a neural network structure known as multilayer perceptron. The following three points highlight the basic characteristics of multilayer perceptrons:

- ✓ The model of each neuron in the network includes a nonlinear activation function that is differentiable.
- ✓ The network contains one or more layers hidden by both the input and output nodes.
- ✓ The network has a high degree of connectivity, the extent of which is determined by the synaptic weights of the network.

A popular method for the formation of multilayer perceptrons is the backpropagation algorithm, which includes the MLP algorithm as a special case. The training takes place in two phases:

1. In the direct phase, the synaptic weights of the network are fixed and the input signal is propagated through the network, layer by layer, until it reaches the output.
2. In the reverse phase, an error signal is produced by comparing the output of the network with a desired response.

This chapter is organized as follows. Section 1 covers the theoretical concepts of the microstrip antenna; the second section deals with concepts of substrate-embedded waveguides that are relevant to the designed antenna, such as antenna power, impedance matching, noise reduction, and so on. Section 3 covers the theory behind the ANNs. are the most commonly used type of neural network specifically used BP. The popular Backpropagation training algorithm is studied in detail. Section 4 shows the designs, all simulation results, including return losses and radiation patterns for these models.

This section organized as follows, the first step describes the antenna by the antenna parameters and the design equations that are needed to design the model. Basically, this step presents all antenna-related terms and parameters of the antenna design features designed, and simulations for each designed state, using HFSS as the software platform. The second step describes the BP architectures chosen to realize the synthesis and optimization of SIW tulip shaped antennas, as well as network sizes, training algorithms, etc. The synthesis and optimization results are then presented in the last step. The neural networks applied as models to the states of the microstrip antenna SIW and the corresponding parameters. Finally, significant conclusions drawn from the results obtained, as well as technical contributions from this research and possible future work, are presented in section 5.

4.2. Principles and classification of antennas

An antenna is an electromagnetic transducer, used to convert, in the transmitting mode, guided waves within transmission lines to radiate free-space waves, or to convert, in the receiving mode, free-space waves to guided waves.

Most fundamentally, an antenna is a way of converting the guided waves present in a waveguide, feeder cable or transmission line into radiating waves travelling in free space, or vice versa. Figure 4.1 shows how the fields trapped in the transmission line travel in one dimension towards the antenna, which converts them into radiating waves, carrying power away from the transmitter in three dimensions into free space [18].

The art of antenna design is to ensure this process takes place as efficiently as possible, with the antenna radiating as much power from the transmitter into useful directions, particularly the direction of the intended receiver, as can practically be achieved [18].

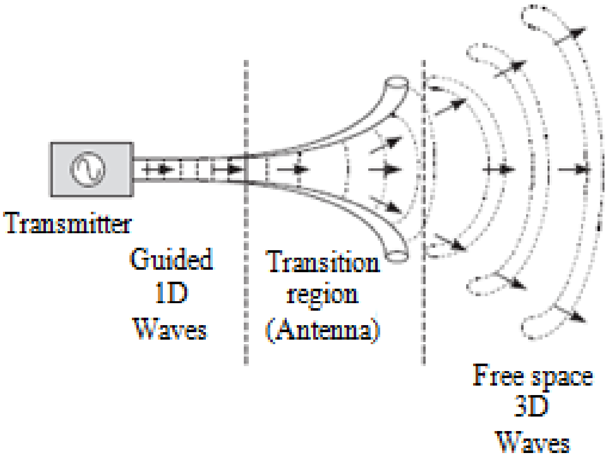

Figure 4.1: The antenna as a transition region between guided and propagating waves

The equivalent circuit of an antenna is given in Figure 4.2. as one can see that there is an impedance *(Z_g)* at the generator. The characteristic impedance of the transmission line *(Z_c)* which does not depend on the length of the transmission line but depends upon the material used in the transmission line and the impedance matching.

The impedance of the antenna *(Z_a)* is given by :

$$Z_a = (R_1 + R_r) + jX_a \tag{4.1}$$

Where R_1 is sum of the conduction and dielectric loss, R_r is the radiation resistance, and X_a is the radiation impedance

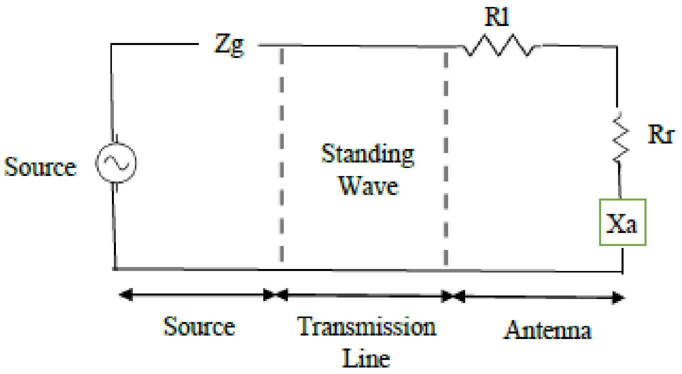

Figure 4.2: Equivalent Circuit Diagram of the antenna as a guiding device

.There is several ways to classify the antennas. If we classify on basis of frequency band we can have narrowband, wideband and ultra-wideband antennas. The antennas can be considered to be classified on the basis of electromagnetic, physical or electrical structure. Directionality also defines the classification in antenna as they can be directional and non-directional in nature. There can be different types of antenna. The following chart in Figure 4.3 depicts the different types of antenna and their combinations or derivatives. The main antenna and their types are mentioned herewith. For further details on types of antenna one can refer to [1].

- **Conducting Wire:** They are mainly constituted of a single wire. These are further arranged in form of dipoles, loops and helices'.
- **Apertures:** They consist of a radiating aperture for higher directivity. These are further subdivided to waveguides and horns.
- **Patch (Microstrip):** These are the majorly used in embedded applications. They can be of various shapes like rectangular, circular etc.
- **Array of elements:** They consist of a group of smaller antennas excited at a fixed phase difference to generate high directivity.
- **Reflector**
- **Lens**

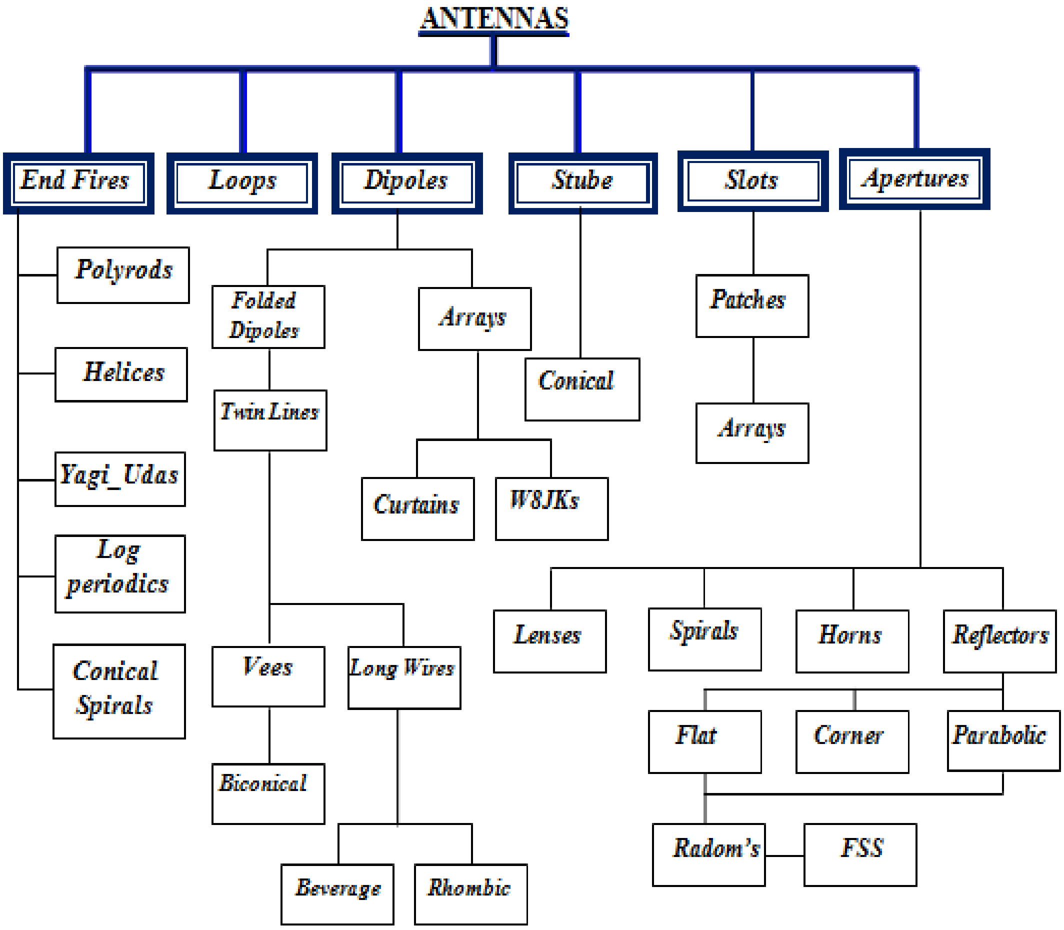

Figure 4.3: Classification of antenna on basis of physical structures

4.3. Microstrip Antennas

A microstrip patch antenna consists of a dielectric substrate sandwiched by a radiating patch on one side and the ground plane on the other side as shown in Figure 4.4. The radiating patch is made of a good conductor material such as annealed copper or gold. It can take any shape in the two dimensional plane and thus unlimited configurations are possible. The shapes can be anything ranging from triangular, circular, semi-circular and rectangular. The feed-lines and the radiating patch are usually photo-etched on the dielectric substrate.

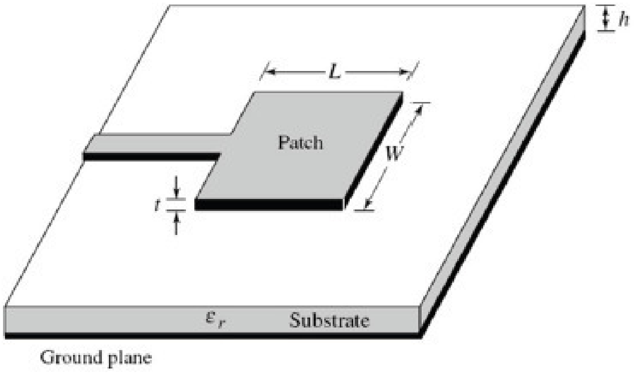

Figure 4.4: Rectangular Microstrip Patch Antenna

Microstrip patch antennas radiate primarily because of the fringing fields between the patch edge and the ground plane. For good antenna performance, a thick dielectric substrate having a low dielectric constant is desirable since this provides better efficiency, larger bandwidth and better radiation [5]. However, such a configuration leads to a larger antenna size. In order to design a compact Microstrip patch antenna, higher dielectric constants must be used which are less efficient and result in narrower bandwidth. Hence a compromise must be reached between antenna dimensions and antenna performance.

4.4. Waves in Microstrip

To understand the intricate mechanisms of transmission and radiation in a microstrip patch one needs to consider a current point source i.e. a Hertz Dipole that is located on top of a grounded dielectric substrate as shown in Figure 4.5. Such a source can radiate electromagnetic radiations and thus based on the transmitting wave’s direction, they fall within three distinct categories, each exhibiting different behaviors.

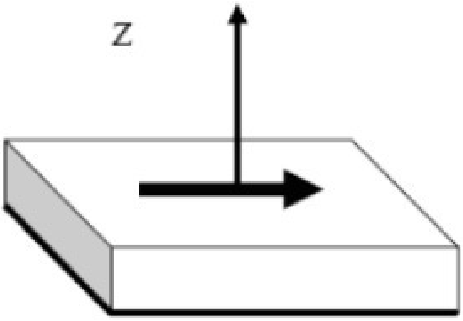

Figure 4.5: Hertz Dipole on a Microstrip Antenna

4.4.1. Surface Waves

When the waves are transmitted slightly downward, having elevation angles between $\pi/2$ radians and $\pi/2 - Arcsin(1/\sqrt{\varepsilon_r})$, meet the ground planes, it reflects them and then reflects back to meet the dielectric air boundary. This dielectric-to-air boundary also reflects back the wave, this causing Total Internal Reflection. These waves build up to meet for some particular radiation angles leading to discrete set of surface wave modes. These modes are similar to those found in metallic waveguides. From the total signal energy, a part of it goes towards surface waves. Thus this energy is wasted and does not reach the user. So it decreases the antenna efficiency due the apparent attenuation and degradation in the antenna performance is observed.

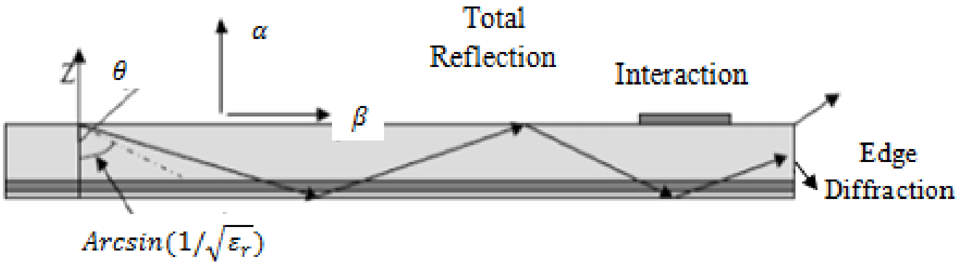

Figure 4.6: Surface Wave in Microstrip Patch

4.4.2. Leakey Waves

The waves that are directed more sharply downwards with angles between $\pi - Arcsin(1/\sqrt{\varepsilon_r})$ and π get reflected by the ground plane. But the dielectric-to-air boundary can only partially reflect it back and so the waves leak from the surface of the antenna eventually. The field amplitude increases as one moves away from the substrate since wave radiates from a point where the signal amplitude is larger.

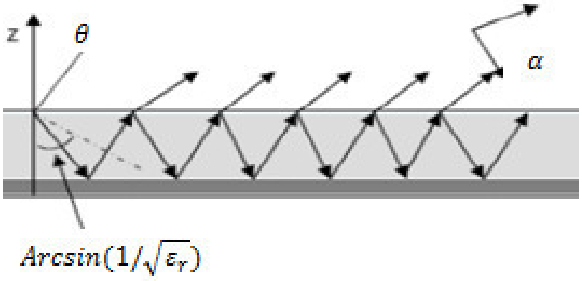

Figure 4.7: Leaky Waves on Microstrip Patch

4.4.3. Guided Waves

For feasibly fabricating printed circuit boards for a microstrip patch antenna a metal layer is locally added over the top of the surface that modifies the geometry thereby introducing an additional reflecting boundary. The guided waves have a normal mode of operation in transmission lines and circuits where the electromagnetic field is concentrated in the bulk below the upper conductor. But such a build-up of electromagnetic energy is not favorable for patch antennas that perform like resonators having limited frequency bandwidth.

4.5. Basic Characteristics

Microstrip antennas received considerable attention starting in the 1970s, although the idea of a microstrip antenna can be traced to 1953 [1] and a patent in 1955 [2]. Microstrip antennas, as shown in Figure (4.8.a), consist of a very thin ($t \ll \lambda_0$, where λ_0 is the free-space wavelength) metallic strip (patch) placed a small fraction of a wavelength ($h \ll \lambda_0$, usually $0.003\lambda_0 \leq h \leq 0.05\lambda_0$) above a ground plane. The microstrip patch is designed so its pattern maximum is normal to the patch (broadside radiator). This is accomplished by properly choosing the mode (field configuration) of excitation beneath the patch. End-fire radiation can also be accomplished by judicious mode selection [3]. For a rectangular patch, the length L of the element is usually $\lambda 0/3 < L < \lambda_0/2$. The strip (patch) and the ground plane are separated by a dielectric sheet (referred to as the substrate), as shown in (Figure 4.8.a).

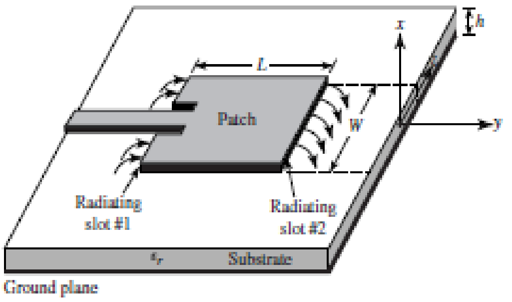

(a) Microstrip Antenna

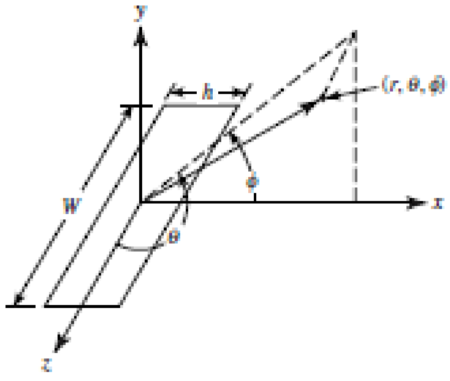

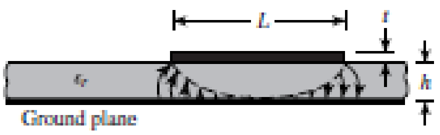

(c) Coordinate system for each radiating slot

(b) Side view

Figure 4.8: Microstrip Antenna and Coordinate System

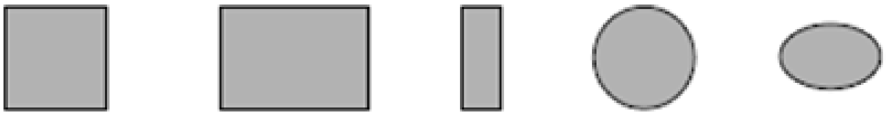

(a) Square (b)Rectangular (c)Dipole (d) Circular (e) Elliptical

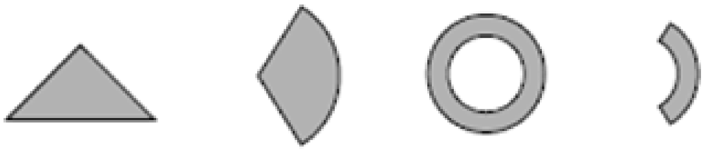

(f) Triangle (g)Disc sector (h)Circular range (i) Ring sector

Figure 4.9: Representative Shapes of Microstrip Patch Elements

There are numerous substrates that can be used for the design of microstrip antennas, and their dielectric constants are usually in the range of $2.2 \leq \varepsilon_r \leq 12$. The ones that are most desirable for good antenna performance are thick substrates whose dielectric constant is in the lower end of the range because they provide better efficiency, larger bandwidth, loosely bound fields for radiation into space, but at the expense of larger element size [4]. Thin substrates with higher dielectric constants are desirable for microwave circuitry because they require tightly bound fields to minimize undesired radiation and coupling, and lead to smaller element sizes; however, because of their greater losses, they are less efficient and have relatively smaller bandwidths [4]. Since microstrip antennas are often integrated with other microwave circuitry, a compromise has to be reached between good antenna performance and circuit design.

Often microstrip antennas are also referred to as *patch* antennas. The radiating elements and the feed lines are usually photo etched on the dielectric substrate. The radiating patch may be square, rectangular, thin strip (dipole), circular, elliptical, triangular, or any other configuration. These and others are illustrated in Figure 4.9. Square, rectangular, dipole (strip), and circular are the most common because of ease of analysis and fabrication, and their attractive radiation characteristics, especially low cross-polarization radiation. Microstrip dipoles are attractive because they inherently possess a large bandwidth and occupy less space, which makes them attractive for arrays [5], [6]. Linear and circular polarizations can be achieved with either single elements or arrays of microstrip antennas. Arrays of microstrip elements, with single or multiple feeds may also be used to introduce scanning capabilities and achieve greater directivities. These will be discussed in later sections.

4.6. Feeding Methods

The excitation of the radiating element is an essential and important factor, which requires careful consideration in designing a most appropriate antenna for a particular application. A wide variety of feed mechanisms are available, not just for coupling energy to individual elements, but also for the controlled distribution of energy to linear or planner array elements. Microstrip patch antennas can be fed using varieties of techniques. The most popular feeding techniques used are microstrip line and coaxial probe which come under direct contact schemes and again aperture coupling and proximity coupling that come under indirect contact.

4.6.1. Microstrip Line

Here the conducting strip is attached directly to one edge of the microstrip patch as shown in the figure (4.10.a) the width of this strip is smaller than the patch and is conducting in nature. Thus it provides a planar structure for feed arrangement. It provides an ease of fabrication and simple modeling. With inset feed precision can be achieved at impedance match. To obtain good impedance matching an inset cut ***(x_0)*** can be made. The length of the inset controls the impedance matching [7]. Figure (4.10.b) shows how to use microstrip as feed technique.

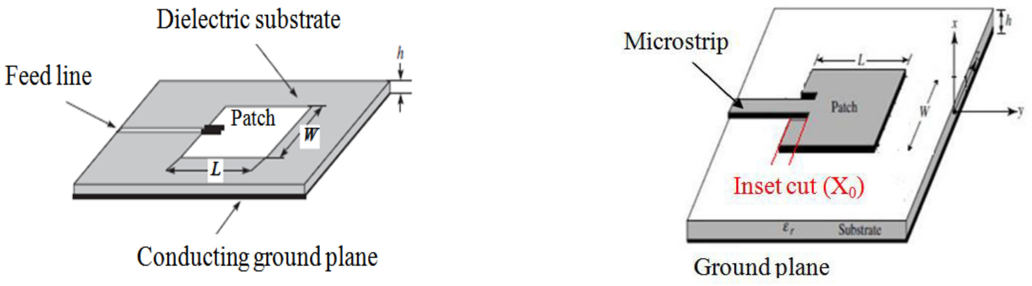

(a) Microstrip line feed *(b) Microstrip inset feed*

Figure 4.10: Microstrip Line Feeding

4.6.2. Co-axial Probe

Co-axial line feed was among the first considered and even today one of the most popular in many application of microstrip patch antenna. In co-axial line feed, the inner conductor of the coax is extends across the dielectric substrate and is connected to the patch while the outer conductor is connected to the ground plane as shown in the figure (4.11).The most important advantage of this method is that the probe can be placed at any location inside the patch to suit the impedance matching. It is easy to fabricate and has lower spurious radiation. Modeling it is difficult and its narrow bandwidth is generally not desired. Again the input impedance becomes more inductive for thicker substrates leading to matching problems.

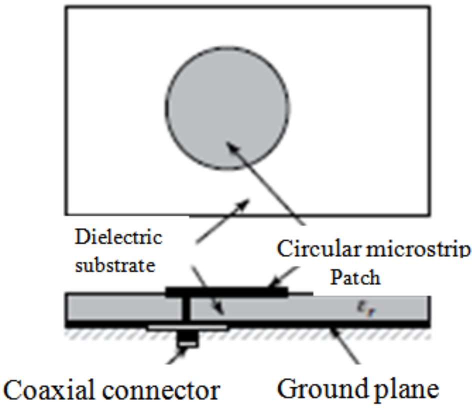

Figure 4.11: Coaxial Feeding Method

4.6.3. Aperture Coupling

In a conventional aperture coupling, the microstrip patch antenna consists of two substrate layers separated by a common ground plane as shown in Figure (4.12). The radiating microstrip layer on the top of the substrate is fed trough an aperture in the ground plane by a microstrip feed line lying on the bottom of the lower substrate. The coupling aperture is usually centered under the patch, leading to lower cross polarization due to symmetry of the configuration. The coupling is made possible through an aperture or slot in the ground plane. This slot is centered on the patch. This leads to lower cross polarization due to configuration symmetry. The shape, size and location of the slot decide the amount of coupling.

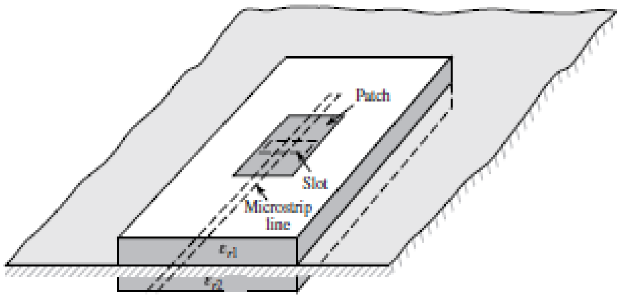

Figure 4.12: Aperture-coupled Feed

4.6.4. Proximity Coupling

In this feeding technique, the coupling of the patch and the feed line is obtained by placing the patch and the feed at different substrate levels as shown in Figure (4.13). A thin layer of high dielectric constant substrate is used to reduce the radiation from the feed lines, where as a thick layer of low dielectric constant substrate is used in the upper layer to increase the radiation of the patch [3]. The main advantage of this feed technique is that it eliminates spurious feed radiation and provides very high bandwidth (as high as 13%), due to overall increase in the thickness of the microstrip patch antenna.

Matching can be achieved by controlling the length of the feed line and the width-to-line ratio of the patch. The major disadvantage of this feed scheme is that it is difficult to fabricate because of the two dielectric layers which need proper alignment. Also, there is an increase in the overall thickness of the antenna.

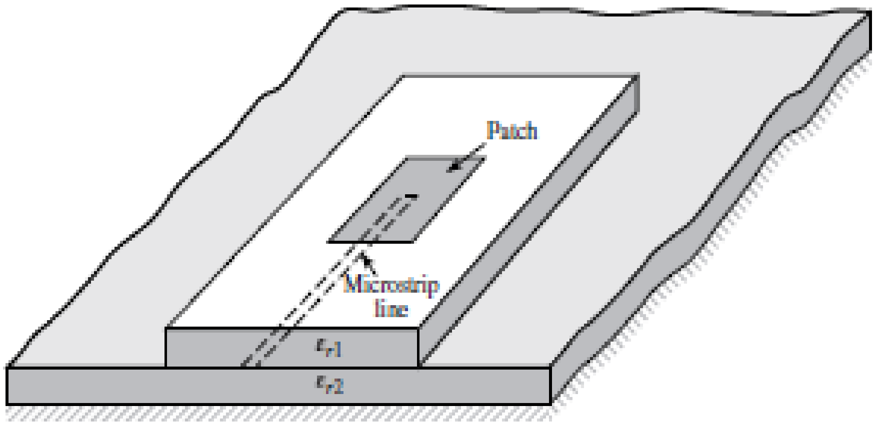

Figure 4.13: Proximity-coupled Feed

4.7. Methods of Analysis

There are many methods of analysis for microstrip antennas. The most popular models are the *transmission-line* [10], [11], *cavity,* and *full wave* (which include primarily integral equations/Moment Method) [6]. The transmission-line model is the easiest of all, it gives good physical insight, but is less accurate and it is more difficult to model coupling. Compared to the transmission-line model, the cavity model is more accurate but at the same time more complex.

4.7.1. Transmission line model

Model of the transmission line is the simplest and provides good physical interpretations, but it is only suitable for rectangular patch antennas. A rectangular microstrip antenna can be represented as an array of two radiating narrow apertures (slots), each of width W and height h, separated by a distance L, as shown in figure 4.14. Basically the transmission line model represents the microstrip antenna separated by a low-impedance Z_c transmission line of length L. Thus the microstrip radiator can be characterized by two slots separated by a transmission line, where each slot is represented by a parallel circuit of conductance (G) and susceptance (B) [12].

For the principal E-plane (xy-plane) fringing is a function of the ratio of the length of the patch L to the height h of the substrate and the relative permittivity ε_r. For L/h >> 1, fringing is reduced; however, this effect cannot be ignored because it influences the resonant frequency of the antenna. For a microstrip line, typical electric field lines are shown in figure (4.14.a). These lines result from the non homogeneous line of two dielectrics: air and substrate. Most of the lines concentrate on the substrate if W/h >> 1 and ε_r>> 1 were taking in account. Fringing makes the microstrip line look wider electrically compared to its physical dimensions. Since some of the waves travel in the substrate and in air, it is introduced an effective relative permittivity ε_{reff} , to account for fringing and the wave propagation in the line. To introduce the effective relative permittivity, the center conductor of the microstrip line (with same dimensions) and height above the ground plane is assumed to be embedded into one dielectric. This constant is defined as the relative permittivity of the uniform dielectric material, so that the line has identical electrical characteristics, particularly propagation constant, as the actual line of figure (4.14.b). For a line with air above the substrate, the effective relative permittivity has values in the range of $1 < \varepsilon_{reff} < \varepsilon_r$. For most applications where the relative permittivity of the substrate is much greater than one (ε_r>> 1), the value of ε_{reff} will be closer to the value of the actual dielectric constant ((ε_r). The effective relative permittivity is also a function of frequency.

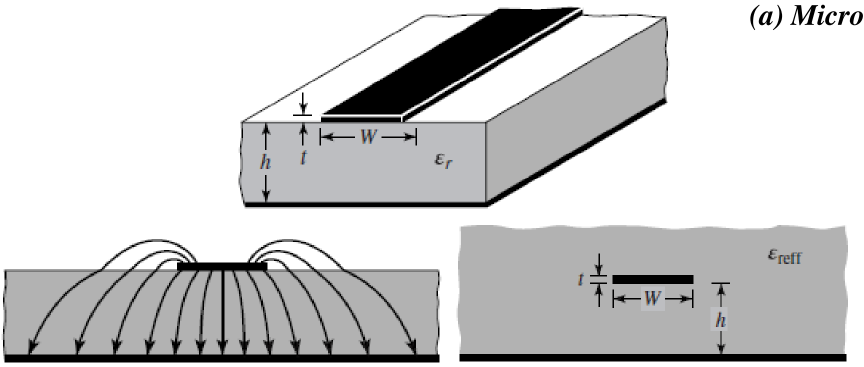

(a) Microstrip line

(b) Electric field lines *(c) Effective dielectric constant*

Figure 4.14: Electric Field Lines and Effective Dielectric Constant Geometry.

For low frequencies the effective dielectric constant is essentially constant. At intermediate frequencies its values begin to monotonically increase and eventually approach the values of the dielectric constant of the substrate. The initial values (at low frequencies) of the effective dielectric constant are referred to as the *static values*, and they are given by [3].

$$\varepsilon_{reff} = \frac{\varepsilon_r + 1}{2} + \frac{\varepsilon_r - 1}{2}\left[1 + 12\frac{h}{W}\right]^{-1/2} \tag{4.2}$$

The equation above assumes that *W/h* > 1. The effects on the effective dielectric constant can be readily examined using this equation by noting that as the frequency increases, the width of the conductor *W* decreases, bringing the value for ε_{reff} closer to ε_r. Referring back to Figure 4.15, the extensions of the length on each side of the conductor are defined as the distance *ΔL*.

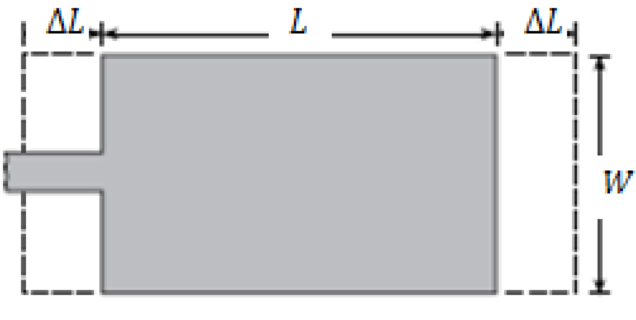

(a) Top view

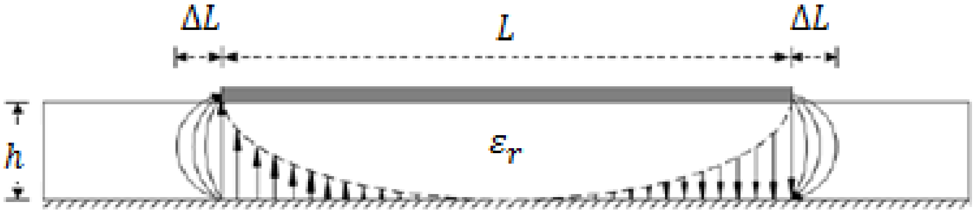

(b) Side view

Figure 4.15: Physical and Effective Lengths of Rectangular Microstrip Patch

a. Effective Length, Resonant Frequency, and Effective Width

Because of the fringing effects, electrically the patch of the microstrip antenna looks greater than its physical dimensions. For the principal E-plane (xy-plane), this is demonstrated in Figure 14.7 where the dimensions of the patch along its length have been extended on each end by a distance ΔL, which is a function of the effective dielectric constant ε_{reff} and the width-to-weight ratio (W/h). A very popular and practical approximate relation for the normalized extension of the length is [13]

$$\frac{\Delta L}{h} = 0.412 \frac{\left(\varepsilon_{reff} + 0.3\right)\left(\frac{W}{h} + 0.264\right)}{\left(\varepsilon_{reff} - 0.258\right)\left(\frac{W}{h} + 0.8\right)} \tag{4.3}$$

Since the length of the patch has been extended by ΔL on each side, the effective length of the patch is now ($L = \lambda/2$ for dominant TM_{010} mode with no fringing) $L_{eff} = L + 2\Delta L$

For the dominant TM_{010} mode, the resonant frequency of the microstrip antenna is a function of its length. Usually it is given by

$$(f_r)_{010} = \frac{1}{2L\sqrt{\varepsilon_r}\sqrt{\mu_0\varepsilon_0}} = \frac{v_0}{2L\sqrt{\varepsilon_r}} \tag{4.4}$$

Where v_0 is the speed of light in freespace. Since (4-4) does not account for fringing, it must be modified to include edge effects and should be computed using

$$(f_{rc})_{010} = \frac{1}{2L_{eff}\sqrt{\varepsilon_{reff}}\sqrt{\mu_0\varepsilon_0}} = \frac{1}{2(L + 2\Delta L)\sqrt{\varepsilon_{reff}}\sqrt{\mu_0\varepsilon_0}} = q\frac{1}{2L\sqrt{\varepsilon_r}\sqrt{\mu_0\varepsilon_0}} = q\frac{v_0}{2L\sqrt{\varepsilon_r}} \tag{4.5}$$

Where

$$q = \frac{(f_{rc})_{010}}{(f_r)_{010}} \tag{4.5.a}$$

The q factor is referred to as the fringe factor (length reduction factor). As the substrate height increases, fringing also increases and leads to larger separations between the radiating edges and lower resonant frequencies. The designed resonant frequency, based on fringing, is lower as the patch looks longer, as indicated in Figure 4.15. The resonant frequency decrease due to fringing is usually 2–6%.

b. Conductance Resonant Input Resistance and Matching Techniques

Microstrip patch antennas can be modeled as two radiating slots along the width of the patch, each of which are in turn modeled by parallel equivalent admittances Y, where each admittance has a conductance G and a susceptance B in parallel. As derived in [14], the equivalent admittance of the first slot can be found by combining the conductance and susceptance as:

$$Y_1 = G_1 + jB_1 \tag{4.6}$$

Where for a slot of finite width W

$$G_1 = \frac{W}{120\lambda_0}\left[1 - \frac{1}{24}(k_0 h)^2\right] \qquad \frac{h}{\lambda_0} < \frac{1}{10} \tag{4.6.a}$$

$$B_1 = \frac{W}{120\lambda_0}\left[1 - 0.636 ln(k_0 h)^2\right] \qquad \frac{h}{\lambda_0} < \frac{1}{10} \tag{4.6.b}$$

Where $k_0 = \frac{2\pi}{\lambda_0} = \frac{\omega}{c}$ is the freespace wave number. This result is accurate only when $W >> \lambda_0$ and $h << \lambda_0$. Now, we can return to the transmission line model where we will represent the two radiating slots with parallel equivalent admittances

slot #1 $Y_1 = G_1 + jB_1$

slot #2 $Y_2 = G_2 + jB_2$

Since slot #2 is identical to slot #1, its equivalent admittance is

$$Y_1 = Y_1 \qquad \Rightarrow \qquad G_1 = G_2 \text{ and } B_1 = B_2$$

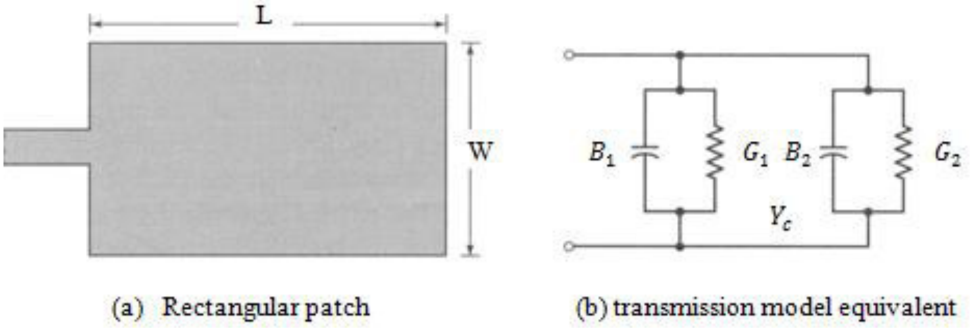

(a) Rectangular patch (b) transmission model equivalent

Figure 4.16: Rectangular Microstrip Patch and its Equivalent Circuit Transmission Model

To find the total admittance at one slot, the admittance of the second slot is transferred to the first using admittance transformation of transmission lines. As it turns out, the resulting transformed admittance of the second slot (assuming the dimensions of the patch are properly chosen) is equal to the complex conjugate of the first slot ($Y_2 = Y_1{}^*$). The transformed admittance of slot #2 becomes:

$$Y_2 = G_2 + jB_2 = G_1 - jB_1 \tag{4.7}$$

or

$$G_2 = G_1 \tag{4.7.a}$$

$$B_2 = -B_1 \tag{4.7.b}$$

Where G_1 is calculated for a slot of width W as:

$$G_1 = \frac{I_1}{120\pi^2} \tag{4.8}$$

where

$$I_1 = \int_0^{\pi} \left[\frac{\sin\left(\frac{k_0 W}{2} cos\theta\right)}{cos\theta} \right]^2 sin^3(\theta) d\theta$$

$$I_1 = -2 + \cos(X) + XS_i(X) + \frac{\sin(X)}{X} \tag{4.8.a}$$

$$X = k_0 W \tag{4.8.b}$$

Asymptotic values of (4.8) and (4.8.a) are

$$G_1 = \begin{cases} \frac{1}{90}\left(\frac{W}{\lambda_0}\right)^2 & W \ll \lambda_0 \\ \frac{1}{120}\left(\frac{W}{\lambda_0}\right) & W \gg \lambda_0 \end{cases} \tag{4.9}$$

The values of (4.9) for $W \gg \lambda_0$ are identical to those given by (4-8a) for $h \ll \lambda_0$. A plot of G as a function of $W/\lambda 0$ is shown in Figure 4.17.

Therefore the total resonant input admittance is real and is given by $Yin = Y_1 + Y_2 = 2G_1$

Assuming the slots do not affect each other, the input impedance of the antenna would just be the inverse of the input admittance. Since the total input admittance is real, the resonant input impedance is also real

$$Z_{in} = \frac{1}{Y_{in}} = R_{in} = \frac{1}{2G_1} \tag{4.10}$$

The resonant input resistance, as given by (4.10), does not take into account mutual effects between the slots. This can be accomplished by modifying (4.10) to [15]

$$R_{in} = \frac{1}{2(G_1 \pm G_{12})} \tag{4.11}$$

Where the conductance add is used for modes with odd (anti-symmetric) resonant voltage distribution beneath the patch and between the slots while subtract when there is used for modes with even (symmetric) resonant voltage distribution.

The mutual conductance G_{12} can be calculated in terms of the far-field with the following equation [15]:

$$G_{12} = \frac{1}{120\pi^2}\int_0^{\pi}\left[\frac{\sin\left(\frac{k_0W}{2}cos\theta\right)}{cos\theta}\right]^2 J_0(k_0Lsin\theta)\,sin^3(\theta)d\theta \tag{4.12}$$

Where J_o is the Bessel function of the first kind of order zero. The mutual conductance is typically much smaller than the conductance at each slot.

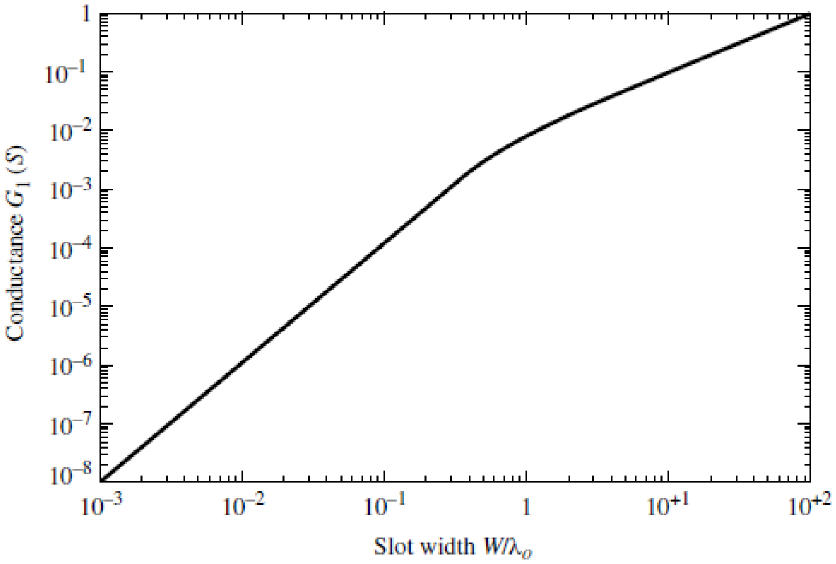

Figure 4.17: Slot Conductances as a Function of Slot Width

Typically, R_{in} is in the range of 150 to 300 Ω. To match a feeding microstrip transmission line to this impedance would require it to be very narrow; moreover, 50 Ω lines are a de facto standard in the RF circuit world.

- R_{in} can be decreased by increasing W. This action is limited to $W/L < 2$ because the aperture efficiency of the slots drops for $W/L > 2$.
- An alternative is to use an inset or recessed microstrip feed (see Figure 4.18**).** This works because the voltage is a maximum and the current a minimum at the edges of the patch, leading to large impedance values. As we go into the patch, the voltage

drops and the current increases, leading to smaller impedances until we reach the midpoint of the patch.

This technique can be used effectively to match the patch antenna using a microstrip line feed whose characteristic impedance is given by [3]

$$Z_c = \begin{cases} \dfrac{60}{\sqrt{\varepsilon_{r,eff}}} \ln\left[\dfrac{8h}{W_0} + \dfrac{W_0}{4h}\right] & \dfrac{W_0}{h} \leq 1 \\ \dfrac{\eta_0}{\sqrt{\varepsilon_{r,eff}\left[\dfrac{W_0}{h} + 1.393 + 0.667 ln\left(\dfrac{W_0}{h} + 1.444\right)\right]}} & \dfrac{W_0}{h} > 1 \end{cases} \tag{4.13}$$

Where W_0 is the width of the microstrip line. However, the resonant input resistance can be changed by using an inset feed, recessed a distance y_0 from slot #1, as shown in (Figure 4.18).

The input resistance of the inset feed is given by:

$$R_{in}(y_0) \cong \frac{1}{2(G_1 \pm G_{12})}\left[cos^2\left(\frac{\pi}{L}y_0\right) + \frac{G_1^2 + B_1^2}{{Y_{c,feed}}^2} sin^2\left(\frac{\pi}{L}y_0\right) - \frac{B_1}{Y_{c,feed}} \sin\left(\frac{2\pi}{L}y_0\right)\right] \tag{4.14}$$

Where $Y_c = 1/Z_c$ and Zc is the characteristic impedance of the feeding microstrip transmission line (width W_0). Note: the inset distance y_0 must be in the range ($0 < y_0 < L/2$). If $G_1/Y_c << 1$ and $B_1/Y_c << 1$ (the typical case since the width of the feeding microstrip is much less than that of the rectangular patch), the input resistance of the inset feed becomes

$$\begin{aligned} R_{in}(y = y_0) &= \frac{1}{2(C_1 \pm C_{12})} cos^2 \frac{\pi}{L} y_0 \\ &= R_{in}(y = 0) cos^2 \frac{\pi}{L} y_0 \end{aligned} \tag{4.14.a}$$

A plot of the normalized value of (4.14-a) is shown in Figure (4.14.b).

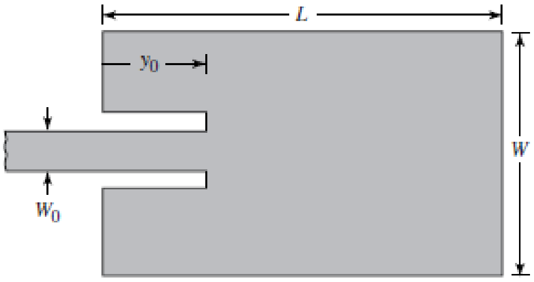

(a) Recessed microstrip-line feed

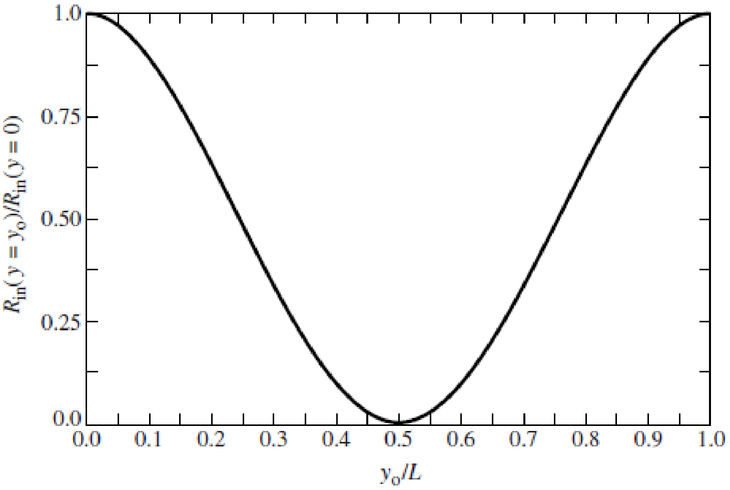

(b) Normalized input resistance

Figure 4.18: Recessed Microstrip-line Feed and Variation of Normalized Input Resistance

If we set R_{in} (y_0) equal to the characteristic impedance of the feeding transmission line Z_c and note that R_{in} (0) → R_{in} in this case, we can solve for the inset length

$$y_0 = \frac{L}{\pi}\cos^{-1}\left(\sqrt{\frac{R_{in}(y_0)}{R_{in}(0)}}\right) = \frac{L}{\pi}\cos^{-1}\left(\sqrt{\frac{Z_{C,feed}}{R_{in}}}\right) \tag{4.14.b}$$

The notch width n on either side of the inset feed introduces some capacitance. This can impact the resonant frequency slightly (≈1%) and can change the input impedance. Also, the feeding microstrip transmission line will perturb the radiation from slot #1 (i.e., Y_1 changes) which argues for minimizing n. As a starting point, select the notch width n to fall in the range $0.2W_0 < n < 0.5W_0$. To get truly accurate results, a full-wave numerical model of the antenna should be run after using the design based on the transmission line model to get accurate lengths and widths. A similar process applies if a coaxial probe feed is used, i.e., the input resistance can be decreased by moving the coaxial probe in from the edge of the patch.

4.7.2. Cavity model

The simplest analytical method to use in microstrip patch antenna is transmission line model. But transmission line model have numerous disadvantages like, it is useful only for patch antenna of rectangular shape, it ignores field variations along the radiating edge and is not adaptable to inclusion of the field. The cavity model for microstrip patch antennas [37, 38] offers considerable improvement over the transmission line model.

The cavity model of the MSA assumes that the patch and the ground plane are electric walls, and the periphery of the patch is a magnetic wall. [17] The fields in the resulting cavity are assumed to be the fields of the antenna and Huygens's Principle is applied at the magnetic wall to determine radiation. To determine the fields within the cavity, a solution of an inhomogeneous wave equation is required. Therefore, the Magnetic Cavity Model is most easily applied when the method of separation of variables is applicable. [The rectangular and circular patch MSAs is symmetric in two planes. Therefore, the cavity model is convenient in both cases. For arbitrarily shaped patches, application of the Method of Moments to the integral equation is necessary to avoid tedious calculations [17]**.**

The magnetic cavity model works best for a thin substrate. In this case the TM modes are superior in the cavity. The cavity model makes the following assumptions:

1. The electric field is z-directed, and the magnetic field has only a transverse component in the cavity.
2. Since the substrate is assumed thin, the fields in the cavity do not vary with z.
3. The tangential component of the magnetic field is negligible at the edge of the patch.
4. The existence of a fringing field can be accounted for by slightly extending the edges of the patch.

The cavity model provides a mathematical solution for the electric and magnetic fields of a microstrip antenna and hence helps to have an insight into the radiation mechanism of the antenna. The solutions are found by representing the antenna using a dielectrically loaded cavity. Although it models the substrate material, but it considers that the material is truncated at the patch edges. Both the patch and ground plane are represented as perfect electric conductors and edges of the substrate are suitably modeled as perfectly conducting magnetic walls. In the figure below one can see the charge distribution as visible not only in the upper and lower surfaces of the patch but also at the bottom of the ground plane. It is controlled by both attractive and repulsive mechanisms by which the charges move in a particular manner causing flow of current at the top and bottom of the patch.

- ✓ The attractive mechanism is between the corresponding opposite charges on the bottom side of the patch and the ground plane, which tends to maintain the charge concentration on the bottom of the patch.
- ✓ The repulsive mechanism is between like charges on the bottom surface of the patch, which tends to push some charges from the bottom of the patch, around its edges, to its top surface.

The movement of these charges creates corresponding current densities J_b and J_t, at the bottom and top surfaces of the patch, respectively, as shown in Figure (4.19).

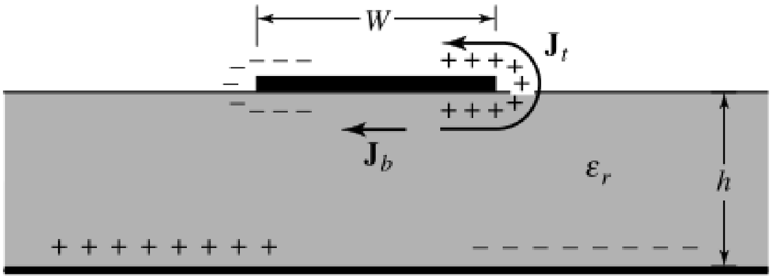

Figure 4.19: Charge Distribution and Current Density Creation on the Microstrip Patch

The cavity model assumes that the height to width ratio (i.e. height of substrate and width of the patch) is very small and as a result of this the attractive mechanism dominates and causes most of the charge concentration and the current to be below the patch surface. A small amount of current flows around the edges of the patch to its top surface. However, this current flow decreases as the height-to-width ratio decreases. The current flow to the top would be zero, which ideally would not create any tangential, magnetic field components to the edges of the patch. Hence, the four sidewalls could be modeled as perfectly magnetic conducting surfaces. This implies that the magnetic fields and the electric field distribution beneath the patch would not be disturbed. However, in practice, a finite width to height ratio would be there and this would not make the tangential magnetic fields to be completely zero, but they being very small, the side walls could be approximated to be perfectly magnetic conducting [16].

Since the walls of the cavity, as well as the material within it are lossless, the cavity would not radiate and its input impedance would be purely reactive. Hence, in order to account for radiation, a loss mechanism has to be introduced; this was taken into account by the radiation resistance R_r and a loss resistance R_L. These two resistances allow the input impedance to be complex and for its function to have complex poles; the imaginary poles representing, through R_r and R_L, the radiation and conduction-dielectric losses. A lossy cavity would now represent an antenna and the loss is taken into account by the effective loss tangent δ_{eff} which is given as:

$$\delta_{eff} = \frac{1}{Q_T} \tag{4.15}$$

1) Q_T : is the total antenna quality factor and has been expressed by [33] in the form:

$$\frac{1}{Q_T} = \frac{1}{Q_d} + \frac{1}{Q_c} + \frac{1}{Q_r} \tag{4.16}$$

2) Q_d represents the quality factor of the dielectric and is given as :

$$Q_d = \frac{\omega_r W_T}{P_d} = \frac{1}{tan\delta} \tag{4.17}$$

Where ω_r is the angular resonant frequency, W_T is the total energy stored in the patch at resonance, P_d is the dielectric loss, and $tan\delta$ is the loss tangent of the dielectric.

3) Q_c represents the quality factor of the conductor and is given as :

$$Q_c = \frac{\omega_r W_T}{P_c} = \frac{h}{\Delta} \tag{4.18}$$

Where P_c is the conductor loss, h is the height of the substrate, and Δ is the skin depth of the conductor.

4) Q_r : represents the quality factor for radiation and is given as:

$$Q_r = \frac{\omega_r W_T}{P_r} \tag{4.19}$$

Where P_r is the power radiated from the patch.

Substituting equations (4.16), (4.17), (4.18) and (4.19) in equation (4.16) gives:

$$\delta_{eff} = tan\delta + \frac{\Delta}{h} + \frac{P_r}{\omega_r W_T} \tag{4.20}$$

Thus, equation (4.20) describes the total effective loss tangent for the microstrip patch antenna. The microstrip patch antennas have inherent disadvantages such as their limited impedance band width and inherently narrow band axial-ratio [2], which hinders their use in wide band systems. Hence, in order to complement this shortcoming in terms of the bulky feeding structure, a feeding network adopting partially substrate integrated waveguide (SIW) technology has been introduced to replace the conventional metallic waveguide [6]. Recently, substrate-integrated waveguide (SIW) [9] has attracted much attention and has been widely used in wireless communication systems because of its light weight, low profile, high Q factor, and easy integration to planar circuits.

4.8. Substrate Integrated Waveguides

As the most mature and popular SIC structure, an SIW is synthesized by two rows of metalized vias or metalized slot trenches embedded in a dielectric substrate with the conductor claddings on the top and bottom broad walls, as shown in Figure 4.20 It can be considered a dielectric-filled rectangular waveguide [42].

4.8.1. SIW design rules

Substrate Integrated Waveguide (SIW) technology has provided a new approach in the design of microwave and millimeter-wave systems. It is replacing the traditional hybrid systems which are combination of both waveguides and stripline circuits. The substrate integrated waveguide (SIW) is sort of a guided transmission line just like a dielectric filled rectangular waveguide. The only difference is that the metallic walls are replaced by two parallel arrays of conductive via holes as shown in Figure 4.20 [42].

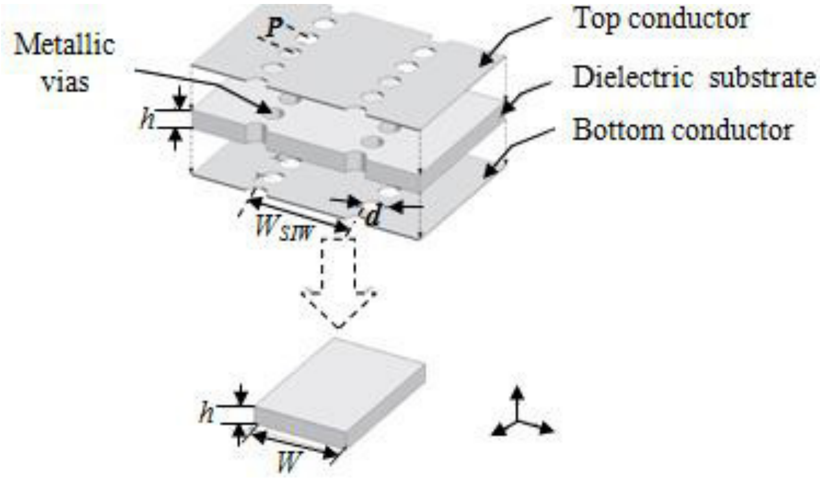

Figure 4.20: Configuration of an SIW

In fact, this periodic structure is more complicated for analysis than the conventional waveguide as the edge of the fictitious electrical side wall is subject to several parameters, especially the post diameter *d*. There are several methods to find out the effective width of the SIWs, *W*, either by using simulation tools or empirical equations. As introduced in [41], the effective width can be obtained by:

$$W = W_{SIW} - \frac{d^2}{0.95 \times P} \tag{4.21}$$

In the above equation parameters W_{SIW}; d and p are the key parameters of SIW design:

- ✓ The spacing between the vias "P" also called pitch,
- ✓ Diameter of vias *"d",*
- ✓ Central distance between via arrays "W_{SIW}" also called integrated waveguide width, and the equivalent SIW width "W_{SIW}".

The SIW parameters should be designed carefully. The pitch *"P"* and diameter *"d"* control the radiation loss and return loss, while the integrated waveguide width "W" determine the cut-off frequency and propagation constant of the fundamental mode [19]. There are two design rules related to the pitch and via diameter as given by [20]:

$$d < \frac{\lambda_g}{5} \tag{4.22}$$

$$P \leq 2d \tag{4.23}$$

$$d/W_{SIW} \leq 0.4 \tag{4.24}$$

Where λ_g is the guide wavelength in the SIW.

Yan et al. reported experimental formula is given by [38], such that:

$$W = W_{SIW}\left(\xi_1 + \frac{\xi_2}{\frac{P}{d} + \frac{\xi_1 + \xi_2 - \xi_3}{\xi_3 - \xi_1}}\right) \tag{4.25}$$

Where:

$$\xi_1 = 1.0198 + \frac{0.3465}{\frac{W_{SIW}}{P} - 1.0684} \tag{4.25.a}$$

$$\xi_2 = -0.1183 - \frac{1.2729}{\frac{W_{SIW}}{P} - 1.2010} \tag{4.25.b}$$

$$\xi_3 = 1.0082 - \frac{0.9163}{\frac{W_{SIW}}{P} + 0.2152} \tag{4.25.c}$$

In 2005, an interesting study of the leakage characteristics of SIW has been carried out by Xu et al. based on a numerical multimode calibration procedure [37].it was demonstrated that a dominant mode cut-off frequency is same as TE_{10} mode of rectangular waveguide. A TE_{10} like mode in the SIW has similar dispersion characteristics to the mode of a dielectric filled rectangular waveguide with an equivalent width. This equivalent width is the effective width of the SIW [41], approximated as follows:

$$W = W_{SIW} - 1.08\frac{d^2}{P} + 0.1\frac{d^2}{W_{SIW}} \tag{4.26}$$

As known, the cut-off frequency of a conventional rectangular air filled waveguide depends on its dimensions (*a, b*).

$$f_c = \frac{c}{2\pi\sqrt{\varepsilon_r}}\sqrt{\left(\frac{m\pi}{a}\right)^2 + \left(\frac{n\pi}{b}\right)^2} \tag{4.27}$$

In previous equation, in a case of a SIW structure, the *b* parameter, representing the height of the side walls, is equal to the thickness of the substrate, *h*, which is much smaller than the SIW width, *w*. The cut-off frequency of the SIW depends only on the SIW width and the dielectric substrate relative permittivity, ε_r [17], as follows:

$$f_c = \frac{c}{2\pi\sqrt{\varepsilon_r}}\left(W_{SIW} - \frac{d^2}{0.95 \times P}\right)^{-1} \tag{4.28}$$

Where "*c*" is the speed of light in vacuum and "ε_r" is the relative permittivity of dielectric material. Characteristic impedance (***50 Ω)*** often defines the input and output ports of a system or test equipment. Typically, the characteristic impedance of an SIW does not equal (***50 Ω)*** and is smaller than the characteristic impedance of a conventional Rectangular (RWG) due to the small h/W_{siw} for SIWs [40]. An approximation to the SIW characteristic impedance is:

$$Z_{0,SIW} = \frac{2h}{W_{SIW}}\frac{\eta_0}{\sqrt{\varepsilon_r}}\left(1 - \left(\frac{f_c}{f}\right)^2\right)^{-0.5} \quad \text{For mode } TE_{10} \tag{4.29}$$

Where η_0 is the intrinsic impedance of the free space. f_c is the cutoff frequency, and f is the operation frequency.

Common ***50 Ω*** input/output ports for planar topology are microstrip lines. The width a microstrip line *W* for desired characteristic impedance Z_0 on a substrate of thickness *t* and permittivity $\varepsilon = \varepsilon_0\varepsilon_r$ can be estimated from the first-order approximation [39]:

$$\frac{W}{h} = \begin{cases} \dfrac{8e^{A}}{e^{2A}-2} & for\,\dfrac{W}{h} < 1 \\ \dfrac{2}{\pi}\left[B - 1 - \ln(2B-1) + \dfrac{\varepsilon_r - 1}{2\varepsilon_r}\left\{\ln\left(B - 1 + 0.39 - \dfrac{0.61}{\varepsilon_r}\right)\right\}\right] & for\,\dfrac{W}{h} > 1 \end{cases} \tag{4.30}$$

Where:

$$A = \frac{Z_0}{60}\sqrt{\frac{\varepsilon_r + 1}{2\varepsilon_r} + \frac{\varepsilon_r - 1}{\varepsilon_r + 1}}\left(0.23 + \frac{0.11}{\varepsilon_r}\right)$$

$$B = \frac{377\pi}{2Z_0\sqrt{\varepsilon_r}}$$

In order to integrate SIWs and other planar circuits, various SIW-planar structure transitions are developed. The first transition was proposed for SIW-microstrip line connection [24]. The design of the SIW-microstrip transition is straightforward, which simply makes use of a tapered microstrip line to excite the waveguide mode, as shown in Figure (4.21).

The width of the ***50 Ω*** microstrip line W_{50} and tapered microstrip section at the SIW opening W_{tap} can be estimated by substituting $Z_0 = 50\ \Omega$ and (4.29) into (4.30), respectively. The length of the tapered microstrip section L_{tap} should be long enough to provide a smooth transition between the quasi-TEM microstrip line modes to the TE_{10} SIW mode and can be approximated by kπ. Once W_{50}, W_{tap}, and L_{tap} have been predicted, full-wave simulation refines these values for optimal performance.

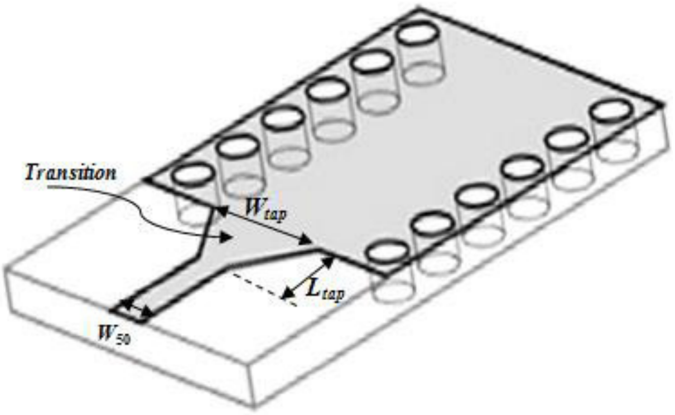

Figure 4.21: Tapered Transition between a 50 Ω Microstrip Line and SIW

4.8.2. Guided wave and Leaky wave Regions of Operation

Most of the properties of conventional rectangular waveguide such as propagation characteristics, high quality-factor and high power-handling remains in SIW structures. Some design rules are proposed in [17], in order to preserve this analogy between SIW and non-planar metallic waveguide. As revealed in Figure 4.22, main design parameters are the diameter d of the vias, the distance $\boldsymbol{p}$ between the adjacent vias and the distance w between the two rows of vias. Furthermore, the substrate thickness and the permittivity of the dielectric are the parameters to be chosen before the SIW design according to the relevant usage and purpose of the design.

When constructing a SIW which guides the incoming wave like a rectangular waveguide, first step is the decision for the via placement. With the help of [43], a guided wave region on the $\boldsymbol{d}$ vs $\boldsymbol{p}$ graph can be determined. As indicated in the study, in order vias not to overlap, the distances between the vias should be greater than the via diameter. This criterion is illustrated on $\boldsymbol{d}$ vs $\boldsymbol{p}$ graph with $\boldsymbol{d=p}$ line and lower side of this line becomes forbidden region. Since the distance $\boldsymbol{p}$ mainly determines the leakage loss, it should be kept as small as possible. Lower limit for $\boldsymbol{p}$ is a fabrication concern as well as an issue about the robustness of the thin structure. Via diameter d has also impact on leakage loss and it should be optimized with $\boldsymbol{p}$. It is shown in [43] that the ratio $\boldsymbol{p/d}$ has a direct relation with leakage loss and should be used as a design parameter. As $\boldsymbol{p/d}$ ratio increases, some of the energy inside the SIW leaks through the vias and SIW no longer guides the wave. Calculating the amount of leakage loss with the help of the formulation in [43], the point where the leakage is insignificant with respect to dielectric and conductor losses can be determined and appropriate $\boldsymbol{p/d}$ ratio can be obtained. According to the study, both dielectric and conductor losses are in the range of 10^{-4} and 10^{-3} for regular SIW applications. Thus, upper limit of $\boldsymbol{p/d}$ ratio is determined as 2 and illustrated in Figure 4.22 [43].

-

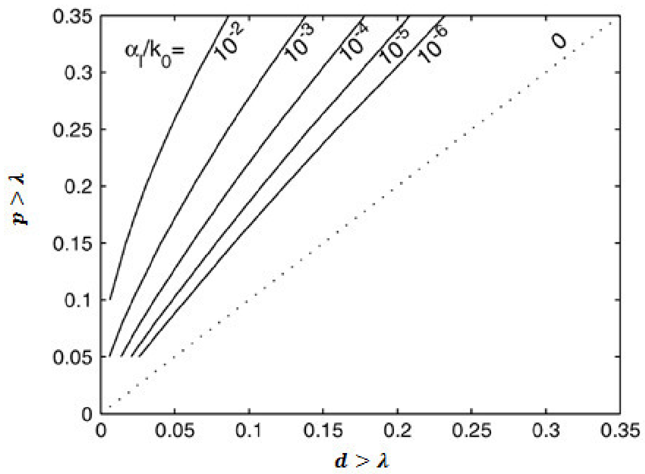

Figure 4.22: Leakage loss curves from 10^{-6} to 10^{-2} Np/rad with respect to distance between the vias and their diameters normalized with the λ_c [3].

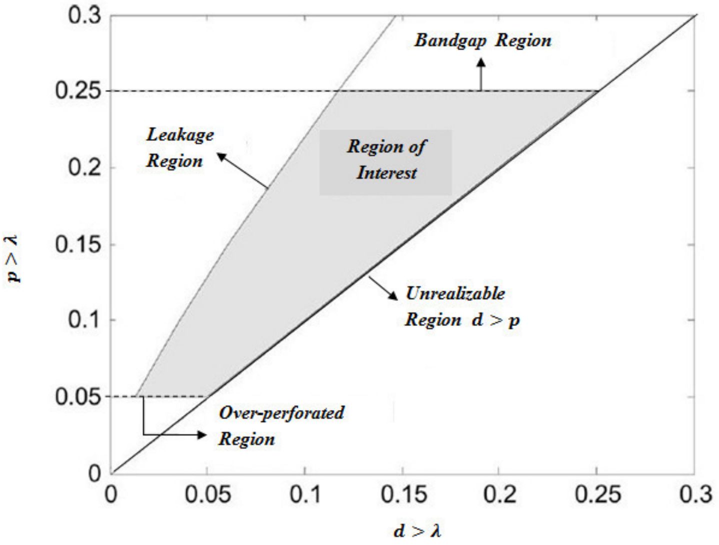

Figure 4.23: Suitable region for SIW design parameters [3].

There are two other restrictions for upper and lower limit for p as indicated in [43]. These four design limits for p and d compose a region that defines the suitable area for SIW design as illustrated in Figure 4.23. As long as the design parameters p and d are in this region, leakage loss due to the discontinuity on the via arrays is insignificant with respect to conductor and dielectric losses.

4.8.3. Circular Substrate Integrated Waveguide Cavity

A circular waveguide cavity (Figure 4.24) is an air-filled or dielectric-filled metal cylinder with both ends covered by metal. Resonant frequency of the cavity (TE and TM modes) is determined by Equation (4.31) and (4.32), where c the speed of light in free space, μ_r is the relative permeability, and ε_r is the relative permittivity, P_{nm} is the root of Bessel functions of first kind, and P'_{nm} is the root of the derivative of Bessel function of first kind. Subscript letters n, m, l indicates the cavity mode, and they can only take on integer values [25].

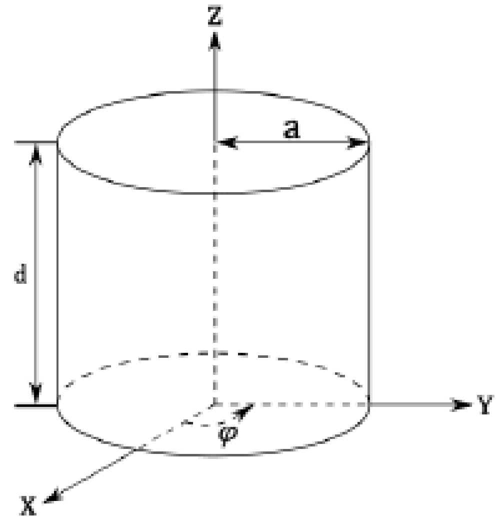

Figure 4.24: Circular Waveguide Cavity

$$TE_{nml}\ \text{Mode}\quad f_{nml}=\frac{c}{2\pi\sqrt{\mu_r\varepsilon_r}}\sqrt{\left(\frac{P'_{nm}}{a}\right)^2+\left(\frac{l\pi}{d}\right)^2} \tag{4.31}$$

$$TM_{nml}\ \text{Mode}\quad f_{nml}=\frac{c}{2\pi\sqrt{\mu_r\varepsilon_r}}\sqrt{\left(\frac{P_{nm}}{a}\right)^2+\left(\frac{l\pi}{d}\right)^2} \tag{4.32}$$

Circular Substrate Integrated Waveguide (SIW) Cavity is usually built on a thin Printed Circuit Board (PCB) substrate (e.g. 62mil). Instead of having solid cylindrical metal wall, circular SIW cavity uses via posts like the ones in Figure (4.25). Depending on the resonance mode in the cavity, Equation (4.31) and (4.32) are valid if spacing, s, is much smaller than one wavelength, λ, (e.g. $P < \lambda$ 10). The spacing between the via posts is acting like a slot in the metal wall, if the slots are parallel to the direction of current flow inside the cavity, RF energy is contained in the circular SIW cavity, and only minor cavity mode perturbation occurs[10].

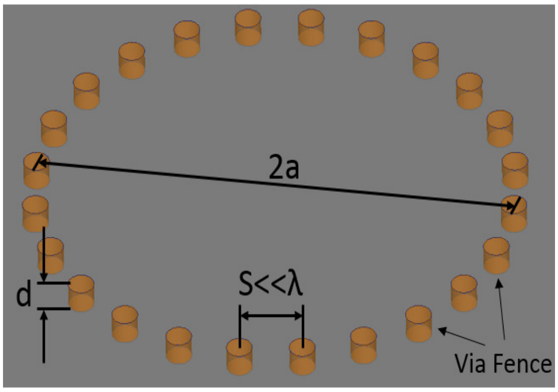

Figure 4.25: Example of Circular SIW Cavity

4.9. Neural Network Algorithm

The previous two parts covered the antenna design process and SIW technology, along with microwave circuit theory considerations for transmission-line design. However, it is important to note that even a single antenna element can produce massive amounts of data when it comes to properly characterizing the antenna’s response to changes in biasing parameters. For the case of a microstrip antenna, where the antenna system itself would produce multiple operating states, the amount of data increases even further. To remedy this problem, artificial neural networks (ANNs) are presented as a viable alternative. Neural networks have recently gained attention as a fast, accurate and flexible tool for RF/microwave modeling, simulation and design. A tutorial has been published in [34] recently. From the view point of application, ANN may be considered as using a model to train formula. This trained formula can be used to do the interpolation and extrapolation in certain ranges as well [16].

Neural networks are information processing systems with their design inspired by the studies of the ability of the human brain to learn from observations and to generalize by abstraction [16].ANNs are used to generate a mapping between some input data and some required output. The basic neuron model includes inputs, weights, a summation, an activation function, and an output as shown in Figure 4.26 [26]. The inputs can come from other neurons or external inputs and are multiplied by adjustable weights corresponding to biological synapses. The weights are determined by using a training algorithm. The weighted inputs are summed, and an activation function determines the output of the neuron. The most common activation functions are linear (ADALINE), binary, sigmoid, hyperbolic tangent, or perceptrons [27]. The output of the neuron varies between zero and one. The simple neuron model is used as a building block for the more complex nonlinear ANN.

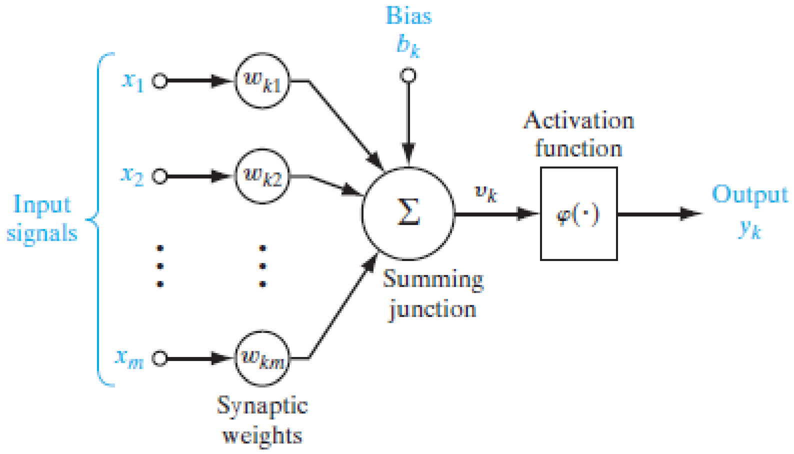

Figure 4.26: Generalized Neuron Model

Figure 4.27 depicts a portion of the multilayer perceptron. Two kinds of signals are identified in this network [28]:

1. *Function Signals.* A function signal is an input signal (stimulus) that comes in at the input end of the network, propagates forward (neuron by neuron) through the network, and emerges at the output end of the network as an output signal. We refer to such a signal as a “function signal” for two reasons. First, it is presumed to perform a useful function at the output of the network. Second, at each neuron of the network through which a function signal passes, the signal is calculated as a function of the inputs and associated weights applied to that neuron. The function signal is also referred to as the input signal.
2. *Error Signals.* An error signal originates at an output neuron of the network and propagates backward (layer by layer) through the network. To it as an “error signal” because its computation by every neuron of the network involves an error-dependent function in one form or another.

The output neurons constitute the output layer of the network. The remaining neurons constitute hidden layers of the network.

Each hidden or output neuron of a multilayer perceptron is designed to perform two computations [28]:

1. The computation of the function signal appearing at the output of each neuron, which is expressed as a continuous nonlinear function of the input signal and synaptic weights associated with that neuron;

2. The computation of an estimate of the gradient vector (i.e., the gradients of the error surface with respect to the weights connected to the inputs of a neuron), which is needed for the backward pass through the network.

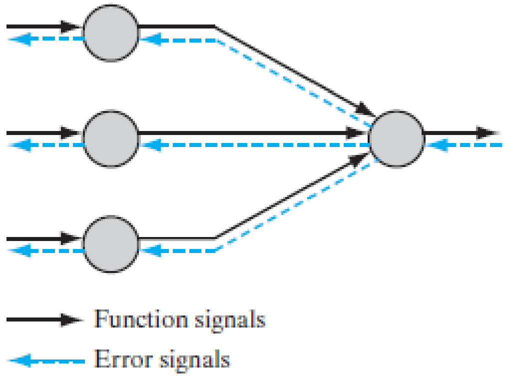

Figure 4.27: Illustration of the directions of two basic signal flows in a multilayer perception: forward propagation of function signals and back propagation of error signals

The mathematical model shown in figure 4.28 is calculated as:

$$y_k = \varphi(w_{k1}x_1 + w_{k2}x_2 + \ldots\ldots\ldots + w_{km}x_m + b_k) \tag{4.33}$$

$$y_k = \varphi(w_k x + b_k)$$

$$u_k = \sum_{i=1}^{n} w_{ki}x_i \tag{4.34}$$

Where x_i and w_{ki} are the input and weight vectors respectively. The McCulloch and Pitts model was the first model introduces in 1943, required proper selection of weight values from the user to function. This model was not efficient since the selection of weights was done on an ad-hoc (trial and error) basis, and the weights would become fixed after the selection. So this model had lack of adaptability. Then in 1958, Frank Rosenblatt introduced the perceptron model, which included a learning algorithm, allowing the initial weight values to be randomly selected, then adapted through the learning algorithm based on expected values of the output given specific input values. Later in 1960 adaline model was introduced by Windrow and Hoff, a similar model (adaline), short for adaptive linear element. Even though the perceptron and adaline models share commonalities, they also have marked differences.

Perceptron model used unit step function as the activation function, wich produce output 1 or 0 based on the obtained value of y_k from (4.34) as:

$$u_k \begin{cases} 0, & u_k < 0 \\ 1, & u_k > 0 \end{cases} \tag{4.35}$$

On the other hand, the adaline model uses the signum function as the activation function, producing a different output:

$$u_k \begin{cases} -1, & u_k < 0 \\ 1, & u_k > 0 \end{cases} \tag{4.36}$$

In order to adapt the initial weights to more desirable values, first an error E is calculated based on the target output values. For the perceptron model, the error is calculated using the output y_k:

$$E = d - y_k \tag{4.37}$$

For the adaline model, the error is calculated using the sum of the weighted inputs u_k:

$$E = d - u_k \tag{4.38}$$

After the error calculation the weights are adjusted in same manner for the both networks

$$w_{ki}[t+1] = w_{ki}[t] + \alpha E x_i \tag{4.39}$$

Where $w_{ki}[t+1]$ is the weight vector for the current iteration, $w_{ki}[t]$ the weight vector from for the previous iteration (the initial assigned weight values in the case of the first iteration), and α is the user-defined learning rate, which can be any constant value greater than zero. The error process is repeated till the value of error become zero or reaches user defined value or maximum number if iteration is reached. The user defined value for error is set to very small value approaching to zero. The utility of perceptron and adaline model was limited to linearly separable problems, as the complexity between input and output data samples increases these networks failed to converge to an acceptable solution. This problem was overcome by adding additional layers of the neurons to the networks lead to introduction of MLP (multi layered perceptron) and madalines in place of adalines. Here only a feed forward multilayer perceptron (MLP) neural network, pictorially represented in Figure 4.28 is introduced, which is suitable for device and circuit modeling [16], [29].

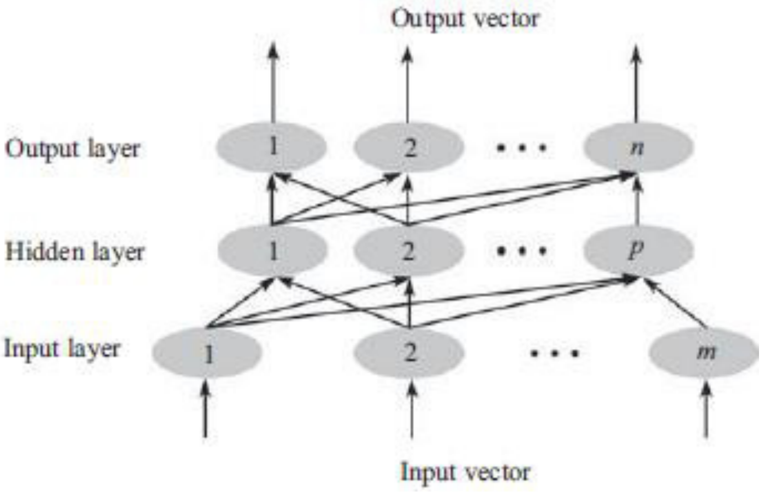

Figure 4.28: Three-layer Neural Networks

A feed-forward multilayer neural network can be described as a mathematical tool which is capable of nonlinear mapping in higher dimension. It has been theoretically proven that a multilayer neural network with at least one hidden layer can model arbitrarily complex nonlinear input/output relation ship $y_k = F(x)$. Typically, a three-layer neural network is employed to model a nonlinear relationship.

The input space, $\mathbf{x}$ of dimension m, is mapped to the n-dimension output space represented as a layer of n neurons, through a hidden layer. This hidden layer has a fixed number of neurons, p, which can vary from problem to problem as will be discussed in the following. The outputs of any given neurons are the weighted linear combination of the outputs of all the neurons in the previous layer reflected off a nonlinear transfer function, the most commonly employed being the sigmoid.

This function must be always normalized and differentiable which is:

$$F(x) = \frac{1}{1 + e^{-x}} \tag{4.40}$$

4.9.1. Feed-forward (Input Signal)

Mathematically, the neural network can be described as the mapping of a set of input vectors **x**, whose i^{th} sample is

$$\mathbf{X}_i = (x_1, x_2, \cdots, x_m)$$

To the corresponding output vector

$$\mathbf{y}_k = (y_{k1}, y_{k2}, \cdots, y_{kn})$$

Through a system of weighting factors and biases, which are defined as *wih*, *bh*, for $i = 1, 2,..,m$ and $h = 1, 2, \cdots, p$ and v_{hj}, *cj*, for $h = 1, 2, \cdots, p$ and $j = 1, 2, \cdots, n$, such that the *n* outputs are:

$$y_k = F(u_k) = \frac{1}{1 + e^{-u_k}} \tag{4.41}$$

where: (4.42)

$$u_k = \sum_{i=1}^{n} w_{ki} x_i$$

Here, $f(u)$ is the sigmoid transfer function and y_k is the output of the k^{th} neuron in the hidden layer. It is seen that **x** is related to **y** by a set of sample data. If the set of samples **x***k*, $k = 1, 2, \cdots, N$, is chosen such that it is representative of the entire Input/output (I/O) space, then the objective mapping function *F* is learned by the neural network.

4.9.2. Back Propagation (Output Error)

The main objective in neural model development is to find an optimal set of weight parameters ***w***, such that $y=y(x,w)$ closely represents (approximates) the original problem behavior. This is achieved through a process called training data is presented to the neural network. The training data are pairs of (x_k, dk), $k=1, 2... P$ where d_k is the desired outputs of the neural model for inputs x_k and P is the total number of training samples. During training the neural network performance is evaluated by computing the difference between actual NN outputs and desired outputs for all the training samples. This is also known as the error. The efficiency of training [16] depends on the following training parameters:

- ✓ *Number of hidden neurons q:* Deciding on the size of the hidden layer is a critical part of the design of a neural network model. Once the number of hidden layers is determined, the number of neurons in the hidden layer will determine the structure of the network. Unfortunately, there are no established methods to determine the appropriate number of hidden neurons required for a given problem. In general, a large number of hidden neurons are required to model complicated relationship. But too many may result in an over trained network that tends to memorize rather than to generalize from data.
- ✓ *Learning rate η:* This parameter is an important training parameter representing the step size of the error convergence process. A small value of it affords stability but increases training time, while a large value of it decreases the stability of the training

process. The step size can be a small fixed constant set by the user, for example, the user set $\eta = 0.1$ and step size remains 0.1 throughout. The step size can also be adaptive during training, that is, the user initially sets $\eta = 0.1$ and later η can be changed during training. For example, η may be set to $\eta = \eta/\gamma$, $\gamma = 0.8$, if *Et* decrease steadily during the recent epochs and equals to $\eta = \eta\gamma$, $\gamma = 0.8$ otherwise.

- ✓ *Momentum α:* The momentum term is used to prevent the training algorithm from settling in local minimum. It also increases the speed of convergence. It is usually set to a positive value less than 1. Similarly α can also be adaptive during the training through the learning rate adaptation γ.
- ✓ *Training tolerance:* The critical learning parameter determines the accuracy of the neural network outputs. A small training tolerance usually increases learning accuracy but can result in less generalization capability as well as longer training time.
- ✓ *Learning rate adaptation γ:* An adaptive learning rate decreases training time by keeping the learning rate reasonably high while insuring stability.

4.10. Results and discussion

4.10.1. Simulation Software

When designing millimeter wave antenna systems, one wants to predict the real behavior of the device as accurately as possible. A good simulation tool that takes into account all high frequency effects is thus indispensable. For all designs that follow High Frequency Structure Simulator (HFSS) simulation software is used. ANSYS HFSS software is a simulation tool for 3-D full-wave electromagnetic field simulation. It is used for the design of high-frequency and high-speed component design. HFSS offers multiple state-of the-art solver technologies based on either the finite element or integral equation method. HFSS is mainly used in particular to calculate S parameters, resonance frequencies and electromagnetic fields. HFSS relies on the finite element method (FEM). This method performs the following tasks:

- ✓ Space discretization: HFSS is an interactive simulator that meshes elementally to overcome the difficulties encountered with 3D structures with unusual shapes and curves.
- ✓ Solving Maxwell equations (differential equations) in a number of discrete points
- ✓ Consideration of boundary conditions

4.10.2. Proposed antennas geometry and design procedures

In this parts two circular-polarized patch antennas which have feeding structures such as a substrate integrated waveguide (SIW), a tulip shape resonator and two different feeding transitions, are proposed and experimentally investigated in terms of electrical performances, including reflection coefficients, optimized parameter values of frequencies and radiation patterns.

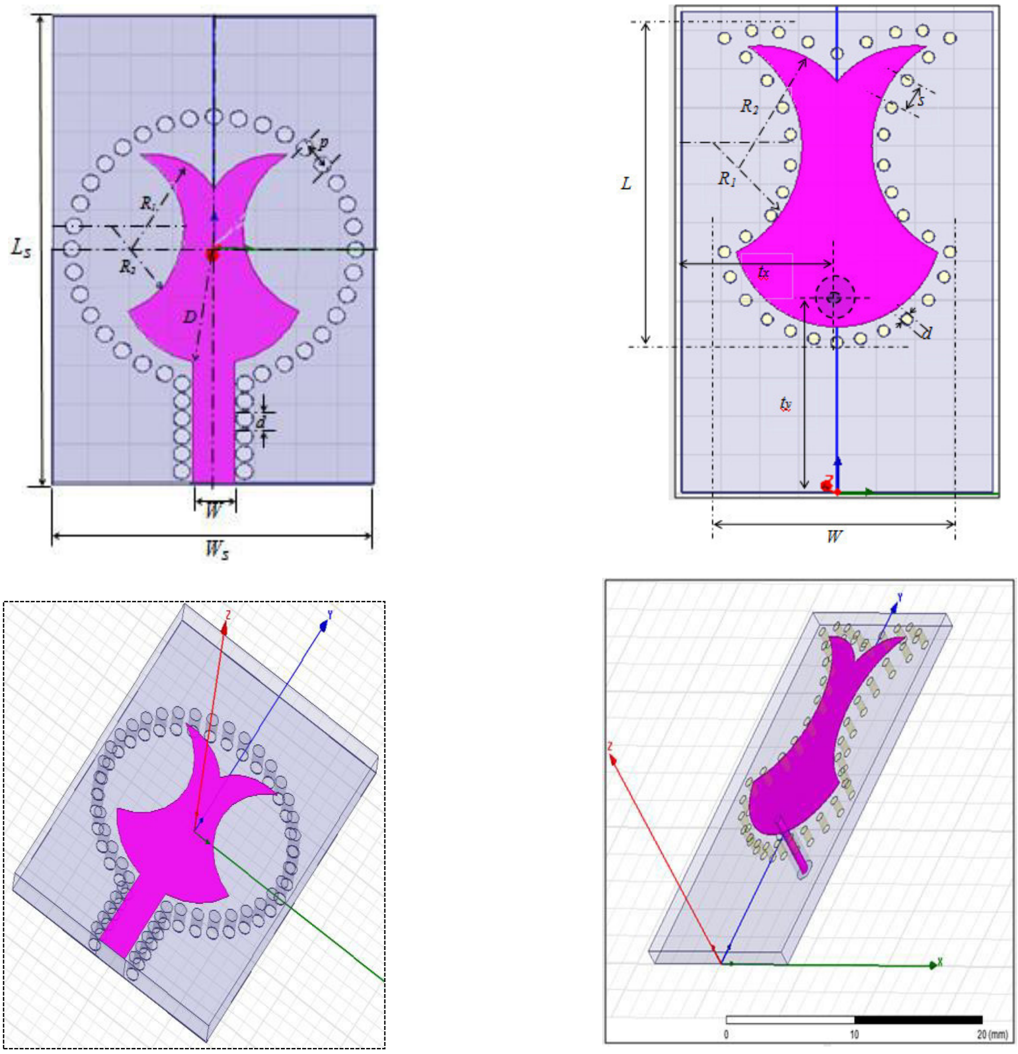

(a) (b)

Figure.4.29: Proposed antenna geometry using (a) microstrip-to-SIW transition and (b) coax-to-SIW transition

The first step in the design of the circular SIW tulip-shape patch antenna test structures uses the Eigen mode to set the desired resonance frequency as the starting point of the patch which gives good radiation yields, from this we use the High Frequency Structure Simulator (HFSS) simulation software.

In the second step, Artificial Neural Network (ANN) techniques [30] have been recognized as an alternative way to create a model instead of fine model where the results of simulation are not available.

The proposed antenna geometry shown in Figure 4.29 is mainly composed of two topologies. The first one is a SIW antenna feed by microstrip-to-SIW transition is shown in Figure (4.29(a)) and the second is a SIW antenna feed by coax-to-SIW transition is shown in Figure (4.29(b)). The entire antennas structures have been designed by employing an FR4_epoxy substrate as having a relative permittivity of 4.4 and loss tangent of 0.02.

4.10.3. Artificial neural network modeling of SIW antenna

Geometrical parameters of the two proposed SIW cavity resonator antenna has been optimized by introducing an ANN model using MATLAB programming, in order to enhance the accuracy of the existing structure through an automated data training process having the ability to capture multi-dimensional arbitrary nonlinear relationships in a very fast way to finally provide an efficient high-level antenna design.

Table 4.1: Proposed antenna and optimized parameters values according to the transition type

Parameters	***Values (mm)***			
	microstrip-to-SIW transition		Coax-to-SIW transition.	
W	*14*			
L	*14*			
d	*0.6*			
P	*1.4*			
W_1	*0.9*			
Initial values	$R_1=3.9$		$R_1=3.9$	
	$R_2=4.6$		$R_2=4.6$	
	$D=4.6$		$D=4.6$	
	$h=1.588$		$h=0.95$	
	Microstrip line	$W=2.2$	*Coax-position*	$\begin{cases} t_x = 8.2 \\ t_y = 10.2 \end{cases}$
Final parameters optimized	*Parameters*	*Values (mm)*	*Parameters*	*Values (mm)*
	W	*2.3431*	R_1	*5.221*
	R_1	*3.3903*	R_2	*6.911*
	R_2	*4.6785*	t_x	*9.603*
	D	*4.3434*	t_y	*9.622*
			d	*0.501*

In this work, a Multilayer Perceptron (MLP) network structure has been adopted for the calculation of the dimensions of the SIW tulip-shape antenna using for training standard, back propagation algorithms [31], [32], in which neurons are grouped into three layers divided into:

first layer which consists of input neurons, output layer which contains the output neurons, and remaining layer presenting the hidden layer. In the last sections a Figure 4.32 and Figure 4.34 illustrates the MLP-ANN architecture used for the simulation and optimization of the both antenna. The final optimized parameter values according to the transition types are listed in Table 4.1.

a. Results and discussion of circular SIW antenna (microstrip-to-SIW transition)

a.1. Data generation

The tulip shape SIW antenna are made up of a rectangular ground plane with dimensions width (W) and length (L) over a ground plane with a substrate thickness h having dielectric constant. The total occupying area including transition region is ($W \times L = 15.4 \times 24\ mm^2$). Accordingly, a set of antenna geometric specifications is proposed for the analysis and optimization by calculating the SIW parameters basing on equations mentioned above, and using HFSS-based Eigen mode solution to determine the remaining antenna parameters including both microstrip line and tulip-shaped patch parameters. Details of geometric configuration and dimensions of the circular SIW antenna proposed for the study are illustrated in figure (4.29.(a)) and table (4.1).

a.2. Network architecture and training

In this work, a Multilayer perceptron (MLP) network structure has been adopted for the calculation of the resonant frequencies and return losses using for training standard, back propagation algorithms [31, 34], in which neurons are grouped into three layers divided into: first layer which consists of input neurons, output layer which contains the output neurons, and remaining layer presenting the hidden layer. In the network there are four input neurons in the input layer, 20 hidden neurons in the hidden layer and four output neurons in the output layer. The inputs of the network are cut off frequencies f_D and f_U and less Return losses (S_{11D} and S_{11U}). The various outputs to the network are coordinates of both dimensions of the tulip shape D, R_1, R_2, and the width of microstrip feed line W. Figure (4.30) illustrates the MLP-ANN architecture used for the simulation and optimization.

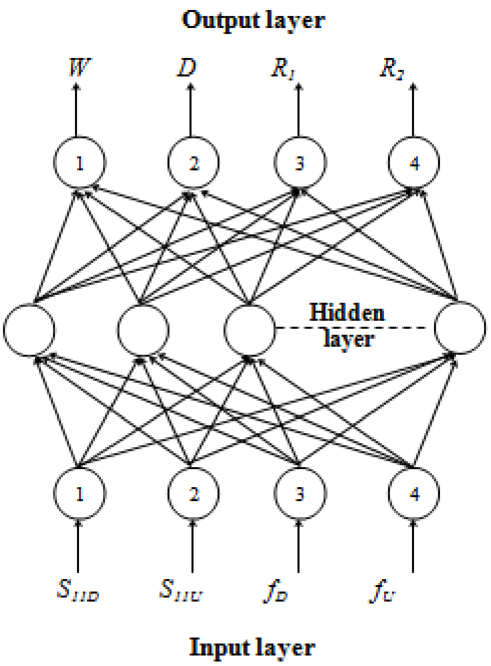

Figure 4.30: MLP-ANN architecture selected for the optimization of microstrip-to-SIW

The increments of frequencies (f_D and f_U) and return losses (S_{11D} and S_{11U}) are 0.01GHz, 0.01 GHz, (0.05dB) and (0.05dB) respectively. In order to get the response under the following specification: the frequency f_D varies from 15.5GHz to17.5GHz; the frequency f_U varies from 19.0GHz to 20.0GHz; the return loss S_{11D} varies from (-22dB to -18dB) and S_{11U} varies from (-32dB to -28dB).

After having defined the antenna's input and output variables as a first stage known as neurons process, training data are generated using multi-HFSS simulations to provide a neural network model that will be incorporated into the simulator again for fast and accurate optimization as a second stage of the overall device called network training process. In this work, Backpropagation algorithm is used for training the proposed neural model and a comparative evaluation of relative performance is carried out for estimating different dimensions of tulip shape antenna. In order to evaluate the performance of proposed MLPFFBP-ANN based model for the design of tulip shape antenna, simulation results are obtained using EM3D Simulator (HFSS) and generated 144 input-output training patterns and 20 inputs-output test patterns to validate the model. Likewise, the training error is automatically calculated, and network weights are being updated after each cycle in order to minimize the training error. The training algorithm most suitable is train LM. The error goal is (1.2×10^{-5}) and learning rate is 0.02.The aim of the network training process is then to teach the network to produce valid response for inputs from outside the training data. This ability is simply called generalization [35].

a.3. Optimization results

Figure 4.31 shows the simulated return losses of the proposed antenna design for *Ku* and *K* frequency bands. It is clearly observed that selected geometric parameters have not presented a good performance in terms of low return losses. These parameters are then optimized through developing an accurate ANN model. Circular SIW antenna's parameters outputted by trained artificial neural network have been implemented by HFSS electromagnetic software to compare antenna responses with those initially provided. Both of these results are shown in figure (4.32) from (a) to (d).

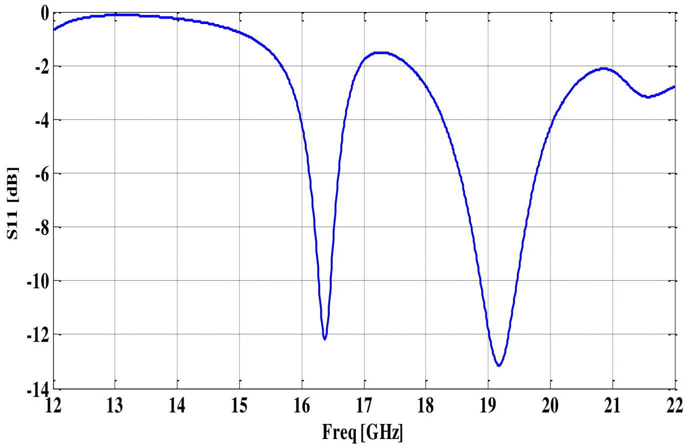

Figure 4.31: Return loss graph in dual-band Ku/K bands of proposed circular SIW antenna
Initial parameters (mm): W = 2.2, D = 4.4, R_1= 3.6, R_2 = 4.4.

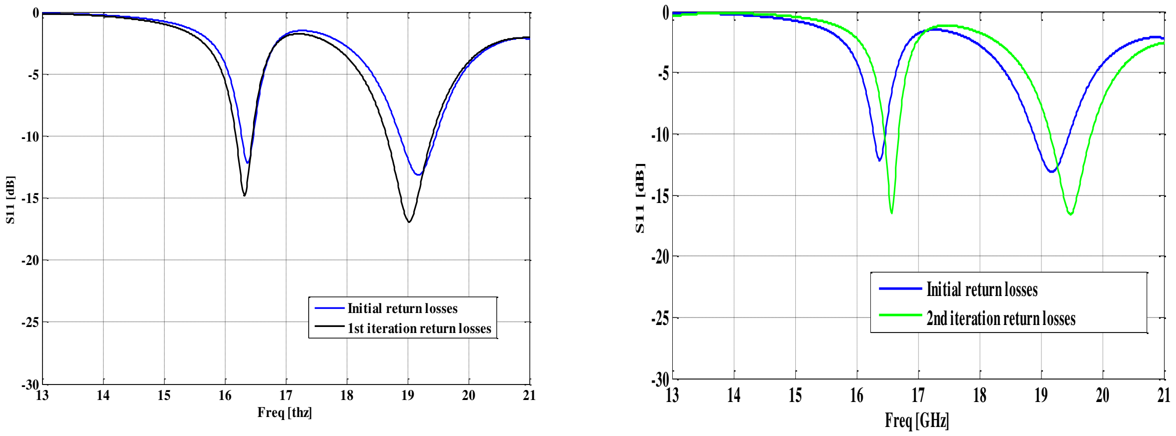

(a) 1st iteration, ANN Output parameters (mm): W = 2.0152, D = 4.6050, R_1= 3.9011, R_2 = 4.6041.

(b) 2nd iteration, ANN Output parameters (mm): W = 2.2017, D = 4.7393, R_1= 4.3348, R_2 = 4.8440.

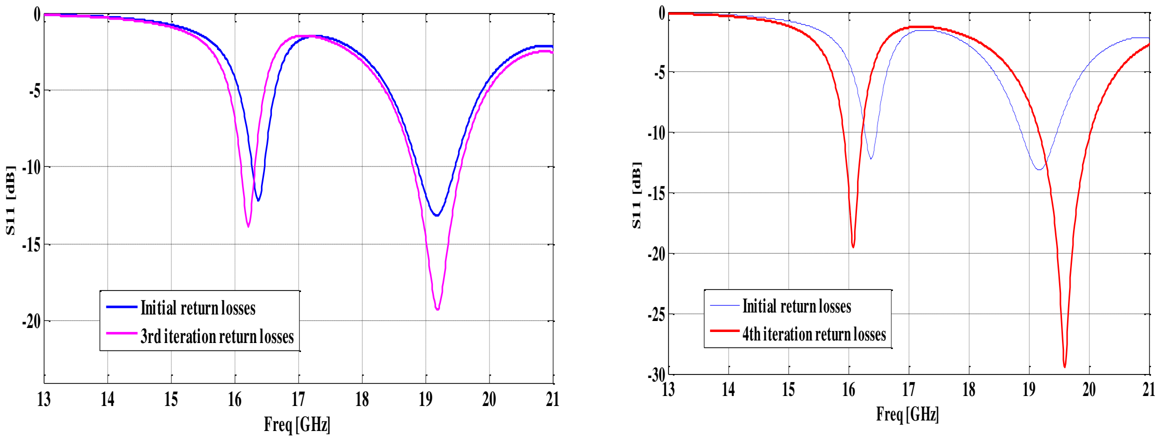

(c) 3rd iteration ANN Output parameters (mm): W = 2.1800,D = 4.6814, R_1= 3.9634, R_2 = 4.6923.

(d) 4th iteration, ANN Output parameters (mm): W = 2.3431,D = 4.3434, R_1= 3.3903, R_2 = 4.6785.

Figure 4.32: Return loss graph in dual-band Ku/K bands of circular SIW antenna based ANN modelling

The results of optimization show that the proposed structure comes with very low return losses over the entire bands of resonance. The antenna has been found to resonate at 16.10 GHz with a return loss of -19.74dB and also at 19.81 GHz with a return loss of -29.54dB (Figure 4.32. (d)). The values obtained from ANNs are very close to target values. The difference between the ANN outputs against target is measured in terms of performance which is very close to set goal to be achieved in testing for better performance of the network model.

The results obtained from testing samples in ANN model are very useful for obtaining at resonance bands of the proposed circular SIW antenna very low return losses. This indicates that ANN model selected for the optimization offers the advantage of superior computational ability to provide an optimal circular SIW antenna geometry due to its high degree of efficiency and interconnectivity for solving complex problems. The final geometric configuration reported from the fourth iteration and used in developing the circular SIW antenna design after optimization is shown in Table (4.1).

b. Results and discussion of SIW antenna (coax-to-SIW transition)

b.1. Data generation

The geometry of the proposed SIW antenna as shown in Figure (4.29.(b)), is mainly composed of walls presented by two rows of metalized via holes with center-to-center distance called (W_{SIW}), embedded into a dielectric substrate and by the top and the bottom metallization of the dielectric substrate.

The structure can be modeled by a conventional cylindrical cavity resonator, mainly defined by its horizontal length (*W*), vertical length (*L*) designed to determine the guide's cut-off frequency and modes of excitation. The diameter (*d*) and walls center-to-center distance (*s*) of via holes can be adjusted while maintaining the conditions of the set of equations (4.43) [36].

$$\begin{cases} d/s \le 0.5 \\ d/\lambda_0 \le 0.1 \end{cases} \tag{4.43}$$

To guarantee a minimum leakage of power through the sidewall of the cavity where (λ_0) denote free space wavelength. To design SIW resonance cavity, the dimensions can be chosen according to desired resonance frequency (f_{mnp}) of (TE_{mnp}) mode that can be calculated according to [37]:

$$f_{mnp} = \frac{c}{2\pi\sqrt{\varepsilon_r \mu_r}} \sqrt{\left(\frac{P_{nm}}{R}\right)^2 + \left(\frac{p\pi}{h}\right)^2} \tag{4.44}$$

In which (R: R_1 or R_2) is the radius of the circular SIW cavity, (μ_r and ε_r) are relative permeability and permittivity of the filling material used for the cavity, and (m, n and p) refer to the numbers of variations in the standing wave pattern. The (P_{nm}) represents the corresponding root of *Bessel* function and (c) stands for light speed in free space. For the TM_{010} (P_{01} = 2.4049) and TM_{110} (P_{11} = 3.832) modes, the resonance frequencies are 10.8 GHz and 14.8 GHz, which belong to X band and K band of frequencies. Note that not every high-order mode can be excited to radiate, which depends on the positions and types of the feeding and radiator. A pseudo cylindrical cavity ($W*L$ = 12.2*16.4mm^2) has been considered. Vias diameter is of (d = 0.6mm) and their separation (center to center) is of (s =P= 0.8mm).

Accordingly, a set of antenna geometric specifications is proposed for the analysis and optimization, after having determining the SIW parameters, and calculating the remaining antenna parameters including both coaxial feeding and tulip patch parameters by using HFSS-based Eigen mode solution. Details of geometric configuration of the SIW cavity resonator antenna proposed for the study, is illustrated in Table 4.2. The centre of the patch is taken as the origin and the feed point location is given by the co-ordinates (t_x and t_y) from the origin. The feed point must be located at that point on the tulip-shaped patch, where the input impedance is 50 ohms for the specified resonant frequency.

Table 4.2: Geometrical parameters of the proposed dual band coaxial-fed SIW cavity resonator antenna

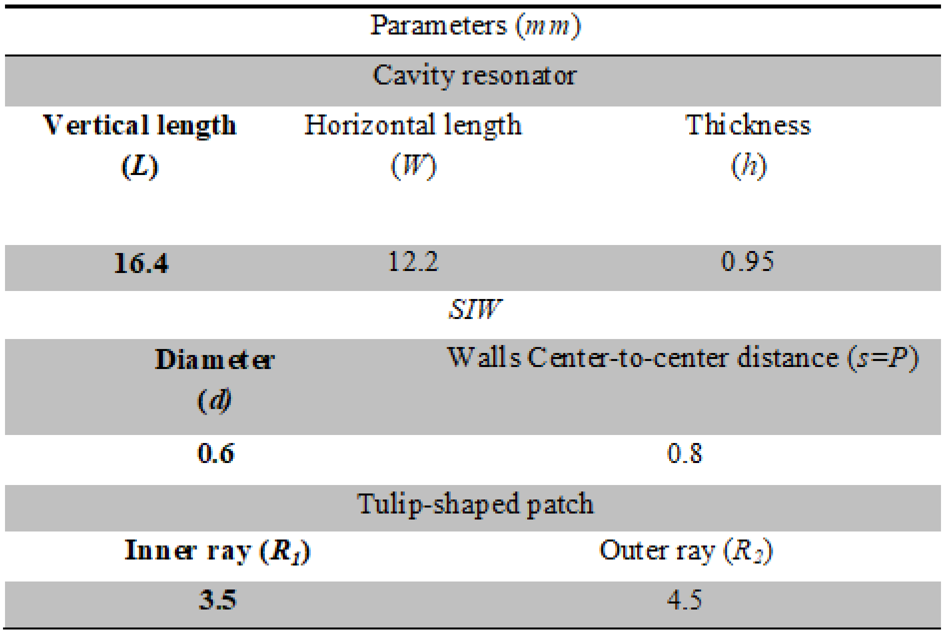

<table>
<tr><th colspan="3">Parameters (mm)</th></tr>
<tr><td colspan="3">Cavity resonator</td></tr>
<tr><td>Vertical length (L)</td><td>Horizontal length (W)</td><td>Thickness (h)</td></tr>
<tr><td>16.4</td><td>12.2</td><td>0.95</td></tr>
<tr><td colspan="3"><i>SIW</i></td></tr>
<tr><td>Diameter (d)</td><td colspan="2">Walls Center-to-center distance ($s=P$)</td></tr>
<tr><td>0.6</td><td colspan="2">0.8</td></tr>
<tr><td colspan="3">Tulip-shaped patch</td></tr>
<tr><td>Inner ray (R_1)</td><td colspan="2">Outer ray (R_2)</td></tr>
<tr><td>3.5</td><td colspan="2">4.5</td></tr>
</table>

Hence, a trial and error method is used to locate the feed point. For different locations of the feed point coordinate (t_x and t_y) , the return loss is recorded and that feed point is selected as the optimum one where the return loss is less than or equal to -10 dB. Hence the data for training and testing the developed neural network is generated by simulating the antenna designs for different values of patch dimensions and feed point coordinates in EM3D Simulator.

b.2. Network architecture and training

Geometrical parameters of the proposed SIW cavity resonator antenna has been optimized by introducing an ANN model using MATLAB programming [11], in order to enhance the accuracy of the existing structure through an automated data training process having the ability to capture multi-dimensional arbitrary nonlinear relationships in a very fast way to finally provide an efficient high-level antenna design. this work, a Multilayer Perceptron (MLP) network structure has been adopted for the calculation of the resonant frequencies and return losses using for training standard, back propagation algorithms [12, 13], in which neurons are grouped into three layers divided into: first layer which consists of input neurons, output layer which contains the output neurons, and remaining layer presenting the hidden layer. Figure (4.33) illustrates the MLP-ANN architecture used for the simulation and optimization. For the considered SIW Cavity resonator antenna, the developed neural model is designed to produce output parameters divided into R_1, R_2, t_x, t_y

and *d*, having down return loss S_{11D}, high return loss S_{11U}, down resonance frequency f_D and upper resonance frequency f_D as inputs.

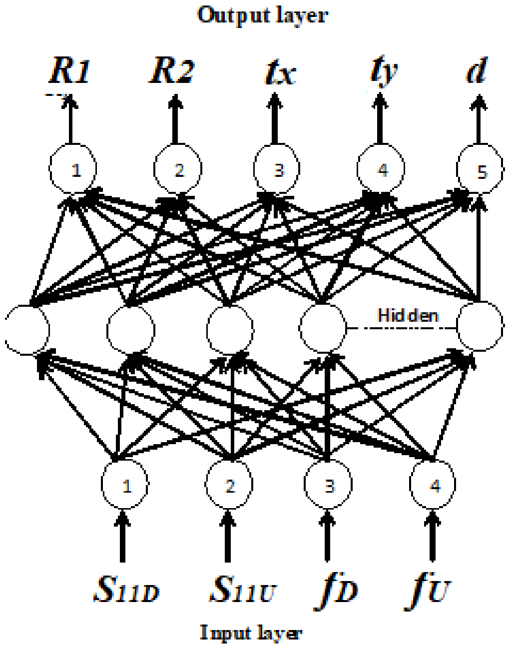

Figure 4.33: MLP-ANN architecture selected for the optimization of coax-to-SIW transition.

The network is estimating the feed positions, inner ray (R_1), outer ray (R_2) and diameter of SIW (d) at the output for the specified inputs i.e. return losses (S_{11D} and S_{11U}) and resonating frequencies (f_D and f_U) of the SIW Cavity resonator tulip shape antenna, antenna in the specified training domain. The full set of training input samples i.e. 220 patterns pass through the neural network to compute the least squared error function MSE, for a given set of input data, say x_k , k = 1, 2, · · · , N, whose corresponding output set is d_k, if the neural network predicts the output to be y_k , the batch-mode back propagation error E is defined as

$$E = \text{MSE} = \sum_{k=1}^{N} E_k = \frac{1}{N}\sum_{k=1}^{N}\left[\frac{1}{2}\sum_{j=1}^{N}(y_{kj} - d_{kj})^2\right] \tag{4.45}$$

Where E_k presents the individual mean-squared error of the k^{th} sample. *E* is the error to be minimized during training. For the calculation of feed point of the patch for the specified training algorithm and tansig as a transfer function. It is mentioned earlier that MLPFFBP is realized with back propagation algorithm it is the LM(Levenberg –Marquardt) training algorithm giving the training performance with minimum MSE in least number of epochs to the maximum accuracy. To evaluate the accuracy of the developed MLPFFBP ANN model,

the parameters of the neural network used in the Back-propagation training algorithm for optimization are presented in Table 4.3.

Table 4.3: ANN parameters of the dual band coaxial-fed SIW cavity resonator antenna

Parameters	Optimized values				
Training algorithm	Feed-forward MLP/ Backpropagation				
Number of neurons	Number of intput Neurons	4			
	Number of output Neurons	5			
	Number of hidden Neurons	15			
Transfer function	Hidden levels	Sigmoïde			
Inputs definition		***f_D (GHz)***	***S_{11D} (dB)***	***f_U (GHz)***	***S_{11U} (dB)***
	Max	11.4	-25	14.4	-30
	Min	10.6	-30	15.2	-35
Learning rate	0.02				
The number of epochs	1000				

b.3. Optimization procedure

Before starting the optimization process, the first step consists to determine an equivalent circuit presenting the antenna design parameters (X_{EM}), based on the multi-HFSS simulation results. Then, the optimization operation will be launched aiming to determine a new antenna configuration providing simulation results close to the target design specifications (X_{target}) initially proposed. The key technique used in this adaptive CAT procedure is explained in details in Table (4.4) which summarizes the acceptable errors, and Figure 4.34 which presents the set of the design process steps.

Table 4.4: Adaptive CAT variables for the optimization process

Sr N°	**ANN inputs**			
	***f_D* (GHz)**	**$S_{11(D)}$ (dB)**	***f_U* (GHz)**	**$S_{11(U)}$ (dB)**
1	10.6	-31	14.2	-32
2	10.7	-33	14.4	-30
3	10.75	-30	14.7	-35
4	10.8	-35	14.8	-28
5	11	-25	14.98	-30
6	11.2	-30	15	-32

Sr N°	**ANN outputs**				
	R_1 (mm)	R_2 (mm)	t_x (mm)		d (mm)
1	4.999	6.149	7.989	9.998	0.280
2	5.201	6.334	8.235	9.093	0.387
3	5.193	6.608	8.242	10.207	0.246
4	4.991	6.299	8.223	9.227	0.522

5	5.199	6.532	9.452	9.213	0.489
6	5.221	6.511	9.603	9.622	0.501

Sr N°	HFSS outputs			
	f_D (GHz)	$S_{11(D)}$ (dB)	f_U (GHz)	$S_{11(U)}$ (dB)
1	10.4	-17.28	14	-13.86
2	10.5	-14.48	14.1	-16.65
3	10.5	-13.75	14.3	-15.98
4	10.6	-19.18	14.2	-13.67
5	10.7	-13.14	14.8	-15.27
6	10.84	-15.18	14.82	-29.83

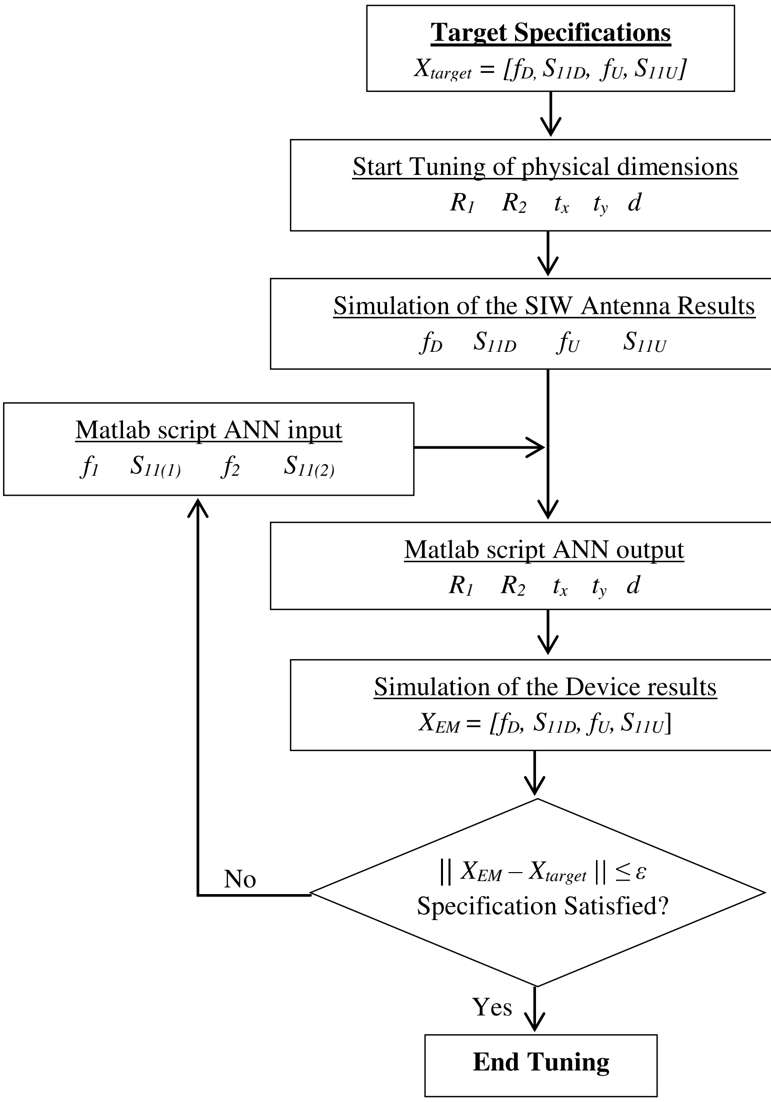

Figure 4. 34: Adaptive CAT procedure for the optimization process

b.4. Simulated Return Losses

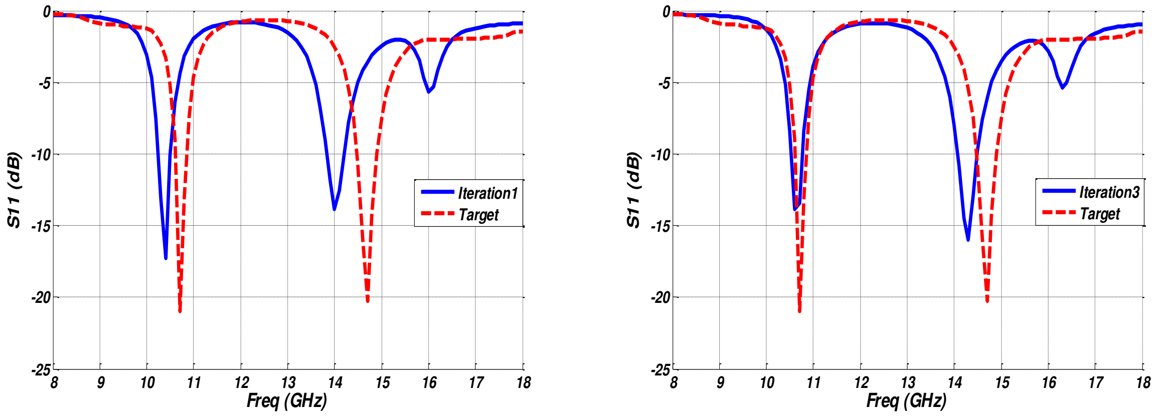

(a) 1st iteration (b) 2nd iteration

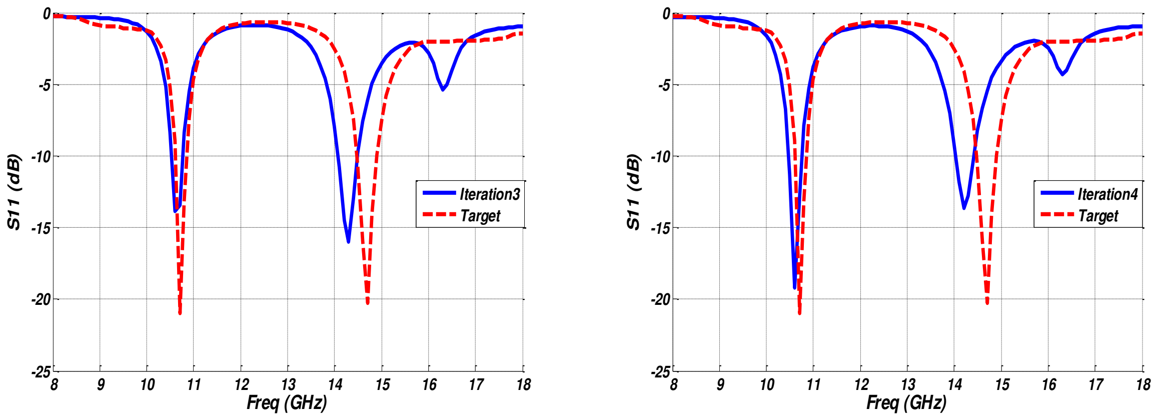

(c) 3rd iteration (d) 4th iteration

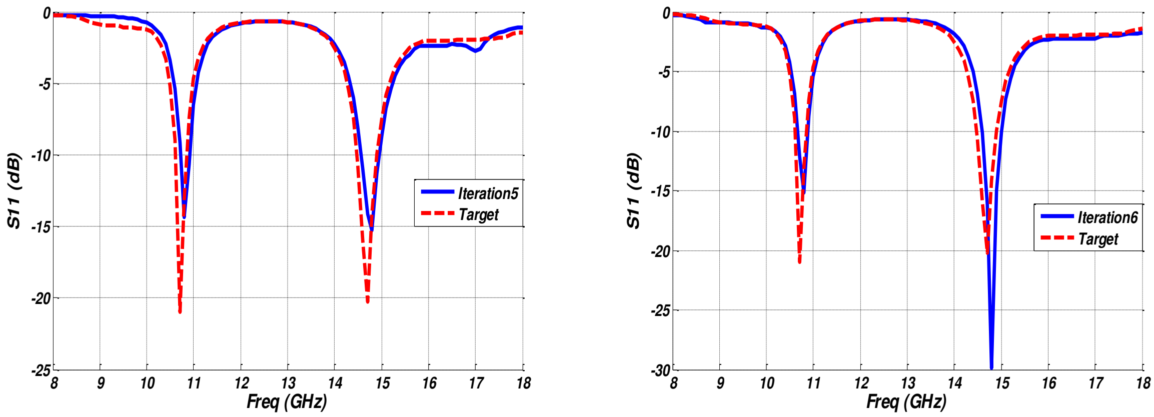

(e) 5th iteration (f) 6th iteration

Figure 4.35. Return loss graph in dual-band X/K bands of the optimized dual band coaxial-fed SIW cavity resonator antenna based ANN modelling

Parameters outputted by the trained ANN model have been implemented by HFSS software to compare the antenna response with the target response. Figure 4.35 (a to f) shows the simulated return losses of the antenna design, optimized using an accurate ANN model. It is clearly observed that the geometric configuration begins to provide low return losses from iteration to other that become very close to the target return losses in the sixth iteration. Figure (4.36.(f)) shows that the antenna structure comes with very low return losses over the entire bands of resonance. The antenna has been found to resonate at 10.84 GHz with a return loss of less than -15dB, and at 14.82 GHz with a return loss of less than -29dB. The values obtained from ANNs are very close to target values. The difference between the ANN outputs against target is measured in terms of performance which is very close to set goal to be achieved in testing for better performance of the network model.

b.5. Input Impedance and Radiation Pattern

The placement of the feeding port along the center line helps to excite corresponding cavity modes with maximum electric field at the center of the cavity resonator. As a result, TM_{010} and TM_{110} mode are excited in the proposed coaxial-fed SIW cavity resonator antenna.

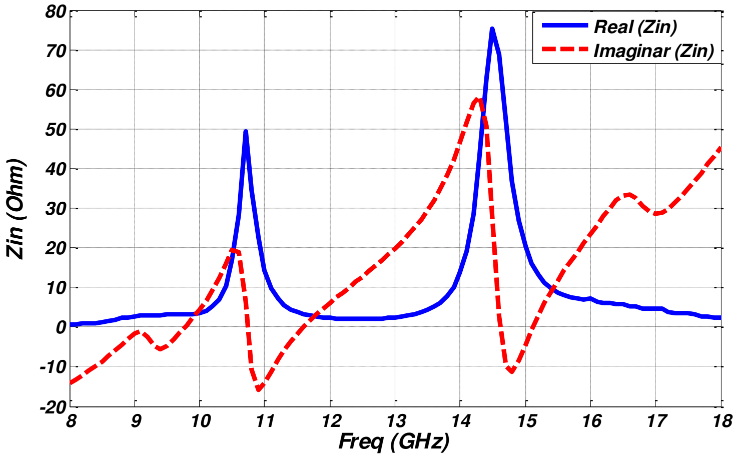

Figure 4.36. Real Z_{in}, and imaginary Z_{in} plots of the cavity resonator

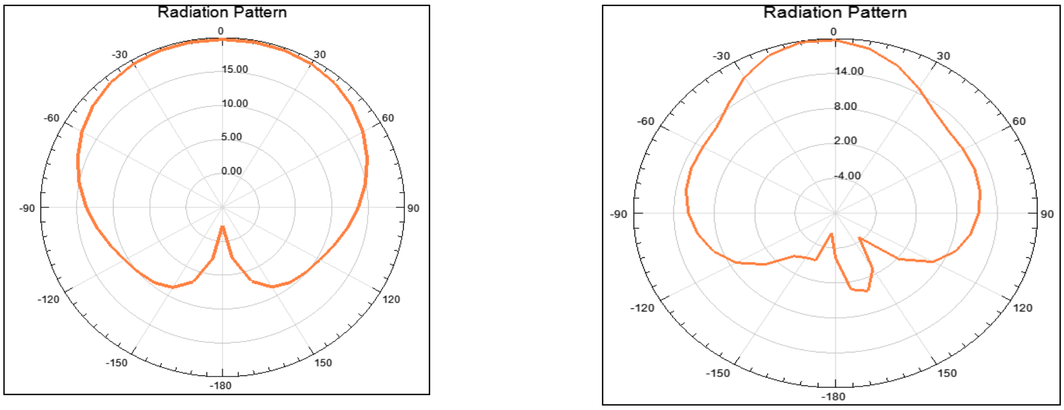

E-plane ***H-plane***

Figure 4.37. Radiation pattern graph of the optimized dual band coaxial-fed SIW cavity resonator antenna.

The optimized dimensions of the cavity are chosen such that the two modes resonate at 10.84 GHz and 14.82 GHz to cover X/Ku band applications. The excitation of different modes can be explained with the help of Z_{in} plots extracted from multi-HFSS after embedding the effect of the coaxial feed line as shown in Figure (4.36). Note that the input impedance of the coaxial-fed SIW cavity resonator antenna is well adapted for ($Z_{in} = 50\Omega$). Finally, due to the optimized SIW cavity resonator parameters, the proposed antenna produces unidirectional radiation pattern resulting in a good directivity as shown in Figure (4.37).

b.6. Equivalent Circuit Model

The coaxial-fed SIW cavity resonator antenna behaviour near to its resonance state is similar to a parallel *RLC* resonator. The lumped element values of the parallel resonator are calculated using the following set of equations (4.45):

$$\begin{cases} C = \frac{1}{2}\frac{d\,Im\left(Y_{in}\right)}{dw}\Big|_{w=w_0} \\ LCw_0^2 = 1 \\ G = \frac{1}{R} = Re\left(Y_{in}\right)\Big|_{w=w_0} \end{cases} \tag{4.45}$$

The values of the lumped elements of the parallel *RLC* resonator presenting the equivalent circuit of the input admittance ($Y_{in}=1/Z_{in}$) of the optimized dual band coaxial-fed SIW cavity resonator antenna, are listed in Table 4.5 the proposed equivalent circuit model is shown in Figure 4.38.

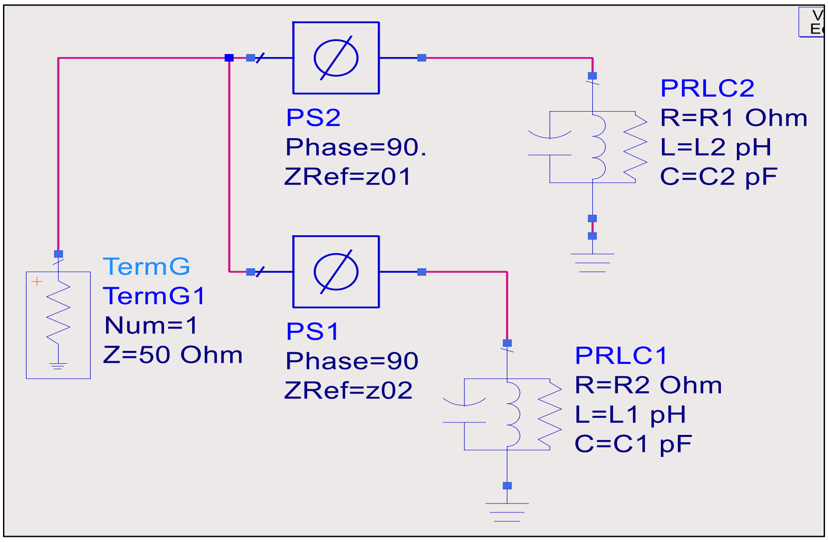

Figure 4.38. Equivalent circuit of the optimized dual band coaxial-fed SIW cavity resonator antenna.

Table 4.5: Geometrical parameters of the equivalent circuit of the optimized dual band coaxial-fed SIW cavity resonator antenna

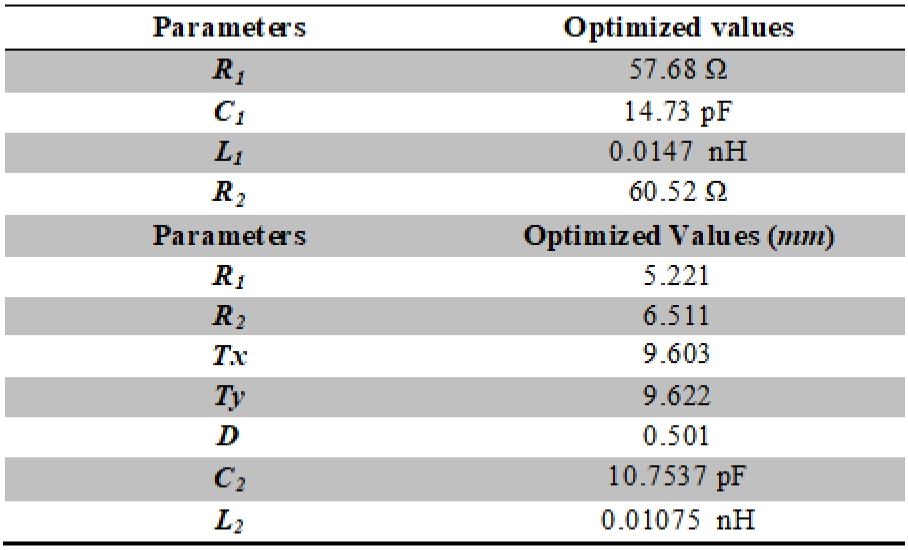

Parameters	**Optimized values**
R_1	57.68 Ω
C_1	14.73 pF
L_1	0.0147 nH
R_2	60.52 Ω
Parameters	**Optimized Values (*mm*)**
R_1	5.221
R_2	6.511
Tx	9.603
Ty	9.622
D	0.501
C_2	10.7537 pF
L_2	0.01075 nH

Table 4.6: Comparison of the optimized dual band coaxial-fed SIW cavity resonator antenna to antennas in [44-46]

The optima-zed Antenna	**Feeding technique: coaxial line**					
	Down band			**Upper band**		
	f_0	BP_D	Gain	f_U	BP_U	Gain
	10.8	410	4.9	14.8	490	6.2
Antenna in [44]	**Feeding technique:** microstrip line					
	Down band			**Upper band**		
	f_0	BP_D	Gain	f_U	BP_U	Gain
	2.4	409	4.7	2.6	420	4.9
Antenna in [45]	**Feeding technique:** SIW Cavity					
	Down band			**Upper band**		
	f_0	BP_D	Gain	f_U	BP_U	Gain
	9.4	134	4.86	16.2	955	6.15
Antenna in [46]	**Feeding technique:** Coaxial line					
	Down band			**Upper band**		
	f_0	BP_D	Gain	f_U	BP_U	Gain
	9.4	190	5.3	13.6	200	4.3

Table (4.5) shows the final geometric configuration reported from the sixth iteration, selected for the dual band coaxial-fed SIW cavity resonator antenna design after optimization.

ANN model developed for the optimization offers the advantage of superior computational ability to provide optimal geometric configurations due to its high efficiency and interconnectivity to solve design problems. The antenna exhibits high performance for a dual band range from 10.545 GHz to 10.950 GHz, and from 14.55 GHz to 15.0405 GHz, with a band pass (BP) of 410 MHz (3.81%), and 490 MHz (3.31%), that is much better as compared with the previous designs in [44-46] as demonstrated Table 4.6.

In this parts a novel dual band coaxial-fed SIW cavity resonator antenna design is proposed for X/Ku band applications by developing an accurate MLP-ANN model and carrying out multiple-HFSS simulations to achieve best approximations to target parameters providing a high structure precision as well as high performance level. About -15dB and -30dB of return losses at approximately 10.84 GHz and 14.82 GHz resonance frequencies have been obtained to be excellent characteristics for the proposed antenna design to operate in X and Ku ranges of frequencies. MLP-ANN model selected for the optimization offers the advantage of superior computational ability to provide an optimal geometric configuration of the dual band coaxial-fed SIW cavity resonator antenna due to its high accordance with user's setting.

4.11. Conclusion

The rectangular patch antennas were designed by changing the feed position, size of the substrate, and shape of the patch to get our objective or target output. This elementary design was based on changing the dimension of length because here various losses are not considered. Microstrip antenna has founded many applications in the real world due to its low-profile feature. Some of the applications are GPS, Bluetooth, Wi-Fi, missiles, and also in radio communication system etc. Many other applications are under research like multiband antenna, array antenna etc.

This chapter presented the state of the art of SIW technology: recent advances in the field of antennas implemented in SIW technology have been described and discussed. The problems related to the modeling and design of the SIW antenna were discussed and the various power solutions proposed for the implementation of the SIW antennas were presented. A microstrip patch antenna, based on SIW tulip patch antennas, was designed to work in the Ku / k bands for the first structure, and the x / ku bands for the second. These antennas were characterized and simulated using HFSS. The two alternative models with a different power supply were presented respectively in figure (4.) and figure (4.). Simulations of antenna elements have shown that they are usable for both uplink and downlink in Ku / k and x / ku bands, with narrow bandwidths and lower return losses (-10 dB) , so that they can be used to develop ANN architectures that would be able to:

a) to synthesize the response parameters, according to the changes in the operating parameters (return losses and frequencies),

b) Optimize the SIW tulip patch antenna according to the desired response parameter levels.

The artificial neural network for circular SIW antennas modified for the different bands (Ku / K bands and X / Ku bands) is proposed. The resonance frequencies (upper and lower) and their return losses are obtained from the neural network which, simulated with the help of the HFSS simulator, gives close results.For the developed MLPFFBP ANN models, we can state the following conclusion:

1. The developed MLPFFBP ANN model is estimating in the first design, a novel Circular SIW antenna design fed by a microstrip line is proposed for Ku and K band applications by developing an accurate MLP-ANN model and carrying out multiple HFSS simulations to achieve best approximations to target parameters providing a high structure precision as well as high performance level. Greater than (-19 dB) and (-29 dB) return losses at approximately 16.10 and 19.81 GHz resonance frequencies have been obtained to be excellent characteristics for the proposed antenna design to operate in Ku and K bands of frequencies. MPL-ANN model selected for the optimization offers the advantage of superior computational ability to provide an optimal circular SIW antenna geometry due to its high accordance with user's setting resonance frequencies and return losses.
2. The developed MLPFFBP ANN model is estimating in the second design, a novel dual band coaxial-fed SIW cavity resonator antenna design is proposed for X/Ku band applications by developing an accurate MLP-ANN model and carrying out multiple HFSS simulations to achieve best approximations to target parameters providing a high structure precision as well as high performance level. About -15dB and -30dB of return losses at approximately 10.84 GHz and 14.82 GHz resonance frequencies have been obtained to be excellent characteristics for the proposed antenna design to operate in X and Ku ranges of frequencies. MPL-ANN model selected for the optimization offers the advantage of superior computational ability to provide an

optimal geometric configuration of the dual band coaxial-fed SIW cavity resonator antenna due to its high accordance with user's setting.

Thus, the proposed artificial neural network model can be used to design an efficient SIW circular patch antenna for dual band applications. In addition, an artificial neural network model may be designed to calculate the dimensions of a tulip shaped circular SIW antenna. The advantage of the neural network model is that it completely eliminates the repetition of data in the calculation of resonant frequencies. In conclusion, these results substantiate that the proposed ANN model can be successfully used to determine the resonant frequencies.

[1] C. A. Balanis, “Antenna Theory: Analysis and Design”, 1997 by John Wiley & Sons, Inc.

[2] H. Gutton and G. Baissinot, “Flat Aerial for Ultra High Frequencies,” French Patent No. 703 113, 1955.

[3] C. A. Balanis, Antenna Theory: Analysis and Design. Hoboken, NJ:Wiley, ch. 14, 2016.

[4] D. M. Pozar, “Microstrip Antennas,” *Proc. IEEE*, Vol. 80, No. 1, pp. 79–81, January 1992.

[5] N. K. Uzunoglu, N. G. Alexopoulos, and J. G. Fikioris, “Radiation Properties of Microstrip Dipoles,” *IEEE Trans. Antennas Propagat.*, Vol. AP-27, No. 6, pp. 853–858, November 1979.

[6]. I. E. Rana and N. G. Alexopoulos, “Current Distribution and Input Impedance of Printed Dipoles,” *IEEE Trans. Antennas Propagat.*, Vol. AP-29, No. 1, pp. 99–105, January 1981.

[7] Balanis, C.A. (2005). *Antenna Theory Analysis and Design, Third edition*, Johan Wiley & Sons. ISBN 0-471-66782-X.

[8] James J.R, P.S. Hall (1989). H*andbook of Microstrip Antennas*, Peter Peregrinus.

ISBN 0 86341 150 9.

[10]. K. R. Carver and J. W. Mink, “Microstrip Antenna Technology,” *IEEE Trans. Antennas Propagat.*, Vol. AP-29, No. 1, pp. 2–24, January 1981.

[11]. J. R. James and P. S. Hall, *Handbook of Microstrip Antennas*, Vols. 1 and 2, Peter Peregrinus, London, UK, 1989.

[12] C. Balanis, Modern Antenna Handbook. John Wiley and Sons, 2008.

[13]. E. O. Hammerstad, “Equations for Microstrip Circuit Design,” *Proc. Fifth European Microwave Conf.*, pp. 268–272, September 1975.

[14] R. F. Harrington, *Time-Harmonic Electromagnetic Fields (IEEE Press Series on*

Electromagnetic Wave Theory), Second Edition, Wiley-IEEE Press, August 2001.

[15]. A. G. Derneryd, “A Theoretical Investigation of the Rectangular Microstrip Antenna Element,” *IEEE Trans. Antennas Propagat.*, Vol. AP-26, No. 4, pp. 532–535, July 1978.

[16] D. G. Fang, Antenna Theory and microstrip antenna , Hirasawa, K., Haneishi, M. (eds.), Analysis, Design, and Measurement of Small and Low-Profile Antennas. Chapter 4: Suzuki, Y. “Key Points in the Design and Measurement of Microstrip Antennas”. Artech House, Boston, 1992.

[17] Z. Kordiboroujeni and J. Bornemann, “Designing the width of substrate integrated waveguide structures,” IEEE Microw. Wireless Compon. Lett., vol. 23, no. 10, pp. 518–520, Oct. 2013.

[18] R.Simon, Sauders, Alejandro , Antennas And Propagation For Wireless Communication Systems, John Wiley & Sons, 2007.

[19] Dominic Deslandes and Ke Wu, “Single-Substrate IntegrationnTechnique of Planar Circuits and Waveguide Filter”, IEEE Transactions on Microwave Theory and Techniques, VOL. 51, NO. 2, Februaryn2003.

[20] Dominic Deslandes and Ke Wu, “Design Consideration and Performance Analysis of Substrate Integrated Waveguide Components”, Microwave Conference, 2002, 32nd European.

[21] Sotoodeh, Z., B. Biglarbegian, F. Hodjat-Kashani, and H. Ameri, “A novel bandpass waveguide filter structure on SIW technology,” *Progress In Electromagnetics Research Letters*, Vol. 2, 141–148, 2008.

[22] Zhang, X.-C., Z.-Y. Yu, andJ. Xu, “Novel band-pass Substrate IntegratedW aveguide (SIW) filter basedon Complementary Split Ring Resonators (CSRRs),” *Progress In Electromagnetics Research*, PIER 72, 39–46, 2007.

[23]. M. Bozzi, A. Georgiadis, and K. Wu, “Review of substrate-integrated waveguide circuits and antennas”, IET Microw. Antennas Propag., vol. 5, no. 8, pp. 909–920, Jun. 2011.

[24] D. Deslandes, and K. Wu, “Integrated microstrip and rectangular waveguide in planar form”, *IEEE Microw. Wireless Compon. Lett.*, vol. 11, no. 2, Feb 2001, pp. 68-70.

[25]. Pozar, D. Microwave Engineering, 4th ed.; Addison Wesley: New York, NY, USA, 1990.

[26] G. A. Tagliarini, J. F. Christ, and E. W. Page, "Optimization Using Neural Networks," *IEEE Transactions on Computers,* vol. 40, pp. 1347-1358, 1991.

[27] R. E. King, *Computational Intelligence in Control Engineering.* New York: Marcel

Dekker, Inc., 1999.

[28] Simon Haykin "Neural Networks and Learning Machines" Third Edition by Pearson Education, Inc, Upper Saddle River, New Jersey 07458.2009

[29] Q. J. Zhang and K. C. Gupta, *Neural Networks for RF and Microwave Design*, Artech House, 2000.

[30] Q. J. Zhang, K. C. Gupta, and V. K. Devabhaktuni, 2003. Artificial neural networks for RF and microwave design from theory to practice, IEEE Trans. Microwave Theory and Tech., vol. 51, no. 4, pp. 1339–1350.

[31] Zhang Q, C. K. Gupta, and K. Devabhaktuni, "Artificial neural networks for RF and microwave design - From theory to practice," *IEEE Trans. on Microw. Theory and Techn.,* Vol. 51, pp. 1339–1350, Apr. 2003.

[32] T. K. Kwok et al "Constructive algorithms for structure learning in feed forward neural networks for regression problems," *IEEE Trans. on Neural Netw.*, Vol. 8, pp. 630–645, May 1997.

[33] W. F. Richards et al., "An improved theory for microstrip antennas and applications," *IEEE Trans. on Antennas and Propagation*, vol. 29, no. 1, pp. 38–46, Jan., 1981.

[34] T. Y. Kwok and D. Y. Yeung, "Constructive algorithms for structure learning in feedforward neural networks for regression problems," IEEE Trans. Neural Networks, vol. 8, pp. 630–645, May 1997.

[35] K. Hornik, M. Stinchcombe, and H. White, "Multilayer feedforward networks are universal approximators," Neural Networks, vol. 2, pp. 359-366, 1989.

[36] G. Q. Luo et al, "Planar slot antenna backed by substrate integrated waveguide cavity," *IEEE Anten. and Wirel. Propag. Lett.*, Vol. 7, pp. 235-239, Apr. 2008.

[37] F. Xu and K. Wu, "Guided-wave and leakage characteristics of substrate integrated waveguide," *IEEE Trans. Microw. Theory Techn.,* Vol. 53, pp. 66–73, Jan. 2005.

[38] L. Yan, W. Hong, G. Hua, J. Chen, K. Wu and T. J. Cui, "Simulation and experiment on SIW slot array antennas," *IEEE Microw. Wireless Comp. Lett*., Vol. 14, No. 9, pp. 446-448, 2004.

[39] D. M. Pozar, *Microwave engineering*. Hoboken, NJ: J. Wiley, 2005.

[40] F. Ishihara and S. Iiguchi, "Equivalent characteristic impedance formula of waveguide and its applications," *Electronics and Communications in Japan (Part II: Electronics),* vol. 75, pp. 54-66, 1992.

[41] Y. Cassivi, L. Perregrini, P. Arcioni, M. Bressan, K. Wu, G. Conciauro, “Dispersion characteristics of substrate integrated rectangular waveguide,” IEEE *Microw. Wireless Comp. Lett.*, Vol. 12, No. 9, pp. 333-335, 2002.

[42] Yu Jian Cheng “Substrate Integrated Antennas and Arrays” by Taylor & Francis Group, LLCCRC Press is an imprint of Taylor & Francis Group, 2016.

[43] Dominic Deslandes and Ke Wu, “Accurate modeling ,wave mechanisms and design consideration of Substrate Integration waveguide ”, IEEE Transactions on Microwave Theory and Techniques, VOL. 54, NO. 6, pp.2516-2526- 2006

[44] S. Lemey, F. Declercq, and H. Rogier, “Dual band substrate integrated waveguide textile antenna with integrated solar harvestor,” *IEEE Anten. Wirel. Propag. Lett.*, Vol. 13, pp. 269–272, 2014

[45] T. Zhang et al, “Design and analysis of SIW cavity backed dual-band antennas with a dual-mode triangular-ring slot,” *IEEE Trans. Anten. Propag.*, Vol. 62, pp. 5007–5016, Oct. 2014.

[46] S. Mukherjee, A. Biswas, K. V. Srivastava, “Substrate integrated waveguide cavity backed dumbbell shaped slot antenna for dual frequency applications,” *IEEE Anten. Wirel. Propag. Lett.,* Vol. 14 , pp. 1314 – 1317, 2015.

General Conclusion

General Conclusion

This thesis depicted a broad reject band Low Pass Filter with a small size using one DGS unit and one microstrip compensated line. The contributed microstrip filter illustrated a good performance in terms of sharp cutoff frequency response, and high rejection in the stopband , low insertion loss(IL) in the passband. The LPF was investigated with the simulation results. It was largely employed for eliminating the undesirable frequency rejections in modern microwave communication systems.

In this thesis we have approached the synthesis of microwave filters, by means of the coupling matrix method, in a general way. In the first part , we have composed the necessary theory to obtain the matrix of (N+2)x(N+2) coupling of a Chebyshev bandpass filter, either in even or odd order. We have also determined the steps necessary to obtain the filter response frequency from the obtained coupling matrix, in order to check its validity.

Secondly, we have extended the developed theory, so that fully canonical filters can be designed, thus overcoming this and other disadvantages of the method based on the (N+2)x(N+2) coupling matrix. Therefore, we have presented the necessary theory to obtain transverse (N+2) coupling matrix, which permits the existence of multiple input/output couplings in bandpass filters. In addition, we include the extension of this formulation to the case of rejected band filters, as well as examples of each case.

In the third step, we have presented different similarity transformation sequences that applied to the filter coupling matrix, lead us to different topologies. Specifically, we have focused on the transformations that lead us to the topologies canonical folded form and parallel connected. We have also presented different examples that prove the validity of the methods used in each case, as well as the Matlab developed.

Fourth, we have addressed the synthesis of filters with zeroes of transmission at finite frequencies arbitrarily situated, using resonant nodes (RN). Likewise, we have made different design examples to validate the synthesis methods developed.

Finally, in the last chapter we have proposed the implementation of different and interesting examples of practical application of all synthesis processes developed throughout the project, as well as the different transformations that applied to the coupling matrix lead to one or another topology. We also include a real structure that implement the designed coaxial cavity microwave filter, testing the validity and utility of all the work done. This thesis illustrated the model of Cauchy extraction technique which produce a lossless polynomial model for coaxial microwave filters ; the microwave filter formulation permit the diagnostic of a model from the simulated S- parameters of the filter, which is suitable for the synthesis of a low pass equivalent circuit (the derived polynomials satisfy the Feldkeller's equation and the transmission zeros are either imaginary or in complex pairs with opposite real part and equal imaginary part). The extraction technique was successfully investigated employing the simulated S- parameters of a coaxial cavity microwave filter.

This thesis depicted the application of the aggressive space mapping (ASM) optimization, in combination with equivalent circuit models based on Cauchy technique, to the design of coaxial cavity microwave filter. According to the principle of the ASM the problems of finding the optimal physical dimension of the microwave filter. Finally a coaxial cavity microwave filter is designed and its optimal physical dimension with ideal response is achieved after six steps. It is obtained that the simulated results agree well with ideal coupling matrix.

In this thesis, a suggested novel dualband coaxial-fed SIW cavity resonator antenna design was presented for X/Ku band applications by developing an accurate MLP-ANN model and carrying out multiple-HFSS simulations to realize the best approximations to obtain target parameters providing a high structure precision as well as high performance level. About -15dB and -30dB of return losses at approximately 10.84 GHz and 14.82 GHz resonance frequencies have been obtained to be excellent characteristics for the proposed antenna design to operate in X and Ku ranges of frequencies. MPL-ANN model selected for the optimization offers the advantage of superior computational ability to provide an optimal geometric configuration of the dualband coaxial-fed SIW cavity resonator antenna thanks to its high accordance with user’s setting.

List of Publications

I. International publications

1. **M. Chetioui**, A. Boudkhil, N. Benabdallah, and N. Benahmed, “Design and analysis of Ku/K-band circular SIW patch antenna using 3D EM-based artificial neural networks,” *TELKOMNIKA*, Vol. 16, Issue 2, pp. 594-599, Apr. 2018.

2. **M. Chetioui**, B. Bouras, R. Bouhmidi, and N. Benahmed, “Design and Optimization of Microwave Coaxial Bandpass Filter based on Cauchy Method and Aggressive Space Mapping Technique,” *International Journal of Microwave and Optical Technology*, Vol. 13, Issue 1, pp. 40-50, Jan. 2018.

3. A. Boudkhil, **M. Chetioui**, N. Benabdallah, and N. Benahmed, “Development and performance enhancement of MEMS helix antenna for THz applications using 3D HFSS-based efficient electromagnetic optimization,” *TELKOMNIKA*, Vol. 16, Issue 1, pp. 210-216, Feb. 2018.

4. **M. Chetioui**, A. Boudkhil, N. Benabdallah, and N. Benahmed, “A novel dualband coaxial-fed SIW cavity resonator antenna using ANN modeling,” *Journal of Engineering Science and Technology Review*, Vol. 11, Issue 2, pp. 82-87, May. 2018.

II. International communications

1. **M. Chetioui**, A. Boudkhil, N. Benabdallah, and N. Benahmed, “Design and optimization of SIW patch antenna for Ku band applications using ANN algorithms,” in the 4th IEEE International Conference of Optimization Applications (ICOA), Apr. 26-27, Casablanca, Morocco, 2018.

2. A. Boudkhil, **M. Chetioui**, N. Benabdallah, A. Ouzzani, and N. Benahmed, “A novel design of THz MEMS Λ-Helix antenna using HFSS-based effective stochastic solvers,” in the 4th IEEE International Conference of Optimization Applications, Apr. 26-27, Casablanca, Morocco, 2018.

Abstract

Coupled resonator circuits are the basis for the design of two-port Bandpass microwave filters. The design approach is based on synthesis of the coupling matrix for multiple coupled resonators using Cauchy method and space mapping optimization. This behavior is achieved through the use of filters made up of electromagnetically coupled resonant structures. Antennas present also an integral part of the microwave systems employed to transmit and receive electromagnetic waves for a multitude of purposes; they serve as a transducer that converts guided waves into free-space waves in the transmitting mode, or vice-versa in the receiving mode. In this view, the present research work describes analytical problems of microwave cascaded filters and patch antennas and explains their physical behaviors with particular emphasis on major optimization challenges facing the device structure complexity. The different microwave devices are optimized using advanced computer aided tuning (CAT) techniques including coupling matrix, Defected Ground Structure (DGS) and Artificial Neural Networks (ANN) to vary the device geometry in order to maximize its performance with a high accuracy for the selective band of frequencies.

Key words: Coupled Resonator Filter, Space mapping, Cauchy method, Patch Antennas, Coupling Matrix, DGS, ANN Optimization.

ملخص

إن دارات الرنين الكهربائية تمثل اللبنات الأساسية لتصميم مرشحات الموجات الميكرومترية ثنائية القطب حول مجال ضيق من التواترات. يعتمد أسلوب التصميم على توليف مصفوفة التأثير الكهرومغناطيسي بين دارات الرنين المتعددة باستخدام طريقة كوشي وطريقة البحث عن القيم المثلى للمتغيرات الفيزيائية للتصميم التي تنتج عنها القيم المطلوبة لمتغيرات مقابلة لها في فضاء محاكي. ويتحقق هذا من خلال استخدام دارات رنين متفاعلة فيما بينها بالتأثير الكهرومغناطيسي نضيف إلى هذا الهوائيات التي تشكل لبنة متكاملة في أنظمة الموجات الميكرومترية والتي تستعمل لبث واستقبال الموجات الكهرومغناطسية وهي بمثابة محولات لموجات داخل دارات إلى موجات تنتشر في الفضاء عند استخدامها كمرسل وعكس هذه العملية عند استخدامها كمستقبل.

في هذا الإطار يتناول هذا البحث كيفية دراسة مرشحات مركبة مع التركيز على تصميمها بدقة مع ما في ذلك من تحد لصعوبة العملية. يعتمد تصميم الأنظمة الميكرومترية على عدة وسائل دعم لإجراء الحسابات المعقدة نذكر منها التعديل المدعوم بالحاسوب إنشاء دارات على الوجه لمعدني القاعدي والشبكات العصبية الاصطناعية. تساعدنا هذه الوسائل في حساب المعطيات الناتجة عن الأنظمة عند تغيير هندستها وأبعادها الفيزيائية لأجل الوصول إلى أحسن أداء يفي بالموصفات المطلوبة .

الكلمات المفتاحية: مرشحات الموجات الميكرومتريةدارات الرنين - طريقة البحث عن القيم المثلى- الشبكات العصبية الاصطناعية - طريقة كوشي

Résumé

Les circuits à résonateurs couplés constituent les éléments de base pour la conception des filtres micro-ondes passe bande à deux ports. L'approche de conception est basée sur la synthèse de la matrice de couplage pour plusieurs résonateurs couplés en utilisant la méthode de Cauchy et la technique d'optimisation space-mapping. Ce comportement est obtenu grâce à l'utilisation de filtres constitués de structures résonantes couplées électro-magnétiquement. Les antennes présentent également une partie intégrante des systèmes à micro-ondes utilisés pour transmettre et recevoir des ondes électromagnétiques à des fins multiples, ils servent de transducteurs qui convertissent les ondes guidées en ondes libres dans le mode de transmission, ou vice versa dans le mode de réception. Dans cette perspective, le présent travail de recherche décrit les problèmes analytiques des filtres en cascade et des antennes patch et explique leurs comportements physiques avec une considération particulière des principales difficultés d'optimisation face à la complexité de la structure. Les différents dispositifs à hyperfréquences sont optimisés à l'aide de techniques avancées d'ajustement assisté par ordinateur (CAT), notamment la matrice de couplage, la structure defected ground et les réseaux neuronaux artificiels (RNA) pour varier la géométrie de la structure en vue de maximiser ses performances et achever une grande précision pour les bandes de fréquences choisies.

Mots clés: Filtres à résonateurs couplés, méthode de Cauchy, méthode de mappage spatial, antennes à patch, matrice de couplage, structures de plan défoncées, réseaux neuronaux artificiels.